ANCHAM

JANUARY 15, 1993

Analytical CHEMISTRY

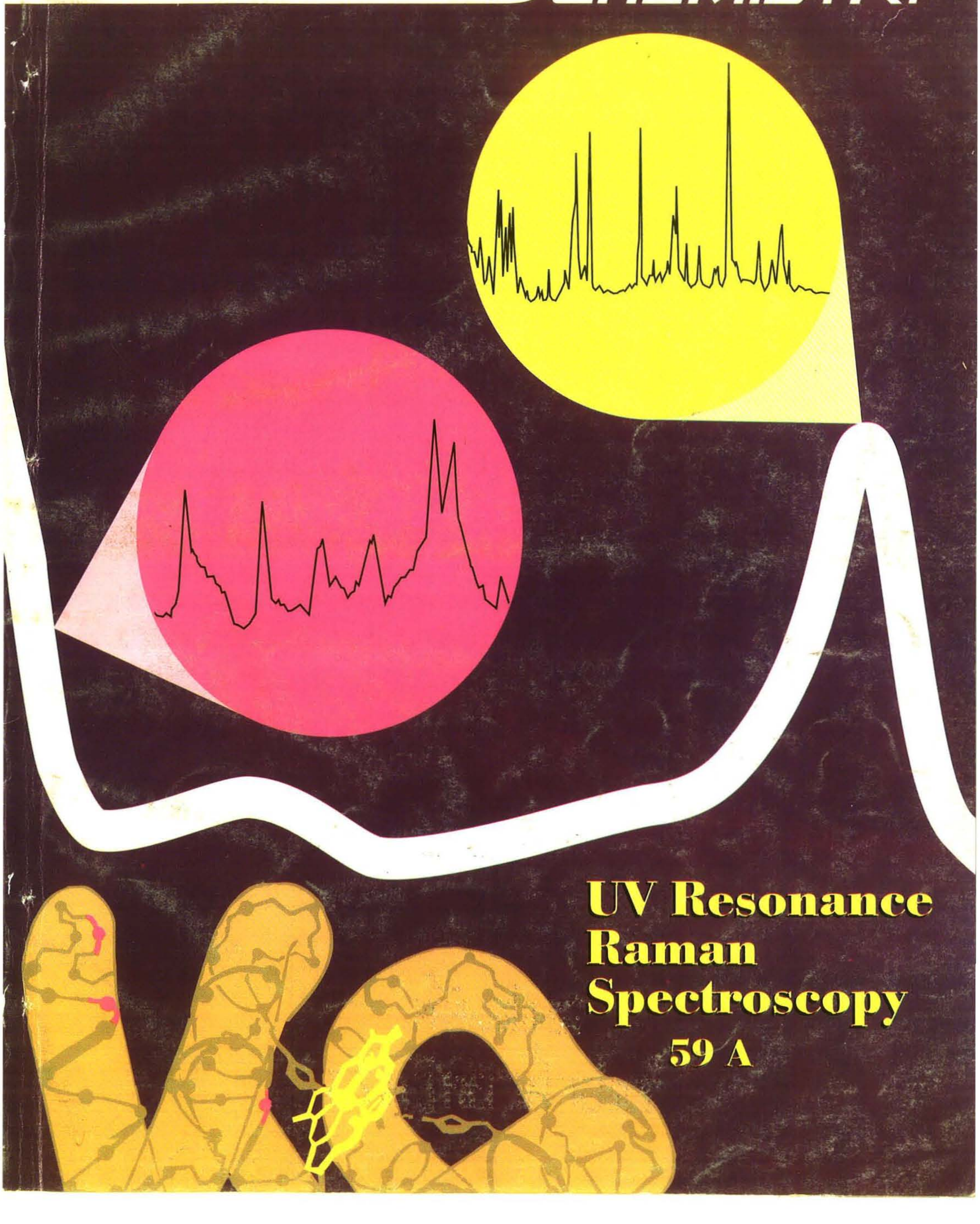

UV Resonance Raman Spectroscopy

59 A

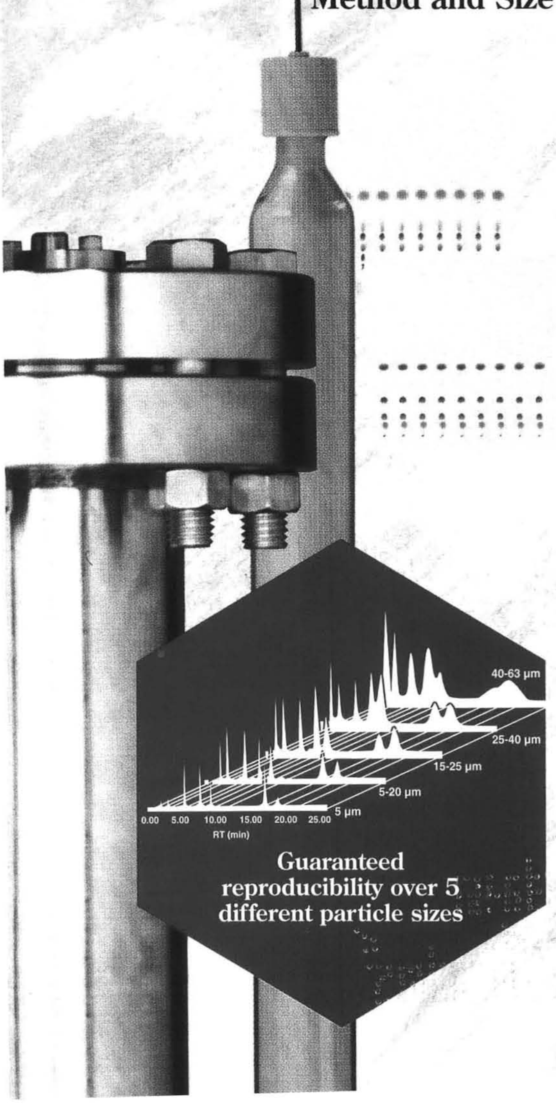
40-63 µm
25-40 µm
15-25 µm
5-20 µm
5 µm
0.00 5.00 10.00 15.00 20.00 25.00
RT (min)


Wyatt Technology Corporation
DETECTOR
DETECTOR VOLTAGE
SELECT
miniDAWN®

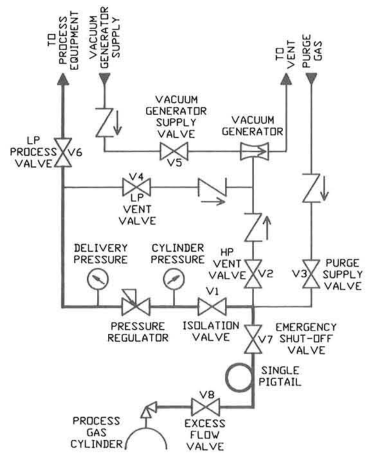
TO PROCESS EQUIPMENT
VACUUM GENERATOR SUPPLY
TO VENT
PURGE GAS
VACUUM GENERATOR SUPPLY VALVE
VACUUM GENERATOR
LP PROCESS VALVE
V6
V5
V4
LP VENT VALVE
DELIVERY PRESSURE
CYLINDER PRESSURE
HP VENT VALVE
V2
V3
PURGE SUPPLY VALVE
V1
PRESSURE REGULATOR
ISOLATION VALVE
EMERGENCY SHUT-OFF VALVE
V7
SINGLE PIGTAIL
V8
PROCESS GAS CYLINDER
EXCESS FLOW VALVE

JANUARY 15, 1993
VOLUME 65
NUMBER 2

The Audit Bureau
ANCHAM
65(2) 47A–82A/97–192 (1993)
ISSN 0003-2700

Registered in U.S. Patent and Trademark Office;

EDITOR: **ROYCE W. MURRAY,** University of North Carolina

ASSOCIATE EDITORS: **Catherine C. Fenselau,** University of Maryland Baltimore County, **William S. Hancock,** Genentech, **James W. Jorgenson,** University of North Carolina, **Robert A. Osteryoung,** North Carolina State University, **Edward S. Yeung,** Iowa State University/Ames Laboratory

Editorial Headquarters, research section
Department of Chemistry
Venable and Kenan Laboratories
University of North Carolina
Chapel Hill, NC 27599-3290
Phone: 919-962-2541
Fax: 919-962-2542
E-mail: Murray @ uncvx1.oit.unc.edu

Editorial Headquarters, A-page section
1155 Sixteenth St., N.W.
Washington, DC 20036
Phone: 202-872-4570
Fax: 202-872-4574
E-mail: rmh96 @ acs.org

Managing Editor: Mary Warner
Senior Editor: Louise Voress
Associate Editor: Grace K. Lee
Assistant Editor: Felicia Wach
Editorial Assistant: Deborah Noble
Contributing Editor: Marcia Vogel

Head, Graphics and Production: Leroy L. Corcoran
Art Director: Alan Kahan
Designers: Peggy Corrigan, Robert Sargent
Production Editor: Elizabeth Wood
Electronic Composition: Wanda R. Gordon
Circulation: David Schulbaum

LabGuide
Managing Editor of Directories and Databases: Kathleen Strum
Associate Editor: Joanne Mullican
Assistant Editor: Susan Barclay

Journals Dept., Columbus, Ohio
Editorial Office Manager: Mary E. Scanlan
Journals Editing Managers: Kathleen E. Duffy, Anne C. O'Melia, Joseph E. Yurvati
Assistant Editors: Stephanie R. Harrell, Diane E. Needham

Publications Division
Director: Robert H. Marks
Head, Special Publications: Anthony Durniak
Head, Journals: Charles R. Bertsch

Analytical® CHEMISTRY

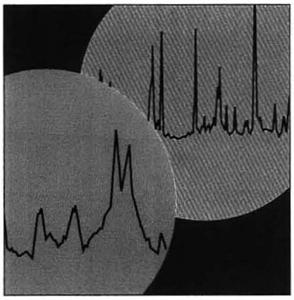

A Unique, New Analysis Technique for Characterizing Materials... Modulated DSC™

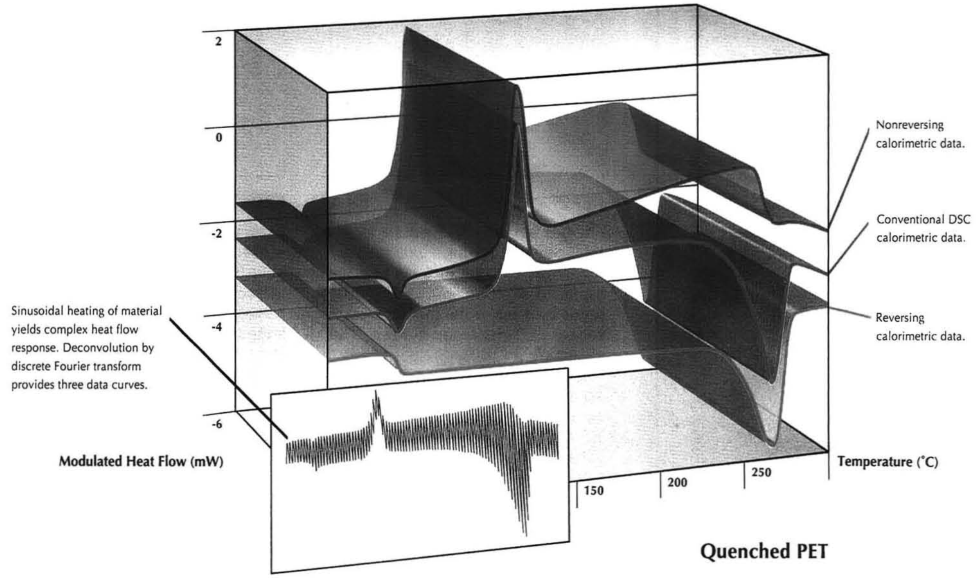

Nonreversing calorimetric data.

Conventional DSC calorimetric data.

Reversing calorimetric data.

Sinusoidal heating of material yields complex heat flow response. Deconvolution by discrete Fourier transform provides three data curves.

Quenched PET

Modulated DSC (MDSC) is a new, patent-pending thermal analysis technique which allows unique insight into the structure and behavior of materials.

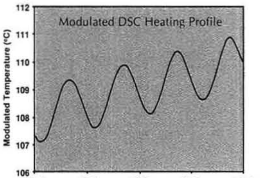

By subjecting sample materials to a sinusoidal, or modulated heating profile rather than a linear heating profile, MDSC provides information which was previously unavailable.

Unique analysis capabilities include:

- *Separation of reversing and nonreversing characteristics of thermal events.*
- *Direct heat capacity measurement.*
- *Improved resolution of closely occurring and overlapping transitions.*
- *Increased sensitivity for subtle transitions.*

In addition, conventional DSC information is available from the same experiment.

Modulated DSC is the latest in a 30 year history of innovations from TA Instruments, the world leader in thermal analysis instrumentation. MDSC complements the high sensitivity and wide temperature range of the TA Instruments Model DSC 2910 Differential Scanning Calorimeter, making it the most versatile thermal analysis instrument available.

Call TA Instruments **TOLL FREE at 800-634-4446** to receive an informative brochure and the latest from our growing list of MDSC application notes.

TA *Instruments*

TA Instruments, Inc.
109 Lukens Drive, New Castle, DE 19720
PHONE (302) 427-4000 • FAX (302) 427-4001

ISO 9000 CERTIFICATION

CIRCLE 102 ON READER SERVICE CARD

Analytical CHEMISTRY

ANALYTICAL CHEMISTRY (ISSN 0003-2700) is published semimonthly by the American Chemical Society, 1155 Sixteenth St., N.W., Washington, DC 20036. Second-class postage paid at Washington, DC, and additional mailing offices. Postmaster: Send address changes to ANALYTICAL CHEMISTRY, Member & Subscriber Services, P.O. Box 3337, Columbus, OH 43210.

Canadian GST Reg. No. R127571347.

Subscription and Business Information

1993 subscription rates include air delivery outside the U.S., Canada, and Mexico. Canadian subscriptions are subject to 7% GST.

	Members	Nonmembers (personal)	Nonmembers (institutional)
U.S.	$ 36	$ 78	$ 415
Canada and Mexico	72	114	451
Europe	117	230	496
Other countries	141	254	520

Nonmember rates in Japan: Rates above do not apply to nonmember subscribers in Japan, who must enter subscription orders with Maruzen Company Ltd., 3–10. Nihonbashi 2-chrome, Chuo-ku, Tokyo 103, Japan. Tel: (03) 272-7211.

For multi-year and other rates, call toll free 800-227-5558 in the U.S. and Canada; in the Washington, DC, metropolitan area and outside the U.S., call 202-872-4363; fax 202-872-4615.

Single issues, current year, $16.00 except review issue, $50.00, and LabGuide, $50.00; **back issues and volumes and microform editions** available by single volume or back issue collection. For information or to order, call the number listed for subscription orders by phone; or write the Microform & Back Issues Office at the Washington address.

Subscription orders by phone may be charged to VISA, MasterCard, or American Express. Call toll free 800-333-9511 in the continental U.S.; in the Washington, DC, metropolitan area and outside the continental U.S., call 202-872-8065. Mail orders for new and renewal subscriptions should be sent with payment to American Chemical Society, Department L-0011, Columbus, OH 43268-0011.

Changes of address must include both old and new addresses with ZIP code and a recent mailing label. Send all address changes to the ACS Columbus address. Please allow 6 weeks for change to become effective. **Claims for missing numbers** will not be allowed if loss was due to failure of notice of change of address to be received in the time specified; if claim is dated (a) North America—more than 90 days beyond issue date, (b) all other foreign—more than 180 days beyond issue date. Hard copy claims are handled at the ACS Columbus address.

ACS membership information: Lorraine Bowlin (202-872-4567)

Articles

*Corresponding author

continued on p. 53 A

What is the chemical structure of a polymer system? Get the answer in this definitive new resource...

Spectroscopy of Polymers

by JACK L. KOENIG

Department of Macromolecular Science
Case Western Reserve University

At last—the definitive resource for scientists, engineers, and graduate students in polymer science on the primary spectroscopic methods of polymer characterization that continues where introductory-level texts end.

Spectroscopy of Polymers was written for those whose knowledge of polymer chemistry includes some familiarity with the basic vibrational and resonance spectroscopic methods, but who have limited experience in applying the modern techniques of FTIR, Raman, and/or NMR spectroscopy. The book provides a solid background in the fundamental aspects and experimental applications of the primary spectroscopic methods and their advantages and disadvantages for particular polymer systems. It brings both professional and student up-to-date on the current techniques and facilitates communication with others in the field.

Throughout the eleven chapters of this book, Koenig provides clear, concise examples to demonstrate the strengths and weaknesses of the various vibrational and NMR techniques and offers the reader practical knowledge of how to select the most appropriate solutions to polymer structure problems. Numerous illustrations accompany both text and examples.

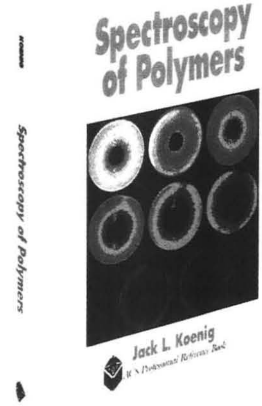

ACS Professional Reference Book
450 pages (1992)
Clothbound: ISBN 0-8412-1904-4 $89.95
Paperback: ISBN 0-8412-1924-9 $49.95

TO ORDER CONTACT:

American Chemical Society
Distribution Office, Dept. 31
1155 Sixteenth Street, N.W.
Washington, DC 20036

To charge your order by phone,
call TOLL-FREE 1-800-227-5558.
In Washington, DC, call 202-872-4363.
Or FAX your order to 202-872-6067.

ABOUT THE AUTHOR

Jack Koenig is the J. Donnell Institute Professor of the Departments of Macromolecular Science and Chemistry at Case Western Reserve University, Cleveland, Ohio, and has over 25 years teaching and research experience to his credit. He has published over 430 papers, edited or authored 5 monographs, and has won numerous awards, among them the prestigious Pittsburgh Scpectroscopy Award, the New York Society of Spectroscopy Gold Medal, the Society of Plastics Engineers Research Award, the ACS Doolittle Award.

CONTENTS

Analytical CHEMISTRY

Editorial Information

Instructions for authors of AC RESEARCH are published in the January 1 issue, p. 91. Guidelines for the INSTRUMENTATION, REPORT, ANALYTICAL APPROACH, and A/C INTERFACE features are published in the January 1 issue, p. 90. Please consult these instructions and guidelines prior to submitting a manuscript for consideration for publication.

Manuscripts for publication in AC RESEARCH (4 copies of text and illustrative material) should be submitted to the Editor at the University of North Carolina address. Please include a signed copyright status form; a copy of this document appears on p. 95 of the January 1 issue. Manuscripts for publication in the A-page section should be submitted to the Washington editorial staff.

For individual reprints of AC RESEARCH or A-page articles, please contact the authors directly. Bulk reprints of individual articles are available from ACS. For information, write or call the Distribution office at the ACS Washington address (202-872-4539; fax 202-872-4615).

ACS Division of Analytical Chemistry
Chair, Joseph L. Glajch (508-671-8413)
Secretary, Sarah Rutan (804-367-1298)

ACS Information

Library Services	202-872-4515
Education Division	202-872-4388
Meetings Dept.	202-872-4397
Member Services	202-872-4414
Employment Services	202-872-6120
Public Outreach	202-872-4091

Supplementary material is noted in the table of contents with a ■. It is available as photocopy ($10.00 for up to 3 pages and $1.50 per page for additional pages, plus $2.00 for foreign postage) or as 24X microfiche ($10.00, plus $1.00 for foreign postage). Canadian residents should add 7% GST. See supplementary material notice at end of journal article for number of pages. Orders *must* state whether for photocopy or for microfiche and give complete title of article, names of authors, journal, issue date, and page numbers. Prepayment is required and prices are subject to change. Order from Microforms & Back Issues Office at the ACS Washington address.

The paper used in this publication meets the minimum requirements of American National Standard for Information Sciences—Permanence of Paper for Printed Library Materials, ANSI Z39.48-1984.

Journals Department
American Chemical Society
2540 Olentangy River Road
P.O. Box 3330
Columbus, OH 43210
614-447-3600, Ext. 3171
TELEX 6842086; Fax 614-447-3745

Member & Subscriber Services
American Chemical Society
P.O. Box 3337
Columbus, OH 43210
614-447-3776
800-333-9511

Technical Notes

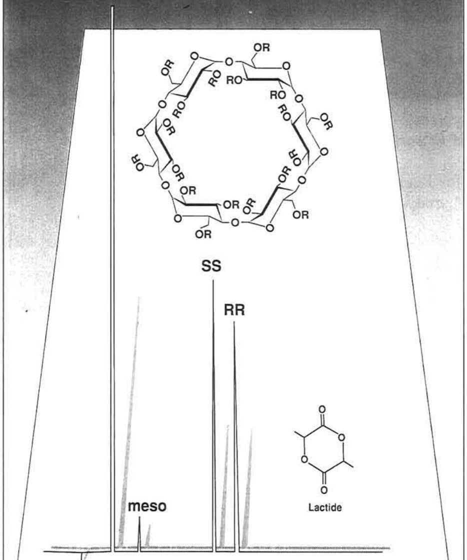
OR
RO
SS
RR
meso
Lactide

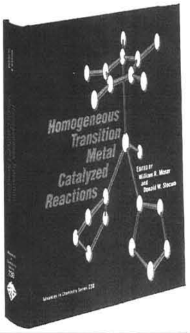
Homogeneous Transition Metal Catalyzed Reactions

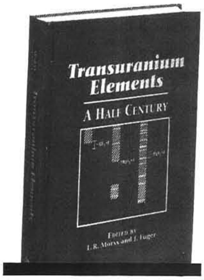
Transuranium Elements
A Half Century

UPCOMING RESEARCH

Measurement of Ambient Ozone Using a Nitrite-Coated Filter

A nitrite-based filter coating is developed for ozone collection using a commercially available passive sampling device. Results obtained with the passive method typically agree to within ± 20% with those obtained using standard ozone-monitoring techniques in laboratory and field validation tests.

Petros Koutrakis*, Jack M. Wolfson, Arnold Bunyaviroch, Susan E. Froehlich, Koichiro Hirano, and James D. Mulik, Department of Environmental Health, Harvard School of Public Health, Boston, MA 02115

Excited-State Proton Transfer in Laser Mass Spectrometry

Molecular ion formation for several bifunctional carboxylic acids is studied to elucidate the role of excited-state proton transfer (ESPT) in UV laser desorption MS. Direct evidence for ESPT is obtained by monitoring Li^+–H^+ exchange and competition between $(M + D)^+$ and $(M + H)^+$ ion formation in the laser desorption mass spectra of compounds known to undergo ESPT in solution.

M. Paul Chiarelli, Andrew G. Sharkey, Jr., and David M. Hercules*, Department of Chemistry, University of Pittsburgh, Pittsburgh, PA 15260

Analysis of First-Order Rate Constant Spectra with Regularized Least-Squares and Expectation Maximization: 1. Theory and Numerical Characterization

Analysis of parallel first-order rate processes by deconvolution of single exponential kernels from experimental data is performed with regularization techniques and the method of expectation maximization.

Brett J. Stanley, Stephen E. Bialkowski, and David B. Marshall*, Department of Chemistry and Biochemistry, Utah State University, Logan, UT 84322-0300

Tandem Mass Spectrometry of Very Large Molecules. 2. Dissociation of Multiply Charged Proline-Containing Molecules from Electrospray Ionization

The collisionally activated dissociation of a number of large peptides and proteins containing proline residues is studied. The observed dissociation products often include abundant complementary ions as a result of dissociation adjacent to proline residues.

Joseph A. Loo, Charles G. Edmonds, and Richard D. Smith*, Chemical Sciences Department, Pacific Northwest Laboratory, Richland, WA 99352

These articles are scheduled to appear in AC RESEARCH in the near future.

*Corresponding author

High Current Density "Wired" Quinoprotein Glucose Dehydrogenase Electrode

Pyrroloquinoline (PQQ) glucose dehydrogenase is electrically "wired" through an osmium-complex-based redox polymer to glassy carbon. The high limiting current density suggests fast electron transfer from PQQ to the osmium centers of the polymer.

Ling Ye*, Martin Hämmerle, Arjen J. J. Olsthoorn, Wolfgang Schuhmann, Hans-Ludwig Schmidt, Johannis A. Duine, and Adam Heller, Department of Chemical Engineering, University of Texas at Austin, TX 78712, Lehrstuhl für Allgemeine Chemie und Biochemie, Technische Universität München, D-8050 Freising-Weihenstephan, Germany, and Department of Microbiology and Enzymology, Delft University of Technology, 2628 BC Delft, The Netherlands

Imaging of Electrophoretic Flow across a Capillary Junction

A system is developed that allows visualization of electroosmotic flow across a capillary junction, where the image of the junction is collected by a microscope and imaged onto a CCD camera. The relevant operational parameters of the CE system are optimized to enhance mass transfer across the junction.

Werner G. Kuhr*, Larry Licklider, and Lawrence Amankwa, Department of Chemistry, University of California, Riverside, CA 92521

Determination of On-Line Refractive Index and Molecular Weight via Gradient HPLC Interfaced with Low Angle Laser Light Scattering, Ultraviolet, and Refractive Index Detection

Gradient ion-exchange HPLC is interfaced with LALLS, UV, and RI detectors connected in series to determine the molecular weight and dn/dc of proteins on line. Isorefractive buffers are used to generate stable baselines for the LALLS and RI detectors.

Rohin Mhatre and Ira S. Krull*, Department of Chemistry, Northeastern University, Boston, MA 02115

Electrochemical Study of the Rate of Activation of the Molybdoheme Protein Sulfite Oxidase by Organic Electron Acceptors

Electrocatalytic rate constant measurements are reported for intraenzyme Mo→heme site (k_{in}) and heme site→organic mediator–oxidant (k_{12}) for the enzyme sulfite oxidase. Although k_{12} depends on the choice of mediator–oxidant, k_{in} does not.

L. A. Coury, Jr., Liu Yang, and Royce W. Murray*, Kenan Laboratories of Chemistry, University of North Carolina, Chapel Hill, NC 27599-3290

CHN:
6 Minutes

CHNS:
8 Minutes

Oxygen:
4 Minutes

ORGANIC **More organic elements in less time.** The PE 2400 Series II CHNS/O Analyzer won't keep you waiting. It's a self-contained, microprocessor-controlled analyzer that allows for the rapid measurement of CHN, CHNS and/or Oxygen in organic materials.

The PE 2400 Series II features multitasking operation. It lets you run samples, add new samples and print results—all at the same time for improved laboratory efficiency. Add the 60-position Autosampler and get results even faster.

PE 2400 Series II CHNS/O Analyzer

For more information on the PE 2400 Series II, contact your local Perkin-Elmer office. For product literature in the U.S., call **1-800-762-4000.**

PERKIN ELMER

The Perkin-Elmer Corporation, Norwalk, CT 06859-0012 U.S.A

CIRCLE 85 ON READER SERVICE CARD

Harnessing Biotechnology for the 21st Century

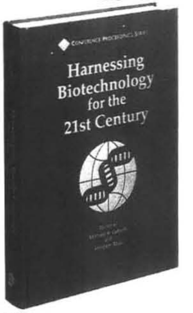

Presenting the proceedings of the Ninth International Biotechnology Symposium, this new volume offers the most recent developments in biotechnology and bioprocessing from leading industrial and academic researchers.

The volume's 139 papers are divided into 11 sections covering

- **Frontiers in Polypeptide Production**
- **Frontiers in Production of Metabolites**
- **Microbiology and Physiology**
- **Biocatalysis and Biotransformation**
- **Bioreactor Engineering**
- **Downstream Processing**
- **Bioinstrumentation and Bioprocessing Control**
- **Policy Issues in Biotechnology**
- **Environmental Engineering and Biology**
- **Agriculture and Food Biotechnology**
- **Biotechnology in Developing Countries**

Harnessing Biotechnology for the 21st Century **is a valuable, concise resource on the latest international developments in biotechnology.**

Michael R. Ladisch, Purdue University, *Editor*
Arindam Bose, Pfizer Central Research, *Editor*

Conference Proceedings Series
640 pages (1992) Clothbound
ISBN 0-8412-2477-3
$149.95

**Order from: American Chemical Society, Distribution Office, Dept. 42
1155 Sixteenth St., N.W., Washington, DC 20036
or CALL TOLL FREE 800-227-5558
(in Washington, D.C. 872-4363) and use your credit card!**

NEW EDITOR!

Today's Best Source of Quantitative Numerical Data of Physics and Chemistry.

JOURNAL OF Physical and Chemical Reference Data

Editor, Jean W. Gallagher
National Institute of Standards and Technology

Published BIMONTHLY by the American Chemical Society, the American Institute of Physics, and the National Institute of Standards and Technology, JPCRD provides you with compilations and reviews produced under the National Standard Reference Data System of the National Institute of Standards and Technology.

JPCRD contains recommended values, uncertainty limits, critical commentary on methods of measurement, and full references to the original papers.

*Call Toll Free 1-800-333-9511
and charge your order!
Outside the U.S. call (614) 447-3776,
or write: American Chemical Society,
Member and Subscriber Services
P.O. Box 3337 Columbus, OH 43210 U.S.A.*

NEWS

New Instrumentation Panel Members

Therese Cotton, Mary Ellen McNally, and J. Michael Ramsey have been appointed to three-year terms on ANALYTICAL CHEMISTRY's Instrumentation Advisory Panel. They replace departing members Daniel Armstrong, University of Missouri–Rolla; Thomas Chester, Procter & Gamble Co.; and Brenda Shaw, University of Connecticut. Six other analytical chemists continue to serve on the panel: Anna Brajter-Toth, University of Florida; Raymond E. Clement, Ontario Ministry of the Environment; Norman J. Dovichi, University of Alberta; Jack D. Henion, Cornell University; John W. Olesik, Ohio State University; and Dallas L. Rabenstein, University of California–Riverside.

Instrumentation Advisory Panel members propose appropriate topics and authors for INSTRUMENTATION and other A-page features. They also contribute to a dialogue on the overall aims and scope for INSTRUMENTATION articles, which introduce and promote interest in various chemical measurement systems (including instrument design and application). These features are written for the nonspecialist and are not comprehensive reviews. In addition to suggestions made primarily by the panel and the Advisory Board, ANALYTICAL CHEMISTRY considers unsolicited articles and topics suggested by readers.

Biographical sketches of the new members follow.

Therese Cotton, professor of chemistry at Iowa State University and Ames Laboratory since 1989, received her Ph.D. in 1976 from Northwestern University and remained there as a postdoctoral associate until 1980. She has held positions at the Illinois Institute of Technology and the University of Nebraska–Lincoln.

Cotton's research interests include analytical applications of electrochemistry, Raman, and surface-enhanced Raman spectroscopy to biochemical problems. She is also interested in the development of photosynthetic model systems at electrode surfaces and fundamental aspects of interfacial electron transfer reactions as probed by spectroscopic techniques.

Mary Ellen McNally, a senior research chemist since 1984 with the Experimental Station at E. I. du-Pont de Nemours and Co., Inc., received her Ph.D. in 1983 from Villanova University under the direction of Robert Grob. She held a postdoctoral position at the University of Georgia under the direction of L. B. Rogers.

McNally's research interests are LC, GC, capillary zone electrophoresis, and supercritical fluid chromatography and extraction. Her work is focused on the environmental fate of agricultural products and ultratrace analysis. McNally has more than 30 publications. With Frank Bright, she co-edited *Supercritical Fluid Technology: Theoretical and Applied Approaches in Analytical Chemistry*; currently she is working on *Supercritical Fluid Extraction: Applications in Industry*. McNally received the American Microchemical Society Steyermark Award in 1982 for her work in microanalysis and the Chromatography Forum Award from the Delaware Valley Chromatography Forum in 1990.

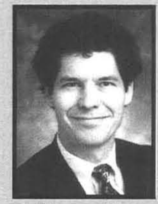

J. Michael Ramsey, group leader and senior research staff member of the Analytical Chemistry Division at Oak Ridge National Laboratory, received his B.S. degree from Bowling Green State University (OH) in 1974 and his Ph.D. from Indiana University in 1979.

Ramsey is primarily interested in laser-based chemical measurement problems. His research interests include digital molecular detection (molecular counting), optical properties of microparticles, real-time chemical characterization of microparticles by laser desorption/MS, chemical vapor deposition processes, nonlinear spectroscopies, and microminiaturization of chemical instrumentation. Ramsey was chair of the Program Planning Committee for the Division of Analytical Chemistry from 1989 to 1991.

Sidney Siggia

The JOURNAL regrets to report the death of Sidney Siggia on Oct. 15, 1992. Siggia was emeritus professor of chemistry at the University of Massachusetts, where he taught for 20 years. He came to academia after making his mark in industry at companies such as GAF Corp. and Olin Corp. He served on the Advisory Board of ANALYTICAL CHEMISTRY from 1961 to 1963.

Wilhelm Simon

Photo from 1983.

The JOURNAL also regrets to report the death of Wilhelm Simon on Nov. 17, 1992. Simon was professor of chemistry at the Swiss Federal Institute of Technology, where he taught for more than 30 years. His research focused on ion selectivity of membranes and structural characterization of organic compounds using combined spectroscopic techniques. Simon served on the Advisory Board of ANALYTICAL CHEMISTRY from 1983 to 1985.

BIGGER ISN'T ALWAYS BETTER.

Finally, a true GC mass flow controller whose price tag matches its size.

With a price tag that matches its compact size and light weight, the new HPC-222 from Teledyne Hastings-Raydist is the most economical and accurate mass flow controller you can buy. ■ Using a piezoelectric valve actuator, the HPC-222's simplified valve construction reduces power requirements and increases efficiency. It's ideal for any gas flow measuring and controlling application, like gas chromatography and pollution control monitoring. Ranges are available from 0-10 SCCM up to 0-1000 SCCM. ■ Sometimes it's better to think small. For more information on the HPC-222 call us today.

TELEDYNE
HASTINGS-RAYDIST
P.O. Box 1436 · Hampton VA 23661
1-800-950-2468

CIRCLE 105 ON READER SERVICE CARD

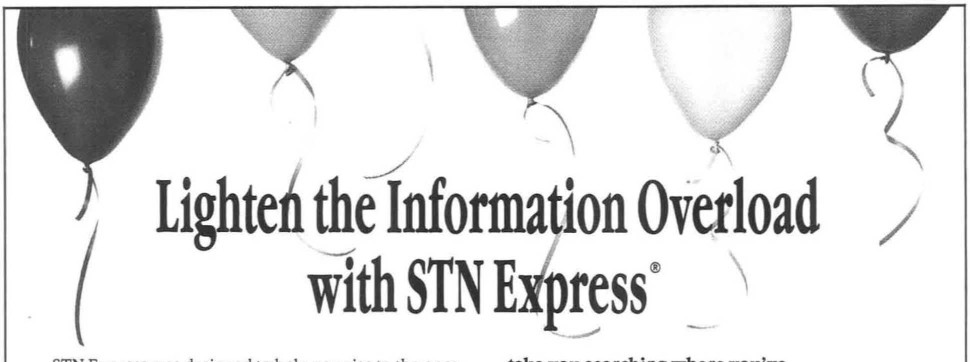

Lighten the Information Overload with STN Express®

STN Express was designed to help you rise to the occasion, when you must search online. STN Express will

eliminate the need for extensive training

- installation is simple
- logon procedures are set once
- menus and windows are the working environment
- help is a keystroke or phone call away
- learning is accomplished by exploring features of interest

allow you to work more efficiently

- offline query preparation is available
- structure drawing help is provided
- report generation is assisted
- guided search and predefined search strategies offer assistance to beginning searchers

take you searching where you've never been before

STN Express will expand your horizons by helping you access the more than 130 scientific and technical databases on STN International®

For more information about how STN Express can lighten your information overload, contact

STN International, c/o CAS, Marketing, Dept. 32093, P.O. Box 3012, Columbus, Ohio 43210-0012. FOR FASTER SERVICE call 614-447-3731 or 800-933-4350 or fax your request to 614-447-3713.

STN INTERNATIONAL®
The Scientific & Technical Information Network

UV Resonance Raman Spectroscopy for Analytical, Physical, and Biophysical Chemistry

Part 1

Sanford A. Asher
Department of Chemistry
University of Pittsburgh
Pittsburgh, PA 15260

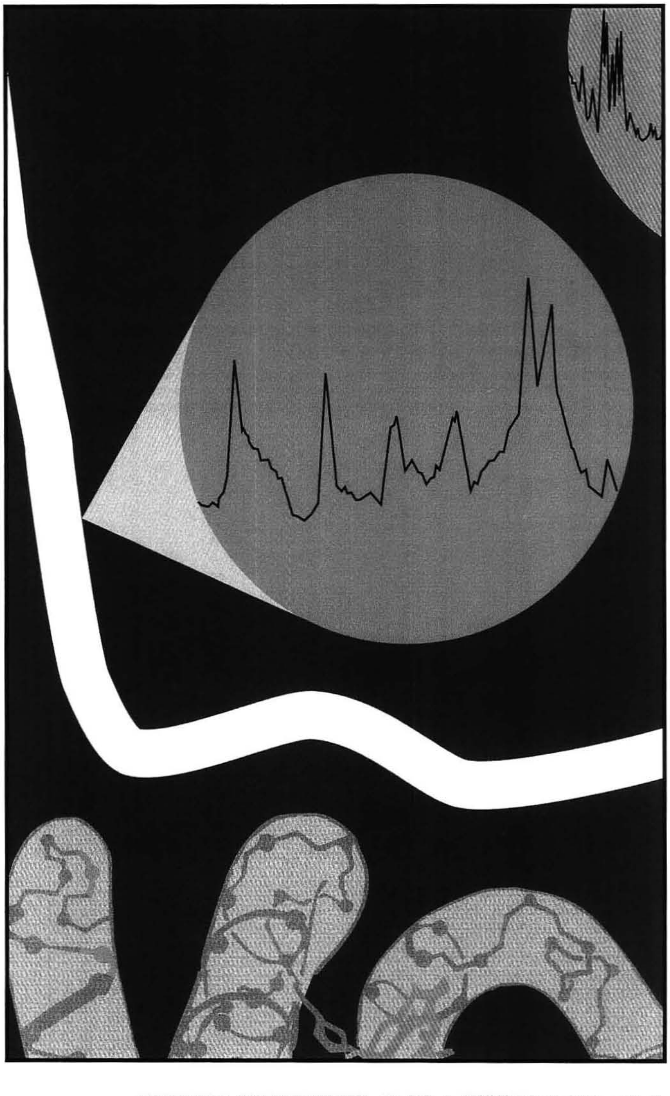

Raman spectroscopy measures the magnitudes and intensities of frequency shifts that occur because of the inelastic scattering of light from matter (*1, 2*). The observed shifts can be used to extract information on molecular structure and dynamics. In addition, important information can be obtained by measuring the change in the electric field orientation of the scattered light relative to that of the incident exciting light.

The experiment is usually performed by illuminating a sample with a high-intensity light beam with a well-defined frequency and a single linear polarization (Figure 1); the scattered light is collected over some solid angle and measured to determine frequency, intensity, and polarization. The inelastic scattering Raman phenomenon, which leads to frequency shifts, is phenomenologically distinct from the relaxed emission denoted as fluorescence (Figure 2) because the inelastic scattering is a single event, and a real emitting excited state is never created.

In contrast, relaxed fluorescence emission (Figure 2) occurs through the population of an excited state, which can subsequently undergo vibrational relaxation prior to fluorescence back to the ground state. The distinction between fluorescence and Raman scattering is more subtle for excitation within the absorption bands of small molecules in the gas phase, where single vibrational-level fluorescence can occur from well-defined vibronic levels (*3*).

The Raman effect is named after Sir C. V. Raman. In his classic 1928 paper, coauthored by K. S. Krishnan, Raman described experimental observations of the inelastic scattering

0003-2700/93/0365-59A/$04.00/0

of sunlight from vibrational quantum levels of numerous liquids (*1*). Raman received the Nobel prize for his work. The possibility of inelastic scattering of light from discrete quantum levels of matter was envisioned in 1923 by A. Smekal (*1*).

Much of the early work centered on vibrational Raman scattering; these studies were central to developing a fundamental understanding of molecular structure and vibrational motion. Before 1945 it was much easier to take Raman spectroscopic measurements than to take mid-IR absorption measurements. Raman excitation used Hg arc emission lines and photographic detection. After 1945 the advent of relatively convenient IR instrumentation decreased enthusiasm for Raman spectroscopy, and it became a specialized field. Much of the work before 1960 centered on examining molecular structure and molecular vibration dynamics. Major advances occurred during this period in the theoretical understanding of Raman spectroscopy and in the resonance Raman phenomenon, where excitation occurs within an electronic absorption band. The first commercial Raman instrument became available in 1953.

The advent of the photomultiplier tube and the He–Ne laser caused a resurgence of interest. In 1928, 58 papers were published on Raman spectroscopy; by 1937, the total was 1785. Between 1987 and 1989, for example, more than 6000 papers were published with the word Raman in their title (*4*). Raman spectroscopy has become a major tool for fundamental studies in physics and physical chemistry as well as for applied studies in the biological sciences and analytical chemistry.

During the 1970s most Raman instrumentation used Ar^+ lasers with excitation between 450 and 520 nm—a region that, unfortunately, is especially prone to interference from fluorescent impurities. The interferences degrade signal-to-noise ratios (S/N), resulting in poor spectra for many complex samples. Many Raman studies involved pure compounds or those samples that proved amenable to visible excitation.

The usefulness of Raman spectroscopy for studying aqueous samples, especially biological samples, was appreciated early on. Because the Raman scattering of water is very weak, it is easy to study species in aqueous environments. IR measurements, in contrast, often suffer from water interferences that cannot be overcome. In 1972 an important paper by T. C. Strekas and T. G. Spiro (*5*) demonstrated the usefulness of the resonance Raman effect in selective studies of the chromophoric hemes of hemoglobin and myoglobin. Very high spectral S/N were obtained from heme protein samples at relatively low concentrations. This technique was quickly adopted by those researchers interested in biological problems. Amazing progress has been made over the past 20 years using this technique to, for example, study heme protein structure and function (*6*) and to elucidate the photochemical mechanisms of visual pigments such as rhodopsin (*7*). Until recently, however, resonance Raman spectroscopy was limited to the small subset of compounds absorbing in the visible or near-UV spectral regions where laser sources typically have been available.

Continuing advances in methods fueled numerous studies in which molecular structure in the gas, liq-

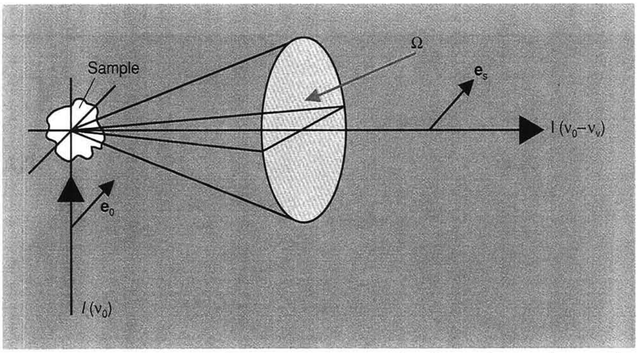

Figure 1. Raman inelastic light-scattering process showing excitation of a sample with light of an intensity $I(\nu_0)$ and frequency ν_0.

The incident light has an electric field of magnitude and direction shown by $\mathbf{e}_0$. Raman scattered light at a frequency $\nu_0 - \nu_v$ (ν_v is the Raman active molecular vibrational frequency) and intensity $I(\nu_0 - \nu_v)$ is collected over the solid angle Ω. A ray of this light is shown with its electric field polarized along $\mathbf{e}_s$ parallel to the incident field.

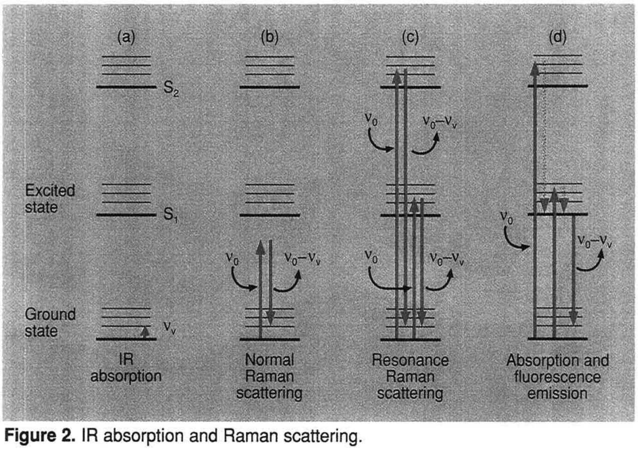

Figure 2. IR absorption and Raman scattering.

(a) Vibrational IR absorption. (b) Inelastic scattering of light of frequency ν_0 to a frequency of $\nu_0 - \nu_v$. The shift in frequency corresponds to a vibrational frequency in this case, and the scattering is known as vibrational Raman scattering. Because the excitation occurs at a frequency far removed from any absorption bands associated with excitations to electronic excited states, the phenomenon is known as normal, or nonresonance, Raman scattering. (c) Excitation occurring within an electronic transition produces resonance Raman scattering. (d) Absorption and fluorescence emission in which an excited state is created. Typical relaxed fluorescence occurs subsequent to the population of an excited state. Prior to emission, this excited state quickly relaxes to the lowest vibrational level of the lowest singlet excited electronic state. Emission is broad and the molecule undergoes a transition to different vibronic levels of the ground state.

uid, and solid phases was examined. The advent of surface-enhanced Raman spectroscopy (*8*) opened the door to studying extremely low concentrations of molecules on surfaces. Nonlinear Raman techniques, such as coherent anti-Stokes Raman spectroscopy, were used to study combustion processes (*1*).

The 1980s saw even more rapid advancements, such as the development of UV-Raman spectroscopy and of FT-Raman spectroscopy (*9*), which uses near-IR excitation. These extensions into spectral regions away from the visible have dramatically increased the utility and applicability of Raman spectroscopy.

In FT-Raman spectroscopy, the multiplex advantage of the Michelson interferometer is used to increase the spectral S/N that is limited by IR detector background noise. FT-Raman spectroscopy has the advantage of excitation in a spectral region that is much less susceptible than visible excitation to fluorescent interferences. Relative intensities from vibrations of different species are roughly proportional to concentrations of those species in the sample, and the Raman-active vibrations have roughly similar intensities. For example, aromatic ring vibrations have intensities similar to those of aliphatic C–C stretching vibrations, which have intensities similar to those of C–H stretching vibrations.

In contrast, UV-Raman spectroscopy uses selective excitation in the UV absorption bands of molecules to produce spectra of particular analytes and chromophoric segments of macromolecules. Resonance excitation has the advantage of selectivity. In addition, UV-Raman measurements of condensed-phase samples excited below 260 nm are not plagued by fluorescent interferences (*10*).

In this article, the first in a two-part series, phenomenology, instrumentation, and fundamental applications will be discussed. In Part II, which will appear in the Feb. 15 issue of ANALYTICAL CHEMISTRY, analytical applications, biological studies, new methods, and future developments will be discussed.

Phenomenology

Figure 3 illustrates the Raman scattering phenomenon. An incident electromagnetic field drives the electron cloud of the molecule at the incident frequency ν_0. An oscillating dipole moment is created by the resulting displacement of electronic charge. Because the charge is accelerating, it radiates energy in the form of electromagnetic radiation. The radiated frequency ν_0 is identical to the excitation frequency; light is elastically scattered. If the scattering species is small compared with the wavelength of light, the scattering is known as Rayleigh scattering. Because charge acceleration induces the radiation, the Rayleigh scattering efficiency increases with the fourth power of the excitation frequency. This phenomenon explains why the sky is blue and the setting (or rising) sun is red.

Other dynamic processes modulate the induced oscillating dipole moment. As shown in Figure 3, a nuclear vibrational motion causes an oscillation of the electron cloud at frequency ν_v. The electron cloud oscillation at ν_0 couples to the vibrationally induced electron cloud oscillation at ν_v to give rise to a beat oscillation at $\nu_0 \pm \nu_v$, which radiates Raman scattered light at this frequency. Those vibrations that most efficiently Raman scatter are those that couple most effectively to the oscillating electron dipole moment induced by the exciting electromagnetic field.

There are particular excitation frequencies that are natural frequencies of oscillation of specific electron oscillators of the molecular electron cloud. These natural frequencies are the molecular electronic absorption band frequencies. Excitation at these frequencies is said to be in "resonance" with the electronic transition (Figure 2); therefore, the Raman scattering is said to be "resonance Raman" scattering. This resonance excitation at the natural frequency of electron cloud oscillation results in an increased oscillating charge displacement and a corresponding increase in the induced dipole moment; this, in turn, directly results in an increased scattering or reradiation efficiency for Raman scattering. The enhancement factor of resonance Raman scattering compared with that of normal Raman scattering can be as high as 10^8.

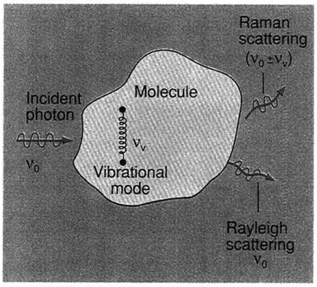

Figure 3. Raman scattering phenomenon.

The presence of a vibration at frequency ν_v is shown by the spring. Light scattered at $\nu_0 - \nu_v$ is known as Stokes Raman scattering; light scattered at $\nu_0 + \nu_v$ is known as anti-Stokes Raman scattering.

The observed Raman band intensities at a particular excitation frequency depend on the degree to which a vibration modulates the molecular polarizability. In a classical sense, the magnitude of the induced dipole moment μ depends linearly on the molecular polarizability α and the incident electromagnetic field $\mathbf{E}$, giving $\mu = \alpha\mathbf{E}$. In the case of Raman scattering, the effective polarizability is not the static polarizability α; it is the Raman polarizability α^R associated with perturbation of the static polarizability by the Raman active vibration $\alpha_R = (\partial\alpha/\partial Q)_0 Q$, where Q is the normal vibrational mode displacement. For excitation at frequency ν_0 , the Raman intensity I_{mn} observed over a unit solid angle for a transition between vibronic levels m and n in the electronic ground-state manifold is (*11*)

$$I_{mn} = \sigma^R N I_0 W(\Omega)$$

where σ^R (cm^2/molc steradian [sr]) is the total differential Raman cross section for a single gas-phase molecule integrated over the Raman peak bandwidth, I_0 is the incident excitation intensity (photons/cm^2 s) into a particular sample volume element of area dA and length dl, N is the number of molecules within that volume element, and $W(\Omega)$ is a parameter that details the optical geometry and includes factors such as the collected solid angle Ω and the spectrometer efficiency.

The resonance Raman effect can lead to important selectivity in Raman spectral measurements. Figure 4 shows the absorption spectrum of a sample with two absorption bands. Raman spectra are shown that are excited at a wavelength longer than any absorption band (Figure 4c, normal Raman) or within the two absorption bands (Figures 4a and 4b, resonance Raman). Excitation away from resonance (Figure 4c) results in comparable Raman intensities from all analytes. The typical scattering cross section is $\sigma^R = 10^{-30}$ cm^2/molc sr (or 1 μBarn/molc sr). (One Barn equals 10^{-24} cm^2.) Resonance excitation within an absorption band can lead to an immense Raman intensity increase. For example, we have measured a Raman cross section of ~50 Barns/molc sr for pyrene.

Figures 4a and 4b show an increased Raman intensity for resonance excitation. Different Raman spectra are observed with excitation in resonance versus not in resonance. In addition, different spectra are observed with resonance excitation within different sample absorption bands—for example, the resonance Raman spectrum in Figure 4a differs from that in Figure 4b. If these absorption bands derive from different analytes in the sample, we selectively enhance the vibrational Raman spectrum of different analytes as we change the excitation wavelength. The selectivity factor can be as large as 10^8.

If the different absorption bands derive from different segments of a molecule, by changing excitation wavelengths we change the segment of the molecule studied. In contrast, if the two absorption bands derive from the same chromophoric segment of a single molecule, the spectra will differ because of differences in the structure of the excited states associated with the two electronic transitions; the different excited states couple differently with the ground-state vibrational motion.

We can easily estimate the number of nonresonance Raman photons that can be detected from a 0.1 M solution of an analyte with a Raman cross section of 1 μBarn/molc sr, illuminated by an incident laser beam of 1 W of 514.5 nm light (2.6×10^{18} photons/s). For a typical case, the limiting aperture is the height of the intensified Reticon detector (2.5 mm), and the spectrometer *f*/#. Let us assume the spectrometer is *f*/7.0, with a slit width of 200 μm, and the collection optic has a magnification of 6. For this case, the laser beam can be efficiently imaged into a column with a 33-μm (maximum) diameter and a 417-μm height that contains 2.2×10^{13} molecules. Ideally, we can collect 0.86 sr of the scattered light. According to the equation, if the spectrometer were 100% efficient, a total of 5.6×10^6 Raman photons/s would be detected for this vibration.

In contrast, the fluorescence cross section of an analyte with a molar absorptivity of 10^4 and a fluorescence quantum yield of 0.1 is equal to 3×10^{-22} cm^2/molc sr; 1.68×10^{15} fluorescence photons would be observed using the same instrument (assuming no self-absorption of the emitted light occurs).

Obviously, the fluorescence experiment is much more sensitive than the Raman experiment and we can observe the same amount of fluorescence signal as the Raman signal using a concentration 3×10^8-fold lower. However, in the case of resonance Raman scattering, Raman cross sections as high as ~ 10^{-22} cm^2/molc sr can occur. The resonance Raman sensitivity is comparable to that of fluorescence. Furthermore, sensitivity can be greater because the Raman spectrum has higher resolution.

Generally, numerous Raman bands exist, and all can be used to determine concentrations. The narrow Raman spectral bands carry a great deal of information on molecular structure, in contrast to the broad fluorescence emission. Also, the Raman cross sections are much less de-

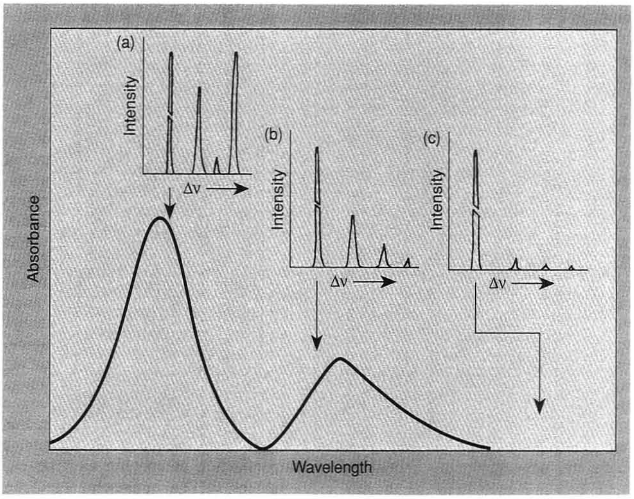

Figure 4. Selectivity available from resonance Raman spectroscopy.

The absorption spectrum is shown for a sample with two absorption bands. These bands could derive from two different analytes, two different chromophoric segments of a macromolecule, or two different electronic transitions of a single molecule. Three different Raman spectra are shown that derive from resonance Raman excitation within either of the two absorption bands (a and b) or from excitation away from the absorption (c). Excitation within resonance leads to much more intense Raman spectra. The most intense feature is the Rayleigh scattering band.

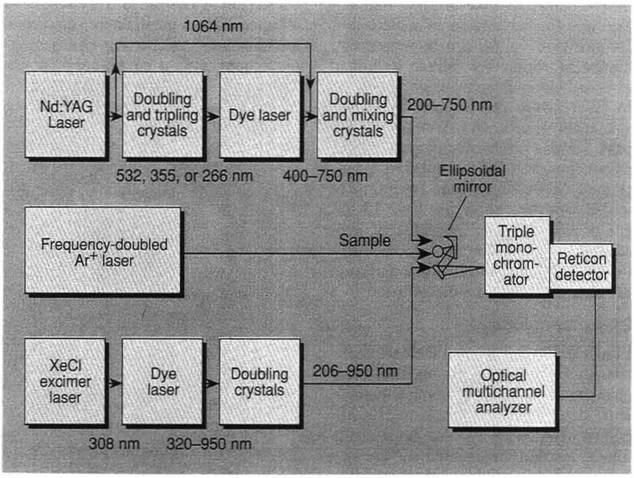

Figure 5. Diagram of basic instrumentation used for UV resonance Raman spectroscopy.

pendent on environment than are the fluorescence quantum yields. Modest changes in solvent composition can cause dramatic changes in fluorescence quantum yields, because the quantum yields are very sensitive to relatively small changes in fluorescence lifetimes. Thus, resonance Raman measurements can be very sensitive, the spectra can provide a great deal of molecular structural and environmental information, and an increased selectivity results from the ability to excite particular species.

Instrumentation

UV-Raman instrumentation has evolved rapidly (Figure 5). The original laser source used a low repetition rate (20 Hz) Nd:YAG laser with ~ 5-ns frequency pulses that were doubled or tripled to pump a dye laser whose frequency was doubled or mixed with the Nd:YAG 1.06-µm fundamental wavelength to generate light between 200 and 400 nm (*12*). The minimum average output power available in this region is 20 mW; in some spectral regions, hundreds of milliwatts are available. Raman shifting of the Nd:YAG harmonics in H_2 gas can also generate numerous wavelengths in the UV, and this approach can be used to construct a simpler, inexpensive UV laser source.

The low duty cycle (10^{-7}) of the Nd:YAG laser represents a major limitation because the laser pulses cannot be focused into a sample volume that can be efficiently imaged into the Raman spectrometer. The Nd:YAG output occurs as ~ 5 ns pulses, at a repetition rate of ~ 20 Hz. An average power of 20 mW corresponds to a peak power level of ~200 kW, which can induce nonlinear optical phenomena in matter. A power flux value of 2.5 GW/cm^2 would occur if this beam were focused into a 100-µm-diameter spot size.

A partial solution to this low duty cycle is to use a higher repetition rate excimer laser to pump a dye laser whose output was frequency-doubled into the UV region (*13*). Modern high-power excimer lasers can have repetition rates between 200 and 500 Hz; at the highest repetition rates the 16-ns laser pulses result in a duty cycle of 8×10^{-6}. This partially alleviates the nonlinear optical phenomena and the sample ground-state depletion that both complicates the Raman spectral measurements and necessitates defocusing the laser excitation beam at the sample.

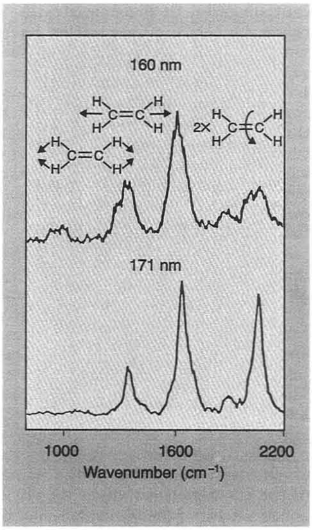

Figure 6. UV resonance Raman spectra of ethylene in the gas phase showing enhancement of the 1344-cm^{-1} C–H bending and the 1625-cm^{-1} C=C stretching vibrations and enhancement of the 2046-cm^{-1} overtone of the torsional vibration.

Different spectra are excited in the first excited singlet state of ethylene at 160 and 171 nm. The unique enhancement of this torsional overtone, whose fundamental is symmetry forbidden, indicates that the excited state is twisted. (Adapted with permission from Reference 20.)

An alternative approach uses a mode-locked Nd:YAG laser to create a quasi-continuous wave UV source with a duty cycle of 0.01 (*14*). A new laser has just become available that is ideal for Raman measurements that do not require continuous tuning (*15*). The Coherent Laser Group (division of Coherent, Inc.) has developed an intracavity frequency-doubled Ar$^+$ laser with five excitation wavelengths in the UV region: 257, 248, 244, 238, and 228.9 nm (400, 180, 400, 100, and 30 mW, respectively). This laser permits a major improvement in spectral S/N and, for the first time, allows UV-Raman studies of solid absorbing samples.

UV-Raman sample handling requires flowing the sample through the laser beam as a liquid jet, through a capillary, or along a waveguided stream. With pulsed lasers, it is essential to exchange each illuminated sample volume before the arrival of the next laser pulse to avoid sample heating; also, the high-energy UV photons might cause photochemical degradation in the samples. Most samples studied to date have not shown significant monophotonic photodegradation during the typical 10-min Raman measurement time.

The collection optics use either an ellipsoidal collection mirror for achromatic imaging or quartz lenses (when accurate relative intensity measurements are not essential). The typical spectrometer is a triple grating instrument in which the initial double monochromator operates in a subtractive configuration to filter out the Rayleigh scattered light. The third-stage spectrograph disperses and images the light onto a multichannel detector such as an intensified Reticon array. This multichannel detector is essential for simultaneous collection of the entire spectrum. A scanning system would have a far inferior S/N because most of the noise comes from the low-stability UV laser source. Charge-coupled detectors may eventually prove superior to the intensified Reticon detectors.

The triple spectrometer is inefficient; at best, only 7% of the Raman scattered light entering the entrance slit is transferred to the detector. Efforts are under way to use the more efficient single spectrograph (*16*); success requires very high quality, low stray light gratings, careful filtering of samples to minimize Rayleigh scattering, and careful optical imaging to avoid any reflections of the incident excitation beam into the spectrograph.

Fundamental applications

Investigations of the structure and dynamics of excited states of small molecules are an especially fertile area for UV-Raman investigations. Examination of the vibrations most enhanced by excitation in resonance with an electronic transition gives information on the excited-state structure and dynamics. The simplest rule of thumb is that resonance Raman-enhanced vibrations are those that distort the ground-state geometry toward the excited-state geometry. If the atomic motions involved in the enhanced vibrations are known, theoretical models can be applied to the measured Raman intensities to calculate the excited-state distortion. Numerous workers are using this information to examine the excited states of small molecules such as oxygen (*17a*), ammonia (*17b*), methyl iodide (*17c, 17e*), carbon disulfide (*17d*), ethylene (*18, 19*), and other species.

For methyl iodide (*17c, 17e*), the excited state is dissociative and the Raman data give information on the short time dynamics of the photodissociation. For ethylene, excitation in the lowest allowed $\pi \rightarrow \pi^*$ transition (Figure 6) results in the unique enhancement of the overtone of a torsional vibration, in addition to the C=C double-bond stretch and the CH_2 bending vibration; the enhancement of this torsional vibration confirms that the ethylene excited state is twisted (*20, 21*). Similar experiments examine the vibrational enhancement of stilbenes (*18*), for example, to determine the photochemical mechanism of photoisomerization. Interested readers are urged to examine the rapidly expanding literature on these insightful studies.

Another example that illustrates the power of the technique to probe excited states is a recent study we made to determine whether vinyls attached to hemes were conjugated into the aromatic porphyrin ring (Figure 7a) (*19, 22*). This is an important question in biochemistry, because the hemes of hemoglobin have vinyl peripheral substituents and the protein may modulate the heme reactivity by controlling the vinyl group conjugation—possibly by altering the vinyl group geometry. In addition, vinyl group conjugation is relevant to electron transfer studies for porphyrins because the vinyl groups could represent a conduit for electron flow.

We were able to demonstrate the lack of vinyl group conjugation by measuring the extent of vinyl group C=C stretching enhancement with excitation in the UV region. Figure 7b shows the Raman spectrum of the (bis)cyanide complex of the heme. The strong peak at 1622 cm^{-1} in the heme complex comes from the C=C vinyl stretch; ^{13}C and deuterium vinyl substitution further confirm this assignment. Excitation of the heme in the UV region results in selective enhancement of the vinyl modes, and little enhancement occurs for the heme vibrational modes. The vinyl Raman cross sections are similar to that of the C=C group in 1-hexene (*19*), which indicates that the vinyl groups are not conjugated with the heme ring π electrons. If the vinyl were conjugated, its $\pi \rightarrow \pi^*$ transition would be intimately mixed with the heme transitions; no selective vinyl enhancement would occur with UV excitation.

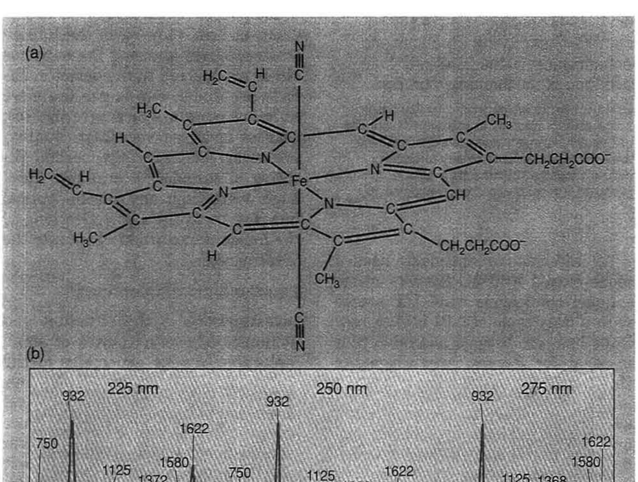

Figure 7. (a) Structure and (b) UV resonance Raman spectra of the bis(cyanide) ferric protoporphyrin IX complex.

The 932-cm^{-1} band is from the internal standard ClO_4. The selective UV enhancement of the vinyl C=C stretch at 1622 cm^{-1} and the band at 1125 cm^{-1} is evident from their relative intensity increases compared with that of the ClO_4 band as the excitation moves farther into the UV region. The band at 1125 cm^{-1} derives from a vibration with a major contribution of motion of the vinyl against the heme ring. Little enhancement occurs for the heme ring vibrations such as the 1368 cm^{-1} ν_4 ring breathing motion. This selective enhancement of the vinyl vibrations in the UV indicates the existence of a vinylic $\pi \rightarrow \pi^*$ transition at $\lambda < 220$ nm; the existence of this vinyl $\pi \rightarrow \pi^*$ transition indicates the absence of vinyl–heme conjugation. (Adapted from Reference 19.)

References

(1) Long, D. A. *Raman Spectroscopy*; McGraw-Hill Int. Book Co.: New York, 1977.
(2) a. Asher, S. A. *Ann. Rev. Phys. Chem.* **1988**, *39*, 537–88. b. Harada, I.; Takeuchi, H. In *Spectroscopy of Biological Systems*; Clark, R. T.; Hester, R. E., Eds.; John Wiley and Sons: New York, 1986. c. Hudson, B.; Mayne, L. *Methods Enzymol.* **1986**, *130*, 331. d. Hudson, B. *Spectroscopy* **1986**, *1*, 22.
(3) Harmon, P. A.; Asher, S. A. *J. Chem. Phys.* **1988**, *88*, 2925–38.
(4) Miller, F. A.; Kauffman, G. B. *J. Chem. Educ.* **1989**, *66*, 795–801.
(5) Strekas, T. C.; Spiro, T. G. *Biochim. Biophys. Acta* **1972**, *263*, 830.
(6) a. Spiro, T G.; Smulevich, G.; Su, C. *Biochemistry* **1990**, *29*, 4497. b. Asher, S. A. *Methods Enzymol.* **1981**, *76*, 372–413.
(7) Mathies, R. A.; Smith, S. O.; Palings, I. In *Biological Applications of RS*; Spiro, T. G., Ed.; John Wiley and Sons: New York, 1987; Vol. II.
(8) Garrell, R. L. *Anal. Chem.* **1989**, *61*, 401 A.
(9) Chase, B. *Anal. Chem.* **1987**, *59*, 881 A.
(10) Asher, S. A.; Johnson, C. R. *Science* **1984**, *225*, 311–13.
(11) Dudik, J. M.; Johnson, C. R.; Asher, S. A. *J. Chem. Phys.* **1985**, *82*, 1732–40.
(12) a. Asher, S. A.; Johnson, C. R.; Murtaugh, J. *Rev. Sci. Instrum.* **1983**, *54*, 1657–62. b. Ziegler, L. D.; Hudson, B. S. *J. Chem. Phys.* **1981**, *74*, 982.
(13) Jones, C. M.; DeVito, V. L.; Harmon, P. A.; Asher, S. A. *Appl. Spectrosc.* **1987**, *41*, 1268–75.
(14) a. Williams, K.P.J.; Klenerman, D. J. *Raman Spectrosc.* **1992**, *23*, 191. b. Gustafson, T. L. *Optics Comm.* **1988**, *67*, 53.
(15) Asher, S. A.; Bormett, R. W.; Chen, X. G.; Lemmon, D. H.; Cho, N.; Peterson, P.; Arrigoni, M.; Spinelli, L.; Cannon, J., submitted for publication in *Appl. Spectrosc.*
(16) Rodgers, K. R.; Su, C.; Subramaniam, S.; Spiro, T. G. *J. Am. Chem. Soc.* **1992**, *114*, 3697–3709.
(17) a. Zhang, Y. P.; Ziegler, L. D. *J. Phys. Chem.* **1989**, *93*, 6665. b. Ziegler, L. D. *J. Chem. Phys.* **1987**, *86*, 1703. c. Phillips, D. L.; Myers, A. B. *J. Chem. Phys.* **1991**, *95*, 226. d. Li, B.; Myers, A. B. *J. Chem. Phys.* **1991**, *94*, 2458. e. Phillips, D. L.; Myers, A. B.; Valentini, J. J. *J. Phys. Chem.* **1992**, *96*, 2039–44.
(18) Ci, X.; Myers, A. B. *Chem. Phys. Lett.* **1989**, *158*, 263–69.
(19) DeVito, V. L.; Asher, S. A. *J. Am. Chem. Soc.* **1989**, *111*, 9143–52.
(20) Sension, R. J.; Hudson, B. S. *J. Chem. Phys.* **1989**, *90*, 1377.
(21) Ziegler, L. D.; Hudson, B. S. *J. Chem. Phys.* **1983**, *79*, 1134.
(22) DeVito, V. L.; Cai, M-Z.; Asher, S. A.; Kehres, L. A.; Smith, K. M. *J. Phys. Chem.* **1992**, *96*, 6917–22.

Radiochemistry, Chemical Sensors, and Microscopy

Chemical Sensor Technology, Vol. 4. Shigeru Yamauchi, Ed. xvii + 270 pp. Kodansha, Tokyo, and Elsevier Science Publishers, 52 Vanderbilt Ave., New York, NY 10017. 1992. $210

Reviewed by Paul D'Orazio, Ciba-Corning Diagnostics, 63 North St., Medfield, MA 02052

Volume 4 of this series, like past volumes, is a collection of review articles describing recent advances in chemical sensor technology. This volume contains 15 articles written by experts in the field. The technologies covered are predominantly electrochemical, and the authors have focused on detailed mechanistic models of the various chemical-sensing approaches. Applications are touched upon, principally in the biochemical and biomedical areas; however, at times the reader is left wondering whether certain technologies are likely to find practical use.

For the most part, the chapters are written in a clear, succinct style. They are rather short, so the reader must rely on the references for more detail and background information. The citations appear to be current but are rather sparse in a few chapters, given the nature of the monograph. The subject index is complete and very useful.

The opening chapter is a personal and professional biography of Naoyoshi Taguchi, one of the pioneers of semiconductor-based gas sensors. This chapter is interesting and entertaining, and it serves as a good introduction to two of the following chapters: "Some Basic Aspects of Semiconductor Gas Sensors" by Yamazoe and Miura and "Characterization of Oxygen Adsorbates on Semiconductive Oxides" by Iwamoto. These chapters contain current research findings on semiconductor gas sensors and reviews of the technology fundamentals.

Some other chapters are noteworthy. "Silicon Technologies for Sensor Fabrication" by Mokwa and "Biosensors with Microvolume Reaction Chambers" by Bousse, Owicki, and Parce describe recent advances in silicon microfabrication techniques as applied to chemical sensors. Modifications of electrode surfaces with ionically and electrically conducting polymers and the advantages of these sensors in chemical analysis are discussed in "Characterization of Poly(dimethyldiallylammonium) Chloride and Its Application to Electrochemical Sensors" by Tieman et al. and in "Enzyme Sensor Utilizing an Immobilized Mediator" by Mizutani and Yabuki. These chapters are timely in view of recent trends in research and development of chemical sensors. Other subjects of interest include sensors based on piezoelectric principles and the latest improvements in CHEMFET technology.

The novice in the field of chemical sensors probably would not benefit much from this book. I would recommend it for the scientist who has a fundamental background in chemical sensing and wishes to be brought up to date quickly in a specific area of sensor technology.

Physical Methods of Chemistry. 2nd ed., Vol. 4. Microscopy. Bryan W. Rossiter and John F. Hamilton, Eds. x + 536 pp. John Wiley & Sons, 605 Third Ave., New York, NY 10158. 1991. $140

Reviewed by John A. Small, National Institute of Standards and Technology, Bldg. 22, Rm. A113, Gaithersburg, MD 20899

This book contains 10 chapters on various aspects of electron and light microscopy. It is heavily biased toward medium- and high-voltage transmission as well as scanning transmission electron microscopies; seven chapters are devoted exclusively to these topics. Three of these chapters are organized around specimen type, and four are organized around instrument techniques—a format that results in some repetition of information. Scanning electron microscopy (SEM), light microscopy, and particle sizing techniques are discussed in the remaining three chapters.

Readers will find the technical level inconsistent. Some chapters, such as those on biological aspects, light microscopy, and particle sizing, are introductory in nature. Other chapters, particularly those on electron imaging and diffraction techniques, are written for an advanced audience with a background in diffraction and crystallography. Most of the information has been covered in previous publications by these authors or other scientists. The majority of the references precede 1988.

The medium- and high-voltage section begins with an introductory chapter describing the instrumentation and imaging techniques available to the analyst. Despite being slightly disorganized with a bias in favor of imaging methods, this chapter gives an adequate overview of the subject. The second chapter, on biological and organic materials, is very readable and provides a basic review of the subject, including informative sections on sample preparation and beam damage.

The next three chapters, which review electron imaging and diffraction, are well written, but most scientists not involved in these areas would find them difficult to understand. The chapter on microanalysis provides an excellent discussion of electron energy loss spectrometry (EELS) but gives only a very short and incomplete discussion of energy-dispersive X-ray spectrometry—despite the fact that the X-ray technique is firmly established, whereas EELS is, to some degree, still a research topic. A more appropriate title for this chapter might have been "Microanalysis in the Medium- and High-Voltage Electron Microscope," given that X-ray analysis is also covered in the SEM chapter. In the final chapter in this section, special techniques are discussed and high-voltage, scanning transmission, and reflection electron microscopy are reviewed. To a certain extent, the section on scanning transmission electron microscopy is redundant.

The remaining three chapters, which review SEM, light microscopy, and particle sizing, are inconsistent with the theme of the first seven chapters—particularly the chapter on particle sizing. The SEM chapter is only a very brief, basic review of the subject. There is essentially no mention of instruments such as environmental scanning electron microscopes or techniques involving low-voltage microscopy and analysis with field emission SEM. The chapter on light microscopy, more than 100 pages long, should have been shortened through the use of references. The length detracts from the chapter and makes it difficult for the reader to extract pertinent information. In addition, there is only a very brief mention in the light microscopy chapter of important techniques such as acoustic, FT-IR, Raman, and scanning confocal microscopies.

The final chapter on particle sizing is, in my opinion, out of place in this volume. By itself, this chapter appears to offer a practical review of the subject, but only its first portion is related to microscopy.

In summary, this book is devoted principally to the topic of medium- and high-voltage electron microscopy for which it offers the reader an adequate review of the subject. The remaining topics—light microscopy, SEM, and particle sizing—appear to be out of place and would best be handled in a review volume devoted to all forms of microscopy or in separate volumes.

Radiochemistry and Nuclear Methods of Analysis. William D. Ehmann and Diane E. Vance. xviii + 531 pp. John Wiley & Sons, 605 Third Ave., New York, NY 10158. 1991. $95

Reviewed by Alan C. Ling, Department of Chemistry, San Jose State University, San Jose, CA 95192

In comparison with other aspects of physical science, nuclear and radiochemistry are small contributors to the overall scheme of things. Nuclear science is, however, an important player in various aspects of medicine, life sciences, industrial technology, physical sciences, archeometry and art, and theoretical/computational sciences. This new book fills the need for a contemporary text with a good mix of simple introductory theory, experimental methodology, and instrumentation for beginning students of nuclear science.

Ehmann and Vance's extensive knowledge and experience in managing training programs for nuclear science enhances their text, providing a well-planned mix of topics. The level of presentation is suitable for introductory junior or senior undergraduate courses in nuclear science; for graduate-level courses in other disciplines (e.g., medicine and archaeology) that make use of nuclear science; and even as a supplementary text for introductory graduate courses in nuclear chemistry, nuclear engineering, or health physics and radiological safety.

> **“Details are provided for neutron, photon, and charged particle activation, as well as for experimental and correction methods.”**

Because each chapter topic often merits a monograph in its own right, the descriptions are necessarily brief. In general, however, the authors have done a good job of introducing topics without overwhelming readers with detail. One general comment is that often an acronym is used in a chapter without having been defined in that chapter. Because instructors may not use all of the chapters, students often must search other parts of the book to interpret acronyms.

Chapter 1, “Introduction to Radiochemistry,” is well written and includes an interesting collection of photographs of the pioneers in nuclear science, together with short descriptions of their contributions to particular topics. In Chapter 2, “Types of Radioactive Decay,” some of the more esoteric modes such as cluster emission and double beta processes are discussed, but this chapter would have benefited from a brief description of the theories pertaining to each major type of decay process.

In Chapter 3, “Nuclear Chemistry and Mass–Energy Relationships,” I would have preferred to see the liquid drop binding energy curve and valley of beta stability discussed under the liquid drop model rather than separately. Likewise, I would have preferred to see the simplified original Weizsacher development, rather than the modifications by Myers and Swiatecki, discussed in an introductory text. The nuclear theory description needs to be fleshed out more. It is important for beginning students to understand the origins of nuclear energy levels and to see how the simple Weizsacher equation and the “magic numbers” from shell theory ideas provide insight for the concept of “super-heavy” elements and the “island of stability.”

Chapter 4, “Nuclear Reactions,” probably provides too much detail for the student who is going into life sciences and too little for the one who plans to become a nuclear chemist or a nuclear physicist but, all in all, it balances nicely between needed and optional topics. In Chapter 5, “Rates of Nuclear Decay,” the authors describe the methods and underlying concepts required to determine half-lives other than the trivial case of “minutes-to-hours” in magnitude, and they present the kinetics governing radioactive equilibrium, secular and otherwise.

Chapter 6, “Interactions of Radiation with Matter,” could have contained a more detailed description of these fundamental processes, because they provide the only rational approach to understanding the various detectors. A brief derivation and discussion of the Compton scattering equation and its relevance to the theoretical expected gamma spectrum from a single gamma-photon emitter, the elastic scattering process for fast neutrons, the linear energy transfer process and the mechanics of the Coulombic excitation interaction for charged particles with applications to radiation biology, and the operating characteristics of charged particle detectors would also strengthen this chapter. Cerenkov interactions could have been more usefully expanded and perhaps directly related to liquid scintillation techniques and Cerenkov detection.

Chapter 7, “Health Physics,” could have included a few descriptions of some of the more spectacular incidents involving human error and health (such as the Mexican wrought iron problems or accelerator accidents where interlocks have been deliberately disabled) to provide more student interest and empathy. In Chapter 8, "Radiochemistry Instrumentation," I would like to have seen real spectra rather than representations, as well as a more detailed description and brief derivation of the dead-time equations.

In Chapter 9, "Nuclear Activation Analysis," details are provided for various neutron activation techniques, photon activation, charged particle activation, depth profiling, and many experimental methods and correction techniques. I thought that this material was well presented and could stand alone as an introductory course for which this text was designed. In Chapter 10, "Radiotracer Methods," isotope dilution techniques as well as their ramifications and modifications are introduced, and a brief but well-presented discussion of certain aspects of nuclear medicine and nuclear pharmacy are included.

Proton-induced X-ray emission (PIXE), Rutherford backscattering and depth profiling methods, Mössbauer spectroscopy, and radiation chemistry as a technique are described in Chapter 11, "Ion Beam Analysis and Chemical Applications of Radioactivity." In Chapter 12, "Nuclear Dating Methods," the authors provide details on many of the more commonly used nuclear clocks, offer some insight about their shortcomings and methods used to try to overcome their limitations, and give approximate ranges of applications for each. It might have been worthwhile and interesting to include some of the associated nuclear methods.

Chapter 13, "Origin of the Chemical Elements," is a well-written overview of cosmology and stellar synthesis that provides enjoyable reading and considerable information for the nonexpert. In Chapter 14, "Particle Generators," a good overview of accelerators and reactors is given. I would like to have seen a brief discussion of the self-focusing aspects inherent to some accelerators and descriptions of standing wave processes, as well as the drift tube concept with alternating polarity to accelerate the particles.

There is a brief and disappointing appendix on radiochemical statistics. It is not that "all" topics are not covered; however, some fundamental aspects are omitted, and incorrect information is given (e.g., the book confuses the error in a count rate with the square root of the count rate). Additional appendices provide useful abbreviated listings of some physical constants and nuclide properties used by practitioners. Use of the Chart of the Nuclides is described, but I would like to have seen a small appendix (or descriptive material added to the text) for the nomenclature as well as use of the Shirley & Lederer compendium of nuclide properties and energy levels.

The instructor at this level will be able to use this text for a comprehensive introductory course (e.g., a lecture course on nuclear science or an associated or independent laboratory course on radiochemistry) without the need for supplementary material. In fact, I used this text for the first time in 1992 for "Summer Schools in Nuclear and Radiochemistry," a program funded by the U.S. Department of Energy that was taught at San Jose State University and at Brookhaven National Laboratories. Students and faculty gave favorable reviews of the text; their consensus was that it is easy to read and well presented.

Books Received

Voltammetric Determination of Molecules of Biological Significance. W. Franklin Smyth. x + 133 pp. John Wiley & Sons, 605 Third Ave., New York, NY 10158. 1992. $80

This nine-chapter book (eight topic chapters plus references) covers recent developments in voltammetry for biochemistry and toxicology. Topics include determination of amino acids and other native compounds, halogen-containing compounds, azo dyes, organometallics, and selected inorganics. Specific applications of methods such as polarography and anodic stripping voltammetry are discussed in the context of their historical development, and methods are compared for each analyte. The text includes extensive tables, spectra, and chemical structures as well as an index of analytes and methods.

Modern Aspects of Electrochemistry, No. 22. J. O'M. Bockris, B. E. Conway, and Ralph E. White, Eds. xi + 551 pp. Plenum Press, 233 Spring St., New York, NY 10013. 1992. $95

Twenty-second in a series, this text presents electrode chemistry in five large chapters, beginning with fundamentals of capacitance models and metal surface chemistry and moving to electrocatalytic oxidation of aliphatics, surface states on semiconductors, new applications for electrodeposition of Ni–Fe alloys, and microelectrode techniques. In addition to a regular index, this book contains cumulative author and title indexes for all 22 volumes.

Handbook of Mass Spectra of Environmental Contaminants, 2nd ed. Ronald A. Hites. 581 pp. Lewis Publishers, 121 S. Main St., P.O. Drawer 519, Chelsea, MI 48118. 1992. $70

This handbook presents a collection of the electron impact mass spectra of 533 common environmental pollutants, an increase of 139 from the first edition. Compounds and spectra selected from U.S. EPA databases and the Merck Index were edited for spurious mass peaks. Spectral plots include structural and empirical formulas, Chemical Abstracts Service (CAS) and Merck Index numbers, and a list of intense peaks. The compounds are indexed by common names, CAS number, first mass spectral peak value, and molecular weight.

Biosensors. Frieder Scheller and Florian Schubert. x + 359 pp. Elsevier Science Publishers, 52 Vanderbilt Ave., New York, NY 10017. 1992. $162

Eleventh in a series on techniques and instrumentation in analytical chemistry, this book describes metabolic and affinity biosensors in six chapters with diagrams of instrumentation as well as enzymatic and cell receptor processes. Topics include technical aspects, such as immobilization of a sensor's receptor component and mathematical modeling of enzyme electrodes, and descriptions of enzyme and affinity sensors for clinical analytes. A list of abbreviations and symbols, a subject index, and references are included.

The Spectroscopy of Semiconductors, Vol. 36. Semiconductors and Semimetals. R. K. Willardson, Albert C. Beer, and Eicke R. Weber, Eds. xiii + 446 pp. Academic Press, 1250 Sixth Ave., San Diego, CA 92101-4311. 1992. $100

This book contains five chapters on spectroscopic techniques for semiconductor analysis. Topics include magneto-optics, Raman scattering, photoluminescence, photoreflectance, piezospectroscopy, ultrafast spectroscopy, and spectroscopy at extremely low temperatures and high magnetic fields. Equations, spectra, and diagrams for instrument setups accompany the text, and a book index and list of volume contents for the entire series are included.

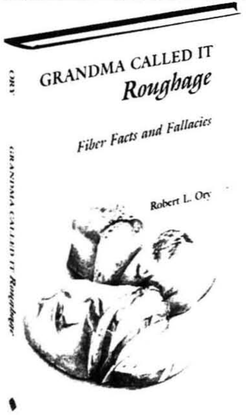

Grandma Called It Roughage

Fiber Facts and Fallacies

This semi-technical volume, written specifically for non-scientists, is must-reading for anyone concerned about health and nutrition. With scientific facts to support the statements made about the known health benefits of fiber, Dr. Ory offers an interesting, sometimes humorous, approach that will appeal to the general reader.

Although not intended to be the final word on dietary fiber (research goes on continually), the book is intended to quell rumors about dietary fiber and to inform those who don't understand enough about fiber's benefits and limitations.

The author also offers some of his own recipes for simple and tasty high-fiber foods, including Bread Pudding, New Orleans Style Red Beans, and Eggplant Lasagna.

Contents

- Fibermania and How It Began
- What Is Fiber and Where Do We Find It?
- Fiber and Metabolism vs. Fat and Cholesterol
- Can Fiber Fight Fat?
- Fiber and the Big "C"—Constipation!
- Can Fiber Cure Cancer, Diabetes, or Other Diseases?
- Fiber and Mineral Nutrition
- Is Fiber an Essential Nutrient?
- Breakfast Cereals: The Battle of the Brans
- Fiber in Fruits and Vegetables
- Can Fiber Be Good for You and Still Taste Good?

Robert L. Ory, Ph.D.
160 pages (1991)
Clothbound: ISBN 0-8412-1749-1
$22.95
Paperbound: ISBN 0-8412-1764-5
$12.95

ORDER FROM

American Chemical Society
Distribution Office, Dept. 21
1155 Sixteenth St., N.W.
Washington, DC 20036
or CALL TOLL FREE

800-227-5558

(in Washington, D.C. 872-4363) and use your credit card!

Announcing Two Dynamic 1993 Sessions of This Popular ACS Short Course!

THERMAL ANALYSIS IN MATERIALS CHARACTERIZATION

EDITH A. TURI, COURSE DIRECTOR

Saturday-Sunday **March 6-7, 1993** **Atlanta, Georgia in conjunction with PITTCON'93**	**Saturday-Sunday** **March 27-28** **Denver, Colorado in conjunction with the 205th ACS National Meeting**

Nine Ways You'll Benefit From Attending This Course

- ☐ Gain an overview of the basic principles of thermal techniques
- ☐ Be able to compare available instruments and define optimal experimental conditions
- ☐ Learn to apply a down-to-earth, systematic approach to a very broad range of materials
- ☐ Learn how to analyze and interpret thermal data, predict performance, improve quality, and increase productivity
- ☐ Optimize quality control methods
- ☐ Learn ways to have direct input in promoting economical and marketing objectives
- ☐ Discuss specific questions, such as problem solving, operation safety, and troubleshooting
- ☐ Receive personal guidance from experts in the field

REGISTER TODAY!

For more information, call the Continuing Education Short Course Office at(800) 227-5558 (TOLL FREE) or (202) 872-4508. FAX: (202) 872-6336.Or, use the coupon below to request a free descriptive brochure on thisauthoritative short course.

American Chemical Society
Dept. of Continuing Education
Meeting Code TAMC93
1155 Sixteenth Street, N.W.
Washington, DC 20036

☐ ***YES!*** Please send me information on the ACS Short Course, *Thermal Analysis in Materials Characterization*, to be held March 6-7 in Atlanta, Georgia, and March 27-28 in Denver, Colorado.

Name ____________________
Title ____________________
Department ____________________
Organization ____________________
Address ____________________
City, State, Zip ____________________

FOCUS

EASTERN ANALYTICAL SYMPOSIUM RETURNS TO SOMERSET

Crisp clear fall weather and the sound of crunching leaves underfoot greeted conferees as they arrived Nov. 16–20 at the Garden State Convention and Exhibit Center and Somerset Plaza Hotel for the 31st annual Eastern Analytical Symposium.

This meeting was the third held at EAS's new home in Somerset, NJ. Since the symposium moved from New York City in 1990, meeting attendance has steadily increased. Approximately 4000 registrants attended the 56 technical sessions, eight poster sessions, workshops, short courses, and exposition.

According to program chairman Satinder Ahuja of Ciba-Geigy Corp., this year's meeting provided an opportunity for those involved in the analytical and allied sciences to learn about the latest techniques in the field, exchange information, and obtain a feel for what is on the horizon in cutting-edge research. The program covered a wide variety of analytical techniques, including chromatography (TLC, GC, HPLC, CZE, electrophoresis, and detectors), spectroscopy (atomic, IR, Raman, and NMR techniques), MS, electrochemistry, chemometrics, chemical sensors, automation, computers, and microscopy. In addition, a broad range of applications were featured, including new materials (e.g., fullerenes), biomedical studies, polymers, pharmaceuticals, environmental chemistry, forensics, and natural products.

Six scientists were honored at award sessions. On Monday, Richard R. Ernst of the ETH–Zentrum, Laboratorium für Physikalische Chemie, and 1991 Nobel Prize Medalist in Chemistry was honored with the EAS Award for Achievements in Magnetic Resonance. Daniel E. Martire of Georgetown University received the EAS Award for Achievements in Chromatography at a symposium on Tuesday. Lois G. Weyer of Hercules, Inc., was also recognized on Tuesday with the EAS Award for Achievements in Near-IR spectroscopy. On Wednesday, Gary M. Hieftje of Indiana University was honored with the EAS Award for Outstanding Achievements in the Fields of Analytical Chemistry. Jack L. Koenig of Case Western Reserve University received the New York Section of the Society for Applied Spectroscopy Gold Medal at a Wednesday afternoon symposium. The final awardee of the meeting was Robert G. Michel of the University of Connecticut, who received the American Microchemical Society's Benedetti–Pichler Memorial Award on Thursday morning.

Several sessions generated special interest. Chiral separations proved to be a hot topic for the pharmaceutical audience in light of the latest Food and Drug Administration guidelines for the development of drugs of chiral compounds. Interesting talks were delivered on the importance of chiral separations of pharmaceuticals (S. Ahuja), mobile phases (Willie Hinze of Wake Forest University and Tom Beesley of Advanced Separation Technologies), chiral techniques and capillary electrophoresis (Gyula Vigh of Texas A&M University and Tim Ward of Millsaps College), and trace-level determinations of enantiomeric impurities (Dan Armstrong of the

University of Missouri–Rolla).

Numerous attendees were drawn to the session on enantioselective LC. "Bioactive LC Reactors for Stereospecific Synthesis with Online Enantioselective Separations" (Tanya Alebic-Kolbah of McGill University) and "Bioactive Chromatography Using Immobilized Biopolymers" (Irving Wainer of McGill University) were among the papers presented.

Sessions on near-IR spectroscopy continue to be popular, as reflected by the attendance at Weyer's award talk entitled "Near IR—What Can It Tell Us?" and at other presentations, including "Noninvasive Process Monitoring with Near IR—Tools for Teaching and for Industry" (Jim Callis, University of Washington) and "Near-IR for Fun and Profit: An Academic View of Industry" (Bill Fateley, DOM Associates).

Ernst's award talk, "NMR on the Carousel, Rotating Spins, Fields, and Samples," drew much attention. Many of the other NMR sessions, which covered topics such as FT-NMR spectroscopy, NMR imaging, natural products, structure determination in solids, and conformation of proteins, also attracted many conferees. To commemorate the quincentennial year of the exploration of America by Columbus, sessions on "Serendipitous Discoveries in Chemistry and Spectroscopy" were held. In addition, authors of textbooks delivered talks at a session designed to address the education of future analytical chemists.

Special sessions were held in memory of two longtime EAS supporters: Joseph Jordan and Irene Nurkiewicz. Jordan, who was emeritus professor at The Pennsylvania State University, was honored at a symposium on Monday afternoon. Known internationally for his pioneering work in bioelectrochemistry and thermometric analysis, Jordan also served on the advisory board of ANALYTICAL CHEMISTRY. He was an active member of the IUPAC and was the 1978 recipient of the Benedetti-Pichler Award. Two of his close colleagues, Karl Kadish of the University of Houston and Clemens Auerbach of Brookhaven National Laboratory, reflected on some aspects of his life and work.

Bill Fateley, Hercules Felder (Permacel), and David Nash (consultant) delivered tributes to Nurkiewicz at the beginning of the Thursday afternoon session entitled "Microanalysis in Today's World," organized by Concetta Paralusz (Permacel). Formerly employed by American Cyanamid as a microchemist, Nurkiewicz served on the EAS Governing Board for numerous years. She was also involved for many years with the EAS Registration Committee.

In addition, the 1992 EAS student awards program was dedicated to the memory of Nurkiewicz. The EAS is one of the few organizations that actively supports the education of undergraduate chemistry majors. Historically, the award recipients have demonstrated a strong continuing interest in analytical chemistry. They were nominated by their professors, selected by the EAS Student Award Selection Committee, and approved by the EAS Governing Board. The six awardees, who attended the meeting as guests of the EAS, are Diadra Bau of Wilkes University (PA), Meredith Daniel of Marist College (NY), Jean DeSimone of Glassboro State College (NJ), Steve Joerg of Albright College (PA), Samuel Toba of Towson State University (MD), and Melanie Woodroffe of the State University of New York at Oswego.

Twenty-eight short courses, among them 15 ACS short courses, covered a broad range of topics, including GC, LC, NMR spectroscopy, laboratory safety, chiral chromatography, SFE and SFC, AA, chemometrics, statistics, capillary electrophoresis, thermal analysis, LIMS, technical writing, and environmental law. According to Lawrence Kobilinsky of John Jay College (NY) and Harry Walsh of the American Chemical Society, more than 490 conferees attended the courses. In addition, 24 workshops, designed to give conferees hands-on experience, covered an equally broad range of topics, including capillary column technology for GC, résumé writing and interview skills, environmental analysis, hyphenated techniques, and robotics. According to Jane Wu of Merck & Co., more than 400 conferees attended the workshops.

The 31st EAS meeting was a great success. Even before the last talk concluded and the conferees headed home, plans were being made for next year's meeting, which will be held Nov. 15–18 in Somerset. Authors wishing to present their work at next year's meeting should submit 100–200-word abstracts of their presentations before April 15 to EAS program committee, P.O. Box 633, Montchanin, DE 19710-0633. Indicate whether the abstract is being submitted for oral or poster format. To suggest topics or speakers, or for further information, call the EAS hotline, 302-738-6218. *Grace K. Lee*

FOCUS

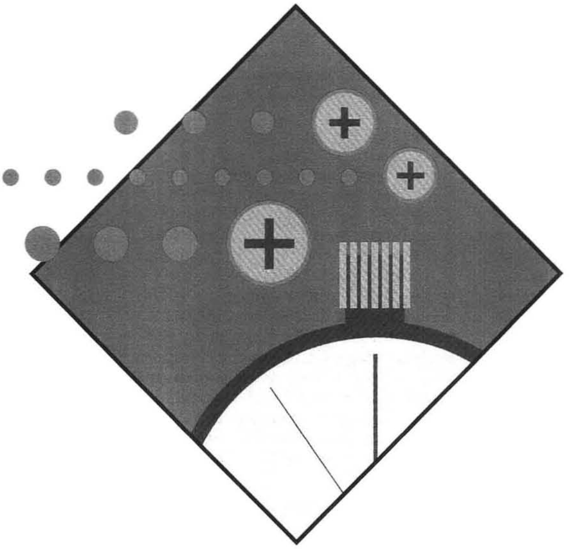

1992 Conference on Instrumentation for Time-of-Flight Mass Spectrometry

The first conference on instrumentation for time-of-flight mass spectrometry (TOFMS), sponsored by the LeCroy Corporation, was held at Woodcliff Lake, NJ, Nov. 11–12. Conceived last March by Walter LeCroy, who founded the high-energy physics and test and measurement instrumentation company in 1964, the conference addressed the instrumentation challenges facing TOF mass spectrometrists. According to LeCroy, this meeting was designed to provide a forum in which instrument designers and users can share their perspectives on existing problems, new ideas ready for development, future directions that merit investigation, and hardware requirements.

Although TOFMS is not new, developments in techniques and applications that make use of the TOF analyzer, such as the study of multiphoton ionization (MPI) processes of organic molecules, plasma desorption mass spectrometry (PDMS), and laser desorption mass spectrometry (LDMS), continue to attract attention. The development of matrix-assisted laser desorption (MALD) in 1988 to determine molecular weights of massive (> 300 kDa) proteins has sparked renewed interest in this analyzer, as have reports of a new commercial PD mass spectrometer and the interfacing of fast atom bombardment and electrospray ionization sources for on-line LC/MS.

This renewed interest was confirmed by an overwhelming response from members of the international academic and industrial TOFMS community to the announcement of the LeCroy meeting. Organizers moved the conference to more spacious quarters when the approximately 100 conferees overflowed the corporate facilities, and they received more than 700 requests for conference proceedings from scientists unable to attend.

Members of the program committee (George Blanar and Len Mooney of the LeCroy Corporation, Brian Chait of The Rockefeller University, Robert Cotter of the Johns Hopkins University, Robert Levis of Wayne State University, and Kevin Owens of Drexel University) emphasized the varied and complementary aspects of developing instrumentation for TOFMS in applications including new spectrometers; detectors; and requirements for MALD, GC, LC, and capillary zone electrophoresis (CZE). The program was divided into four sections: methodology, continuous ionization sources, current implementations, and techniques and components.

Methodology

Ken Standing of the University of Manitoba (Canada) began the methodology portion of the program by discussing some problems in TOF measurements. A major concern is the resolution of a TOF measurement, which is limited by the initial time, space, and velocity of the observed ions. He noted that the initial temporal dispersion in techniques such as PDMS and secondary ion MS is normally small and that spatial differences can be compensated for by ejecting the ions from a plane equipotential surface. This leaves the initial velocity dispersion as the primary limiting factor in resolution measurements. Its effect can be greatly reduced by the use of an ion mirror (reflectron), even in the more complicated case of LD, but a limit is set by the time spread in the acceleration region. Some space can be saved by using a two-stage mirror in place of a simple single-stage mirror, but the limiting resolution is not significantly better.

Kevin Owens, who is also working to maximize mass resolution, has attacked the problem with a simulation approach. He used simplex optimization techniques to design a reflectron-type TOF mass spectrometer. Ion peak shapes are simulated by use of a Monte Carlo approach and include the effects of ion formation time, position of ionization, and initial ion velocity. The lensing effect of wire mesh grids commonly used to define the electric fields in various regions in the instrument is also included in the model. The simplex results can be explained in terms of the commonly used space and energy focusing conditions, and permit a better understanding of the effect of grid mesh size, ion mass, and initial ion formation conditions on maximum achievable mass resolution.

Continuous ionization sources

Michael Guilhaus of the University of New South Wales (Australia) has developed an approach that he calls orthogonal acceleration TOF (TOF-oa). In contrast to techniques in which ions are gated from a continuous ion beam into a flight tube perpendicular to the ion beam, his group uses a simple ion-optical arrangement involving a nonperpendicular flight tube. This approach offers advantages in sensitivity over linear instruments and mass resolution well in excess of 2000 (fwhm), prompting interest in interfacing it with continuous ionization sources for applications such as LC/MS, ICPMS, and GC/MS. Because the fundamental physical resolution limitations inherent in conventional linear TOF instruments with gaseous sources are reduced with TOF-oa, the limitation of the resolution of the detector and detection electronics becomes a key issue.

Liang Li's research group at the University of Alberta (Canada) hopes to capitalize on the strengths of TOFMS (high ion transmission, lack of mass limit, high spectral acquisition rate, pulsed ion detection, and versatility) in their efforts to combine it with solution-based separation methods for biochemical analysis. Their work is concentrated in two areas. The first involves the use of a pulsed sample introduction interface for linking conventional LC with TOFMS, and the second is the development of a continuous-flow (CF) MALD system for coupling micro-LC or CE with TOFMS for peptide and protein analysis. This CF-MALD method uses a flow probe to deliver sample and matrix (3-nitrobenzyl alcohol) through a capillary tube and onto a stainless steel frit; laser desorption/ionization is then carried out on the frit.

Current implementations

Bob Cotter described a compact tandem TOF instrument developed in his laboratory that incorporates two dual-stage reflectron analyzers and a collision region for producing product ions by high-energy collision-induced dissociation. Ions of a particular mass are selected by deflecting them from stable trajectory angles as they enter the second reflectron. To avoid differential pumping of the collision region, the design incorporates a pulsed valve through which the collision gas is introduced. Mass resolution for the primary beam, recorded through both reflectrons, is greater than one part in 4000, and mass dispersion can be increased by reaccelerating the product ions exiting the collision chamber.

David Lubman of the University of Michigan is using laser radiation to detect selectively microtrace quantities of organic compounds with various TOF configurations. For applications such as the discrimination of isobars, isotopes, isomers, and trace target species in complicated matrices he employs supersonic jet expansions and reflectron energy analyzers. Detection and discrimination of metabolites of indoleamines, catecholamines, and small peptides at the femtomole level have been achieved. His group also developed an ion trap storage/TOF device that uses ion storage as a means to enhance sensitivity and resolution, and has used it to study long-lived metastable decay and external injection with atmospheric pressure ionization and electrospray sources.

Rick Fletcher's research at the University of Idaho has involved the vaporization of matrix-isolated molecules by ablation and compaction of an organic polymer. The technique uses a high-velocity polymer disk to vaporize matrix-isolated molecules and other nonvolatile samples by adiabatic compression. Disks as large as 200 µg and 1 mm in diameter have been created and accelerated to supersonic velocities by laser vaporization of a contained bulk polymer target. The disks generate transient pressures of 0.1–10 GPa (10^3–10^5 atm), sufficient to vaporize frozen hydrocarbon glasses at 77 K. His group has developed a prototype vaporization source based on this technique that can be coupled with a TOF mass spectrometer or used for laser-induced fluorescence (LIF) characterization of vaporized molecules. Fletcher also described how the vaporization source can be used as a general interface between various chromatographs (gas, liquid, and supercritical fluid) and a TOF mass spectrometer.

Another area of considerable interest involves the study of ion–solid interactions and trace surface analysis. Nick Winograd of The Pennsylvania State University described an approach that combines energetic particle bombardment with multiphoton resonance ionization spectroscopy to analyze atoms and molecules absorbed on solid surfaces. The species on the surface of a target are desorbed by a pulsed ion beam. These particles travel in space for a few hundred nanoseconds and are ionized when they intersect a laser beam positioned a few millimeters above the target and tuned to a resonance of the gas-phase species. Winograd's group has been able to detect impurity atoms at the part-per-trillion level in semiconductor targets and has found that it is possible to detect a variety of molecules from surface layers with detection limits in the attomole range, which corresponds to just a few hundred atoms/cm^2 and a few hundred thousand molecules/cm^2.

DNA sequencing of the human genome is also an exciting area of application for TOF. According to Robert Levis, advances in laser-based methods suggest that a sequencing technique based on resonance-enhanced MPI-TOFMS may offer a faster and less expensive alternative to current sequencing methods. His group's ability to laser-vaporize single-stranded DNA molecules having chain lengths of more than 1000 nucleotides into the gas phase with no discernible bond cleavage is the basis of a TOFMS-based sequencing technique. Dideoxy sequence products labeled with an anthracene tag are generated, tagged products from sequencing reactions are vaporized, the anthracene linked to gas-phase neutral DNA strands is ionized, and the TOF mass spectrum of singly charged dideoxy-terminated DNA strands is obtained. To determine the sequence, the experiment would be repeated for the four complementary dideoxy sequencing reactions. Levis predicts that the method would allow determination of a 300-base DNA sequence in < 1 s, and that an instrument based on this technology could generate sequencing data in excess of 25 million bases per day.

Techniques and components

Werner Ens of the University of Manitoba began his talk on digital and analog methods for TOFMS by noting that TOF mass spectra are normally measured by time-to-digital conversion (TDC) after single-ion counting or with a transient recorder after current measurement. When only a few ions are produced in each timing event, TDC is preferable; when signals from many ions are produced per event, a transient recorder is preferred. Thus, applications such as MALD, where ~ 10^4 molecular ions may be produced in a single laser shot, or electrospray MS, where the ion current is high, suggest use of a transient recorder. However, given the advantages of TDC (typically better resolution, higher dynamic range, and the capability of a higher repetition rate) and the fact that single-ion counting methods allow charged and neutral products to be identified by correlation techniques, Ens has investigated the use of TDC in experiments for MALD and electrospray TOF. He identified no analytical advantage of using TDC for MALD, an intrinsically pulsed technique. However, electrospray is a continuous ion source, so a high repetition rate is extremely important to maximize the duty cycle and therefore the sensitivity. Morever, with the normal losses in preliminary electrospray TOF experiments, the number of ions per pulse is well within the range that a multistop time-to-digital converter can handle. Therefore Ens suggested that a time-to-digital converter may be more appropriate in this application than a transient recorder.

Jack Holland of Michigan State University described a technique called time-array detection (TAD) that uses all of the mass-resolved information contained in each transient waveform after every ion-source extraction. By summing successive transients, he produces scan files at a rate of 20–200 per second that enhance the sensitivity, limit of detection, dynamic range, and S/N while maintaining a bandpass sufficient for all the information from a secondary source such as GC/MS, HPLC, or CZE.

His group has designed an integrating transient recorder (ITR) to accommodate TAD in sampling systems whose temporal characteristics cannot be controlled. The ITR can use the information from all the scans continuously over long periods of time, providing a detector that can monitor the eluent from high-resolution columns without loss of chromatographic information while operating at less than full capacity. This reserve has made it possible to develop time-compressed chromatography (TCC) that uses short columns or high linear flow rates to reduce analysis time. The rapid scanning of the TOF mass spectrometer creates scan files of high data quality and density, the chromatographic resolution lost by compression is recovered with deconvolution routines that resolve the true mass spectrum for each compound detected, and analysis can be performed on the mathematically isolated individual component profiles. Application of TCC to GC has reduced data analysis times by a factor of 20 or more with no loss of analytical information.

According to Ihor Lys of Carnegie–Mellon University, issues related to the acquisition and subsequent processing of TOFMS data are often overlooked. Although a large number of researchers are actively pursuing the development of TOFMS techniques, he believes that relatively few research the acquisition and data processing aspects involved. The use of signal averaging and smoothing has become common, but other signal processing techniques with the potential to improve sensitivity and resolution are available. However, they generally are not included as built-in functions on the digital storage oscilloscopes used in TOF experiments and, as a result, off-line analysis provides the best means to use such signal processing techniques. His presentation, which focused primarily on LD instruments, highlighted noise analysis, prefiltering, postfiltering, signal averaging, resolution enhancement, and frequency-domain analysis as the more promising signal processing methods. He also emphasized the possibility of improving instrument design through careful data analysis, and discussed the application of deconvolution, FFTs, and IFFTs to filtering and correlation.

David Reed's presentation focused on the use of data generation and acquisition analysis in surface microanalysis using TOF instrumentation. He noted the increase in popularity of TOF as a technique that allows researchers to record the mass spectra from a variety of ion sources, which he attributes to the ability to generate large amounts of data with high instantaneous data rates because of TOF's high transmission, high mass resolution, and complete mass spectral acquisition. For example, a mass spectrum with 156-ps-wide time windows (mass resolution of 5000–15,000 fwhm) over a mass range of 1–4000 amu contains nearly 1 million channels.

His research at Charles Evans & Associates involves surface microanalysis of biological and materials science samples. By undertaking microanalysis through the acquisition of secondary ion images it is possible to obtain an entire mass spectrum for each pixel in the image (256 × 256 mass spectra). As might be expected, efforts to acquire, store, and manipulate such data arrays are demanding, and the hardware and software considerations are complex.

Specific components of importance in TOFMS were discussed by three speakers. Marc Kramer of STI Optronics described tunable solid-state lasers for visible and mid-IR wavelengths as well as future laser developments. Ian Fraser of ETP Electron Multipliers described his firm's work to develop discrete dynode detectors for TOFMS. Len Mooney reviewed the history of digital data acquisition over the past decade, described the current state of the art with respect to digital storage oscilloscope technology, and predicted future developments.

Plans for future conferences are forthcoming. For more information, or to request a copy of the conference proceedings, contact George Blanar or Ana Iriarte at LeCroy Corporation, 700 Chestnut Ridge Rd., Chestnut Ridge, NY 10977-6499 (914-425-2000; fax 914-425-8967).

Louise Voress

NEW PRODUCTS

D912-P and D912-TC thermometer systems for dense liquids and slurries have weighted drop probes with either platinum-RTD or thermocouple functions, respectively. The probes can penetrate liquid asphalt, crude oil, and other liquids to a depth of 40 ft. while suspended from a lead wire that connects to a portable thermometer unit. The D912-P offers system accuracy of ± 0.3 °F at ice point and ± 0.5% from −150 to 500 °F. The D912-TC has meter accuracy of ± 0.2% from −100 to 2500 °F. Wahl Instruments **401**

Instrumentation

Sample cleanup. GPC-Prep, designed for environmental and food-testing sample cleanup, is an automated gel permeation chromatography system that loads from 1 to 20 samples sequentially. The modular design is expandable, includes an optional UV detector for column calibration, and can be hooked up to a PC for automatic documentation and program storage. Fluid Management Systems **402**

GC. Disposable sample-drying device for GC contains 1.5 g anhydrous sodium sulfate in a polypropylene cartridge with a built-in 0.2-µm polypropylene filter and can remove up to 0.5 mL of water. The tube tip can be removed, and several units snap together to remove larger amounts of water. Whatman **403**

Density measurement. AccuPyc 1330 automated density analyzer has sample temperature readout to ± 0.1 °C for materials showing significant variation of density with temperature. Performance is traceable to NIST standards and, with a communications software package, data can be imported directly into spreadsheets for analysis. Micromeritics **404**

GC. Discharge ionization detector, an upgrade for the Series 580 Isothermal gas chromatograph, is sensitive from 1 to 10 ppm for trace gas analysis. The detector, which has a heater, a metering valve, and column connections with VCR fittings, comes with an electronic control unit that includes an electrometer, digital display for DC voltage and discharge current, high-voltage and polarization power supply, and detector temperature control with digital readout. The detector is nonradioactive, universal, and concentration dependent. GOW-MAC Instrument **405**

Environmental testing. Extraction thimbles of cellulose or glass fiber are designed for Soxhlet extraction of nonvolatile and semivolatile organics from soils, sludges, and waste; determination of oil and grease content in wastewater; or determination of total petroleum hydrocarbons. Borosilicate glass thimbles sample suspended particles from industrial smoke stacks and chimneys with DOP efficiency equal to 99.98%. Schleicher & Schuell **406**

HPLC. Ultra-ware sparging manifolds are designed to sparge three mobile-phase reservoirs from one gas cylinder. Each reservoir line has separate sparge and vent on/off valves to sparge, vent, or blanket, and a check valve prevents solvent backflow. Individual reservoirs can be blanketed while others are sparging; a pressure regulator maintains 3–6 psi in the reservoir with the vent valve closed. Kontes **407**

HPLC/GPC and SFC. The 950/14 fiber-optic universal detector for HPLC/GPC and SFC is temperature-controlled up to 300 °C for polymer analysis and, because detector response is proportional to reflected light, the range of analytes is unrestricted. The detector features a liquid crystal display and gives access to menus via a touch-sensitive membrane keypad. Applied Chromatography Systems **408**

GC. Quick-Connect installation device uses standard graphite-vespel or metal ferrules to connect capillary columns onto gas chromatographs without a wrench. The unit, which causes no extra-chromatographic effects, is installed onto gas chromatograph inlet/outlet fittings. A capillary column of any size is plugged in, and the unit connects the column with the flip of a lever. Quadrex **409**

TOC. A-100P SE organics analyzer is the portable version of an on-line TOC analyzer for ultrapure water facilities. The analyzer detects organics in the range of 0.05–9999 ppb, with resolution of 0.01 ppb below 20 ppb and analysis time of 3–10 min per sample. Reports are generated via an LED display or a printer, both contained within the briefcase-sized unit. Anatel **410**

Benzene monitor. MSI-301B, a portable microcomputer-controlled gas chromatograph for on-site or continuous determination of benzene, can monitor and record benzene concentrations ranging from 5 ppb to 500 ppm. Applications include soil and water sampling and industrial hygiene processes requiring continuous unattended monitoring. Microsensor Systems **411**

Fermentation monitoring. Steam-sterilizable insertion sensor for fermentation vessels and reactors features a combination pH or redox electrode with a sealed high-temperature KNO_3 reference electrolyte outer chamber that is unreactive in the presence of ions such as sulfides. Electrodes can withstand repeated sterilization cycles, be installed vertically or via side entry ports of 19 or 25 mm diameter, and be replaced quickly without dismantling the as-

HOT Topics, HOT Books!

New Titles in Medicinal and Pharmaceutical Chemistry

From the American Chemical Society

Polymeric Drugs and Drug Delivery Systems

Covering a broad spectrum of methods of drug delivery and focusing on the use of polymers and materials, this volume presents new materials and methods for controlled drug release. Emphasizing selection of materials for drug delivery rather than just reviewing current methods, the editors challenge researchers to venture into new areas and consider new methods. Included is an examination of recent advances in biodegradable and bioerodible polymer matrices for drug delivery.

Richard L. Dunn and Raphael M. Ottenbrite, Editors
ACS Symposium Series No. 469
314 pages (1991) Clothbound
ISBN 0-8412-2105-7
$74.95

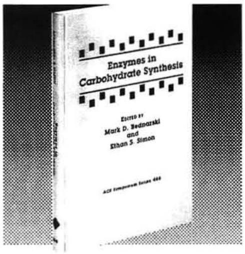

Protein Refolding

Bridging the gap between fundamental and applied studies in protein refolding, this volume addresses such topics as in vivo protein refolding, protein aggregation and inclusion body formation, elucidation of the folding pathway, characterization of folding intermediates, and practical considerations in protein renaturation. An overview chapter provides historical highlights of the key aspects of protein folding, aggregation, and refolding, both in the laboratory and in industry.

George Georgiou and Eliana De Bernardez-Clark, Editors
ACS Symposium Series No. 470
216 pages (1991) Clothbound
ISBN 0-8412-2107-3
$49.95

Selective Fluorination in Organic and Bioorganic Chemistry

Recent applications of organofluorine chemistry to problems in biological chemistry are explored in this new volume. Its 14 chapters address theoretical and synthetic problems, as well as applications of selective fluorination to biological systems. The overview chapter, an excellent tutorial, begins with the fundamental and unique aspects of fluorine chemistry and reviews methods of introducing fluorine into molecules and work done on biomolecules.

John T. Welch, Editor
ACS Symposium Series No. 456
215 pages (1991) Clothbound
ISBN 0-8412-1948-6
$57.95

Cell Separation Science and Technology

Providing theoretical and practical information on the state of the science of cell separation, this new volume covers the four principal modern methods: flow sorting and optical methods; sedimentation and flow fractionation; affinity adsorption and extraction methods; and electrophoresis and magnetic methods. Readers will be able to choose, evaluate, and in some cases, build cell separation procedures and equipment for their own purposes based on the contents of the book, which also covers many applications of each method.

Dhinakar S. Kompala and Paul Todd, Editors
ACS Symposium Series No. 464
302 pages (1991) Clothbound
ISBN 0-8412-2090-5
$69.95

Chiral Separations by Liquid Chromatography

Here is the definitive reference for researchers working on problems involving chirality. Presenting state-of-the-art information, this volume covers all the major modes of separation and offers contributions from the leading researchers who developed these techniques. Four chapters provide a detailed review of the commonly used columns: brush type, cyclodextrin, polysaccharide carbonate, and protein. Many of the papers focus on HPLC, a technique which is also ideally suited for large scale preparation of optical isomers. In addition, the volume provides significant discussion on the use of chiral discriminators or selectors.

Satinder Ahuja, Editor
ACS Symposium Series No. 471
240 pages (1991) Clothbound
ISBN 0-8412-2116-2
$59.95

Cholinesterases: Structure, Function, Mechanism, Genetics, and Cell Biology

Presenting the proceedings of the Third International Meeting on Cholinesterases, this volume provides a wealth of new information on current cholinesterase research, including important advances resulting from new concepts and methodologies such as monoclonal antibodies and molecular genetics. Among the topics covered in its 49 full papers and 140 posters papers are polymorphism and structure, cellular biology, gene structure and expression, catalytic mechanism, pharmacological utilization of anticholinesterase agents, and noncholinergic roles of cholinesterases.

Jean Massoulie, Francis Bacou, Eric Barnard, Arnaud Chatonnet, Bhupendra P. Doctor, and Daniel M. Quinn, Editors
Conference Proceedings Series
400 pages (1991) Clothbound
ISBN 0-8412-2008-5
$89.95

Inositol Phosphates and Derivatives: Synthesis, Biochemistry, and Therapeutic Potential

This new volume examines the synthesis, biochemistry, and pharmacological evaluation aspects of inositol phosphate research . Two overview chapters provide comprehensive background information on stereochemistry and nomenclature of inositol phosphates, basic biochemistry, synthetic challenges, and related pharmacology. Subsequent chapters describe novel methods of preparation, including the use of unusual starting materials and mediation by microorganisms, therapeutic potential and bioactivity, structure-activity relations, and separation.

Allen B. Reitz, Editor
ACS Symposium Series No. 463
224 pages (1991) Clothbound
ISBN 0-8412-2086-7
$59.95

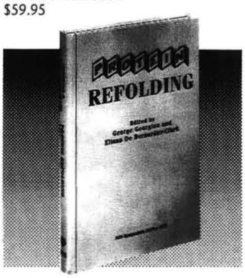

Enzymes in Carbohydrate Synthesis

Not only assessing the past, present, and future uses of enzymes to synthesize carbohydrates, this volume also illustrates the significance of carbohydrate chemistry and describes how the combination of use of modern enzyme chemistry can advance exploration in the field. It details research at the interface of chemistry and biology for carbohydrate chemistry by demonstrating how to integrate chemical reactions and biological techniques that can be used to synthesize complex bioactive monosaccharides, oligosaccharides, and glycoconjugates.

Mark D. Bednarski and Ethan S. Simon, Editors
ACS Symposium Series No. 466
132 pages (1991) Clothbound
ISBN 0-8412-2097-2
$34.95

Order from:

American Chemical Society
Distribution Office, Dept. 162
1155 Sixteenth St., N.W.
Washington, DC 20036
or CALL TOLL FREE
800-227-5558
or in Washington DC
(202) 872-4363
and use your credit card!

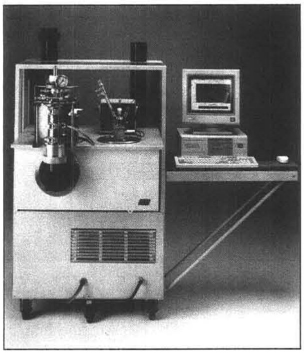

ReactIR reaction analysis systems, designed for chemical product and process development, can be configured for specific application requirements. The systems permit quantitative analysis of reactants, intermediates, and products without disturbing reaction conditions. Mechanisms and kinetics can be determined in real time. Applied Systems **412**

sembly. The sensor has a peripheral ceramic junction to prevent clogging. Van London **413**

HPLC. Shodex RI-71 analytical and RI-72 preparative refractive index detectors for HPLC are designed for measurement of analytes with no UV absorption, for use with eluents that absorb UV, or for measurement of molecular weight distribution of polymer samples. The RI-71 has a maximum flow rate of 10 mL/min and linearity range to 60×10^{-5} RIU; the RI-72 preparative model has a maximum flow rate of 100 mL/min and linearity to 80×10^{-4} RIU. JM Science **414**

Software

Electronic handbooks. "Selected Tables" contains more than 80 data tables from the *CRC Handbook of Chemistry and Physics, 73rd ed.*, including basic constants, element properties, thermodynamics, biochemistry and analytical chemistry, properties of solids, math tables, and health and safety information. The Mathcad live document interface allows users to lift equations, formulas, and diagrams from the handbook and enter them into another document, calculate results, change parameters and plots, and display results in the handbook or on a worksheet. MathSoft **415**

Reaction database. ChemInform RX is the electronic version of *ChemInform*, a weekly compendium of reaction information extracted from 250 chemistry journals covering syntheses and preparative methods. The database cross-correlates reactions through data fields and an indexing system for reaction types, compound classes, and other criteria. The first release contains 62,000 reactions and associated data from the 1991 issues of *ChemInform*; 60,000 reactions will be added annually. Molecular Design **416**

Data acquisition. Chartstream Recorder/Analyzer records up to 48 channels simultaneously with total throughput up to 32,000 samples/s, displaying results in real time in tabular, strip-chart, scatter, or *x-y* plots. User-defined parameters and analysis features allow for added flexibility. The analyzer imports data files in a variety of common formats, including ASCII and Lotus 1-2-3, and graphs can be generated on most common printers. Intelligent Instrumentation **417**

Manufacturers' Literature

Environmental monitoring. "Performance-Based Specifications" document lists analytes and quantitation limits for I-CHEM sample containers and compares them with EPA Superfund specifications. Fourteen new pesticides and PCBs have been added to the list of inorganic, volatile and semivolatile organic, pesticide, and PCB analytes. I-CHEM **418**

Electron microscopy. Electron Optics Bulletin No. 132 contains articles describing enhancements for high-resolution EM to characterize surface reactions, microscopic evaluation of magnetic storage materials, and observation of the atomic structure of $CoSi_2/Si$. Philips Analytical **419**

HPLC. *Troubleshooting Guide for HPLC Injection Problems* covers leaks, artifact peaks, nonreproducible results, decreased system pressure, blockage and high back pressure, and noise and drift. Injection ports are illustrated, and margin comments accompany text. 36 pp. Rheodyne **420**

GC/SFC. DET Report No. 23 features articles on thermionic detection of oxygenates in gasolines, including a section on commercial alcohol-in-gasoline reference standards, and discusses selective detection of linear chain hydrocarbons with a TID-1-N_2 detector. Chromatograms are included. 12 pp. Detector Engineering & Technology **421**

MS. Brochure describes the Quattro MS/MS instrument line, including single and triple quadrupole mass spectrometers and an APcI-electrospray instrument for LC/MS/MS. Component diagrams and assemblies, functional screen displays from MassLynx data acquisition, and instrument control software for Windows are illustrated. 24 pp. Fisons Instruments **422**

Catalogs

Laboratory products. Catalog features more than 35,000 products such as analytical balances, elemental analysis instrumentation, pH/ORP indicators and controllers, flow meters, microdispensers, and pumps. Also included are sections on technical data, conversion factors, and fittings. 1536 pp. Cole-Parmer **423**

Stable isotopes. Catalog lists physical data, application information, structures, and packaging types for stable isotopes. Some equipment listings are included, and an NMR section features spectra for deuterated NMR solvents. 44 pp. Aldrich **424**

Gene libraries. *ATCC/NIH Repository Catalogue of Human and Mouse DNA Probes and Libraries, 6th ed.* provides a directory for probes, cloned genes, genomic libraries, bacterial hosts, and the CEPH/ATCC chromosome 1 mapping kit. The catalog includes literature citations and general information on handling cultures. Expanded information is available through online access and PC diskettes. 136 pp. American Type Culture Collection **425**

Viscosity testing. Catalog offers viscometers, pressure reaction vessels, balances, furnaces, liquid dispensers, stirring motors, and tubing couplings for viscosity-specific research, quality control, and in-process applications. 20 pp. Thomas Scientific **426**

For more information, please circle the appropriate numbers on one of our Readers' Service Cards.

INDEX TO ADVERTISERS IN THIS ISSUE

CIRCLE INQUIRY NO.	ADVERTISERS	PAGE NO.
30	**EM Separations** Scientific Marketing Services, Inc.	IFC
45, 46	***Hewlett-Packard Company**	OBC
70	**Macherey-Nagel GmbH & Co., KG** MP Design Werbeagentur	54A
72	***Matheson Gas Products** Kenyon Hoag Associates	48A
85	***Perkin-Elmer Corporation** Keiler Advertising	56A
102	**TA Instruments, Inc.**. Kenyon Hoag Associates	50A
105	**Teledyne Hastings-Raydist** TRL Productions	58A
120	***Wyatt Technology Corporation**	47A

Directory section, see page 80A.
** See ad in ACS LabGuide.*

Advertising Management for the American Chemical Society Publications

CENTCOM, LTD.

President
James A. Byrne

Executive Vice President
Benjamin W. Jones

Joseph P. Stenza, *Production Director*

1599 Post Road East
P.O. Box 231
Westport, Connecticut 06881-0231
(Area Code 203) 256-8211
Fax No. 203-256-8175

DIRECTOR, ADVERTISING SALES, LABORATORY PRODUCTS
Bruce E. Poorman

ADVERTISING PRODUCTION MANAGER
Jane F. Gatenby

SALES REPRESENTATIVES

Philadelphia, PA. . . . Matthew J. McCloskey, CENTCOM, LTD. GSB Building, Suite 405, 1 Belmont Ave., Bala Cynwyd, PA. 19004. Telephone: 215-667-9666, FAX: 215-667-9353

New York/New Jersey . . . Dean A. Baldwin, John F. Raftery, CENTCOM, LTD., Schoolhouse Plaza, 720 King Georges Post Road, Fords, NJ 08863, Telephone: 908-738-8200, FAX: 908-738-6128

Westport, CT./Boston, MA. . . . Dean A. Baldwin, Michael J. Pak, CENTCOM, LTD., 1599 Post Road East, P.O. Box 231, Westport, CT 06881-0231. Telephone: 203-256-8211, FAX: 203-256-8175

Cleveland, OH. . . . Bruce E. Poorman, Dean A. Baldwin, CENTCOM, LTD., 325 Front St., Suite 2, Berea, OH 44017. Telephone: 216-234-1333, FAX: 216-234-3425

Chicago, IL. . . . Michael J. Pak, CENTCOM, LTD., 540 Frontage Rd., Northfield, IL. 60093. Telephone: 708-441-6383, FAX: 708-441-6382

Houston, TX./Atlanta, GA. . . . Edward M. Black, CENTCOM, LTD., 1599 Post Road East, P.O. Box 231, Westport, CT 06881-0231. Telephone: 203-256-8211, FAX: 203-256-8175

San Francisco, CA. . . .Paul M. Butts, Jay S. Francis, CENTCOM, LTD., Suite 808, 2672 Bayshore Parkway, Mountain View, CA 94043. Telephone: 415-969-4604, FAX: 415-969-2104

United Kingdom, Scandinavia and Europe (Except: Germany, Switzerland, Austria) . . . Malcolm Thiele, Technomedia Ltd., Wood Cottage, Shurlock Row, Reading RG10 OQE, Berkshire, England. Telephone: 0734-343302, FAX: 0734-343848

Germany, Switzerland, Austria . . . InterMedia Partners, GmbH, Deutscher Ring 40, 5600 Wuppertall 11, Germany. Telephone: (0202) 711091, FAX: (0202) 712431

Tokyo, Japan . . . Sumio Oka, International Media Representatives Ltd., 1-11-5-502, Tamazutsumi, Setagaya-ku, Tokyo 158 Japan. Telephone: 502-0656, Telex #22633, FAX: 5706-7349

Asia (Except Japan) . . . Bruce E. Poorman, CENTCOM, LTD., 325 Front St., Suite 2, Berea, OH 44017. Telephone: 216-234-1333, FAX: 216-234-3425

South America . . .Bruce E. Poorman, CENTCOM, LTD., 325 Front St., Suite 2, Berea, OH 44017. Telephone: 216-234-1333, FAX: 216-234-3425

LABORATORY SERVICE CENTER

NMR ANALYSIS
Multinuclear Multifield
Liquid or Solid State
GLP Compliance
Spectral Data Services, Inc.
818 Pioneer, Champaign, IL 61820
(217) 352-7084 Fax (217) 352-9748

FREE DATA, FAST

To quickly amass data on all of the products you need, consult the Lab Data Service section on our *Analytical Chemistry* reader reply card insert.

LABORATORY SERVICE CENTER

(Equipment, Materials, Services, Instruments for Leasing), Maximum space — 4 inches per advertisement. Column width, 2-3/16″; two column width, 4-9/16″. Artwork accepted. No combination of directory rates with ROP advertising. Rates based on number of inches used within 12 months from first date of first insertion.

Per inch: **1″ — $185; 12″ — $180; 24″ — $175; 36″ — $170; 48″ — $165.**

CALL OR WRITE JANE GATENBY

ANALYTICAL CHEMISTRY
1599 Post Road East
P.O. Box 231
Westport, CT 06881
203-256-8211
FAX: 203-256-8175

HELP WANTED ADS

ROP display at ROP rates. Rate based on number of insertions within contract year. Cannot be combined for frequency.

Unit	1-TI	6-TI
1″ (25 mm)	$210	$190
	12-TI	24-TI
	$180	$170

CALL OR WRITE JANE GATENBY

ANALYTICAL CHEMISTRY
1599 Post Road East
P.O. Box 231
Westport, CT 06881
203-256-8211
FAX: 203-256-8175

INDUSTRIAL & ENGINEERING CHEMISTRY RESEARCH

Editor: Donald R. Paul
University of Texas, Austin
Published by the American Chemical Society

Quality information that gives you the leading edge

Covering the broad, interdisciplinary field of chemical engineering and industrial chemistry, *Industrial & Engineering Chemistry Research* delivers peer-reviewed, monthly reports with a focus on the fundamental and theoretical aspects of chemical engineering, process design and development, and product R&D.

A typical issue contains original studies in the areas of kinetics and catalysis, materials and interfaces, process engineering and design, separations, and other topics, with an emphasis on new areas of science and technology.

Don't miss a single issue, Subscribe Today!

Call Toll Free (U.S. only): 1-800-333-9511
Outside the U.S.: 614-447-3776
FAX: 614-447-3671

Or Write:
American Chemical Society
Member and Subscriber Services
P.O. Box 3337
Columbus, OH 43210

Volume 32 (1993) Printed	U.S.	Canada & Mexico	Europe*	All Other Countries*
ACS Members				
One Year	$ 64	$ 84	$108	$120
Two Years	$115	$155	$203	$227
Nonmembers	$567	$587	$611	$623

* Air Service Included.

Member subscription rates are for personal use only. Subscriptions are based on a calendar year. Foreign payment must be made in U.S. currency by international money order, UNESCO coupons, or U.S. bank draft, or order through your subscription agency. For nonmember rates in Japan, contact Maruzen Co., Ltd. This publication is available on microfilm, microfiche, and the full text is available online on STN International.

Anal. Chem. 1993, 65, 97–103

AC RESEARCH

Characterization of an Interface Allowing either Nebulization or Gas Chromatography as the Sample Introduction System in ICPMS

Gregory R. Peters and Diane Beauchemin*

Department of Chemistry, Queen's University, Kingston, Ontario, Canada K7L 3N6

An interface which allows the coupling of a gas chromatograph with an inductively coupled plasma (ICP) mass spectrometer as well as conventional solution analysis with a nebulizer/spray chamber system has been characterized. In the nebulization mode, parameters investigated include sensitivity, detection limits, and signal-to-background ratio for aqueous solutions containing Al, V, Cr, Mn, Co, Ni, Zn, Ga, As, Mo, Cd, Sb, La, and Pb. The application of heat to the interface between the spray chamber and plasma torch results in improved performance and detection limits which are lower than those with a conventional spray chamber/plasma torch configuration. The characteristics of this heated interface for the gas chromatographic determination of two chlorine-containing compounds (1,1,1-trichloroethane and trichloroethylene) have also been investigated, and elemental detection limits for these compounds were determined to be 10 and 15 ng of Cl, respectively. Gas chromatographic separation of tetramethyltin and tetraethyltin with ^{120}Sn-selective ICP mass spectrometric detection has been successfully performed with elemental detection limits of 4.5 and 12 pg of Sn, respectively. Isotopic ratios were also determined for ^{116}Sn, ^{117}Sn, ^{118}Sn, ^{119}Sn, and ^{120}Sn from the gas chromatographic peak heights. Values obtained for these ratios were within 0.3% and 5% of literature values.

Interest has grown in developing methods for measuring not only total elemental concentrations in samples but also for separating and determining the actual chemical forms of these elements. Tin compounds are a good example of this need for their use has become quite widespread and the toxicity of these compounds varies greatly from one species to another.[1] Organotin compounds have found use in applications as diverse as wood preservatives, antifouling agents (especially in the marine environment), fungicides, miticides as well as industrial applications such as polymer stabilizers and polymerization catalysts.[2,3] Volatile tetraalkyltin compounds have been identified as being one of the classes of organotin species which are of environmental concern and which require sensitive and species-specific methods for their determination.[1]

Inductively coupled plasma mass spectrometry (ICPMS), while still a relatively new technique, has already proven itself to be a sensitive method, with low detection limits, for multielement and isotopic analysis.[4] On its own, however, ICPMS does not provide any information as to the chemical species of the elements determined. Extending the capabilities of ICPMS to allow speciation studies would increase the applications for which this powerful detector may be used.

Various chromatographic methods have been interfaced with ICPMS to achieve this goal, including various liquid chromatography techniques[3,5–7] supercritical fluid chromatography (SFC),[8] and gas chromatography (GC).[9–11] The chromatographic technique chosen is often dictated by the nature of the analytes, and each method has its advantages and disadvantages. Many ionic compounds may be separated by liquid chromatography prior to introduction into the plasma. Liquid chromatography is relatively simple to interface with an existing nebulizer/spray chamber sample introduction system; however, organic solvents (commonly used in mobile phases for HPLC) tend to complicate ICPMS analysis. When interfaced with a traditional nebulizer/spray chamber system, the performance of ICPMS is degraded due to solvent loading in the plasma, soot deposition problems, as well as the formation of interfering polyatomic ions.[3] The problems of signal depression and soot deposition by an organic solvent in LC–ICPMS have been addressed by Shum and co-workers who utilized direct injection nebulization

---

(1) Chau, Y. K.; Wong, P. T. S.; Bengert, G. A. *Anal. Chem.* 1982, *54*, 246–49.

(2) Lakata, W. G.; Lankmayr, E. P.; Müller, K. *Fresenius' Z. Anal. Chem.* 1984, *319*, 563–68.

(3) Suyani, H.; Heitkemper, D.; Creed, J.; Caruso, J. *Appl. Spectrosc.* 1989, *43*, 962–67.

(4) Horlick, G. *Spectroscopy* 1992, *7*, 22–29.

(5) Jarvis, K. E.; Gray, A. L.; Houk, R. S. *Handbook of Inductively Coupled Plasma Mass Spectrometry*; Chapman and Hall: New York, 1992; Chapter 4, pp 112–119.

(6) McLaren, J. W.; Siu, K. W. M.; Lam, J. W.; Willie, S. N.; Maxwell, P. S.; Palepu, A.; Koether, M.; Berman, S. S. *Fresenius' Z. Anal. Chem.* 1990, 337, 721–28.

(7) Al-Rashdan, A.; Vela, N. P.; Caruso, J. A. *J. Anal. At. Spectrom.* 1992, *7*, 551–55.

(8) Shen, W.-L.; Vela, N. P.; Sheppard, B. S.; Caruso, J. A. *Anal. Chem.* 1991, *63*, 1491–96.

(9) Van Loon, J. C.; Alcock, L. R.; Pinchin, W. H.; French, J. B. *Spectrosc. Lett.* 1986, *19*, 1125–35.

(10) Chong, N. S.; Houk, R. S. *Appl. Spectrosc.* 1987, *41*, 66–74.

(11) Bi, C.; Evens, H.; Caruso, J. A. Presented at the 1992 Winter Conference on Plasma Spectrochemistry, San Diego, CA, January 6th–11th, 1992.

0003-2700/93/0365-0097$04.00/0

(DIN) with the effluent being sprayed directly into the plasma.[12] This also solves the sample transport limitations imposed by a spray chamber system. Micellar liquid chromatography has proven to be an alternative to organic solvent elution.[3] However, it is still limited by the sample loss in the spray chamber (typically only 2–5% of sample reaches the plasma), and solvent is still entering the plasma simultaneously with the analyte, which may induce spectroscopic and/or nonspectroscopic interferences. Supercritical fluid chromatography may reduce many of these problems[8] but is not yet as widespread as other chromatographic methods.

For many volatile compounds, gas chromatography is the most attractive separation technique, for the carrier may be argon, which does not add anything to the background signal from the plasma, and the solvent is physically separated from the analyte prior to entering the plasma. The GC effluent may also be fed directly into the plasma torch, resulting in 100% sample introduction. Furthermore, not only is the need for desolvation eliminated, but the analyte is already in the gaseous form, removing the need for volatilization in the plasma as well. It would be reasonable to assume that this approach could result in more complete ionization of the analyte (especially elements with high ionization energies) in the plasma, which would enhance ICPMS performance. In addition, the broadening of the sample stream usually seen with aerosols is much smaller when a gaseous sample is introduced in the plasma. The ions may thus be formed in a narrower spacial zone which would result in a more precisely defined region of optimal sampling by the mass spectrometer (i.e. a higher sampling efficiency and improved sensitivity).

Existing GC–ICPMS (and SFC–ICPMS) systems require the disconnection of the nebulizer/spray chamber system and the installation of a column or transfer line to the base of the plasma torch resulting in a GC–ICPMS instrument[9–11] (the same is true for SFC–ICPMS[8]). In contrast, the interface used in this study allows the selection of either gas chromatography or solution nebulization with only the turning of a valve. This interface is a modified version of a system described previously.[13] In this paper, the revised interface is characterized for ICPMS with conventional nebulization, as well as GC–ICPMS.

EXPERIMENTAL SECTION

Apparatus. The ICP mass spectrometer used was a Perkin-Elmer SCIEX ELAN 500 (Thornhill, Ontario, Canada) with some modifications. Mass flow controllers (MKS Instruments Inc., Andover, MA) were used to regulate the flow rates of argon in the nebulizer (Meinhard-C type) as well as in the sheathing device. The conventional torch was replaced with a low-flow PlasmaTherm model (SCP Science, Montréal, Québec, Canada) to conserve argon. The torch was aligned with the mass spectrometer sampler orifice using a homemade *X–Y–Z* translation stage (resolution = 0.001 in.) on which the torch box was mounted. The ICPMS operating conditions are summarized in Table I. The conventional nickel sampler was replaced with one machined, in house, out of brass (see Table I). The spray chamber assembly was moved and reinstalled approximately 10 cm further from the plasma torch to facilitate installation of the interface. A new hole was drilled in the plate of the torch box for the drain of the spray chamber, and the old hole was covered with a metal plate to minimize rf noise leakage from the torch box.

Table I. ICPMS Operating Conditions

plasma	
torch	low flow (short)
plasma gas	10 L/min
auxiliary gas	2.0 L/min
forward rf power	1.2 kW
reflected rf power	<5 W
mass spectrometer	
sampler orifice (brass)	1.14 mm
skimmer orifice (nickel)	0.89 mm
expansion region pressure	900 mtorr
analyzer region pressure	1.4×10^{-5} torr
ion lens settings	$B = 6.10$ V $E1 = -14.23$ V $P = -13.86$ V $S2 = -8.04$ V
measurement	
measuring mode	graphics
scanning mode	peak hop
sweeps/reading	1
resolution[a]	1.1 units
points/spectral peak	3 (nebulization) 1 (GC)
dwell time	100 ms

[a] Peak width at 10% peak height.

Gas Chromatography. The gas chromatograph used was an SRI 8610 GC (SRI Instruments, Torrance, CA) with a glass column (2-mm i.d. × 175 cm) packed with 6% OV-101 on Chromosorb W (AW-DCMS, 80/100 mesh) (Chromatographic Specialties, Brockville, Ontario, Canada). The GC oven was held at 70 °C for chlorinated compound determinations and ramped from 70 to 145 °C at 15 °C/min with an argon carrier gas maintained at a flow rate of 10 mL/min. A 45-cm length of $^1/_8$-in.-o.d., 0.75-mm-i.d., glass-lined stainless steel tubing (Mandel Scientific Co., Guelph, Ontario, Canada), which was heated and held at 140 °C (for chlorinated compounds) and at 220 °C (for organotin compounds) with heating tape (Fisher Scientific, Ottawa, Ontario, Canada) and a Variac controller (Staco Inc., Dayton, OH), served as a transfer line between the gas chromatograph and the ICPMS instrument. To provide the shortest possible path between the gas chromatograph and the plasma torch assembly, as well as leaving the front of the instrument available for service, the GC oven was located behind the ICP mass spectrometer. A 386SX personal computer (Altair, Kingston, Ontario, Canada) controlled the GC oven temperature using the PEAKSIMPLE II software (version 2.50) provided with the GC instrument.

Interface. The interface has been described elsewhere[13] and consists of a PTFE "zero dead volume" switching tee (Omnifit, New York, NY) which was used to select either aerosol or GC effluent as well as a glass sheathing device which was fabricated in house. The last 20 cm of the transfer line as well as the sheathing device, PTFE tee, and the exit port of the spray chamber were heated to approximately 120 °C with heating tape which was controlled with a Variac controller. Both the metal transfer line and the heating tape were grounded to the ICP mass spectrometer to prevent rf leakage from the torch box. No adverse effects on the plasma were observed with the heating tape operating inside the plasma torch box.

The inner diameter of the tee and central channel of the sheathing device used in the earlier version of the interface (approximately 1 mm)[13] constricted the aerosol flow from the spray chamber to the plasma torch and resulted in both reduced aerosol flow to the torch and condensation of the solution on the inner walls of the central channel of the sheathing device (as discussed in greater detail below). The reduced aerosol transport was believed to be the major cause of the significantly reduced sensitivity.[13] To minimize the constriction of aerosol flow, a new sheathing device (described below) was fabricated, and the inner diameter of the tee was enlarged such that a 2-mm-diameter path was available for aerosol transport through the entire length of the interface. This is smaller than the 5-mm channel which is typical of the direct spray chamber/plasma torch junction; however, the tee which was used could not be enlarged any further without destroying the switching mechanism. The 5-mm inner diameter of the entrance to the injector of the plasma torch also limited the degree to which the central channel (in particular, that of the sheathing device) could be enlarged.

---

(12) Shum, S. C. K.; Neddersen, R.; Houk, R. S. *Analyst* **1992**, *117*, 577–82.

(13) Peters, G. R.; Beauchemin, D. *J. Anal. At. Spectrom.* **1992**, *7*, 965–69.

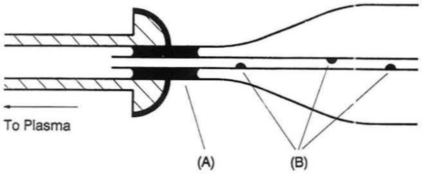

Figure 1. Diagram of the sheathing device/plasma torch junction showing major areas of water accumulation: (A) pooling in the outer channel of the sheathing device; (B) condensation of droplets in the inner (central) channel of the sheathing device.

Table II. Sensitivities[a] Observed for Solution Nebulization with and without the Interface Present, as Well as with Heating Applied to the Interface

	sensitivity ((counts/s)/(μg/L))		
isotope	interface absent (A)	interface present, no heating (B)	interface present, heated (C)
Al-27	1490	173	511
V-51	1980	245	814
Cr-52	1790	240	755
Mn-55	2260	351	1020
Co-59	1980	293	900
Ni-60	400	61.6	193
Zn-68	142	23.7	79.8
Ga-69	1140	208	568
As-75	114	13.1	46.8
Mo-98	482	92.1	289
Cd-114	254	56.5	180
Sb-121	267	56.0	180
La-139	1360	190	983
Pb-208	403	173	408

[a] Estimated from the averaged signals (with relative standard deviations of approximately 5%) of a 100 μg/L multielement standard solution.

The condensation in the previous sheathing device[13] caused larger drops of water to form (see region B of Figure 1) and then be swept into the plasma at irregular intervals, which resulted in increased plasma instability and signal noise. The inner diameter of the central channel of the device was therefore increased to 2 mm (instead of 1 mm) in an attempt to eliminate this problem. Water also tended to pool in the outer channel of the device due to surface tension effects as well as the slight turbulence created at the sheathing device/plasma torch joint (region A in Figure 1). With a sheathing gas present, a continuous sputtering of the solution was observed in this region which also increased the signal noise. To help overcome this pooling and sputtering, the central channel of the new sheathing device was extended to protrude past the ball joint region (approximately 9 mm into the injector tube of the torch).

Materials and Reagents. For nebulization studies, a solution containing 100 μg/L each of Al, V, Cr, Mn, Co, Ni, Zn, Ga, As, Mo, Cd, Sb, La, and Pb was prepared by diluting standard 1000 mg/L solutions of each element (SPEX Industries Inc., Edison, NJ) with 1% HNO_3 prepared with deionized distilled water (Milli-Q Plus, Millipore, Mississauga, Ontario, Canada) and high purity nitric acid (Seastar, Sidney, British Columbia, Canada). Reagent-grade 1,1,1-trichloroethane (BDH Inc., Toronto, Ontario, Canada), trichloroethylene (The McArthur Chemical Co. Ltd., Montréal, Québec, Canada), tetramethyltin (Me_4Sn, 99.5%, Alfa Products, Danvers, MA) and tetraethyltin (Et_4Sn, unknown purity, Johnson Matthey Catalog Company, Ward Hill, MA) were used without further purification. Standard solutions of these compounds were prepared in glass distilled *n*-pentane (BDH Inc., Toronto, Ontario, Canada), and the total volume injected was 0.1 μL for all samples.

Data Acquisition and Processing. The ICP mass spectrometer was controlled by and data were collected with upgraded Elan 5000 software. For nebulization studies, sensitivities were estimated using the signal from a 100 μg/L multielement solution as well as a 1% HNO_3 blank. Signal-to-background ratios (S/B) were determined for the 100 μg/L solution by dividing the blank-subtracted signal by the blank signal. For chromatographic studies, sensitivities were calculated from the slope of calibration curves. Data from all chromatographic analyses were saved in ASCII format and smoothed using a Fourier transform smoothing program (cutoff at 0.5 of maximum frequencies) with LabCalc software (Galactic Industries Corporation, Salem, NH) prior to processing with a spreadsheet. Peak heights and areas were calculated using the LabCalc software.

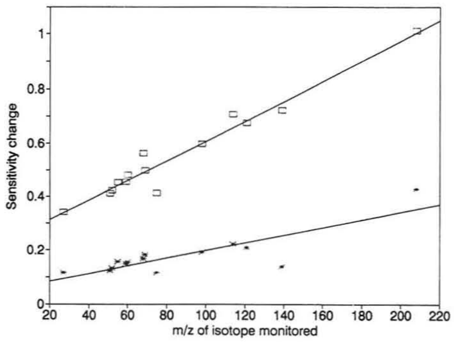

Figure 2. Plot of relative sensitivities vs *m/z* of isotope of metal ions monitored by ICPMS with the interface in the nebulization mode. "Sensitivity change" represents the ratio of sensitivities with the unheated interface (*) and heated interface (□) to sensitivity with no interface present (i.e. of Table II, column B/column A and column C/column A, respectively). The straight lines drawn through the points were determined by linear regression.

Table III. Detection Limits Obtained for Solution Nebulization with and without the Interface Present, as Well as with Heating Applied to the Interface[a]

	detection limits[b] (μg/L)			comparison of detection limits[c]	
isotope	interface absent (A)	interface present, no heating (B)	interface present, heated (C)	columns B/A	columns C/A
Al-27	0.3	1	0.2	5	0.6
V-51	0.03	0.2	0.02	6	0.5
Cr-52	0.1	0.4	0.04	4	0.3
Mn-55	0.08	0.3	0.02	3	0.2
Co-59	0.01	0.2	0.009	14	0.8
Ni-60	0.4	0.6	0.06	2	0.2
Zn-68	0.8	7	0.3	9	0.4
Ga-69	0.03	0.3	0.03	10	0.8
As-75	1	5	0.2	4	0.2
Mo-98	5	0.5	0.07	0.1	0.01
Cd-114	0.2	0.6	0.08	3	0.4
Sb-121	0.1	0.5	0.06	5	0.6
La-139	0.02	0.3	0.009	16	0.5
Pb-208	3	4	0.3	2	0.1

[a] Comparisons indicate the relative improvement/degradation of detection limits with the interface present (heated and unheated) relative to those with the interface absent. [b] Detection limit is based on three times the standard deviation of the blank signal. [c] Comparisons were calculated using two significant digits for the detection limits to avoid gross rounding errors.

RESULTS AND DISCUSSION

Solution Nebulization. A minimum argon flow of 15 mL/min through the sheathing device was maintained for the analyses carried out without heating. During the optimization process, the sensitivity was always highest with no sheathing gas flow (whether heat was applied or not); however, the presence of this sheathing gas was necessary to minimize

Table IV. Signal-to-Background[a] (S/B) Ratios for Solution Nebulization with and without the Interface Present, as Well as with Heating Applied to the Interface[b]

	signal-to-background ratio (for 100 μg/L solution)			comparison of ratios	
isotope	interface absent (A)	interface present, no heating (B)	interface present, heated (C)	columns B/A	columns C/A
Al-27	120	97.7	657	0.811	5.45
V-51	4440	1140	21100	0.256	4.74
Cr-52	403	390	5930	0.966	14.7
Mn-55	733	633	11500	0.864	15.7
Co-59	16800	1230	50000	0.0731	2.98
Ni-60	179	337	6570	1.89	36.8
Zn-68	94.3	27.3	757	0.289	8.03
Ga-69	5510	563	15200	0.102	2.76
As-75	61.6	60.4	1900	0.982	30.8
Mo-98	363	343	5130	0.947	14.2
Cd-114	544	384	4340	0.706	7.97
Sb-121	1750	404	4830	0.231	2.76
La-139	10200	876	54600	0.0862	5.38
Pb-208	15.6	23.3	364	1.49	23.3

[a] All S/B ratios are calculated from averaged signals with relative standard deviations of approximately 5%. [b] Comparisons indicate relative improvement/degradation of the signal-to-background ratios with the interface present (heated and unheated) relative to those with the interface absent. Operating conditions were optimized to maximize S/B ratios for each configuration.

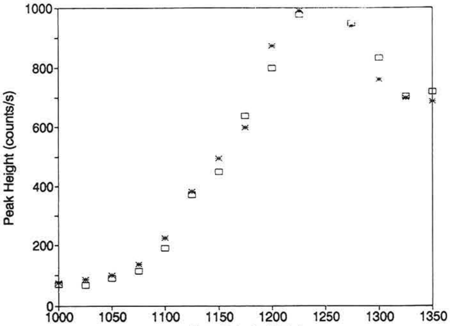

Figure 3. Plot of GC–ICPMS peak height ($^{35}Cl^+$ was monitored) for 1,1,1-trichloroethane (*) and trichloroethylene (□) versus sheathing gas flow rate, showing a maximum for both compounds at 1225 mL/min.

water accumulation which still occurred, to a lesser extent, at the exit of the sheathing device when no heat was applied. The location of this water accumulation is shown in region A of Figure 1. The sputtering caused by the flow of the sheathing gas in this region, as well as the irregular transport of large droplets, which had condensed on the inner walls of the central channel (Figure 1B), resulted in increased noise and occasional spikes in the analyte signal. Once heat was applied (approximately 120–130 °C) the aerosol no longer condensed on the walls and the pooling and sputtering was no longer observed. Because of this, the sheathing gas was eliminated when the system was heated to maximize sensitivity.

For each configuration, the argon flow rate through the central channel of the plasma was optimized by adjusting the nebulizer gas flow until maximum sensitivity was obtained. With the interface absent, a nebulizer flow rate of 825 mL/min was necessary for optimum sensitivity, whereas when the interface was installed and heated, the optimum flow rate was 925 mL/min. Because desolvation and evaporation were partially accomplished in the heated interface, the region of optimum ionization occurred axially lower in the plasma, and a higher flow rate was required to move this region further into the plasma toward the mass spectrometer sampler. Physically moving the plasma torch and sampler closer together would have probably also accomplished this; however, the torch and load coil were already as close to the mass spectrometer interface as this particular instrument would allow.

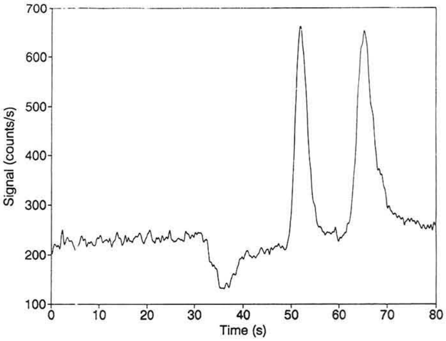

Figure 4. GC–ICPMS chromatogram with $^{35}Cl^+$-selective detection showing (in order of elution) 67 ng of 1,1,1-trichloroethane and 73 ng of trichloroethylene. The slight dip at 35 s is a background signal depression due to the solvent eluting from the column.

(a) Sensitivity. Table II shows the sensitivities for the 15 isotopes monitored with a conventional configuration of spray chamber and torch as well as with the interface present (i.e. with the sheathing device and tee in place). With the interface, heating of a 13-cm region between the spray chamber and the plasma torch was possible, which induced some vaporization of the aerosol and a corresponding decrease in the size of the remaining aerosol droplets. The application of heat to this transfer region resulted in a significant improvement in sensitivity over that for the same configuration without heating (the average ratio of column C over column B is 3.23). With more of the solvent in the vapor form when it enters the plasma, more energy from the plasma is available for the atomization and ionization of the analyte which probably results in enhanced ionization and, hence, greater sensitivity. Furthermore, smaller droplets may also cause the zone where ions are produced to be narrower, therefore improving the sampling efficiency at the mass spectrometer interface and leading to higher sensitivity.

Even with the increased sensitivity obtained by heating the interface, when the sensitivities of each element obtained with the heated interface are compared with those obtained with no interface present, a significant drop is observed (the average ratio of column C over column A is 0.55). In order to determine if this drop arose from the smaller exit hole of the spray chamber when the interface was in place, the transport of a spray chamber with a 2-mm-i.d. exit hole as well as that for a conventional spray chamber with a 5-mm exit hold were tested by the following method. A tube with dried preweighed silica gel was connected to the exit hole, and water was nebulized at 1 L/min argon flow for 2 min. The percentage of water which exited the chamber through the hole was determined by comparing the increase in mass of the silica gel relative to the mass of water which entered the spray chamber. With a 5-mm exit hole, 3.7% of the aerosol was transported to the plasma while with the 2-mm exit hole, the sample transport was only 2.1% of the generated aerosol. This represents a 43% decrease in solution exiting the spray chamber to the plasma, which corresponds fairly well with

Table V. Figures of Merit for GC–ICPMS with the Heated Interface

	H_3CCCl_3[a]	$HClC{=}CCl_2$[a]	Me_4Sn[b]	Et_4Sn[b]
retention time[c] (s)	53.7 ± 0.3%[d]	67.8 ± 0.5%[e]	49.8 ± 4.1%[f]	206 ± 3.2%[g]
peak height[c] (counts/s)	898 ± 5.3%[d]	859 ± 9.6%[e]	20021 ± 5.3%[f]	5802 ± 14%[g]
peak width[c,h] (s)	2.73 ± 3.1%[d]	3.47 ± 7.0%[e]	2.7 ± 6.6%[f]	5.2 ± 6.8%[g]
sensitivity[i] (counts/s/ng)	3.70 ± 0.09	2.72 ± 0.07	597 ± 39	214 ± 25
detection limit[j]	13 ng	18 ng	7.4 pg	21 pg
elemental det lim[j]	10 ng of Cl	15 ng of Cl	4.5 pg of Sn	12 pg of Sn

[a] ^{35}Cl detection. [b] ^{120}Sn detection. [c] Averaged from four replicate injections of each; the error is expressed as the relative standard deviation. [d] Determined from injections of 133 ng of H_3CCCl_3. [e] Determined from injections of 146 ng of $HClC{=}CCl_2$. [f] Determined from injections of 32.8 ng of Me_4Sn. [g] Determined from injections of 30.2 ng of Et_4Sn. [h] Measured at half of the peak height. [i] Defined as the slope of the calibration curve; the error expressed as the standard deviation of the slope as determined by linear regression. [j] Defined as the mass of the element necessary to yield a net signal equivalent to three times the standard deviation of the background noise.

the average drop in sensitivity.

A plot of the relative sensitivities with the heated and unheated interface (normalized to those with no interface) as a function of the m/z of the isotope determined (Figure 2) shows a clear trend in both cases. While the correlation coefficient for the unheated interface (0.71) indicates that this trend is not well defined and the slope is small (0.014 $unit^{-1}$), both the linearity and slope increased (correlation coefficient = 0.95, slope = 0.037 $unit^{-1}$) when heat was applied, suggesting that heating enhances a certain mass discrimination effect associated with this interface.

(b) Detection Limits. The detection limits obtained with a normal configuration as well those obtained with the interface installed (both heated and unheated) are given in Table III. As was previously observed, the decrease in sensitivity coupled with the noise generated by the sputtering at the exit of the sheathing device caused a degradation in detection limits for almost all elements when the interface was installed (the average ratio of column B to column A is 6). The application of heat to the transfer region reduced both of these problems and actually resulted in detection limits which are superior to those obtained without the interface in place (the average ratio of column C to column A is 0.4). A significant decrease in size (and even elimination) of the water droplets should have a beneficial effect on the signal noise. Because an aerosol is highly nonhomogeneous, droplets of different sizes will undergo desolvation, vaporization, atomization, and ionization at different positions in the plasma. For instance, Olesik and Fister[14] showed that the vaporization of a droplet in a plasma induced signal fluctuations; smaller droplets of more uniform size would therefore result in a more stable plasma as well as in a decrease of signal noise. The logical extreme of this is to eliminate the droplets completely, resulting in a mixture containing gas, water vapor, and dried solid particles of the analyte entering the plasma. The heating of the transfer region results in an analyte stream which is much closer to this, as demonstrated by the observed improvement in detection limits despite a concurrent decrease in sensitivities. With the heated interface, the standard deviation of the signal level for a blank solution of 1% HNO_3 ranged from 1% to 40% (with an average of only 21%) of that obtained with the interface absent, depending on the element.

(c) Signal-to-Background (S/B) Ratio. The S/B's obtained with a 100 μg/L solution of each element are presented in Table IV for configurations with the interface absent as well as installed (both heated and unheated). For each configuration, the operating conditions were adjusted to optimize signal intensity. The presence of the interface resulted in a drop in S/B (the average ratio of column B to column A is 0.69). However, heating the system resulted in a significant increase in S/B for the interface (the average ratio of column C to column B is 23.0). Overall, the heated interface resulted in an average improvement in S/B of more than 1 order of magnitude over a traditional system without interface (the average ratio of column C to column A is 12.5). In the light of the decrease in sensitivity, the primary cause for the increase in S/B is therefore a suppression of the background level when heat is applied. This would also be the main reason for the improved detection limits, since a lower noise is usually associated with a lower background level.

Although this interface only evaporates the solvent from the analyte (i.e. the solvent still enters the plasma along with the analyte), a comparison of the sensitivity changes obtained with it to those observed with systems where the solvent is physically removed from the analyte stream before it enters the plasma may be useful. As was mentioned earlier, the loss in sensitivity observed when the interace was installed is probably due to the decreased sample transport from the spray chamber. Alves and co-workers,[15] however, reported that cryogenic desolvation based on repeated heating and cooling of the analyte stream resulted in a decrease in sensitivity by a factor of approximately 2, even though ultrasonic nebulization was used and the output from the desolvation system was fed directly to the torch. This decrease in sensitivity was tentatively attributed to either analyte loss in the cryogenic desolvation process or a lower yield of analyte ions in the plasma caused by the complete removal of water or molecular gas from the analyte stream. Jakubowski et al.,[16] on the other hand, reported that desolvation (noncryogenic) with a single heating/cooling cycle actually resulted in an increase in analyte signal by a factor of 2-5.

Gas Chromatography. In order to compare this new interface to the previous one,[13] its performance was first investigated with two chlorinated test compounds: 1,1,1-trichloroethane (H_3CCCl_3) and trichloroethylene ($HClC{=}CCl_2$). Figure 3 shows a plot of peak height versus sheathing gas flow rate for these two compounds. The optimum flow rate of 1225 mL/min, when added to the 18 mL/min GC carrier flow rate, results in a total flow of 1243 mL/min through the injector channel of the plasma torch which is significantly higher than the flow rate of 1025 mL/min which was the optimum for aerosol introduction. As discussed previously,[13] this higher optimum flow rate through the injector is probably due to the fact that the analyte is not only physically separated from the solvent, but is already in vapor form so the energy from the plasma need only atomize and ionize it. As the desolvation and evaporation steps are eliminated, the ionization occurs axially lower in the plasma and, as was mentioned in the solution nebulization section with the heated interface, a higher flow rate is required to move the region

---

(14) Olesik, J. W.; Fister, J. C. III, *Spectrochim. Acta* **1991**, *46B*, 851–68.

(15) Alves, L. C.; Wiederin, D. R.; Houk, R. S. *Anal. Chem.* **1992**, *64*, 1164–69.

(16) Jakubowski, N.; Feldmann, I.; Stuewer, D. *Spectrochim. Acta* **1992**, *47B*, 107–18.

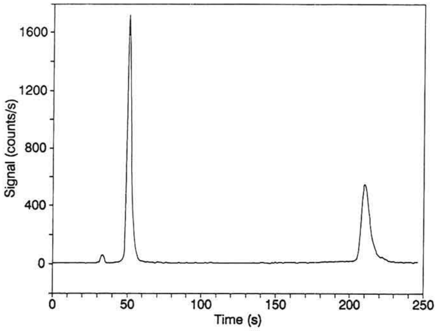

Figure 5. GC–ICPMS chromatogram with $^{120}Sn^+$-selective detection showing (in order of elution) 3.3 ng of tetramethyltin and 3.0 ng of tetraethyltin. The average count rate for the background signal (between the two peaks) is approximately 7 counts/s. The small peak at 35 s is a trace of an unidentified tin-containing impurity which is coeluting with the solvent.

of optimum ionization toward the sampler. An increased flow rate through the central channel of the plasma will also decrease the lateral diffusion, resulting in a radially smaller region of ionized analyte, which will increase the efficiency of sampling by the mass spectrometer interface.

A $^{35}Cl^+$-selective chromatogram of 67 ng of 1,1,1-trichloroethane and 73 ng of trichloroethylene is displayed in Figure 4. The chromatographic characteristics for these compounds, including reproducibilities, are given in Table V. Mixtures of both compounds (containing respectively 66.5, 133, 665, and 6650 ng of 1,1,1-trichloroethane, as well as respectively 73, 146, 730, and 7300 ng of trichloroethylene) were injected to establish a calibration. A straight line was obtained using peak heights for both compounds over 2 orders of magnitude (with a correlation coefficient of 0.998 for both compounds). Peak heights were used for calculations as the calibration curves proved to be more linear than those obtained with peak areas (the average of the correlation coefficients was then 0.860). The detection limits for these compounds are slightly degraded from those reported previously[13] with a smaller inner diameter tee and sheathing device (2.2 ng for 1,1,1-trichloroethane and 2.6 ng for trichloroethylene). This is probably due to the larger bore of the tee and central channel of the sheathing device used in this work, which results in decreased transport velocity toward the torch of the GC effluent and a larger dead volume. Nonetheless, these detection limits are still superior to that obtained (40 ng Cl) with a transfer line inserted directly into the central channel of the plasma torch[10] although the ICPMS instrument used for that study was significantly different and had a much higher background count rate (up to 1000 counts/s), rendering direct comparison of these results difficult.

The peak widths obtained with this modified configuration were only slightly less than those reported previously[13] even though the length of the transfer line, as well as its inner diameter, were decreased by 50% for this study. This implies that the decrease in peak widths expected with this smaller transfer line was almost completely offset by broadening due to the increased inner diameter of the region between the tee and the plasma torch. (The inner diameter of this region was doubled relative to that previously used to improve nebulization performance). As a result, a further increase in the inner diameter of this region to recover lost nebulization sensitivity would seriously degrade the chromatograpic separation obtainable with this system. The inner diameter of the tee and sheathing device used in this interface was considered to be the best compromise for these two sample introduction methods.

Organotin Speciation. The interface was successfully used for the gas chromatographic separation of tetramethyltin (TeMT) and tetraethyltin (TeET) with detection by ICPMS. Figure 5 shows a $^{120}Sn^+$-selective chromatogram of 3.3 ng of TeMT and 3.0 ng of TeET. The chromatographic characteristics of this system for these species are summarized in Table V. Calibrations were established by injecting mixtures of the two compounds (consisting of respectively 1.64, 3.28, 16.4, and 32.8 ng of TeMT, as well as respectively 1.51, 3.02, 15.1, and 30.2 ng of TeET). The plots obtained using peak heights again proved to be more linear (with an average correlation coefficient of 0.983) than those obtained using peak areas (with an average correlation coefficient of 0.933), and were therefore used to calculate sensitivities and detection limits. The latter are compared, in Table VI, to the detection limits obtained with other gas chromatographic techniques used to detect tetraalkytin species. While there are other specialized detection methods which offer still lower detection limits, isotope selective detection of these organotin species by ICPMS with this interface provides detection limits which are superior to those obtained with most other reported techniques (see Table VI). Furthermore, the extremely low (approximately 7 counts/s) background count rate for ^{120}Sn in this configuration may be an advantage of GC–ICPMS over LC–ICPMS separation of tin-containing compounds where the background count rate is much higher.

Isotope Ratio Determination. Because ICPMS is an isotope-specific detector, isotope ratio calculations are possible for the species eluting from the gas chromatograph. Five of the major isotopes of tin (^{116}Sn, ^{117}Sn, ^{118}Sn, ^{119}Sn, and ^{120}Sn) were monitored for these two species, and their relative abundances were calculated based on peak heights. The ratios of signals for the four lighter isotopes relative to that for the ^{120}Sn isotope are reported in Table VII, as well as the expected values from the literature,[17] and show very good agreement. The precision of each determination was calculated as the absolute standard deviation of three replicate determinations and is reported as the (±) value following each ratio. This feature of ICPMS, combined with competitive detection limits, makes it unique for GC detection, compared to the other detectors listed in Table VI.

---

(17) Friedlander, G.; Kennedy, J. W.; Macias, E. S.; Miller, J. M. *Nuclear and Radiochemistry*, 3rd ed.; Wiley: New York, 1981; Appendix D.

(18) Hill, H. H., Jr.; Aue, W. A. *J. Chromatogr.* **1972**, *74*, 311–18.

(19) Burns, D. T.; Glockling, F.; Harriott, M. *Analyst* **1981**, *106*, 921–30.

(20) Windsor, D. L.; Denton, M. B. *J. Chromatogr. Sci.* **1979**, *17*, 492–96.

(21) Parris, G. E.; Blair, W. R.; Brinckman, F. E. *Anal. Chem.* **1977**, *49*, 378–86.

(22) Ombaba, J. M.; Barry, E. F. *J. Chromatogr.* **1992**, *598*, 97–103.

(23) Matthias, C. L.; Bellama, J. M.; Olson, G. J.; Brinckmann, F. E. *Environ. Sci. Technol.* **1986**, *20*, 609–15.

(24) Meinema, H. A.; Burger-Wiersma, T.; Versluis-de Haan, G.; Gevers, E. C. *Environ. Sci. Technol.* **1978**, *12*, 288–93.

(25) Maguire, R. J.; Huneault, H. *J. Chromatogr.* **1981**, *209*, 458–62.

(26) Estes, S. A.; Uden, P. C.; Barnes, R. M. *J. Chromatogr.* **1982**, *239*, 181–89.

(27) Estes, S. A.; Uden, P. C.; Barnes, R. M. *Anal. Chem.* **1981**, *53*, 1829–37.

(28) Hansen, D. R.; Gilfoil, T. J.; Hill, H. H., Jr. *Anal. Chem.* **1981**, *53*, 857–61.

(29) Aue, W. A.; Hill, H. H., Jr. *J. Chromatogr.* **1972**, *74*, 319–24.

(30) Müller, M. D. *Anal. Chem.* **1987**, *59*, 617–23.

(31) Hansen, D. R.; Lillie, C. H.; Hill, H. H., Jr. *J. Chromatogr. Sci.* **1985**, *23*, 208–13.

(32) Suyani, H.; Creed, J.; Caruso, J.; Satzger, R. D. *J. Anal. At. Spectrom.* **1989**, *4*, 777–82.

(33) Łobiński, R.; Dirkx, W. M. R.; Ceulemans, M.; Adams, F. C. *Anal. Chem.* **1992**, *64*, 159–65.

(34) Aue, W. A.; Flinn, C. G. *Anal. Chem.* **1980**, *52*, 1537–38.

Table VI. Comparison of Different Gas Chromatographic Detection Methods for the Determination of Tetraalkyltin Species

detection method[a]	compounds analyzed	detection limit (DL) (pg)	S/N ratio at DL	ref
FPD	Et_4Sn	5000	nm[b]	18
ICPMS[c]	$Me_nPe_{(4-n)}Sn$ (n = 1–3)	3000–6500[d]	3	9
AAS (quartz tube)	Me_4Sn, Et_4Sn	995, 1059[d]	3[e]	19
ICPAES	Me_4Sn	900	nm	20
AAS (graphite furnace)	Me_4Sn	796[d]	nm	21
HeACPAES[f]	Bu_4Sn	530	3	22
FPD	Bu_4Sn	420	3[e]	23
AAS (silica tube)	$Me_nBu_{(4-n)}Sn$ (n = 1–4)	150	3[e]	1
MS	$Me_nBu_{(4-n)}Sn$ (n = 1–3)	77–108[d]	nm	24
FPD	$Bu_nPe_{(4-n)}Sn$ (n = 0–3)	60–67[d]	nm	25
HeMIPAES[f]	Et_4Sn, Pr_4Sn	9.2	3[e]	26, 27
HAFID	Et_4Sn, Pr_4Sn, Bu_4Sn	9.0–24[d]	nm	28
FID (H_2 rich)	Et_4Sn	8.1[d]	nm	29
ICPMS[g]	Me_4Sn, Et_4Sn	4.5, 12	3	this work
FPD (H_2 rich)	$EtBu_3Sn$	1.7[d]	3[e]	30
FID[f] (quenching)	Et_4Sn	0.38[d]	3[e]	31
HeMIPMS[f]	Et_4Sn, Bu_4Sn, $(vinyl)_4Sn$	1.9, 0.9, 4.5	3	32
HeMIPMS[f] (Ta torch)	Et_4Sn, Bu_4Sn, $(vinyl)_4Sn$	0.12, 0.09, 0.35	3	32
HeAED	Bu_4Sn, Pr_4Sn	0.05	3	33
FPD[h]	Pr_4Sn	0.016[d]	nm	34

[a] FPD = flame photometric detection, AAS = atomic absorption spectrometry, AES = atomic emission spectrometry, ACP = alternating current plasma, MIP = microwave induced plasma, HAFID = hydrogen atmosphere flame ionization detection. AED = atomic emission detection (MIP). [b] nm = method of detection limit determination not mentioned. [c] GC transfer line inserted directly into the plasma torch. [d] Mass of compound adjusted to mass Sn. [e] Detection limits adjusted from S/N = 2 to S/N = 3 for comparison. [f] Fused silica column used for chromatography (all others used packed columns). [g] GC transfer line connected to plasma torch via switchable interface. [h] Detector modified by insertion of quartz wool.

Table VII. Isotopic Ratios (±RSD) Determined by GC–ICPMS for Major Isotopes of Sn in Me_4Sn and Et_4Sn

	measured ratio	accepted value[17]	deviation from true value (%)
	Me_4Sn		
$^{116}Sn/^{120}Sn$	0.431 ± 1.8%	0.4537	5
$^{117}Sn/^{120}Sn$	0.2369 ± 0.29%	0.2377	0.3
$^{118}Sn/^{120}Sn$	0.73 ± 2.9%	0.7500	2
$^{119}Sn/^{120}Sn$	0.260 ± 1.3%	0.2654	2
	Et_4Sn		
$^{116}Sn/^{120}Sn$	0.435 ± 1.5%	0.4537	4
$^{117}Sn/^{120}Sn$	0.225 ± 3.6%	0.2377	5
$^{118}Sn/^{120}Sn$	0.74 ± 3.3%	0.7500	1
$^{119}Sn/^{120}Sn$	0.264 ± 1.7%	0.2654	0.5

CONCLUSION

The interface described is effective for both solution nebulization as well as gas chromatographic analysis by ICPMS. The system may remain permanently on the ICP mass spectrometer since detection limits for the analysis of solutions are improved (compared to those obtained without the interface). Future work will investigate the addition of a molecular gas (e.g. nitrogen) to the GC effluent in an attempt to improve the energy transfer within the plasma and hopefully enhance the sensitivity of elements with a high ionization potential, such as chlorine.

ACKNOWLEDGMENT

The authors are grateful to the Natural Sciences and Engineering Research Council of Canada (Grant OCP0039487 to D.B.) for its financial assistance. The fabrication of the glass portions of the interface by R. Campbell and the machining of a sampler by F. Babcock are also greatly appreciated. Finally, the gift of packing material for the GC column from K. W. M. Siu of the National Research Council of Canada, and the donation of the ELAN 5000 software by Perkin-Elmer (Norwalk, CT) are gratefully acknowledged.

RECEIVED for review August 11, 1992. Accepted October 19, 1992.

Response Ratio Chromatograms from a Dual-Channel Detector[†]

Brian Millier, Xun-Yun Sun,[‡] and Walter A. Aue*

Department of Chemistry, Dalhousie University, Halifax, Nova Scotia B3H 4J3, Canada

A computer algorithm and various readout modes have been developed that allow the average slope ratios from a dual-channel flame photometric detector (FPD) to be calculated for peak sections in manual mode and for whole or split peaks in automatic modes. The latter are available in numeric and (chromato)graphic form on printer, screen, and recorder. Such response ratio chromatograms routinely add a chemical dimension to the physical dimensions of quantity and retention, as depicted by conventional chromatograms. In the case of the FPD, they indicate the presence and nature of FPD-active elements. Response ratios can also assess peak homogeneity, confirm peak identity, and facilitate "subtraction" and "element-specific" chromatographies. The use of automatically procured response ratios for these routines is demonstrated on computer-stored separations of compounds containing various transition and main-group elements.

INTRODUCTION

Concept and Prior Knowledge. Conventional chromatograms provide the analyst with two physical dimensions of the separated compounds: peak size and peak retention. We propose to add a third, chemical dimension. It will address peak identity and purity; it will also support derivative chromatograms of significantly higher selectivity. If the third dimension is to prove acceptable—i.e. if it is to be habitually incorporated into analytical methodology—it must be derivable in a simple manner and displayable in a chromatogram-like format. The signals required for a first demonstration of that concept can be conveniently obtained from a dual-channel sensor such as the flame photometric detector (FPD). Recently, we used the FPD to obtain background-corrected or element-specific chromatograms; now we shall use it again to provide the desired chemical dimension in the form of response ratio chromatograms (RRC's).

Dual-channel response ratios have been used before to improve selectivity in various analytical areas, of which the FPD represents just one.[1,2] Despite the fact that the FPD is a simple, low-resolution transducer and that its monitors (usually) broad molecular bands originating from chromatographic solutes in a hydrogen-rich flame[3] of low temperature, it can attain extremely high selectivity by computer-assisted manipulation of its signals from two optically disparate channels.[4,5] There are basically two types of derivative chromatograms that a computer can produce. The first, a "subtraction" or "differential" chromatogram[5] shows the response of all elements except one. The second, a "conditional access" (CONDAC) chromatogram,[4] records the response of one element and excludes all others. Both subtraction and CONDAC type chromatograms have been developed on the dual-channel FPD and, hence, deal with *elements*. However, we are not aware of any fundamental reason that would prevent these techniques from operating on all kinds of synchronous detector channels and monitoring all kinds of chemical properties.

Once the two-channel record of a separation is suitably stored in the computer, *several* chromatograms can be derived from it. CONDAC chromatograms from the FPD are each specific for a particular element, and a variety of organometallic analytes have been successfully processed in this manner.[4] More often than not, the spectral conditions for achieving apparent elemental specificity are easily satisfied by any of a wide variety of wavelength-selective devices. This means that the main effort of the analyst in obtaining CONDAC chromatograms is reduced to defining the necessary response ratio for each element. Similarly dependent on correct response ratios are subtraction chromatograms.[5] And, in survey-type chromatograms the analyst may have to determine the response ratios of hundreds of compounds in a single separation. But obtaining accurate response ratios is, at present, cumbersome and time consuming. Clearly, a better way needs to be found. If the habitual use of response ratios is to be incorporated into the analytical repertoire, they will need to be generated by a facile and preferably continuous process.

Information Content and Measurement of Response Ratios. Response ratios are qualitative indicators of the FPD-active element contained in each peak. Our choice of spectral FPD ratios as a convenient chemical dimension for "demonstration of concept" is based on the several practical purposes these ratios can serve: they allow the fast perusal of many types of samples; they aid in confirming peak identity; they provide numbers crucial for obtaining CONDAC or subtraction chromatograms; they signal changes in spectral output; they monitor peak purity; and, perhaps most importantly, they draw the attention of the analyst to those peaks in complex environmental or biological samples that contain heteroelements and are therefore of prima facie interest. Below, we shall briefly describe four methods for determining response ratios. These are based on the consideration of heights, shapes, areas, and slopes of chromatographic peaks.

1. Peak Heights. The simplest and crudest approach is to measure the ratio of peak heights in the two channels (i.e. on the two chromatograms). For automated (as opposed to manual) methodology this approach harbors problems—e.g. how to get around the relatively large uncertainty in a single data pair and how to define the baseline from which this data pair (the peak apex) is to be measured.

2. Peak Scaling. A far more accurate, and lengthy, approach is to use the CRT screen for amplitudinal scaling of one (or more) peaks from the second channel until their

---

[†] Presented at the 75th CIC Conference, Edmonton, Alberta, Canada, June 1992.

[‡] Part of doctoral thesis.

(1) Bowman, Malcolm C.; Beroza, Morton. *Anal. Chem.* 1968, *40*, 1448–1452.

(2) Joonson, V. A.; Loog, E. P. *J. Chromatogr.* 1976, *120*, 285–290.

(3) Dressler, Milan. *Selective Gas Chromatographic Detectors*; Journal of Chromatography Library; Elsevier: Amsterdam, 1986; Vol. 36.

(4) Aue, Walter A.; Millier, Brian; Sun, Xun-Yun. *Anal. Chem.* 1991, *63*, 2951–2955.

(5) Aue, Walter A.; Millier, Brian; Sun, Xun-Yun. *Can. J. Chem.* 1992, *70*, 1143–1155.

0003-2700/93/0365-0104$04.00/0

shapes match those of their counterparts in the first channel, i.e. until a subtraction chromatogram (the difference of the two signals) shows little or no evidence of their presence. The final scaling factor is then identical with the sought response ratio. In practice, the computer presents an iteratively scaled sequence of subtraction chromatograms to the operator for selection of "the best one".[5] This procedure can deal efficiently with a single or at most with a few peaks. (Its initial and still valid purpose was to provide subtraction chromatograms for their own sake, i.e. for canceling matrix components.) While it should be possible to obtain from the computer a, e.g., least-squares Gaussian fit for each peak pair, this scaling procedure could turn out unwieldy (and too slow for routine use) when a larger number of peaks need to be evaluated.

3. Peak Area Integration. A simpler approach is to use the digital outputs of two conventional peak integrator modules for continuous calculation of the peak area ratios. The most immediate problem here is the lack of correlation between the two sets of baseline definition and start/stop commands, particularly if the two chromatograms are noisy and differ strongly in their relative peak heights, susceptibilities to interference, and/or drifts in baseline.

4. Peak Slope Ratios. A further possibility is to use the ratios of peak *slopes*. The experimental slope ratio SR_{exp} of the slopes S_A and S_B in channels A and B

$$SR_{exp} = S_A/S_B \quad (1)$$

ties in particularly well with CONDAC chromatograms,[4] whose operational acceptance algorithm (in its latest version) is

$$(S_A - fS_A) < S_B SR_{theor} < (S_A + fS_A) \quad (2)$$

Here the operator-selected tolerance factor f defines the maximum fractional deviation of the experimental from the theoretical slope ratio. That this is so can be easily seen if the condition above is divided by S_B

$$SR_{exp}(1 - f) < SR_{theor} < SR_{exp}(1 + f) \quad (3)$$

Use of Slope Ratios. Beyond intrinsic compatibility with CONDAC-type algorithms, there are a number of further advantages to using *slope* ratios in an initial investigation. They have to do with the easier avoidance of baseline problems, with the lesser influence of noise on steeper slopes, and with the greater convenience of slopes for defining where peaks start, crest, and end.

A theoretical disadvantage may be that a slope, by virtue of being a first differential, is more strongly affected by noise than an integrated signal. However, since a new slope ratio is measured every $^1/_{10}$th of a second, *many* sequential slope ratios are averaged in determining the response ratio of a typical peak. Furthermore, most approaches that use integration have to rely anyway on *slope* measurements for defining where peaks start and end, thereby reintroducing the noise problem. It seems reasonable, then, to base the determination of response ratios right away on the slopes (rather than on the heights or areas) of dual-channel peaks.

To do this, a fast algorithm is needed that yields response ratios by averaging the individual slope ratios contained in relevant peak sections and does so according to parameters chosen by the analyst (or, as envisioned for routine situations, by the computer). Typical analytical needs suggest *three* distinct modes. We shall list these by their operational addresses: first the "manual" mode, in which the *analyst* slices a *single* peak into vertical (temporal) segments and lets the computer calculate the response ratios for each; then the two "continuous" modes, in which the *computer* identifies *all* peaks and uses them in either "whole" or "split" form for calculating the RR values.

1. Manual Mode. The manual mode calculates the response ratio of any single peak or peak segment as defined by vertical cursors on the screen. This allows the operator to focus on only the peak of an internal standard or to avoid overlapping and noisy peak fragments or to carry out a purity check of different parts of a peak. (Note: it is common practice in other techniques, e.g. in the spectrophotometry of HPLC solutes, to judge peak purity by how constant the ratio of signals from two wavelengths remains during elution.)

2. Continuous Whole-Peak Mode. Continuous modes automatically determine the slope ratios of *all* peaks and represent them in (chromato)graphic form on screen and recorder, as well as in digital form on printer. As the name indicates, this version calculates the (weighted) average of all 0.1-s slope ratios for the *whole* peak (see the later eq 4 for the weighting and averaging algorithm). The start and end of the peak are determined by the more stringent of two criteria that are entered via the keyboard and define the minimum absolute slope value and the minimum acceptable signal value. The minimum slope value is entered as a number (percent of full scale per minute of chromatographic time), while the minimum acceptable signal value is established for the two chromatograms on screen by two horizontal cursors.

In order to cover the *whole* peak in the weighted averaging of slope ratios, the start and end of the peak remain subject to the minimum-slope threshold, but the top of the peak (where the slope goes through zero) does not. Since this operation is carried out on *two* channels, the more stringent of the two cut-on/cutoff conditions is programmed to prevail. Algorithmically, that means that the slope ratio S_A/S_B is calculated only if *both* slope values, S_A and S_B, meet *all* threshold criteria. Additional conditions, which ensure that the algorithm is not fooled by noise or mistakes a spike for a peak, are discussed in the Experimental Section.

For setting the minimum acceptable signal value, the horizontal cursors are moved so as to cut off the (flat or corrected) baseline, whose slope values are close to zero and hence useless for calculation anyway. Minimum acceptable slope values, on the other hand, are set so as to accommodate different peak widths in different types of chromatography. It would, of course, be possible for the computer to assess the height, dispersion and asymmetry of each individual peak in a chromatogram, compare it to the prevailing noise level and baseline drift and, accordingly, assign cut-on/cut-off points for calculation. This has not proven necessary for the gradient separations of this study, but it may be required for isothermal or isocratic analyses (and/or for overworked or underqualified technicians).

3. Continuous Split-Peak Mode. This mode provides additional information on the purity of peaks and the validity of elemental assignments. Weighted averages of slope ratios are calculated for each substantial positive or negative slope segment. The start and end of each segment is determined by the minimum-slope threshold. The top of the peak is not algorithmically protected as in the whole-peak routine. Therefore, it is cut off (meaning its S_A and S_B values are removed from further computation) as the slope of the apex slowly goes through zero. Each peak is thus split in the middle, with slope ratio averages being calculated for each of its sides and with the split between the sides (e.g. the return of the recorder pen to the noncommittal zero line) marking the chromatographic "retention time". Consequently, each split peak is represented by *two* response ratios that, in the ideal case, are identical (and equal to the whole-peak value); *two* partially overlapping peaks are normally represented by *four* values, and so forth. If two overlapping peaks contain different emitters (elements), the first and the fourth value (i.e. the initial positive and the terminal negative slope ratio) will most closely approach the two "true" response ratios.

Splitting a peak in that manner introduces a simple and automatic "elemental confirmation" technique. Identical ratios from a peak's positive and negative slopes would suggest, while different ratios would question or deny, that the peak is homogenous.

Note: Overlapping peaks that are exactly coincidental in retention time or response ratio, or peaks that contain two or more heteroelements and/or generate two emitters by different-order rate laws, or peaks that give rise to spectrochemically interacting emitters are all able to foil this type of scrutiny. For instance, an overlap of sulfur and selenium—with linear SeS, quadratic S_2 and Se_2, and other luminescences coexisting—can lead to peculiar variations of response ratios. However, in all but the perfect coincidence case (which is very rare), one look at a split-peak RRC will usually be enough to alert the analyst to analytically problematic but compositionally interesting peaks. These can then be examined in much greater detail by the manual mode.

EXPERIMENTAL SECTION

The Shimadzu gas chromatograph with dual-channel flame photometric detector (GC-4BMPF) and the 12-mHz 80286-class computer with 1-Mbyte memory, 40-meg hard disk, 80287 math coprocessor, VGA display adapter and monitor, as well as some convenient interfaces,[5] were the same items as used before.[4]

Briefly, the column was a 100- × 0.30-cm borosilicate tube packed with 5% OV-101 on Chromosorb W, AW, 100–120 mesh, purged by a nitrogen flow of 20–22 mL/min. Optical filters were mostly of the three-cavity interference type (Ditric). Detector conditions were chosen to suit roughly the various elements contained in the test mixtures. Main-group elements (for all figures except Figure 4) were run with 200 mL/min of hydrogen and 45 mL/min of air, with the commercial quartz chimney in place and with Hamamatsu R-374 photomultiplier tubes (multialkali, 180–850 nm, 420-nm maximum). Transition elements (for Figure 4) were run with 300 mL/min of hydrogen, 60 mL/min of air, and 18 mL/min of (additional) nitrogen, with the quartz chimney removed, and with Hamamatsu R-268 photomultiplier tubes (bialkali, 300–650 nm, 420-nm maximum). Note: the use of different phototubes is of little consequence in this context; the use or nonuse of the quartz chimney, however, is significant. Transition elements respond stronger in the Shimadzu Model 4 FPD when the chimney is removed, while sulfur responds stronger when the chimney is in place. These effects can easily amount to 1 order of magnitude.

A computer program called "SR" was developed according to the guidelines discussed in the Introduction. It calculates slope ratio values for all or for a defined ("zoomed") range of peaks from a dual-channel chromatogram in manual, split-peak, and whole-peak modes and forwards the results to the screen, recorder, and printer (the manual mode activates the screen only). The whole SR program was incorporated into an existing, lab-developed, dual-channel program now called CHROM-8, which contains the necessary input/output functions; the helpful digital filtering, baseline correction, and zoom modes; and also some of the peak matching, subtraction, noise definition, and conditional peak acceptance (CONDAC) routines developed in the course of earlier investigations. Certain rarely invoked functions (such as "REVERSE", which makes the chromatogram run backwards) are stored outside the CHROM-8 program. (Researchers interested in this program for noncommercial purposes are invited to contact the first author.)

The SR program applies a simple weighting routine to the averaging of slope ratios. To make use of the fact that noise is the less apparent the steeper the slope, the averaging process is weighted in favor of *large* slope values (by using the slope itself as the weighting factor). Thus, if S_A and S_B are the slopes (absolute changes in signal per 0.1-s sampling time) in the two channels, the average slope ratio $\overline{SR}$ (synonymous with the response ratio RR) is calculated as

$$\overline{SR} = \sum |S_A{}^2/S_B| / \sum |S_A| \ (=RR) \qquad (4)$$

The numerical result of this calculation is displayed on the screen in the manual mode. In the continuous split-peak and whole-peak modes it is forwarded to a printer, while both the screen and recorder show in log scale the "response ratio chromatogram" (RRC). (Note: since the FPD-RRC is designed as a chromatographic representation, it also follows the same time scale as the conventional chromatogram.) On the screen this representation is superimposed on the two original chromatograms; on the recorder it is preceded by a staircase calibration with steps at log SR = 1.5, 1.0, 0.5, 0, −0.5, −1.0, and −1.5. When no peak is present (i.e. when S_A or S_B or both are essentially zero) or when no peak is recognized by the computer, the RRC retreats to a "no information" line that is arbitrarily drawn at log RR = 0, i.e. that coincides with RR = 1. (Note: a peak with a response ratio of precisely unity would consequently be invisible in the RRC; however, this should be an extremely rare and, in any case, easily recognized phenomenon.) The built-in calibration obviates the need for recorder adjustment, while the logarithmic amplitude allows a wide range of slope ratios—from above 30 to below $^1/_{30}$—to be presented with directly comparable error bands.

Note: RR values above 30 and below $^1/_{30}$ can be determined but would be of little analytical merit, since it is the less well responding of the two channels that essentially determines the noise level and hence the precision and application range of the RR values. For example, assuming equal, and normally distributed, noise in the two channels, a peak pair of, e.g., amplitudes 1 and 0.03 leads to a relative error in response ratio that is roughly 20 times worse than for a case in which both amplitudes are 1. A similar relationship prevails for the signal/noise ratio of, e.g., a subtraction chromatogram obtained from the two channels.

For the continuous modes, two further parameters need to be defined by the operator. While this large extent of operator control is preferable for a still developing system, analyst input may eventually be replaced by default values or, better, by values derived from on-line peak diagnostics. Here the two parameters are set manually in response to screen prompts and in accordance with peak width and baseline noise.

The first prompt requests a numerical value for "n", the number of 0.1-s intervals to be included in the slope calculation for each data point. The slope is calculated from time $(i - n/2)$ to time $(i + n/2)$; with i being the data point under consideration. (Note that, in this procedure, the time ranges for sequential slope calculations overlap, since data points are *also* established every 0.1 s. Reasonable values for n are thus small even integers. For instance, this study used most often $n = 2$ or 4. Broader peaks would typically demand larger values.)

The second prompt asks how many sequential slope ratio values have to be of the same sign (positive or negative) before the algorithm decides, retroactively, that the ascending or descending portions of a peak have begun or ended and that cut-on or cut-off commands are to be issued. (Typical values in our studies ranged from 1 to 4 depending on the noise level.)

The two prompts are meant to add reliability to peak definition; they help to distinguish a true peak from the mere puff of the flame. Answering them should be done with some caution and the particular type of chromatogram in mind. In this they are similar to parameters used in the (here also available) baseline correction or digital filtering routines: too little correction, filtering, or damping can render the subsequent calculation technically impossible; too much can render it analytically unreliable.

RESULTS AND DISCUSSION

The procedure for continuously obtaining response ratios (RR values) in both numerical and graphic form is difficult to describe, but its results are easy to display. Typically, a full screen (close to 0.5 h) of chromatographic separation requires less than 0.5 min of calculation time from user request to computer compliance. For convenient chromatographic and analytical evaluation, the CRT shows the plotted log RR values superimposed in different color on the signals (peaks) of the two channels. Accurate retention times can be requested for any cursor position. (In contrast to the *calculation*-determined speed with which RRC's appear on the screen, numerical data are typed at the *printer's* pace and graphic data are drawn by the recorder at the rate of the *chromatographic separation*.)

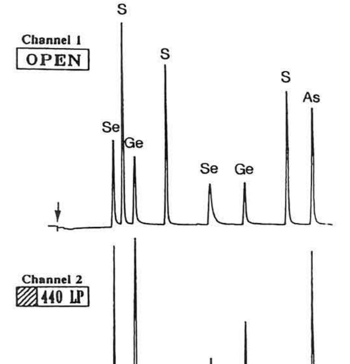

Figure 1. Individual channels and split-peak response ratio chromatogram of a mixture of main-group compounds. Channel 1: open (no filter); channel 2: 440-nm long-pass filter. Compounds in order of elution: 1 μL of acetone (solvent), 2.9 ng of dimethyl diselenide, 5.9 ng of diethyl disulfide, 50 ng of tetraethylgermane, 6.9 ng of bis(*tert*-butyl) disulfide, 80 ng of methylbenzoselenazole, 56 ng of tetra-*n*-butylgermane, 9.6 ng of thianthrene, and 480 ng of triphenylarsine. Note: the same time axis applies to all three chromatograms.

In other words, the analyst facing the screen is almost instantly served a response ratio chromatogram on top of two conventional chromatograms. Because this speed far exceeds that of a typical chromatographic separation, it should be fairly easy to include such data in (close to) real-time printer or plotter outputs.

The significance of continuous slope–ratio monitoring can perhaps be best appreciated by a reader who looks at dual-channel traditional chromatograms that are juxtaposed with the corresponding response ratio chromatogram and that are followed by those derivative chromatograms that the computer can obtain from the former with the help of the latter. For this exercise we shall make use of a couple of extremely simple separations of multielement mixtures. (A visual presentation, by its and our nature, is far more convincing than a verbal one!) In the following paragraphs, the first example uses main-group elements[6] of medium concentration, the second uses transition metals[4] of low concentration, and the third uses overlapping peaks. Different readouts and usages of response ratios will be chosen so that each mode is adequately represented.

The further inclusion of subtraction[5] and CONDAC[4] chromatograms—approaches that have been described before—is not done for their own sake. Rather, these have been produced by the computer relying on the automatically calculated whole-peak RRC: *it* provided the RR values so crucial to subtraction and CONDAC routines. Successful subtraction and CONDAC chromatograms therefore imply successful RRC's; and they demonstrate the ease, speed, and reliability with which this methodology operates.

Figures 1 through 3 are all based on the same, one-time separation of simple test compounds containing Se, S, Ge, and As. (Many more separations were done with these and compounds of other main-group elements such as Sn, B, and P; both under similar and under somewhat different optical conditions. The same kinds of pictures emerged and lead to similar conclusions; hence only this one separation will be accorded a full set of derivative chromatograms.)

Figure 1 displays the two original chromatograms as received from the two FPD channels and stored in the computer. All other chromatograms are to be derived from these two. The first channel is "open"; i.e. no interference filter is used and the spectral range is that of its R-374 photomultiplier. The second channel uses a 440-nm long-pass (cut-on) filter and the same type of photomultiplier. Thus the spectral discrimination is deliberately held to a minimum: on one hand to demonstrate the ease with which further data can be obtained from a very simple optical system, on the other to make use of the fact that broader spectral ranges can accommodate a wider selection of elements with greater sensitivity. The two chromatograms are shown, and will be used, "as received", i.e. untouched by digital filtering or baseline correction routines. To allow unfiltered operation, the compounds are used at medium (not low) concentration levels.

Below the two original signal traces in Figure 1 is displayed a split-peak response ratio chromatogram (RRC). The rectangles shown on the left define in symbolic form the optical configuration of the two channels. The circular inset depicts the RRC representation of a split peak in true shape, i.e. as it would appear on the screen (with expanded time axis). As drawn by a sluggish recorder, however, and as reduced by an electrostatic copier for this particular picture, the resolution appears much worse than that of the original. (For a clearer, recorder-drawn example of RRC split-peak shapes, see Figure 5.)

Since the range of response ratios (RR's) displayed here is much smaller than the 3 orders of magnitude the system routinely accepts, the staircase calibration is truncated to save display space. For reader's convenience, a "percent change" scale has been added (which is valid not just for germanium but, appropriately raised or lowered, for any element). It shows the expected result: response ratios are values that are characteristic of elements and constant within prevailing error bands. An exception is the first sulfur peak that, as the scale indicates, is almost 10% off.

The reason for this clear deviation has not been elucidated. Response ratios among peaks of the same element should vary only if the spectral distribution varies. The most likely explanation is therefore that the immediately preceding Se peak overlapped enough to inject a trace of Se_2 and form a significant amount of the interchalcogen emitter SeS.[7] Other scenarios, based on solvent effects and sulfur emitters with different kinetics,[8] also appear possible.

---

(6) Aue, Walter A.; Sun, Xun-Yun; Millier, Brian. *J. Chromatogr.* **1992**, *606*, 73–86.

(7) Aue, Walter A.; Flinn, Christopher, G. *J. Chromatogr.* **1978**, *158*, 161–170.

Table I. Printout of a Split-Peak Response Ratio Chromatogram[a]

retention time (slope start), min	retention time (slope end), min	ratio	slope	element
4:34.6	4:39.4	0.352	pos	Se
4:39.7	4:48.2	0.361	neg	Se
5:13.9	5:18.7	2.122	pos	S
5:18.9	5:28.8	2.073	neg	S
6:01.1	6:06.8	0.280	pos	Ge
6:07.7	6:16.1	0.279	neg	Ge
8:08.6	8:12.7	2.317	pos	S
8:12.9	8:21.5	2.290	neg	S
11:04.8	11:09.7	0.346	pos	Se
11:12.0	11:18.2	0.357	neg	Se
13:24.5	13:29.1	0.277	pos	Ge
13:30.3	13:37.0	0.276	neg	Ge
16:19.3	16:23.7	2.360	pos	S
16:24.0	16:33.9	2.329	neg	S
17:57.7	18:03.1	0.508	pos	As
18:03.4	18:13.2	0.513	neg	As

[a] Note: The separation is the same as shown in Figure 1. For easy comparison, the peak designations (the FPD-active elements) have been added; and a 1-s computer glitch, which occurred on the tail of the second selenium peak, has been removed.

The visual representation of the response ratio chromatogram uses the logarithmic format; however, simultaneous with its appearance on the screen (superimposed there on the two original chromatograms), the same information is sent in antilogarithmic format to the printer. These plain RR values are useful for feeding computer routines (see below), for keeping permanent records, for determining standard deviations, etc. The printout for split-peak RR's shown in Figure 1 is reproduced as an example in Table I. It lists the numerical values for the response ratios, records chromatographic time (start and end of the slope measurement), and indicates whether a particular slope is *pos*itive (up the peak) or *neg*ative (down the peak). (We have added the elemental designations for ease of comparison with Figure 1.) Obviously, the information could be combined with the initial chromatograms not just on the screen but on a more conventional record, e.g. one obtained from a plotter. The slight differences in response ratios between the leading and trailing slopes of each peak appear to be random experimental error. This is in accord with uncompromised peak integrity throughout the RRC.

The response ratios, thus determined, can be used to provide different types of "computer-manipulated" readouts from the two stored chromatograms. We illustrate this by showing, in this one case, all subtraction chromatograms[5] and conditional access chromatograms[4] that can be reasonably derived from the traces and response ratios of Figure 1. (Note: the main purpose here is not to display computer-manipulated chromatograms but to demonstrate that these can now be obtained by using the automatically produced RR values. Earlier subtraction chromatograms had to rely on complex and time-consuming methods for measuring the necessary RR values with sufficient accuracy.)

Briefly recalled, to obtain a subtraction (or differential) chromatogram,[5] the signal of channel 2 is first multiplied by the response ratio for the chosen element and then subtracted from the signal of channel 1. To obtain a CONDAC chromatogram,[4] the measured response ratio is used as the SR_{theor} value in the earlier given access algorithm (eq 2).

The subtraction thus suppresses peaks of the chosen element (i.e. peaks of a defined response ratio), while all (or most) of the other elements do show up. Contrariwise, in a conditional access (CONDAC) chromatogram the peaks of the chosen element are the only ones to appear, while those of all other elements are denied access.

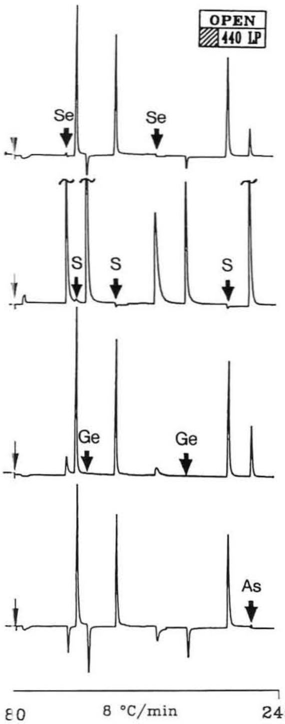

Figure 2. Four subtraction chromatograms. These are derived from the two channels shown in Figure 1.

The subtraction chromatograms of the mixture are shown in Figure 2 with elemental symbols and arrows pointing to the location of the suppressed peaks. Subtraction chromatograms can be used for suppressing analytes,[5] for suppressing matrix components,[9] or as demonstrated in a subsequent example, for restoring or resolving overlapping peaks (of two different elements). They can also provide a measure of *qualitative* characterization: for instance, the inverted peaks in the uppermost chromatogram of Figure 2 suggest the presence of germanium (in the sense that germanium is the only element in the mixture that, at the chosen settings, produces *inverted* peaks).

The CONDAC chromatograms of the mixture are shown in Figure 3, closely stacked above the same time axis and below a repeat of the open channel (for easier orientation). The first sulfur peak does show up, since the CONDAC tolerance factor (see equation 3) was set wide enough to grant it access. Below the CONDAC chromatograms is shown another response ratio chromatogram, but this time in whole-peak mode. As expected, its RR values are practically identical with those of the split-peak mode shown in Figure 1. (A case like this strongly suggests, though it does not perfectly prove, that the elemental identity of the peaks has not been compromised.)

Transferring the response ratio of the desired element to the CONDAC program occurs at present via the keyboard; however, a slight change in the program would allow the analyst to designate a peak on the screen (perhaps the peak of an internal standard or of an otherwise interesting or

---

(8) Aue, Walter A.; Millier, Brian; Sun, Xun-Yun. Response Ratios in Chromatography. 75th CIC Conference, Edmonton, Alberta, Canada, June 1992.

(9) Aue, Walter A.; Millier, Brian; Sun, Xun-Yun. *Anal. Chem.* **1990**, *62*, 2453–2457.

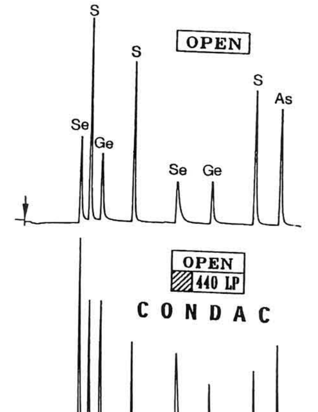

Figure 3. Four CONDAC chromatograms and a whole-peak response ratio chromatogram. These are derived from the two channels shown in Figure 1. The open channel is reproduced on top for ease of comparison.

unusual compound) and have the computer automatically display, by way of a CONDAC program, all peaks of the same response ratio (i.e. of the same FPD-active elemental composition). Normally, RR numbers are used unaltered, but on occasion a defensive minor adjustment will guard more effectively against violations of specificity by another element that just happens to claim—under the prevailing spectral conditions—an adjoining or even slightly overlapping RR range.

Which approach, i.e. the whole-peak or the split-peak mode, the analyst may want to select in a real-life situation depends, in our opinion, on the type and quality of the chromatogram and the purpose it is supposed to serve. *One* RR value per peak—in the whole-peak mode—provides the simplest and hence fastest scanned record. *Two* RR values per peak—in the split-peak mode—provide more detailed and hence slower evaluated information. Such information is very useful, however, for characterizing first-encounter chromatograms, confirming the identity of analytes, or providing records for quality-assurance inspectors. *Split*-peak RRC's can thus prove most valuable for samples where peak overlap is endemic and peak identity elusive. Note, however, that the use of RR values in assessing peak purity is limited to cases where peak overlap occurs with a compound of a *different* element (or, among hydrocarbons, with a compound of a different degree of unsaturation).

In contrast to the main-group elements used at medium concentrations in the first example, the second example uses (mainly) transition metals at *low* concentrations. Much is yet unknown about the behavior of transition metals in the FPD, but CONDAC[4] and subtraction[5] chromatograms have been run on such mixtures. Here we are simply using an old dual-channel chromatogram from our files to derive and display as examples the whole-peak and the split-peak response ratio chromatograms. A "reverse-mode" split-peak RRC is also included.

In reverse mode, the algorithm processes the temporally inverted chromatogram. Whether obtained by the algorithm operating forward or backward in time, the resulting RRC's should be identical when derived from ideal two-channel data. However, if the noise level is high, "spikes" are frequent, and the baseline is subject to drift, there may arise differences between the two. The processing algorithm—just as most chromatographic peaks—is not entirely symmetric with regard to time. Congruity of forward- and backward-run RRC's will thus provide (limited) reassurance of proper electronic function; incongruity will point to possible trouble spots. The latter will also support estimates of precision. A further example of the usefulness of time-reversed operation will be given later.

Figure 4 shows the open channel (only) on top of the three RRC's. Note that the original two signal trains (chromatograms) had been run before through digital filtering and baseline correction routines. While these routines ameliorate noise and drift, respectively, they also produce changes in slope and, consequently, introduce some variation of their own into the response ratio chromatograms. Obviously, the selection of processing parameters represents a compromise between the suppression of noise/drift and the preservation of true response ratios. However, we felt it necessary to include in this study a separation done at such low analyte concentrations that substantial electronic smoothing and straightening would have to be used, but that, nevertheless, some short-term and long-term fluctuations would continue to persist in the chromatograms. Only this type of challenge can test the robustness and intrinsic suitability of RRC's for trace analysis.

Not surprisingly, then, the variation of response ratios is much more pronounced for the (originally) noise-encrusted peaks of Figure 4 than it was for the much cleaner peaks of Figure 1. A careful scrutiny of the RRC's suggests that much if not all of this variation is random noise. For this scrutiny, split-peak RRC's processed both forward and backward in chromatographic time prove decidely helpful. As a general experience, the response ratios remain constant as the analyte concentration is lowered. (Sulfur, due to the quadratic nature of its response, can prove an exception.) This means that the method is about as robust as can be hoped for. However, a truly *comprehensive* examination of the constancy of RR values (e.g. under extreme conditions of quenching, or beyond the linear range of the calibration curves, etc.) falls outside the scope of this manuscript.

The RRC's also show that some response ratios for different elements happen to lie very close to each other. (The mixture contains only one example of two peaks containing the *same* transition metal, i.e. manganese). Wider and overlapping RR error bands are responsible for the fact that the CONDAC chromatograms of this particular separation—which are not shown here—turned out successful (meaning element-specific) for only six out of nine FPD-active elements. Still, that is

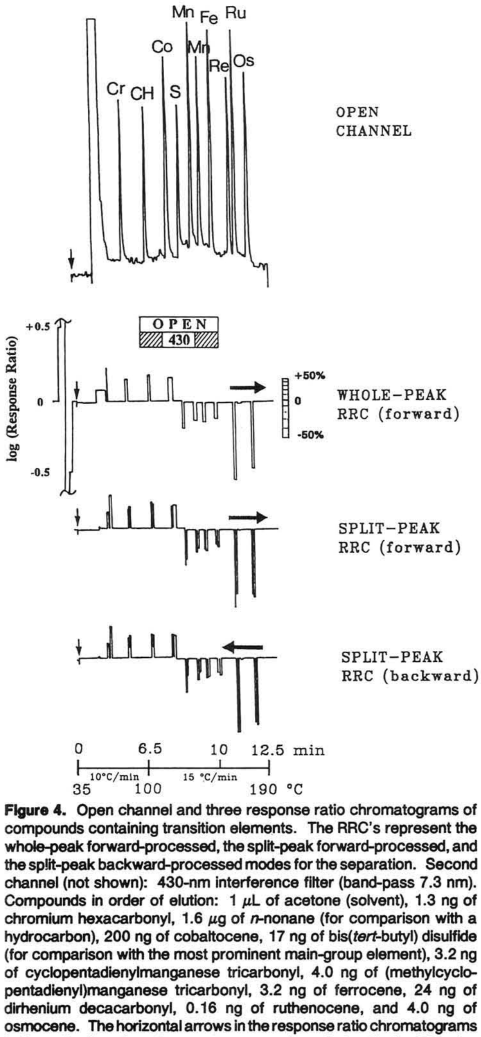

Figure 4. Open channel and three response ratio chromatograms of compounds containing transition elements. The RRC's represent the whole-peak forward-processed, the split-peak forward-processed, and the split-peak backward-processed modes for the separation. Second channel (not shown): 430-nm interference filter (band-pass 7.3 nm). Compounds in order of elution: 1 μL of acetone (solvent), 1.3 ng of chromium hexacarbonyl, 1.6 μg of *n*-nonane (for comparison with a hydrocarbon), 200 ng of cobaltocene, 17 ng of bis(*tert*-butyl) disulfide (for comparison with the most prominent main-group element), 3.2 ng of cyclopentadienylmanganese tricarbonyl, 4.0 ng of (methylcyclopentadienyl)manganese tricarbonyl, 3.2 ng of ferrocene, 24 ng of dirhenium decacarbonyl, 0.16 ng of ruthenocene, and 4.0 ng of osmocene. The horizontal arrows in the response ratio chromatograms indicate the direction of computer processing. Note: the log RR value for Ru is close to zero and barely shows up in reproduction.

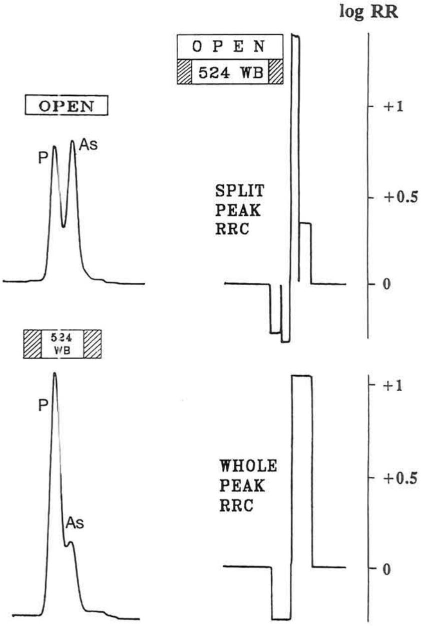

Figure 5. Individual channels, with split-peak and whole-peak response ratio chromatograms of overlapping peaks. Compounds in order of elution: triphenylphosphine and triphenylarsine. First channel: open; second channel: 524-nm wide-band filter (40-nm band-pass).

quite good for a single separation carried out at the trace level. But, could we have done better?

The optical filter for the second channel had been selected rather haphazardly from a larger number of possible wavelength ranges; a more careful spectral choice, and some trial and error, may indeed have done better. However, while the determination of the best wavelength combination to achieve CONDAC specificity for *each one* of the nine elements may be an interesting (if somewhat contrived) spectroscopic problem, our primary interest here was to demonstrate how readily the continuous determination of response ratios can be achieved even from a chromatogram of poor quality. Still, this demonstration chromatogram, though noisy, had one definite advantage over many real-life chromatograms: all of its peaks were cleanly separated from one another.

In real-life chromatography—particularly of heteroorganic or organometallic trace analytes contained in the complex matrices of environmental or physiological origin—even the best column will fail to bring about complete separation. (Note that all chromatographies of this study were deliberately carried out at *low* resolution, i.e. on just a 1-m packed column.) Hence peak interference must be reckoned with and, as the simplest possible demonstration of how response ratios are determined and how subtraction and CONDAC chromatograms based on automatically determined RR values succeed or fail under these circumstances, we shall examine a two-peak overlap.

Figure 5 shows on the left the two initial channels of a separation of triphenylphosphine and triphenylarsine. Note that the separation is (deliberately) very poor. Split-peak and whole-peak response ratio chromatograms appear on the right. The former strongly indicates the need for further scrutiny.

A manual examination of response ratios from successive slices of the bimodal concentration profile shows the RR values first remaining relatively constant (and agreeing with the authentic value for phosphorus), then turning unjustifiedly high, and then again becoming relatively constant (and agreeing with the authentic value for arsenic). The continuous split-peak RRC reflects these changes, although in much coarser fashion. The outer (first and last) RR values are characteristic of phosphorus and arsenic, respectively; the two inner (middle) values are not.

In particular, one very large RR value seems to jut out of nowhere. It is not due to a third species, however. Rather, it arises from the fact that the position on the time axis of the lowest point in the valley between the two peaks is different in the two channels. Slope ratios in the time interval between the two minima are therefore computed from slopes of a different sign. Right at one nadir, the slope ratio is zero; at the other, infinity. This and the about even mixture of elements present in this most intense region of overlap render the inner RR values useless as chemical indicators. The outer

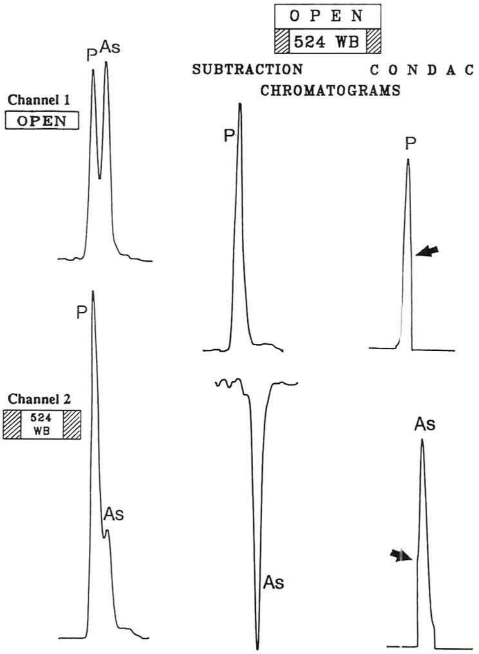

Figure 6. Subtraction and CONDAC chromatograms of overlapping peaks. The individual channels (the same as in Figure 5) are repeated on the left for easier orientation.

RR values, however, still can play that role. The whole-peak RR values, which combine the inner and outer RR values, are obviously spurious. Indeed, they could prove downright misleading if consulted in isolation. It is, of course, the very situation of overlapping, interfering, anomalous, and/or otherwise interesting peaks for whose benefit the manual and the split-peak modes have been developed in the first place.

What can be done with the two (outer) response ratios from the split-peak mode? What do subtraction and CONDAC chromatograms look like under these circumstances? Figure 6 repeats the initial single channels for easier orientation and then records the results of the two dual-channel manipulation techniques.

The subtraction chromatograms restore (deconvolute) the two peaks that constitute the original doublets. The arsenic peak is shown inverted here, simply because that is how it appears on screen and recorder. It could, of course, be returned to its familiar upright form by using a multiplication factor of −1 on the computer or by flicking a switch on the recorder. The peaks are vertically attenuated but otherwise of the same shape as those of singly injected, pure compounds. They are therefore perfectly suited to height or area quantitation—provided they are compared to peaks of a suitable internal standard or assessed against an appropriate external standard measured in the same subtraction mode.

No like area-based quantitation is possible for the CONDAC peaks. These peaks are not fully restored but are merely parts of peaks imported from (in this case) the first channel. The signals break off (i.e. return to the noncommittal zero line) when the experimental response ratio strays too far from the theoretical one. In this manner CONDAC peaks with large missing sections simply alert the analyst to the occurrence of peak overlap. In Figure 6, the exact location of the two break-off points is marked by arrows for easy orientation.

Beyond the basic SR tolerance band as defined earlier (eq 3), there are several further conditions involved in CONDAC chromatograms.[4] For instance, the start of a peak is given greater weight for peak definition than the end (a not unreasonable approach for chromatographies with many tailing peaks). A certain number of slope segments have to register positive in immediate succession before the algorithm (retroactively) declares the start of a peak. The lack of symmetry implicit in that treatment can be rectified by storing the original signals in both forward and reverse chromatographic time and then obtaining CONDAC chromatograms for each. The reverse mode, although redundant for "clean" chromatograms, is often helpful as a backup or confirmation or averaging technique for doubtful ones. The algorithm experienced some difficulties in declaring the start of the arsenic peak in the forward mode. Channel 2 in Figure 6 shows why: the positive slope segment on which the algorithm was supposed to base its assessment is short and ill suited to the task. In the reverse mode, however, two substantial positive slope segments are offered and the CONDAC algorithm easily succeeds. (Note: time-reversed processing can entail changes in RR or CONDAC chromatograms, but it does not affect subtraction chromatograms.)

CONCLUSIONS

Figures 5 and 6 have been discussed at considerable length, in part to demonstrate how RR's can (or cannot) improve a poor chromatographic separation and in part to show, on a visual basis, how the RR-based algorithm reacts to such a situation. However, dealing with "difficult" separations is not the main purpose of this study. The far more important aspect of response ratio, subtraction, and conditional access chromatograms is that they directly convey qualitative chemical information. It is well-known, of course, that dual-channel and multichannel detectors can offer chemical in addition to physical information. However, such information, while immanent, is hidden in the traditional chromatographic representation. It has therefore been the objective of this study to demonstrate that the multichannel detectors can offer information that is not only complementary in information content but also concordant in format and convenient in application.

It was reasonable and expedient for this study to choose the FPD as a tool for demonstration of concept. However, other detectors or detector modes could benefit from the developed approaches as well. All that is demanded of two or more detector channels is that they portray the passing peak (concentration profile) in a synchronous, linear, and chemically differentiating fashion. The chemical information need not be optical in form and elemental in content as in this manuscript; it could, for instance, be electrical and structural. What counts is the degree of analytic relevance and reliability; what matters is the ease of electronic derivation and display.

ACKNOWLEDGMENT

This study has been supported by NSERC Operating Grant A-9604.

RECEIVED for review May 21, 1992. Accepted October 16, 1992.

Anal. Chem. **1993,** *65,* 112–117

Forward-Scattering Degenerate Four-Wave Mixing as a Simple Sub-Attomole-Sensitive Nonlinear Laser Analytical Spectrometric Method

Zhiqiang Wu and William G. Tong*

Department of Chemistry, San Diego State University, San Diego, California 92182

Optical phase conjugation by "forward-scattering" degenerate four-wave mixing in an absorbing liquid analyte solution is reported as a sensitive and simple nonlinear laser spectroscopic method. Since only two input laser beams are used in this nonlinear four-wave mixing setup, it offers important advantages including ease of optical alignment, efficient use of input photon density, low laser power requirements, and high wave-mixing efficiency. In addition, since the phase-conjugate signal is a laser beam, optical signal detection is very efficient and the signal-to-noise is excellent. Important characteristics of this novel nonlinear laser technique, including signal dependence on analyte concentration, individual input beam power, and modulation frequencies, are examined. Excellent detection sensitivity, small detection volume, and convenient sample introduction promise many applications for this nonlinear laser spectroscopic method. Preliminary detection limits of 0.7 amol of eosin B and 45 amol of iodine inside a probe volume of 98 pL are reported using a forward-scattering degenerate four-wave mixing setup.

INTRODUCTION

Most of the degenerate four-wave mixing (D4WM) research so far has been directed toward the studies and applications of the optical phase conjugation property using a "backward-scattering" degenerate four-wave mixing (B-D4WM) optical setup.[1-3] In a B-D4WM experiment, two counter-propagating pump beams and a probe beam are mixed inside a nonlinear medium, and a phase-conjugate signal beam is generated via one of the four-wave mixing mechanisms. Since the signal beam is a wavefront-reversed replica of the probe beam, any optical aberration suffered by the probe beam while propagating through a distorting medium will be canceled in this double-pass geometry. Applications based on spatial properties of nonlinear optical phase conjugation by B-D4WM in the fields of nonlinear optics and quantum electronics include: wavefront aberration compensation,[4] polarization aberration compensation,[5] lensless imaging,[6] real-time image processing,[7] and interferometry.[8] Using B-D4WM setups, we have demonstrated D4WM spectroscopy to be very effective for analytical measurements in discharge atomizers,[9-11] flame atomizers,[12-15] and room-temperature flow cells.[16,17]

In a B-D4WM setup, the forward pump beam and the probe beam propagate in one direction (forward) and the backward pump beam propagates in the opposite direction, and hence, the fourth beam (i.e., the signal beam) also comes out in the backward direction. In a F-D4WM optical setup, all input beams propagate in one direction (forward), and hence, the signal beam propagates also in the same direction (forward).

Furthermore, in a F-D4WM experiment, a phase-conjugate signal beam can be generated by using either a two-input-beam optical setup[18] or a three-input-beam noncoplanar "boxcar" configuration.[19-21] Although both forward-scattering D4WM and backward-scattering D4WM methods can be used to generate phase-conjugate wave fronts, B-D4WM receives more interests since some F-D4WM setups suffer from phase-matching constraints and from finite-interaction-length-induced distortion effects.[22] However, these constraint are negligible when a thin analyte sample cell is used and when the angle between the two input is small.[23] Hence, these F-D4WM setups are suitable for many ultrasensitive analytical measurements where the analyte cell is usually thin (e.g., a capillary cell) and where the angles between the two input beams are usually very small (less than 1.5°).

In this paper, we demonstrate "forward-scattering" D4WM as a sensitive analytical laser spectroscopic method for room-temperature flowing liquid analytes using only a few milliwatts of argon ion laser power. Compared to B-D4WM setups, the F-D4WM optical alignment is much simpler since only two input beams, instead of three, are used. Aligning, focusing, and mixing of the two input beams (one pump, one probe) is unusually easy for a nonlinear method, even when using very small capillary flow cells. Since all input beams can be focused and mixed by using a single lens, the photon density is very high and the wave mixing is highly efficient. Hence, laser power requirements are much lower for F-D4WM setups as compared to B-D4WM configurations. Relatively strong

---

* Author to whom correspondence should be addressed.

(1) Zel'dovich, B. Ya.; Pilipetsky, N. F.; Shkunov, V. V. *Principles of Phase Conjugation*; Springer-Verlag, New York, 1985.

(2) Hellwarth, R. W. *J. Opt. Soc. Am.* **1977,** *67,* 1–3.

(3) Yariv, A. *IEEE J. Quantum Electron.* **1978,** QE-14, 650–660.

(4) Wang, V.; Giuliano, C. R. *Opt. Lett.* **1978,** *2,* 4–6.

(5) Martin, G.; Lam, L. K.; Hellwarth, R. W. *Opt. Lett.* **1980,** *5,* 185–187.

(6) Levenson, M. D.; Johnson, K. M.; Hanchett, V. C.; Chiang, K. *J. Opt. Soc. Am.* **1981,** *71,* 737–743.

(7) Huignard, J. P.; Herriau, J. P.; Pechon, L.; Marrakchi, A. *Opt. Lett.* **1980,** *5,* 436–438.

(8) Hopf, F. A. *J. Opt. Soc. Am.* **1980,** *70,* 1320–1323.

(9) Tong, W. G.; Chen, D. A. *Appl. Spectrosc.* **1987,** *41,* 586–590.

(10) Chen, D. A.; Tong, W. G. *J. Anal. Atom. Spectrom.* **1988,** *3,* 531–535.

(11) Wu, Z.; Tong, W. G. *Spectrochim. Acta B* **1992,** *47B,* 449–457.

(12) Tong, W. G.; Andrews, J. M.; Wu, Z. *Anal. Chem.* **1987,** *59,* 896–899.

(13) Andrews, J. M.; Tong, W. G. *Spectrochim. Acta* **1989,** *44B,* 101–107.

(14) Andrews, J. M.; Weed, K. M.; Tong, W. G. *Appl. Spectrosc.* **1991,** *45,* 697–700.

(15) Wu, Z.; Tong, W. G. *Anal. Chem.* **1991,** *63,* 899–903.

(16) Wu, Z.; Tong, W. G. *Anal. Chem.* **1989,** *61,* 998–1001.

(17) Wu, Z.; Tong, W. G. *Anal. Chem.* **1991,** *63,* 1943–1947.

(18) Carman, R. L.; Chiao, R. Y.; Kelley, P. L. *Phys. Rev. Lett.* **1966,** *17,* 1281–1283.

(19) Khyzniak, A.; et al. *J. Opt. Soc. Am. A* **1984,** *1,* 169–175.

(20) Anavev, Yu.; Solovev, V. D. *Opt. Spectrosc. (USSR)* **1983,** *54,* 77–81.

(21) Du, W.; et al. *Opt. Commun.* **1991,** *86,* 428–430.

(22) Fisher, R. A., Ed. *Optical Phase Conjugation*; Academic Press: New York, 1983; p 73.

(23) Heer, C. V.; Griffen, N. C. *Opt. Lett.* **1979,** *4,* 239–241.

0003-2700/93/0365-0112$04.00/0

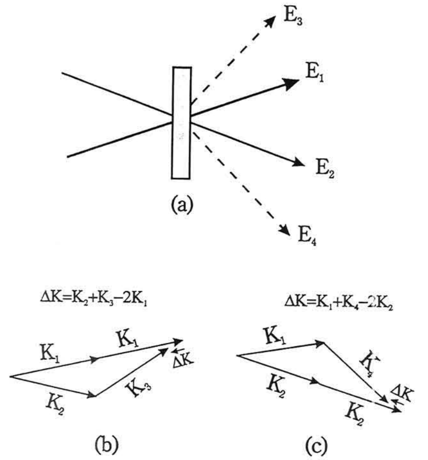

Figure 1. Different forward-scattering degenerate four-wave mixing setups: (a) schematic diagram for a two-beam F-D4WM method; E_1 and E_2, input beams; E_3 and E_4, generated signal beams; (b) vector diagram for a F-D4WM process when E_1 is more intense than E_2; (c) vector diagram for a F-D4WM process when E_2 is more intense than E_1. In order to show the vectors clearly, the angle between $\mathbf{K}_1$ and $\mathbf{K}_2$ is exaggerated in the vector diagrams.

F-D4WM signal is still visible to the naked eye even when using total laser power levels as low as 5 mW. A sub-attomole detection limit for eosin B is reported using this unusually simple nonlinear laser technique.

THEORY

A two-input-beam F-D4WM experimental configuration is illustrated in Figure 1. When both input beams, E_1 and E_2, have the same intensity, two signal beams, E_3 and E_4, with the same intensity are observed (Figure 1a). However, if the intensity of E_1 is much stronger than that of E_2, the signal beam E_3 is much stronger than the signal beam E_4 (Figure 1b). Similarly, if the intensity of E_2 is much stronger than that of E_1, the signal beam E_4 is much stronger than the signal beam E_3 (Figure 1c). As in B-D4WM experiments, generation of signal beams in a F-D4WM setup can be described in terms of dynamic holography. Constructive interference between E_1 and E_2 waves creates a dynamic grating with a period of Λ, where $\Lambda = \lambda/[2\sin(\theta/2)]$, λ is the laser wavelength, and θ is the angle between the two input beams. The signal beams, E_3 and E_4, are then generated by the scattering of E_2 and E_1, respectively, off the grating. As required in all nonlinear four-wave mixing processes, both energy and momentum conservations must be satisfied in F-D4WM experiments for effective energy transfer. The energy conservation requires that

$$\omega_3 = 2\omega_1 - \omega_2 = 2\omega - \omega = \omega \qquad (1)$$

and

$$\omega_4 = 2\omega_2 - \omega_1 = 2\omega - \omega = \omega \qquad (2)$$

Since all incident beams have the same frequency, the phase-conjugate signal also has the same frequency. Furthermore, momentum conservation requires that

$$\mathbf{K}_3 = 2\mathbf{K}_1 - \mathbf{K}_2 \qquad (3)$$

and

$$\mathbf{K}_4 = 2\mathbf{K}_2 - \mathbf{K}_1 \qquad (4)$$

where $\mathbf{K}_i$ ($i = 1, 2, 3, 4$) is the wave vector of the corresponding beam. Equations 3 and 4 indicate that the F-D4WM signal beam is most effectively generated in the K_3 and K_4 directions as shown in Figure 1.

Although only two input beams are used in the F-D4WM methods shown in Figure 1b,c, they are still considered *four*-wave mixing methods, since the E_1 input beam provides two waves, the E_2 input beam provides the third wave, and the signal beam becomes the fourth wave, making the process a *four*-wave mixing method. In Figure 1b, the more powerful input beam (i.e., E_1) serves as the pump beam that consists of two forward waves, and the other input beam (i.e., E_2) serves as the probe beam that generates the signal beam E_3. Similarly in Figure 1c, the more powerful input beam (i.e., E_2) serves as the pump beam that consists of two forward waves and the other input beam (i.e., E_1) serves as the probe beam that generates the signal beam E_4.

In an absorbing liquid solution, the phase-conjugate signal is generated mostly by thermally induced nonlinear effects.[24] When two coherent beams, E_1 and E_2, intersect in the absorbing solution, thermally induced refractive index change is obtained following the absorption of input photons by the analyte species and the subsequent thermalization via rapid radiationless relaxation of optically excited analyte species. Hence, a thermally induced refractive index grating is formed, from which E_1 and E_2 input beams are scattered to produce the phase-conjugate signal beams, E_3 and E_4, respectively. The resulting F-D4WM signal intensities, I_3 and I_4, can be expressed as[25,26]

$$I_3 = C I_1^2 I_2 \frac{\lambda^2}{\sin^2\theta}\left[\frac{dn}{dT}\right]^2 m^2 \left[\frac{\alpha}{k}\right]^2 \qquad (5)$$

$$I_4 = C I_1 I_2^2 \frac{\lambda^2}{\sin^2\theta}\left[\frac{dn}{dT}\right]^2 m^2 \left[\frac{\alpha}{k}\right]^2 \qquad (6)$$

where C is a constant, dn/dT is the temperature coefficient of the refractive index, m is the fringe modulation level, α is the absorption coefficient of the nonlinear analyte medium, and k is the thermal conductivity.

In eqs 5 and 6, one can find several important characteristic properties of the F-D4WM signal, including its quadratic dependence on the pump beam intensity, its quadratic dependence on the refractive-index change due to temperature change, and its quadratic dependence on the absorption coefficient, and hence, on the analyte concentration. Equation 5 also indicates that the signal beam intensity I_3 has a linear dependence on the probe beam intensity I_2, a quadratic dependence on the pump beam intensity I_1, and hence, a cubic dependence on the total intensity of all input beams. Similarly, eq 6 shows that the signal beam intensity I_4 has a linear dependence on the probe beam intensity I_1, a quadratic dependence on the pump beam intensity I_2, and hence, a cubic dependence on the total laser intensity of all input beams. Experimental observations of these predictions are described below.

EXPERIMENTAL SECTION

Figure 2 shows a schematic diagram of the F-D4WM experimental arrangement. The excitation light source is a continuous-wave argon ion laser (Coherent, Palo Alto, CA, Model Innova 90-6) operating at the 514.5-nm line. The laser beam is split by

---

[24] Hoffman, H. J. *IEEE J. Quantum Electron.* **1986**, QE-22, 552–562.

[25] Richard, L.; Maurin, J.; Huignard, J. P. *Opt. Commun.* **1986**, *57*, 365–370.

[26] Simoni, F.; Cipparrone, G.; Duca, D.; Khoo, I. C. *Opt. Lett.* **1991**, *16*, 360–362.

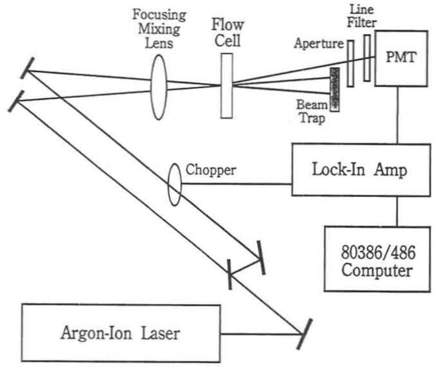

Figure 2. Experimental arrangement for forward-scattering degenerate four-wave mixing.

a beam splitter (%R/T = 30/70) to form E_1 and E_2 input waves. Relative intensities of the two input beams arriving at the sample cell, I_1:I_2, is 7:3. A single 100-mm focusing lens is used to focus and mix both input beams, and the sample cell is placed at the lens's focal point. The diameter of both E_1 and E_2 beam spots on the sample cell is 34 μm. These two beams intersect inside the sample cell with an intersect angle of 1.5°. In order to optimize the phase-conjugate signal strength, the difference in path lengths (or distances traveled) for E_1 and E_2 beams is kept less than the coherence length of the laser (i.e., 5 cm for the argon ion laser). A mechanical light chopper (Photon Technology International Inc., Princeton, NJ, Model 03-OC4000) is used to modulate the amplitude of the E_2 input beam. The phase-conjugate signal beam generated in the sample cell is directed to a photomultiplier tube (Hamamatsu Corp., Middlesex, NJ, Model R928) after passing through a 250-mm focal length lens and a 514.5-nm laser-line filter. A small aperture is used in front of the photomultiplier tube to minimize background noise due to the scattering of E_1 wave. The output signal of the photomultiplier tube is then sent to a current-to-voltage converter, monitored by a lock-in amplifier (Princeton Applied Research, Princeton, NJ, Model 5207), recorded by a strip-chart recorder, and digitized by a personal computer. The liquid analyte cell is a rectangular glass flow cell with a 0.1-mm optical path length (Starna Cells, Inc., Atascadero, CA, Type 48). A peristaltic pump (Rainin Instrument, Woburn, MA, Rabbit Minipuls 2) is used to deliver the analyte solution through the thin analyte flow cell. Eosin B and iodine analyte solutions are prepared by dissolving them in ethanol and carbon tetrachloride, respectively.

Since only two input laser beams are used and the signal beam is visible to the naked eye, the optical alignment of this nonlinear F-D4WM laser method is very simple even when compared to many conventional one-beam or two-beam laser methods. After the two input beams pass through the analyte cell, they are blocked by a beam trap, and the signal beam is easily separated and directed toward the detector. An analyte solution with a relatively high concentration (e.g., 5×10^{-6} M eosin B) is used as an "alignment solution" to optimize the optical alignment since a micromolar-level solution can already generate a strong signal that is visible to the naked eye. Signal optimization is performed simply by adjusting the mirrors and the lenses, and by carefully adjusting the flow cell position so that it is at the focal point of the wave-mixing lens, while observing the strength of the visible signal spot on a card (or on a photodetector for trace-concentration analytes). Once the optical alignment is optimized, the alignment and the signal remain very stable and different analyte solutions could be flowed through and analyzed without any further adjustments.

RESULTS AND DISCUSSION

As shown in Figure 1, input beams E_1 and E_2 constructively interfere to form a thermal grating, which then scatters the corresponding input waves to generate the F-D4WM signal beams, E_3 and E_4. Hence, if one places a screen behind the analyte cell, one observes four laser spots, two bright ones inside and two smaller ones on the outer wings. Experimental observation of these four laser spots is shown in the photograph (Figure 3) taken off a screen by a simple 35-mm camera. To be able to photograph bright signal spots using regular ISA 100 color print films, a relative high eosin B concentration (i.e., 1×10^{-5} M) is used. To avoid overheating of the sample solution, the focusing lens is removed for this high concentration solution. The intensity ratio of the two input beams arriving at the sample cell, I_1:I_2, is 7:3.

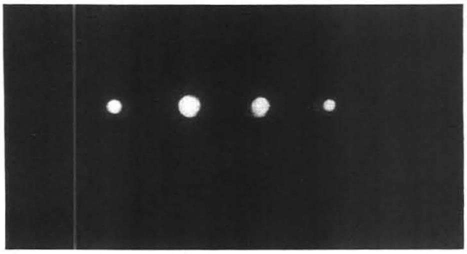

Figure 3. Photograph of input and signal beam spots: from left to right, E_3 signal beam, E_1 input beam, E_2 input beam, and E_4 signal beam.

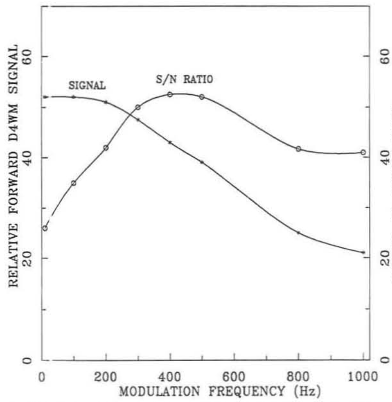

Figure 4. Dependence of forward-scattering degenerate four-wave mixing signal and signal-to-noise ratio on light modulation frequency. Eosin B concentration used is 5×10^{-7} M and the total laser power for all input beams is 0.3 W.

A two-input-beam F-D4WM optical setup offers several advantages as a novel nonlinear laser spectroscopic method. Compared to backward-scattering D4WM and other four-wave mixing methods, where three input beams are used, the optical alignment of a two-beam F-D4WM method is significantly easier. For example, in a "boxcar" F-D4WM configuration, where two pump beams and one probe beam are required, the optical alignment is not as simple. In addition, its wave-mixing efficiency strongly depends on the angle of the probe beam relative to the thermal grating for Bragg scattering condition, although the effect of the angle between the two pump beams is negligible.[19] Furthermore, these three input beams must be perfectly overlapped in order to obtain maximum wave-mixing efficiency, and hence, optical alignment is more complicated for a "boxcar" F-D4WM method as compared to that for a two-beam F-D4WM method.

In addition to simpler input beam alignments, it is also easier to mix waves with high efficiency in a two-beam F-D4WM method since only a single lens is needed to focus

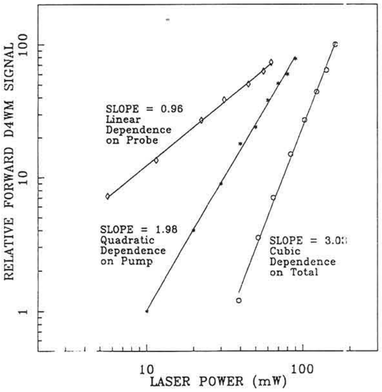

Figure 5. Dependence of forward-scattering degenerate four-wave mixing signal on different input beam intensity: (a) linear dependence on the probe beam intensity with 0.96 slope; (b) quadratic dependence on the pump beam intensity with 1.98 slope; (c) cubic dependence on the total input laser intensity with 3.03 slope. Eosin B concentration used is 2 × 10^{-6} M.

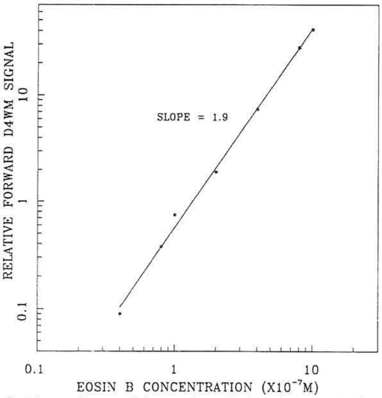

Figure 6. Dependence of forward-scattering degenerate four-wave mixing signal on eosin B concentration. Total laser power used for all input beams is 0.3 W.

and mix all the input beams as shown in Figure 2 (instead of two or three lenses needed in a B-D4WM method). Hence, it is relatively easy to use microsample cells or many popular small-diameter capillary flow cells for a two-beam F-D4WM detector. In our two-beam F-D4WM setup, the diameter of the focused beam spots at the sample cell is 34 μm, and hence, the laser probe volume inside the sample cell is 98 pL. Therefore, this F-D4WM detection method has many potential applications as an ultrasensitive detector for both fluorescing and nonfluorescing analytes for a capillary chromatography system or a capillary electrophoresis system. As indicated in eq 5, the F-D4WM signal has a cubic dependence on total input laser intensity, and hence, the signal could be enhanced significantly by increasing the input intensity.

The forward-scattering D4WM signal can be also enhanced by optimizing several other parameters. The efficiency of a F-D4WM grating, formed by E_1 and E_2 beams inside the nonlinear medium, is strongly affected by (1) the angle θ between the two input beams, (2) the difference in input wave arrival times or the difference in input beam path length, and (3) the beam intensity ratio of the two input beams. The angle θ between the two input beams should be kept as small as possible in order to obtain optimum phase matching especially when using thin analyte cells.[23] In addition, the smaller the angle θ between the two input beams, the wider and sharper the F-D4WM grating period will be. Since a grating with a larger period is less vulnerable to grating washout due to thermal motion, better grating efficiency and higher signal strength can be expected. Furthermore, a smaller angle θ also increases the beam interaction volume and, hence, strengthens the F-D4WM signal. By reducing the angle θ, a significant increase in signal strength is observed in our two-beam F-D4WM setup. Since an angle as wide as 1.5° could already yield excellent detection limits, optical alignment requirements are not as restricted as one might expect. Small-angle alignments are especially easier to perform in this two-input-beam F-D4WM setup since a single focusing lens could be used to focus all input beams instead of two or three lenses usually required in a three-input-beam D4WM method.

Another important parameter that could affect the grating sharpness is the difference of the path lengths or arrival times of the two input beams. Optimum constructive interference between the two input coherent beams can be obtained when the phase matching of the waves is at a maximum. Hence, it is important to keep the path length difference shorter than the laser coherence length ($L = c/\pi\Delta\nu$) in order to form sharp F-D4WM gratings. Even a simple argon ion laser has a relatively long coherence length (e.g., 5 cm) and more sophisticated narrow-bandwidth lasers such as dye lasers have much longer coherence length or coherence time. Hence, many popular lasers offer sufficient room for convenient optical alignments.

The F-D4WM signal-to-noise ratio can be optimized significantly by carefully adjusting the intensity distribution ratio for the two input beams. In a F-D4WM setup where E_3 is monitored as the signal beam, as shown in Figure 1b, a stronger E_3 signal beam is obtained when the E_1 input beam is stronger than the E_2 input beam, since E_3 is generated by E_1 scattering off the thermal grating formed by E_1 and E_2. However, using a stronger E_1 input beam also increases the background noise due to the scattering of the E_1 beam itself. Hence, one must use an optimum intensity for the E_1 input beam in order to obtain both maximum signal strength and minimum background noise. Our results indicate that the best compromise for the input beams for S/N optimization is an intensity ratio I_1:I_2 of 7:3.

To further improve signal-to-noise ratio, one could suppress the background noise by using an amplitude-modulated detection scheme. If E_3 is monitored as the signal beam as shown in Figure 1b, most of the background noise comes from the scattering of the pump beam E_1, and hence, one should modulate the probe beam E_2, instead of the pump beam E_1, in order to obtain maximum noise suppression. Similarly, if the signal beam E_4 is monitored as shown in Figure 1c, one should modulate the probe beam E_1, instead of the pump beam E_2, in order to obtain maximum suppression of noise originating mostly from the E_2 beam.

Figure 4 shows the dependence of signal and signal-to-noise ratio on the chopper modulation frequency. As expected, the signal intensity remains strong at low modulation frequencies since sufficient time is allowed between on–off cycles for the F-D4WM grating to form completely. The signal decreases slowly as the modulation frequency is increased since less time is available to form a complete and sharp grating.[17] On the other hand, the background noise level is high at the low frequency region, and the noise can be better suppressed by a lock-in amplifier at a higher modulation frequency. Although the signal is weaker at a higher

Table I. Comparison of Detection Limits by Laser-Based Methods for Trace Analysis

laser method	laser(s)	detection limit[a]		ref
		eosin B	iodine	
backward D4WM	argon ion laser	2.9 amol 2.1×10^{-11} M (0.5-mm cell)		16
backward D4WM	excimer-pumped dye laser		15.8 fmol[a] 7.9×10^{-8} M (1-mm cell)	28
laser-induced thermal diffraction	argon ion and He–Ne lasers		138 fmol[a] 8.1×10^{-7} M (1-mm cell)	27
forward D4WM	argon ion laser	0.7 amol 7.1×10^{-9} M (0.1-mm cell)	45 amol 4.6×10^{-7} M (0.1-mm cell)	this work

[a] Converted from reported detection limits.

modulation frequency, the signal-to-noise ratio actually remains reasonably high and stable at higher frequencies (e.g., >1000 Hz).

Equations 5 and 6 reveal several important properties of the F-D4WM signal, including its dependence on the intensities of the two input beams, I_1 and I_2, and the quadratic dependence of the signal on the analyte absorption coefficient, and hence, the analyte concentration. Equation 5 suggests that the F-D4WM signal has a linear dependence on the probe beam intensity, a quadratic dependence on the pump beam intensity, and a cubic dependence on the total input intensity. Figure 5 shows experimental verification of eq 5. Using the optical alignment shown in Figure 1b, and monitoring E_3 as the signal beam, the F-D4WM signal is observed to have a linear dependence (slope = 0.96) on the probe beam intensity I_2, a quadratic dependence (slope = 1.98) on the pump beam intensity I_1, and a cubic dependence (slope = 3.03) on the total input laser intensity.

Similarly, when the optical alignment shown in Figure 1c is used, and when E_4 is monitrored as the signal beam, the F-D4WM signal is observed to have a linear dependence on the probe beam intensity I_1, a quadratic dependence on the pump beam intensity I_2, and a cubic dependence on the total input laser intensity. This nonlinear dependence of signal on laser intensity is one of many important characteristics of the F-D4WM method that yield excellent detection sensitivity. For instance, an order of magnitude increase in total laser intensity would result in a 3 orders of magnitude increase for the F-D4WM signal. Although this property could also generate a higher level of noise at the absorption line center due to, for example, source laser light fluctuation, as compared to those of conventional laser methods, this noise problem is easily overcome by (a) the availability of enormous amounts of signal intensity and by (b) the signal collection efficiency that is virtually 100% (i.e., signal is a laser beam). In addition, other types of noise, such as background scattering off of optics, increase only linearly with laser power while the signal increases as the cube of the laser power. Hence, the net gain in signal-to-noise ratio is still better than those of conventional methods, and hence, making it possible for a nonlinear laser method to yield excellent S/N and detection limits.

Figure 6 shows experimental observation of quadratic dependence of signal on eosin B concentration as suggested by eqs 5 and 6. Compared to linear relationships observed in conventional laser methods, the nonlinear dependence of F-D4WM signal on analyte concentration could be viewed advantageously or disadvantageously since the rate of signal change accelerates as concentration increases or decreases, respectively. Nevertheless, D4WM detection methods are suitable for ultrasensitive analytical measurements since they can yield sub-attomole detection sensitivity and they are capable of detecting both fluorescing and nonfluorescing analytes.

A preliminary F-D4WM detection limit of 7.1×10^{-9} M (S/N = 2) for eosin B is determined using a 0.1-mm-thick flow cell and a total argon ion laser power of 0.5 W. This corresponds to a mass detection limit of 7×10^{-19} mol of eosin B within a detection probe volume of 98 pL. Using the same F-D4WM setup, a detection limit of 4.6×10^{-7} M or 45×10^{-18} mol for iodine in CCl_4 is also determined.

Table I summarizes results from a few four-wave mixing laser spectroscopic methods using different experimental configurations. It is important to note that, a F-D4WM method requires a much simpler optical setup and a much lower laser power and yet it still yields comparable detection limits as compared to backward-scattering D4WM methods. When compared to a B-D4WM method using a pulsed excimer-pumped dye laser,[28] our F-D4WM detection method yields an iodine mass detection limit that is 351 times better, and yet it does not require a dye laser. When compared to a laser-induced thermal diffraction method using both an argon ion laser and a He–Ne laser,[27] our F-D4WM detection method yields an iodine concentration detection limit that is 1.8 times better (and an iodine mass detection limit that is 3067 times better), and yet it only employs a simpler optical setup with only a single laser instead of two different lasers.

Although there are similar features between degenerate four-wave mixing methods and holography (or holography-like spectroscopic methods relying on two-color pumped-probed thermal gratings), the two processes are not totally identical. While holography is a sequential process where recording and reconstruction (writing and reading) steps are separate (or time delayed), these steps occur simultaneously in a degenerate four-wave mixing experiment. While only two photons need to exist simultaneously in holography, four photons must exist simultaneously in four-wave mixing methods. Another distinctive difference between holography and four-wave mixing is the different types of diffraction gratings generated. While only spatial diffraction gratings are involved in holography, both spatial diffraction gratings and temporal diffraction gratings could be used in four-wave mixing.[15,29] The B-D4WM complex signal vector amplitude can be described as[15] $P^{(3)} \propto (A\mathbf{e}_b\mathbf{e}_p{}^*\cdot\mathbf{e}_f + B\mathbf{e}_f\mathbf{e}_p{}^*\cdot\mathbf{e}_b + C\mathbf{e}_p{}^*\mathbf{e}_f\cdot\mathbf{e}_b)E_fE_bE_p{}^*$, where A, B, and C are constants depending on the nonlinear susceptibility of the analyte and $\mathbf{e}_f$, $\mathbf{e}_b$, $\mathbf{e}_p$ are polarization-state vectors of the forward, backward, and probe beams, respectively. In the equation above, the first and

---

(27) Pelletier, M. J.; Thorsheim, H. R.; Harris, J. M. *Anal. Chem.* **1982**, *54*, 239–242.

(28) Fujiwara, K.; et al. *Spectrosc. Lett.* **1987**, *20*, 633–643.

(29) Sakai, J. C., *Phase Conjugate Optics*; McGraw-Hill: New York, 1992.

second terms describe contributions from the volume gratings formed by forward-probe and backward-probe beam pairs, respectively. These two terms can be used also to describe processes in holography. However, the third term describes contribution from the temporal grating (i.e., coherent grating), and this grating is characteristic of B-D4WM.[29] Another important and useful characteristic property of both forward- and backward-scattering four-wave mixing methods is the phase-conjugate property of the signal beam.[15,23] The phase-conjugate property in our forward-scattering D4WM signal beam is verified by placing a thin wire in the probe beam path and observing its image on a white screen that is positioned in the signal beam path. The image of the object (i.e., a wire or anything small that can be placed inside the probe beam path) is "carried" and projected very clearly on the screen by the phase-conjugate signal beam when the distance between the image screen and the nonlinear medium (i.e., analyte cell) is the same as the distance between the object and the analyte cell. The phase-conjugate property of the signal beam generated by the analyte (i.e., the nonlinear medium) in a D4WM method has many potential applications including autocorrection of beam distortion or optical aberration.

The use of a single short-focal length lens for all the input beams not only simplifies focusing and mixing simultaneously, it also maximizes photon density available at the sample cell significantly, and hence, allowing the use of low-power (milliwatts) lasers in a nonlinear spectroscopic method. In our two-beam F-D4WM setup, the signal is still strong even when laser power as low as 5 mW is used. Tight focusing and compact wave mixing available with this new two-beam F-D4WM configuration could reduce the laser power requirements low enough that low-cost lasers, such as He–Ne lasers or diode lasers, could be used eventually as excitation light sources for the first time in a nonlinear method. These studies are underway in our laboratory and will be reported later.

CONCLUSIONS

We have demonstrated the use of a simple nonlinear laser method based on optical phase conjugation by F-D4WM as an ultrasensitive detection method for liquid analytes using laser powers at the milliwatt range. Since only two input laser beams are involved in this four-wave mixing process, the optical alignment is much easier compared to other four-wave mixing methods, and there are no critical optical alignment constraints. Excellent sub-attomole detection sensitivity, picoliter probe volume, simple one-laser one-wavelength setup, and convenient analyte introduction promise many potential applications, including its use as a relatively inexpensive, simple, ultrasensitive detector for HPLC and HPCE. The laser power requirement for producing a strong F-D4WM signal is unusually low (milliwatt range) compared to conventional backward-D4WM experiments. Works on capillary D4WM detectors[30,31] suitable for chromatography and electrophoresis and on milliwatt-laser-based F-D4WM methods, using even lower power lasers such as 2-mW (or less) He–Ne lasers, are underway in our laboratories.

ACKNOWLEDGMENT

We gratefully acknowledge partial support of this work from the National Institute of General Medical Sciences, National Institutes of Health under Grant No. 5-R01-GM41032, and the National Science Foundation under Grant No. CHE-8719843.

RECEIVED for review July 20, 1992. Accepted October 15, 1992.

---

(30) Tong, W. G. *Proceedings of the International Conference on Lasers '90* **1990**, 749–755.

(31) Tong, W. G. *Proceedings of the International Society for Optical Engineering, SPIE* **1992**, *1637*, 25–32.

Anal. Chem. **1993**, *65*, 118–122

Graphite Furnace Vaporization with Laser-Enhanced Ionization Detection[‡]

B. W. Smith, G. A. Petrucci, R. G. Badini,[†] and J. D. Winefordner[*]

Department of Chemistry, University of Florida, Gainesville, Florida 32611

A graphite furnace is used to vaporize samples which are transferred in an argon carrier gas to a low-noise miniflame laser-enhanced ionization detection system. Two-step excitation is provided by dual Nd:YAG pumped dye lasers operating at 30 Hz. The limiting noise is 6 fC, and the detection limits for Mg, Tl, and In, limited by temporal probing inefficiencies and losses in sample transport, range from 1 to 260 fg.

INTRODUCTION

Laser-enhanced ionization in flames (LEI) has now been studied as an analytical technique for nearly 15 years. The collisionally assisted, resonantly pumped ionization which takes place in combustion flames has been used to detect at least 34 elements, generally with exceptionally good detection limits.[1] The mechanism is now well understood,[2–4] and studies have been made concerning the analysis of real samples.[1,2,5,6] When two laser-pumped excitation steps are used, the selectivity is extremely good, although for complex, and especially easily ionized matrices, the detection capability suffers due in large part to modifications in the charge collection process caused by the matrix. These problems have been studied and brought under some degree of control by improvements in electrode design.[7–9] Nevertheless, despite the phenomenal detection capability, LEI has found limited use as an analytical method. The requirement of a dual dye laser system, once considered a substantial complexity, is nowadays no longer a particularly serious disadvantage. More important are the potential for unpredictable interferences and the poor atomization efficiency of many elements in suitable combustion flames. Unfortunately, the flame is an essential component if one wishes to induce and observe ionization at atmospheric pressure, as it provides the necessary collisional redistribution and an electrically conductive environment. The problems associated with measurements in complex matrices have limited applications of LEI mostly to simple aqueous systems such as lake and river waters.[6,8–10]

It is instructive to examine a selection of LEI limits of detection. Table I lists some of the better results for several elements, along with the wavelengths used. Only two-step excitation schemes have been chosen, these being, with a few exceptions, 10–1000× more sensitive than single-step excitation. The generally accepted theoretical limit of detection for LEI[12] is on the order of 1 pg mL^{-1} or about 10^4 atoms cm^{-3}. Typically, the laser beams occupy a volume in the flame of ca. 0.1 cm^3, so this corresponds in a single laser shot to an absolute detection limit of about 10^3 atoms. This comes about from considering the limiting noise to be due to the fluctuation in the several microamperes of current carried by the native charged species present in the flame. Note that for several elements (Pb, Cs, Na, In, Li, Tl, and Mg), this theoretical limit has been reached. This implies an ionization yield (defined as the number of charge pairs produced per atom in the probe volume) near unity and indeed, ionization yields of this magnitude have been measured[13,14] and have been predicted theoretically.[15] It is clear from the energy defects listed in Table I (ΔE, the energy difference between the highest level populated by the excitation lasers and the ionization potential) that the collisional rate in the flame is sufficient to provide complete ionization for atoms within about 1 eV of the ionization limit. The efficiency of charge collection has also been shown to be unity.[16] In general, when this ultimate detection capability has not been achieved, it has been due to a poor choice of excitation wavelengths (to levels farther than 1 eV from the ionization limit), poor atomization in the flame, or low laser pulse energy (insufficient to saturate the transitions involved) or to unusual sources of limiting noise such as multiphoton ionization of native flame species and, particularly, radio-frequency noise from the firing of the pump laser. With the exception of incomplete atomization in the flame, all of these difficulties can be avoided in properly designed experiments.

Because of the problems encountered in dealing with real samples in LEI and the atomization inefficiencies associated with flames, attempts have been made to observe LEI in alternate atom reservoirs. The inductively coupled plasma (ICP) has been tried with very limited success because of the extremely large radio-frequency noise background associated with the plasma.[17] The graphite furnace is an attractive possibility because of the great improvement in atomization efficiency, especially due to the confinement of the atomized sample to a small volume which can be closely matched to the optical probe volume. Several studies have been reported where detection was carried out by inserting a thin electrode wire into the graphite furnace tube.[18,19] Two difficult

---

[*] Author to whom correspondence should be sent.

[†] On leave from Departamento de Fisicoquímica, Facultad de Ciencias Quimicas, Universidad Nacional de Córdoba, Suc. 16, C.C. 61, RA 5016, Argentina.

[‡] Research supported by DOE-DEOFGO5-88ER 13881.

(1) Axner, O.; Rubinsztein-Dunlop, H. *Spectrochim. Acta* **1989**, *44B*, 835.

(2) Havrilla, G. J.; Carter, C. C. *Appl. Opt.* **1987**, *26*, 3510.

(3) Omenetto, N.; Berthoud, T.; Cavalli, P.; Rossi, G. *Anal. Chem.* **1985**, *57*, 1256.

(4) Marunkov, A. G.; Reutova, T. V.; Chekalin, N. V. *J. Anal. Chem. USSR (Engl. Transl.)* **1986**, *41*, 539.

(5) Turk, G. C. *J. Anal. At. Spectrom.* **1987**, *2*, 573.

(6) Turk, G. C.; Kingston, H. M. *J. Anal. At. Spectrom.* **1990**, *5*, 595.

(7) Trask, T. O.; Green, R. B. *Spectrochim. Acta* **1983**, *38B*, 503.

(8) Turk, G. C. *Anal. Chem.* **1981**, *53*, 1187.

(9) Axner, O.; Magnusson, I.; Perersson, J.; Sjöström, S. *Appl. Spectrosc.* **1987**, *41*, 19.

(10) Chaplygin, V. I.; Zorov, N. B.; Kuzyakov, Yu Ya. *Talanta* **1983**, *30*, 505.

(11) Chaplygin, V. I.; Kuzyakov, Yu Ya; Novodvorsky, O. A.; Zorov, N. B. *Talanta* **1987**, *34*, 191.

(12) Travis, J. C.; Turk, G. L.; Green, R. B. *Anal. Chem.* **1982**, *54*, 1006A.

(13) Smith, B. W.; Hart, L. P.; Omenetto, N. *Anal. Chem.* **1986**, *58*, 2147.

(14) Axner, O.; Berglind, T. *Appl. Spectrosc.* **1989**, *43*, 940.

(15) Omenetto, N.; Smith, B. W.; Hart, L. P. *Fresenius' Z. Anal. Chem.* **1986**, *324*, 683.

(16) Schenck, P. K.; Travis, J. C.; Turk, G. C.; O'Haver, T. C. *J. Phys. Chem.* **1981**, *85*, 2547.

(17) Turk, G. C.; Watters, R. L. *Anal. Chem.* **1985**, *57*, 1979.

0003-2700/93/0365-0118$04.00/0

Table I. LEI Limits of Detection

element	λ_1 (nm)	λ_2 (nm)	ΔE (eV)	LOD (pg/mL)	ref
Ag	328.1	421.1	0.85	50	28
Ca	422.6	585.7	1.06	30	5
Cd	228.8	466.2	0.92	100	30
Co	315.9	531.7	1.6	200	2
Co	252.1	591.7	0.85	80	30
Cs	455.5		1.17	4	33
In	451.1	571.0	0.87	0.9	31
Li	670.8	460.3	0.85	0.3	28
Mg	285.2	470.3	0.66	1	32
Mn	279.5	521.5	0.62	20	29
Na	589.0	568.8	0.85	0.6	33
Na	589.0	568.8	0.85	2	11
Ni	282.1	501.4	0.76	40	34
Pb	283.3	600.2	0.98	1	4
Tl	291.8	377.6	0.90	8	3
Yb	555.6	581.2	1.8	100	33

problems have been encountered. The high current (ca. 200 A) used to electrically heat the graphite furnace induces a large background current in the measurement at the same point in time as the sample atomization. Thermionic emission from the heated graphite tube is also directly detected. Thus, the limiting noise is orders of magnitude higher than in a flame. Despite the added noise, the absolute detection limits are quite good, indicating that an improvement in sampling and probing efficiency has been achieved. However, the ionization yield in the graphite furnace is poorer than in a combustion flame, typically no better than about 10^{-5} because of the low collisional rate available in the furnace environment. The use of a T-shaped furnace which separated the atomization and ionization/detection processes reduced the furnace-related noise greatly and provided a substantial improvement.[20] Detection limits of 1 and 2 fg were obtained for Mn and Sr, respectively. Butcher and co-workers[21] have made a detailed study of LEI in a graphite tube furnace using a graphite probe for sample introduction and signal aquisition. They reported similar difficulties with high background noise and observed a significant signal depression from the presence of sodium in the sample matrix. For elements which were excited to within 7000 cm^{-1} of the ionization limit (Tl, In, and Li), they obtained limits of detection ranging from 0.7 to 2 pg.

A more successful approach to discrete atomization in LEIS has been made by Chekalin and co-workers.[22,23] They have placed the graphite furnace, in the form of a tube or rod, directly in the LEI flame. Signal collection is carried out by a pair of electrodes placed above the furnace. Thus the sample is rapidly vaporized into the probe region and very efficiently detected. Even though the furnace is heated by the flame, considerable control over the atomization is obtained through resistive heating of the graphite tube. These workers have analyzed trace species in several interesting matrixes including orthophosphoric acid, CdHgTe, and germanium. For aqueous solutions, they have obtained limits of detection of 0.8–200 fg for In, Cu, Au, and Na. By using *direct solid sample introduction* (10 mg of CdHgTe) with no sample treatment, they obtained a limit of detection for In of 1 pg/g. This level of detection power in real matrixes has not been achieved by any other analytical method.

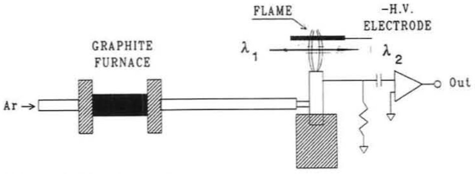

Figure 1. Experimental setup.

In this work, we have interfaced a graphite furnace vaporation step with a flame LEI detection step in order to acquire the advantages of both graphite furnace vaporization and flame ionization detection while maintaining independent control of each process.

The graphite furnace has been interfaced successfully to microwave and radio-frequency plasma sources for analysis of small-volume samples. Samples which have been vaporized in the furnace can be transported easily in an argon carrier gas and subsequently detected by emission, absorption, mass spectrometry, or in this case, laser-enhanced ionization. The key to designing an efficient interface is to maintain a dense atomic vapor with a minimum of dilution before detection. This was done using a miniburner miniflame LEI system which we have developed for use as a resonance ionization detector.[24] This device couples with very little dilution to the argon carrier gas from the furnace and presents an active volume which can be very efficiently spatially illuminated with the pump lasers. Detection of the ionization signal is done in the usual manner with a water-cooled stainless steel electrode immersed in the flame. In our studies of the resonance ionization detector, the small size of the burner and electrode reduced greatly the radio-frequency pickup from the firing of the laser.

EXPERIMENTAL SECTION

Figure 1 shows schematically the experimental system. The Nd-YAG-dual dye laser system used[24] and the modified furnace design[25] have been described previously. The major modification is a chamber consisting of a ring machined from boron nitride and tightly fitted in a specially shaped stainless steel housing firmly secured with O-rings between the two holders carrying the original left-hand graphite contact cylinders of the HGA-400 (Perkin-Elmer, Norwalk, CT) graphite furnace system. Two holes appropriately positioned in the housing allow sample introduction and operation of the conventional temperature sensor device. The housing rests on the original pneumatic cylinder of the atomizer. A mechanical clamp was fashioned to ensure good electrical contact between the electrodes and graphite tube. One of the window holders was replaced with a modified $^1/_4$-in. Ultra-Torr (Cajon Co., Macedonia, OH) connector. A 30-cm-long PTFE tube (0.65-cm o.d., 0.19-cm i.d.) inserted into the connector was used to transfer the vaporized sample to the flame. A ball valve, inserted in the transfer line near the burner, was closed during sample introduction into the graphite furnace to prevent flashback of the flame. A PTFE stopper was used to block gas flow from the sample introduction hole in the graphite furnace during atomization.

The small flows of transport gas (Ar) were provided from a gas tank and metering system independent of the original furnace gas supply. Carrier gas was introduced by way of the original internal and external gas inlet tubes which feed into the furnace and had been disconnected from the conventional (original) gas supply. The small flows required to prevent blowout of the miniature flame could not be obtained with the original gas supply. Typical Ar carrier gas flow rates were in the range 50–500 mL min^{-1}. The miniature flame has been previously described[24] and consisted of a single 0.32-cm-o.d. stainless steel capillary tube

---

(18) Magnusson, I.; Axner, O.; Lindgren, I.; Rubinsztein-Dunlop, H. *Appl. Spectrosc.* **1986**, *40*, 968.

(19) Magnusson, I.; Sjöström, S.; Lejon, M.; Rubinsztein-Dunlop, H. *Spectrochim. Acta* **1987**, *42B*, 713.

(20) Sjöström, S.; Magnusson, I.; Lejon, M.; Rubinsztein-Dunlop, H. *Anal. Chem.* **1988**, *10*, 1631.

(21) Butcher, D. J.; Irwin, R. L.; Sjöström, S.; Walton, A. P.; Michel, B. G. *Spectrochim. Acta* **1991**, *46B*, 9.

(22) Chekalin, N. V.; Pavlutskaya, V. I.; Vlasov, I. I. *Inst. Phys. Conf. Ser.* **1990**, *114*, 283.

(23) Chekalin, N. V.; Vlasov, I. I. *J. Anal. At. Spectrom.* **1992**, *7*, 225.

(24) Petrucci, G. A.; Badini, R. G.; Winefordner, J. D. *J. Anal. At. Spectrom.* **1992**, *7*, 481.

(25) Crabi, G.; Cavalli, P.; Achilli, M.; Rossi, G.; Omenetto, N. *At. Spectrosc.* **1982**, *3* (4), 81.

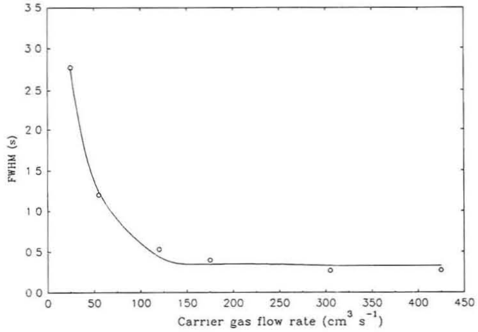

Figure 2. Plot of fwhm of signal peak vs carrier gas flow rate. The curve is an exponential fit to the data.

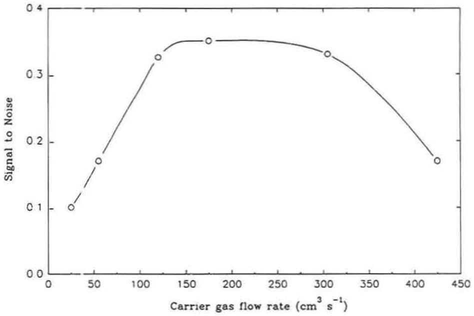

Figure 3. Plot of signal-to-noise vs carrier gas flow rate.

cemented in the center of a 2.54-cm-o.d. phenolic cylinder which in turn fit into the burner sleeve of a commercial premix burner chamber. Argon carrier gas from the graphite furnace was introduced through another 0.32-cm-o.d. tube cemented through the side of the phenolic cylinder.

The Mg determinations were carried out using a pyrolytically coated graphite tube. The In determinations were performed using a pyrolytically coated graphite tube containing a stabilized temperature platform. The Tl determinations were done using both types of tube configurations. The temperature programs used were those recommended by the furnace manufacturer for atomic absorption analysis.[26]

The charge collection method used in conventional flame LEI was employed and has been described elsewhere.[8] Briefly, the electric field (ca. −1200 V) was applied across a 0.32-cm-o.d. ($^1/_8$-in.) stainless steel water-cooled electrode and the tip of the stainless steel capillary burner. The pulsed signals were collected at the burner by a capacitatively-coupled transimpedance amplifier (Model A1, THORN EMI Gencom, Inc., Fairfield, NJ) and recorded through a boxcar averager. Direct current measurements were made using a calibrated transimpedance amplifier (Model 454, Keithley Instruments, Cleveland, OH). Both detection systems were capable of measuring total absolute charge produced at the flame.

Studies of LEI signals as a function of gas flow rate were carried out using a burner of different design because the single capillary burner was incapable of supporting a stable flame over a wide range of gas flow rates. This burner consisted of a single capillary (0.32-cm o.d.) through which passed the entire Ar flow from the furnace surrounded by an array of capillary tubes which independently carried the premixed combustion gasses. Both burners produced identical LEI signals. The single capillary version described above had slightly lower noise characteristics and was therefore used for the analytical studies.

RESULTS AND DISCUSSION

In experiments where analyte vapor is transported to a secondary reservoir for detection, a compromise must often be reached between minimizing diffusional and transport losses and analyte peak broadening and maximizing residence time in the detection reservoir. A study of the signal to noise (S/N) and signal peak width versus carrier gas flow rate was performed. As stated in the Experimental Section, a different burner design, which could support a much larger range of carrier gas flow rates, was used for this study. Figure 2 shows the full width at half-maximum (fwhm) of the Tl signal peak as a function of the carrier gas flow rate. The curve in the figure is an exponential fit to the data. From Figure 2, we see that diffusional broadening in the transfer line reaches a minimum at a flow rate of approximately 150 cm^3 min^{-1} and remains constant at higher flow rates. Figure 3 is a plot of the S/N also as a function of carrier gas flow rate, obtained by measuring peak height and rms background noise due to blank atomization. Two limiting cases are observed. At lower carrier gas flow rates, while the residence time in the flame is maximized, diffusional broadening of the analyte band in the transfer tube results in a relatively poor S/N. The S/N reaches a maximum and plateaus at 150 cm^3 min^{-1}, corresponding to the minimum in the curve in Figure 2, where diffusional broadening is minimized. At higher flow rates, while the diffusional broadening is minimized, the residence time in the laser beam is greatly reduced, leading again to a degradation in the S/N. For all further experiments, an optimum carrier gas flow rate of approximately 200 cm^3 min^{-1} was used.

The absolute mass transport efficiency of analyte from the furnace to the flame was estimated by measuring the total dc charge produced in the flame by thermal ionization due to the atomization in the furnace of known amounts of Cs. Cesium was chosen because of its small β-value[27] of 0.02 (i.e., >98% ionization in an acetylene/air flame). Typical signal peak shapes from the impulse vaporization in the graphite furnace are shown in Figure 4. Since this is a dc measurement, the peak shapes directly reflect the timing of the vaporization and transport processes. As can be seen from the inset in Figure 4, which is an expanded plot of the first peak, the base width of a typical peak is approximately 3 s. This is in good agreement with peak widths observed in conventional graphite furnace atomic absorption spectrometry, indicating little broadening of the plug of analyte vapor in the transport process. Using the absolute gain, in volts per ampere, of the transimpedance amplifier used to make the current measurement, the amount of charge formed from vaporization of the Cs sample in the graphite furnace was measured by calculating the area under the signal peak, in volt seconds. A ratio of the number of charge pairs formed to the number of atoms injected then yields the mass transport ratio. Each peak in Figure 4, corrected for the mean blank signal, corresponds to 6×10^{-5} C of charge (4×10^{14} electrons). Using

---

(26) Perkin-Elmer Corp. Analytical Techniques for Graphite Furnace Atomic Absorption Spectrometry. Publication No. B332; Perkin-Elmer Corp.: Norwalk, CT, 1984.

(27) Parsons, M. L.; McElfresch, P. M. *Appl. Spectrosc.* **1972**, *26*, 472.

(28) Omenetto, N.; Smith, B. W.; Hart, L. P. *Fresenius' Z. Anal. Chem.* **1986**, *324*, 683.

(29) Turk, G. C.; Travis, J. C.; DeVoe, J. R. *J. Phys. Colloq.*, **1983**, *44*, C7–301.

(30) Turk, G. C.; DeVoe, J. R.; Travis, J. C. *Anal. Chem.* **1982**, *54*, 643.

(31) Bykov, I. V.; Chekalin, N. V.; Tikhomirova, E. I. *J. Anal. Chem. USSR (Engl. Transl.)* **1986**, *40*, 1579.

(32) Magnusson, I.; Axner, O.; Rubinsztein-Dunlop, H. *Phys. Scr.* **1986**, *33*, 429.

(33) Bykov, I. V.; Skortsov, A. B.; Tatsii, Tu. G.; Chekalin, N. V. *J. Phys. Colloq.* **1983**, *44*, C7–345.

(34) Axner, O.; Lejon, M.; Magnusson, I.; Rubinsztein-Dunlop, H.; Sjöström, S. *Appl. Opt.* **1987**, *26*, 3521.

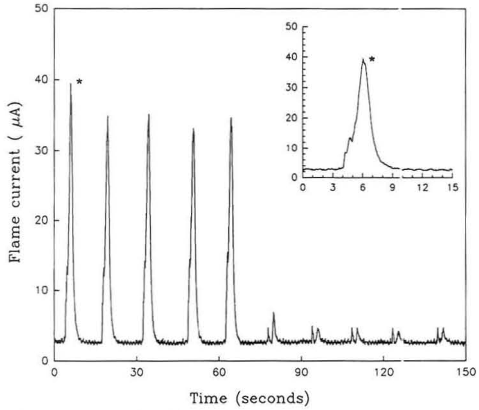

Figure 4. dc signal peaks for a ca. 200-ng injection of Cs into the graphite furnace. The latter five peaks are for injection of deionized water blanks. The inset shows an expanded view of the first signal peak.

samples of ca. 200 ng of Cs (1×10^{15} atoms), a mass transport of at least 40% was obtained. The mass transport efficiency was noted to be independent of the length (between 30 and 100 cm) or material of the transfer tubing. Also shown in Figure 4 are signal peaks obtained from injection of 10-μL aliquots of deionized water blanks.

A temporal probing efficiency, ϵ_t, also needs to be considered since a pulsed laser was used. Since the laser pulse duration is on the order of 10 ns, the temporal probing efficiency is given by

$$\epsilon_t = D_B f/\nu \tag{1}$$

where D_B is the diameter (centimeters) of the laser beams in the flame, f is the repetition rate (hertz) of the laser, and ν is the total linear flow velocity (centimeters per second) of the flame gases and carrier gas. In our case, using 0.2-cm-diameter laser beams and a gas flow velocity of 230 cm s^{-1}, the residence time of the sample passing through the laser beams is 0.9 ms. Note that the short duration of the laser pulse does not come into play here; virtually all atoms which reside in the probe volume when the laser fires will undergo ionization if both excitation steps are saturated and the energy deficit to the ionization limit is on the order of 1 eV or less. Using our 30 Hz laser, we were able to obtain a temporal probing efficiency of only 2.6%. Therefore, more than 97% of the atoms passing into the flame were not probed.

We have studied magnesium, thallium, and indium. Figure 5 shows typical ionization signals for a series of sequential injections, each containing 40 pg of Mg in 10 μL of water. The baseline noise in Figure 5 is due to the analog-to-digital converter and is not indicative of the true limiting noise, which was due to the transimpedance amplifier used. All three elements exhibited good linearity over at least 5 orders of magnitude. No memory effects were observed. Table II summarizes the analytical figures of merit for the three elements, along with the excitation transitions used and the energy deficit between the highest excited level pumped by the lasers and the ionization potential. Signal magnitude was quantified as the peak area (C), and the noise (6 fC rms) was taken as the fluctuation in the area resulting from repeated blank vaporizations with a 0.2-s measurement time constant. The limiting noise was actually independent of the furnace vaporization cycle and was due to the transimpedance amplifier. Previous studies have shown this limiting noise to be only about 2× the noise due to native charge carriers in the flame.[24] The limit of detection is taken as the analyte mass corresponding to a signal which is 3 times the background rms noise. Note that the sensitivities for Mg and Tl are similar, ca. 20 C mol^{-1}, while that of In is somewhat lower. We believe this to be due to the inability to saturate the excited-state transition of the second step at 786.4 nm. This excitation step pumps to a high-lying state of the In atom. The oscillator strength of this transition is not known but is not expected to be large, since the probability of absorption of a photon decreases by a factor proportional to n^3, where n is the principal quantum number. For Mg and Tl, both excitation transitions were saturated. The difference between the experimental efficiency of 20 C mol^{-1} and the theoretical maximum of 96 487 C mol^{-1} can be partially accounted for by a small transport loss and the temporal probing efficiency of 0.026. If both of these factors were increased to 100%, the experimental sensitivity would increase to about 4000 C mol^{-1}. The ionization efficiency for Mg in this experimental system was measured during a previous study and was 0.8.[24] The reasons for the discrepancy between the experimental sensitivity and the theoretical maximum are uncertain.

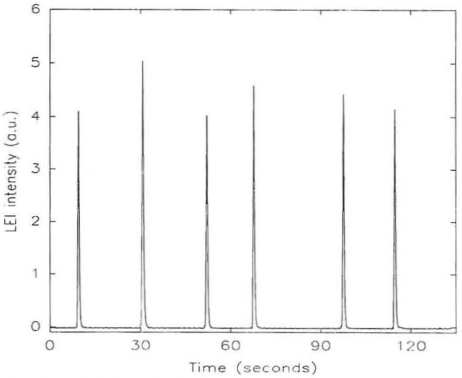

Figure 5. Typical LEI signal peaks obtained for 40-pg injections of Mg into the graphite furnace.

Table II. Analytical Figures of Merit with Corresponding Excitation Schemes for Mg, Tl, and In

element	ΔE (eV)	$\lambda_1 - \lambda_2$ (nm)	sensitivity (pC $pmol^{-1}$)	LOD (fg)
Mg	0.1	285.2 – 435.2	25.3	17
Tl	1	377.6 – 655.6	20.4	118
In	<0.1	303.9 – 786.4	6.8	260

CONCLUSIONS

Laser-enhanced ionization spectroscopy in a miniature acetylene/air flame, following sample vaporization in a conventional graphite furnace atomizer, has been shown to be an extremely sensitive technique with absolute limits of detection in the femtogram region. Sensitivities approaching the theoretical maximum are shown to be possible and may be attainable for many elements, depending on the availability of suitable laser sources and adequate atomization in the small LEI flame. The main experimental deficiency was determined to be the poor temporal probing efficiency resulting from the use of a low repetition rate laser. The probing efficiency, however, could readily be improved by increasing D_B and/or f. In the case of Mg, we were able to improve the limit of detection 10-fold (1 fg) by simply expanding the laser beams (using a cylindrical lens to match the flame geometry) to increase D_B. This however, requires that both lasers remain capable of saturating the transitions after beam expansion, which was possible for our system for Mg but might be less likely for other elements. A more dependable approach would be to increase the repetition frequency of the laser system. For example, ϵ_t will approach 100% by increasing the laser repetition rate to 500 Hz. At this repetition frequency, limits of detection in the femtogram range may be possible even for elements which are poorly atomized in the detection flame.

A final note should be made with respect to the potential use of this technique as an absolute or standardless technique. As noted above, at least for the three model elements chosen for this study, the near-unity probability of ionization from the uppermost laser populated level and unity charge collection leads to an absolute sensitivity which is independent of the element being determined. As such, in certain cases, e.g. when good atomization efficiency in the flame can be assured, the detection method (LEIS) may not need to be calibrated.

ACKNOWLEDGMENT

R.G.B. thanks the Consejo Nacional de Investigaciones Científicas y Técnicas de la República Argentina for the Fellowship which made possible his stay at the University of Florida.

RECEIVED for review August 17, 1992. Accepted October 12, 1992.

Novel Type of Ion-Selective Fluorosensor Based on the Inner Filter Effect: An Optrode for Potassium

Huarui He, Hong Li, Gerhard Mohr, Barna Kovács, Tobias Werner, and Otto S. Wolfbeis*

Analytical Division, Institute of Organic Chemistry, Karl-Franzens University, Heinrich St. 28, A-8010 Graz, Austria

An optrode for potassium ion has been designed that exploits the inner filter effect (IFE) of fluorescence. The sensing scheme makes use of neutral ion carriers as described by Simon et al., but transduction is based on the use of two different dyes, viz. an absorber and a fluorescer. The absorber acts as the proton carrier, while the other is a stable and pH-independent fluorophore bound to minute particles contained in the sensor membrane. Fluorescence varies as a result of the varying absorption of the dye which in turn is modulated by the potassium concentration through the IFE. The sensor material is extremely sensitive to potassium to which it fully reversibly responds over the 1 μM to 10 mM concentration range with a useful dynamic range from 1 μM to 1 mM. The sensing approach presented here is generic in that it can be applied to almost any species for which respective carriers are known. Thus, by replacing valinomycin by carriers for ammonium and calcium ion, respective ion sensors are obtained without requiring any changes in the optical system.

INTRODUCTION

Reliable and sensitive ion sensors are highly needed for various applications including clinical ion sensing. Quite a number of schemes for optically sensing alkali and earth alkali ions have been reported in the past few years.[1-3] While some are based on the use of chromoionophores[4] or crown ethers,[5] the most promising sensing schemes at present appear to rely on the use of neutral ion carriers.[3,6-10] Three different methods based on the use of ion carriers (such as valinomycin) have been reported. One is based on the use of potential-sensitive indicators,[6] the other on the use of proton carrier dyes,[7-9] and the third on a widely unexplored mechanism through the use of lipophilized acridinium dyes whose fluorescence obviously is highly polarity-sensitive.[10]

The recently introduced ion-exchange or coextraction sensing schemes[7-13] have provided a most promising way for sensing a number of ions. Here, the carrier-mediated transport of a cation into a PVC membrane is coupled to the release of a proton from a lipophilic proton carrier contained in the sensing membrane. This deprotonation causes a change in the optical properties of the proton carrier to occur. Most sensors of that kind reported so far are based on absorbance measurements. We prefer, however, to design fluorosensors because of the intrinsic sensitivity of fluorescence, its almost complete inertness to turbidity effects, and its flexibility with respect to geometric arrangements.

We therefore were looking for fluorescent dyes fulfilling the following requirements in order to be useful in carrier-based ion sensors: (a) longwave excitation and emission wavelength to make the sensor LED-compatible, i.e., excitable by the inexpensive light-emitting diodes which, in addition, can be modulated at extremely high frequencies; (b) solubility in plasticized PVC; (c) high lipophilicity in order to keep the dye in the lipophilic PVC membrane; (d) appropriate pK_a values so to cover a wide dynamic range and to achieve low detection limits; (e) high photostability; (f) high fluorescence quantum yield. It turned out, however, that none of the dyes taken into consideration fulfilled all the requirements.

In this report we want to demonstrate that many of the problems resulting from the use of one singe dye (where a number of compromises has to be made) can be overcome by making use of two dyes, the first serving as the proton carrier that can be optimized with respect to absorption wavelengths, pK_a value, lipophilicity, and photostability, the other being an extremely stable and strongly fluorescent dye contained in minute beads and whose excitation or emission bands overlap the absorption band of the protonable absorber dye. The sensor material has a potassium-dependent absorption which results in in a variable excitation efficiency for the fluorophore because of the so-called inner filter effect (IFE). The absorber-modulated intensity of the fluorescence of the particles is the analytical information of this system.

The IFE has been shown to be useful for optical sensing by Walt et al.,[14] although cuvette experiments with dissolved pH indicators and fluorphores were reported only, rather than sensor membranes or materials. Our approach for sensing alkali ions is different in that (a) we make use of synthetic ion carriers and couple the recognition process and ion transport to a protonation/deprotonation step, (b) solid particles are being used which we incorporate into plasticized PVC membranes, and (c) the sensing scheme clearly is based on an IFE and not on energy transfer.

The membrane material can be obtained in a simple fashion in that all components are dissolved (suspended) in tetrahydrofuran and then spread as a membrane, or placed on a waveguide structure. The particles cannot be washed out because they are mechanically incorporated into the PVC membrane. We think this method has almost all the advantages of fluorescence-based sensors. It is broadly

---

[1] Edmonds, T. E. *Chemical Sensors*; Blackie: Glasgow and London, 1987.

[2] Seitz, R. W. *CRC Crit. Rev. Anal. Chem.* **1987**, *19*, 135–194.

[3] Wolfbeis, O. S., Ed. *Fiber Optic Chemical Sensors and Biosensors*; CRC Press: Boca Raton, FL, 1991; Vols. 1 and 2.

[4] Alder, J. F.; Sworth, D. C.; Narayanaswamy, N.; Moss, R. E.; Sutherland, I. O. *Analyst* **1987**, *112*, 1191–1196.

[5] Wolfbeis, O. S.; Offenbacher, H. *Monatsh. Chem.* **1984**, *115*, 647–654.

[6] Wolfbeis, O. S.; Schaffar, B. P. H. *Anal. Chim. Acta* **1987**, *198*, 1–7.

[7] Morf, W. E.; Seiler, K.; Lehmann, B.; Behringer, C.; Hartmann, C.; Simon, W. *Pure Appl. Chem.* **1989**, *61*, 1613–1620.

[8] Ozawa, S.; Hauser, P. C.; Seiler, K.; Tan, S. S. S.; Morf, W. E.; Simon, W. *Anal. Chem.* **1991**, *63*, 640–645.

[9] Suzuki, K.; Ohzara, H.; Tohda, K.; Miyazaki, K.; Watanabe, K.; Inoue, H.; Shirai, T. *Anal. Chim. Acta* **1990**, *237*, 155–162.

[10] Kawabata, Y.; Tahara, R.; Kamichika, T.; Imasaka, T.; Ishibashi, N. *Anal. Chem.* **1990**, *62*, 1528–1531.

[11] Tan, S. S. S.; Hauser, P. C.; Wang, K.; Fluri, K.; Seiler, K.; Rusterholz, B.; Suter, G.; Krüttli, M.; Spichiger, U.; Simon, W. *Anal. Chim. Acta* **1991**, *255*, 35–41.

[12] Périsset, P. M. J.; Hauser, P. C.; Tan, S. S. S.; Seiler, K.; Morf, W. E.; Simon, W. *Chimia* **1989**, *43*, 10–13.

[13] He, H.; Uray, G.; Wolfbeis, O. S. *Fresenius J. Anal. Chem.* **1992**, *343*, 313–318.

[14] Gabor, G.; Walt, D. R. *Anal. Chem.* **1991**, *63*, 793–797.

0003-2700/93/0365-0123$04.00/0

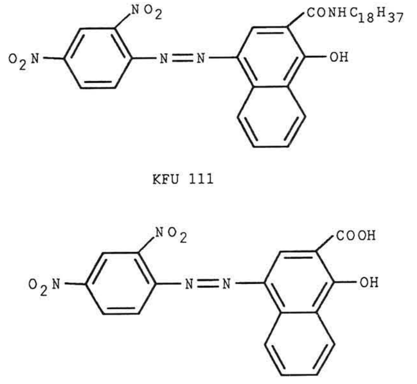

Figure 1. Chemical structures of the lipophilized proton-carrying dye used in this work (KFU 111) and its precursor dye (KFU 110).

applicable because it is a generic approach which can be adapted to almost any ion for which a carrier is known.

EXPERIMENTAL SECTION

Reagents. Poly(vinyl chloride) (PVC, high molecular grade), valinomycin, potassium tetrakis(4-chlorophenyl)borate (PTCB), 2-nitrophenyloctyl ether (NPOE), and tetrahydrofuran (THF) were obtained from Fluka AG (Buchs, Switzerland). The fluorophore particles (FluoSphere) were purchased from Molecular Probes Inc. (Eugene, OR). The excitation/emission maxima of the particles are at 580/605 nm, respectively. The high-purity potassium chloride was obtained from Merck (Darmstadt, FRG). All buffers components (citric acid, Tris, HCl) were from Merck. Aqueous buffers were 0.05 M in each citric acids and Tris, and the pH was adjusted with 1 M NaOH or HCl to the appropriate value.

Synthesis of Lipophilic pH Indicators. The pH-sensitive absorber dye, viz. 4-((2′,4′-dinitrophenyl)azo)-2-((octadecylamino)carbonyl)-1-naphthol (KFU 111) was prepared by the following procedure:

(*a*) *4-((2-Dinitrophenyl)azo)-1-hydroxynaphthalene-2-carboxylic Acid (KFU 110). Solution A.* Concentrated sulfuric acid (16 g) was stirred and cooled to below 5 °C in an ice bath. Then, 1.4 g (20 mmol) of finely ground sodium nitrite was added slowly. The temperature of the mixture was kept at below 5 °C until the addition of nitrite was complete. Thereafter, the temperature was slowly raised to 70 °C and the the mixture became clear. After cooling to 20 °C, 3.7 g (20 mmol) of finely ground 2,4-dinitroaniline was added slowly, and the mixture stirred for 10 min and finally poured onto 48 g of ice.

Solution B. 1-Hydroxynaphthalene-2-carboxylic acid (3.7 g, 20 mmol) was dissolved in 200 mL of water containing 30 g of sodium carbonate. The residue was filtered, and the filtrate was cooled to 0 °C.

Solution A was dropped into solution B within about 30 min with strong stirring. The resulting precipitate was filtered, washed three times with 500 mL of 1 M sulfuric acid, and dried at 50 °C for 24 h to yield 6.5 g (84%) of crude yellow dye whose structure is given in Figure 1. Anal. Calcd: C, 53.41; H, 2.64; N, 14.66. Found: C, 53.04; H, 2.74; N, 13.38. The absorption maxima are at 485 nm at water of pH 4.00, and at 615 nm at an aqueous solution of pH 10.00. The pK_a, as calculated from the titration curve, was found to be 8.98 ± 0.06 at 21 °C and an ionic strength of 100 mM sodium chloride.

(*b*) *4-((2′,4′-Dinitrophenyl)azo)-2-((octadecylamino)carbonyl)-1-naphthol (KFU 111).* Crude KFU 110 (0.38 g) and 0.28 g of octadecylamine were dissolved in 200 mL of THF containing 0.22 g of *N,N′*-dicyclohexylcarbodiimide, and the mixture was stirred at room temperature for 4 h. The suspension was filtered in order to remove the white precipitate (*N,N′*-dicyclohexylurea). The solvent was evaporated and the yellow residue redissolved in 150 mL of dichloromethane. This solution was washed with 5% aqueous sodium carbonate solution until the organic phase became colorless. The solvent was evaporated and the residue purified by flash chromatography (ethyl acetate/petroleum ether, 1:4, v/v) to yield 100 mg (15%) of the dye. The chemical structures of KFU 110 and KFU 111 are shown in Figure 1. Anal. Calcd: C, 66.33; H, 7.47; N, 11.05. Found: C, 65.91; H, 7.56; N, 11.21.

The absorption maximum of the base form of KFU 111 in chloroform (to which a drop of triethylamine was added in order to create the blue anion) is at 640 nm, the molar absorption coefficient is 97 000 M^{-1} cm^{-1}. The following NMR and IR data confirm the structure: ^1H NMR ($CDCl_3$, 200 MHz) δ 0.90 (t, CH_3), 1.25 (m, 32 H), 3.45 (m, NCH_2), 7.25 (br s, HNCO), 7.75 (m, 2 H, phenyl), 8.25 (2 H), 8.45 (2 H), 8.55 (1 H, m, naphthyl), 8.90 (hydrogen bonded OH), and 9.15 (1 H, dinitrophenyl) ppm; IR (KBr) ν 3300 (NH, OH), 2900 (CH_2CH_2), 1670 (C=)), 1630 (N=N), 1510, 1590 (C=C), 1310, 1330, 1360 (CH), 780, 840, and 920 (Ar-H) cm^{-1}.

Instruments. Optical measurements were performed using an Aminco SPF 500 spectrofluorometer equipped with a tungsten halogen lamp as a light source. Data were transferred onto a HP 9825A desk calculator and plotted. Sample solutions were pumped through the flow-through cell containing the sensing membrane, using a Ventilomat autosampler (Fa. Ziegler, Graz, Austria). Absorption measurements were performed with a Perkin-Elmer Lambda 5 spectrophotometer. pH measurements for both the buffer preparations, and pK_a determinations were performed at 21 °C with a Metrohm pH meter (Metrohm, Buchs, Switzerland) calibrated with Aldrich pH standards of pH 4.00, 7.00, and 10.00, respectively.

Membrane Preparation. The membranes were prepared from a batch of 2.4 mg of PVC, 0.4 mg of PTCB, 1.8 mg of valinomycin, 30 mg of the aqueous suspension of the FluoSphere particles, 0.4 mg of KFU 111, and 6.0 mg of NPOE, all of which were dissolved in 1.5 mL of freshly distilled tetrahydrofuran. One hundred microliters of the turbid solution was pipetted onto a 12 × 50-mm dust-free glass plate which then was placed in a THF-saturated atmosphere in an exsiccator. After about 15 min the glass plate with the sensing membrane on it was removed and placed in ambient air for 15 min for complete drying. Before measurements, the membrane was placed in a 0.1 M potassium chloride solution for activation. From the amount of materials employed we estimate the thickness of the membranes to be between 2 and 3 μm.

Experimental Procedure. The glass plate with the PVC membrane was mounted in a flow-through cell. The measuring system was arranged according to ref 6. Standard solutions, prepared from double-distilled water, were pumped over the sensing membranes, and the fluorescence intensity was observed at excitation/emission wavelengths of 550/605 nm. The photostability of fluorophore and absorber were tested by illuminating the dry sensing membrane with the 250-W tungsten halogen lamp at 550 nm and a bandpass of 8 nm. Leaching effects were tested by passing a continuous flow of a pH 5.22 buffer over the membrane at a rate of 1.5 mL·min^{-1}.

RESULTS

Selection of Absorber and Fluorophore. The approach presented here requires the presence of two dyes, one acting as the analyte-sensitive primary absorber, the other as the analyte-independent fluorophore whose excitation or emission intensity is modulated by the varying absorption of the primary absorber. This requires the absorption band of the absorber to overlap with the excitation or fluoroscence emission band of the fluorophore. The primary absorber is homogeneously distributed in the sensor material, while the fluorophore is presented in the form of small particles which cannot be washed out of the PVC membrane. Both KFU 110 and KFU 111 nicely match the absorption (excitation) band of the FluoSphere particles, thus giving rise to a significant IFE in the presence of potassium ion. KFU 111 is the preferred dye because the octadecyl side chain provides both high solubility in PVC and insolubility in water.

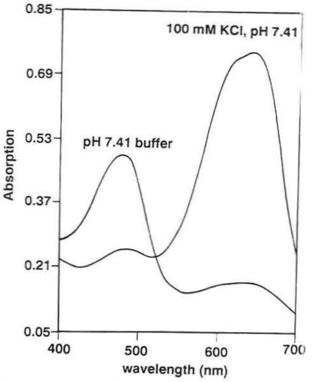

Figure 2. Absorption spectra of KFU 111 in a plasticized PVC membrane containing PTCB and valinomycin, in contact with a 100 mM aqueous solution of KCl of pH 7.41, and with plain potassium-free buffer of pH 7.41.

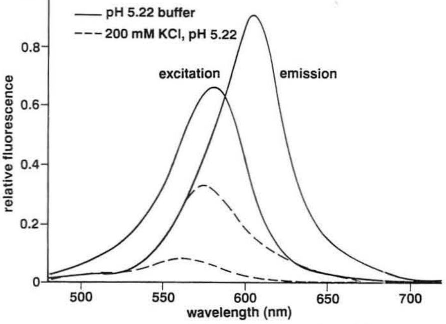

Figure 3. Excitation and emission spectra of FluoSphere particles contained in a plasticized PVC membrane containing PTCB, valinomycin, and KFU 111 contacted with a 200 mM KCl solution of pH 5.22 (- - -) and with plain buffer of pH 5.22 (—), demonstrating the dramatic inner filter caused by the blue form of the absorber dye.

The Sensing Scheme. Neutral ion carriers such as valinomycin are known to specifically recognize and bind alkali ions and to transport them into the plasticized PVC membrane. In case of ion-selective electrodes, a potential is created which is measured by potentiometry.[15] In case of optrodes, several options exist: One is to measure the potential by optical means,[6] the other is to couple the ion transport into the membrane to a proton transport out of the membrane.[7] This is the mechanism of this sensing scheme: Upon potassium transport into the plasticized PVC membrane, a proton is released by the dye (the primary absorber in the membrane) into the sample solution, thereby undergoing a measurable change in its optical properties. Figure 2 shows the absorption spectra of a membrane containing 111, but no fluorescent particles. The maxima of the alkaline form (which is present in the membrane when it is contacted with a 100 mM solution of potassium ion) and the acidic form (present when contacted with plain, potassium-free buffer) are at 640 and 480 nm, respectively. The alkaline form has a strong shoulder at 605 nm.

In Figure 3, the fluorescence spectra of the same membrane after addition of fluorophore particles are given. Due to spectra distortion caused by the IFE, the maxima of excitation and emission are at 580 and 605 nm now. The emission band obviously matches the absorption of KFU 111. When this membrane is contacted with 200 mM potassium solution, the pH-sensitive dye becomes fully deprotonated, resulting in an increase in the 640-nm band which absorbs the emission of the fluorophore. As a result, the fluorescence intensity at 605 nm is decreased. In the presence of 200 mM potassium, the excitation and emission bands are even more distorted.

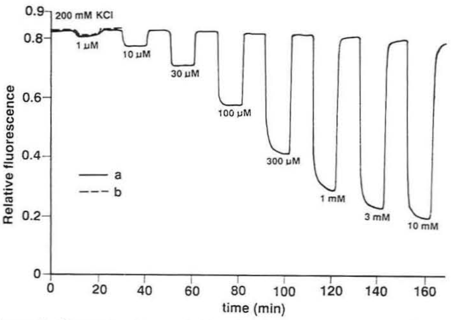

Figure 4. Response time, relative signal change, and reversibility of the potassium sensor (a) in the presence (—) and (b) absence (- - -) of dye KFU 111 in the membrane; pH 5.82, excitation/emission wavelengths set to 560/605 nm. The small signal change that can be seen in the dotted line was obtained after exposure of the sensor to 200 mM potassium and is comparable in intensity with the signal obtained with 1 µM (!) potassium when the absorber dye KFU 111 is added.

Dynamic Response of the Sensor Membrane. Figure 4 shows the dynamic response of such a sensing membrane when exposed to various levels of potassium ion. The signal is fully reversible, with response times (of a 2-µm membrane) in the order of 6 min for the full signal change to occur in the forward direction, but only 2 min for the reverse response. The response time increases proportionally with the square of the thickness of the sensing layer. The sensor reponds to potassium over the 1 µM to about 10 mM concentration range, with a detection limit (defined as 3 times the background) of around 1 µM potassium. Detection limits are virtually unaffected by the thickness of the sensing layer. Even with membranes as thin as 1 µm, a signal-to-noise ratio of >500 was obtained with these sensor membranes. The dotted line in Figure 4 shows the response of the membrane *without* a pH-sensitive absorber dye being added. The membrane has little response even to 200 mM potassium. The weak signal observed may be due to the fact that the fluorophore is a weak potential sensitive dye.

Figure 5 shows the pH dependence of the response curves in the presence and absence of fluorophore. Obviously, the dynamic range is shifted to the lower potassium concentration range in the presence of the fluorophore. Furthermore, the linear range of curve b (ranging from 10 µM to 3 mM) occurs at a much lower concentration range than that of curve c (100 µM to 100 mM).

Sensor Stability. The shelf lifetimes of the sensor membrane exceeds 3 months when stored in the dark at 4 °C. The limiting factors determining the stability of the mebrane include (a) the photostability of the primary absorber (which is moderate), (b) the photostability of the fluorescent particles (which is excellent), and (c) the leaching of valinomycin, borate, and plasticizer from the membrane when under operation (or in contact with aqueous standards). The sum of effects result in a sensor drift of −4% over a period of 2.5 h when sensing aqueous samples. Photobleaching of KFU 111 seems to be responsible for most of the drift.

---

(15) Morf, W. E. *The Principles of Ion-selective Electrodes and of Membrane Transport*; Elsevier: Amsterdam, 1981.

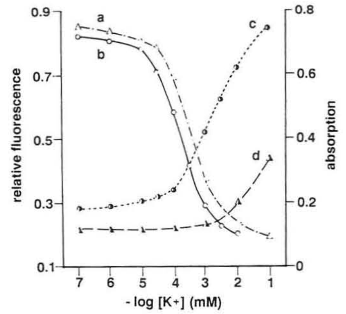

Figure 5. pH dependence of the calibration curve of the potassium-sensitive membrane, excitation/emission wavelengths set to 560/605 nm, absorption measured at 640 nm: (a) fluorescence measurements at pH 5.22; (b) fluorescence measurements at pH 5.82; (c) absorption measurements at pH 7.41; and (d) absorption measurements at pH 5.22.

DISCUSSION

The Sensing Scheme. The results demonstrate the feasibility of sensing alkali ions via the inner filter effect of fluorescence (IFE) by making use of fluorescently dyed particles added to the sensor material. The scheme offers an attractive alternative to absorptiometric, reflectometric, or fluorimetric techniques using one single dye. By making use of two dyes (can primary absorber and a fluorescer), a more versatile system is obtained which can be optimized in terms of the properties of both the absorber and fluorescer. An absorber dye needs to be adjusted to the proper pK_a value (in order to make it an ideal proton carrier) and made highly lipophilic so to remain in the PVC phase. The fluorophor is expected to display a high quantum yield and to match the absorption band of one of the two forms of the primary absorber. Unlike for the absorber dye, there is no need for the fluorophore to be homogeneously distributed in the sensor material. We use a commercially available material with a quantum yield close to unity.

The only additional requirement for this approach over the one where a single dye acts as both a proton carrier and a fluorphor is an overlap of the absorption of the primary absorber with the excitation or emission band of the fluorophor. This is rather easy to accomplish; the dye and the FluoSphere particles used here are a nicely matched pair of dyes. In addition, both are LED-compatible.

Sensor Features. There are a number of promising aspects of this type of sensor: (1) It allows every absorption-based sensor to be made a fluorescent sensor, even if no appropriate fluorescent primary absorber can be found.

(2) The tremendous wealth and variety of neutral ion carriers which have been optimized for electrochemical sensing purposes in the past 20 years—mainly due to the pioneering work of Simon and co-workers[7,8,11,12,15,17]—can be exploited for optical sensing purposes as well. Hence, by simply replacing the potassium carrier by another one, the sensor can be made responsive to any other analyte for which an ion carrier is known. In instrumentation design this has the tremendous advantage of an identical optoelectronic system for all kinds of sensors.

(3) The linear range of the reponse curve is distinctly shifted to the lower concentrations range; this is important in practice where blood samples will be diluted with buffer in order to adjust a constant pH and to reduce the lipophilicity of the blood sample (which tends to extract carriers and plasticizers); hence, this sensor material is ideally suited for determination of potassium in diluted serum. Serum dilution also is known to considerably prolong the operational lifetime of sensor membranes.

Table I. Comparison of Dynamic Ranges (DR), Limits of Detection (LD), and Response Times (RT), of the Membrane Components of This Work with That of Previous Methods

method (ref)	DR (mM)	LD (mM)	RT (min)
this method	0.001–10	0.001	5.0
Wolfbeis (6)	0.01–100	0.007	4.0
Suzuki (9)	0.1–100	0.01	1.5
Kawabata (10)	0.01–100	0.01	0.5
Simon (12)	0.1–100	–[a]	–[a]
Verkman (18)	0.0005–10	0.0005	0.1–1.6

[a] Not specified.

(4) The work described here also overcomes a fundamental limitation of the previous approach of Simon et al., viz., an insufficient sensitivity at near-neutral pH, although there are exceptions.[17]

Comparisons with Other Methods. Dynamic ranges, limits of detection, and response times of the membranes used in this method have been compared with those of other methods (Table I). The data show the method presented here to have a much smaller limit of detection, typically 1 μM. It probably can be even improved by increasing the dye-to-fluorophore ratio. This way we have overcome a major problem of the Simon type optrodes based on the ion exchange mechanism whose limits of detection sometimes can be in the order of 10–50 μM. The response times are longer, probably due to the heterogeneity of the sensing membrane. The fluorophore beads are not homogeneously dispersed, so diffusion is slow and not free into all directions.

The improvement in the limit of detection caused by the inner filter effect has been reported first by Walt and co-workers.[14] In this case, however, pH modulates both dyes employed: While the absorbance of the one species (the absorber) goes into one direction, that of the fluorophore goes into the other. We attribute the enhanced sensitivity of our system—where only *one* dye is analyte-sensitive—to the relative excess of primary absorber over the fluorophore. As a result, even small changes in the fraction of the acid-to-base form of the dye cause a substantial change in the optical density of the membrane and in its permeability for fluorescent light. One may consider the fluorescent particles as a light source inside the membrane and the dye (KFU 111) as the modulator that acts as the screen for fluorescence.

Fluorescence energy transfer has been exploited in another type of potassium ion sensor[18] also based on the use of valinomycin. The sensing material consists of a hydrophobic pH indicator and another fluorophore, both contained in a plasticized PVC membrane along with valinomycin. Both fluorescence intensity and fluorescence lifetime (1.16 ns) decrease with increasing potassium ion concentration, indicating that in this case resonance energy transfer is the dominant mechanism for the interaction in the membrane. In the kind of sensor reported here, resonance energy transfer certainly is of little significance (if of any at all) because of the insufficient closeness of donor and acceptor molecules which is required in order to enable energy transfer.

---

(16) He, H.; Wolfbeis, O. S. *Proc. Soc. Photoinstrum. Engs. (SPIE)* **1990**, *1368*, 165–174.

(17) Seiler, K.; Simon, W. *Anal. Chim. Acta* **1992**, *266*, 73–87 and references cited therein.

(18) Roe, J. N.; Szoka, F. C.; Verkman, A. S. *Analyst* **1990**, *115*, 353–358.

In contrast to electrochemical methods and the measurement of potassium via the optical measurement of membrane potential, the method of coextraction suffers from the disadvantage of being highly pH-dependent. This is a serious limitation when these sensors are to be used with samples of varying pH. Rather than measuring in whole blood, a more likely application of such sensors will therefore be in mainframe instrumentation where the pH can be kept constant.

ACKNOWLEDGMENT

This work supported by the Austrian Science Foundation (FWF) within project S5702-PHY which is gratefully acknowledged.

RECEIVED for review August 21, 1992. Accepted October 26, 1992.

Uncoupling the Effects of Convection and Diffusion on Refractive Index Gradient Detection in High-Temperature Liquid Chromatography

Lawrence R. Lima, III, and Robert E. Synovec*

Department of Chemistry BG-10, University of Washington, Seattle, Washington 98195

A model based on Poiseuille flow is expanded upon to describe the coupled effects of diffusion and convection on the sensitivity of the radial refractive index gradient (RIG) measurement with the Z-configuration flow cell for high-performance liquid chromatography (HPLC) detection. Diffusion and convection are shown to affect the radial concentration profile probed by RIG measurements. These effects were characterized by first examining the response for a polymer series with a diffusion coefficient range of 10^{-5} to 10^{-7} cm^2/s at room temperature for a range of flow rates to determine the relative contribution of convection and diffusion as a function of analyte residence time within the flow cell. Experimentally, it was determined that the flow cell dependent convection contribution to the change in the radial concentration gradient was 43.34 ± 4.26 μm. Diffusion is shown to appreciably affect RIG sensitivity when the translational migration of an analyte within the flow cell, as predicted by the Stokes–Einstein equation, is greater than 20 μm. Diffusion and convection effects were then examined at a single, well-characterized flow rate over a range of temperatures from 25 to 125 °C. Sensitivity for analytes in the convection-dominated response region remained constant, while those in the diffusion-sensitive response area demonstrated a temperature dependence. The presence of diffusion- and convection-dominated sensitivity response regions and the existence of a smooth transition between the two regions suggested that the effects of diffusion and convection were coupled but could be readily uncoupled. Since translational diffusion increases with temperature, this temperature dependence is consistent with the proposed model. Lastly, the effect of temperature on relative baseline position and noise was examined. The flow rate dependent slope of the deflected angle for RIG baseline measurements was shown to have a temperature dependence, as the formation of a thermal lens within the flow cell caused a constant deflection of the probe beam. Baseline noise levels increased less than a factor of 3 over the 100-deg temperature range examined, thus the RIG detector is compatible with high-temperature and thermal gradient microbore HPLC.

INTRODUCTION

The development of a sensitive universal detector for use with high-temperature and thermal gradient applications of high-performance liquid chromatography is an on going process.[1-13] Refractive index based detectors show promise in this regard but are traditionally plagued by baseline drift and increases in baseline noise level which accompany changes in mobile-phase temperature. We present further examination of a refractive index based detector which is amenable to thermal gradient applications in liquid chromatography,[2-8,11-13] along with the characterization of detector performance as a function of changing temperature. In order to fully understand detector performance the factors which affect the probed analyte concentration profile, and therefore detector sensitivity, must be understood. Specifically, the effects of hydrodynamic convection and analyte diffusion must be characterized. We present a characterization, in the form of a model, which describes the dependence of analyte detection sensitivity upon the affects which convection and analyte diffusion have upon an analyte concentration profile.

The influence of laminar flow on an analyte concentration profile has been shown to create a bolus-shaped concentration distribution. Dispersion in a cylindrical tube of this distribution by axial (along the flow) and radial (orthogonal to the flow) diffusion mechanisms is described by the fundamental work of Taylor.[14] Similarly, Golay and Atwood described the dispersion caused by convection on this information-abundant concentration distribution.[15,16]

The axial and radial concentration gradients, which result from the effects of convection and diffusion, have been the primary focus of flow injection analysis (FIA) and high-performance liquid chromatography (HPLC) in recent years.[17-23] Refractive index gradient detection, pioneered by Pawliszyn,[9,10] has been shown to be a sensitive method for analytical measurements. Recently, the use of concentration gradient based detectors has become popular since good detection limits and gradient elution are compatible with this universal detector. Furthermore, the seldom measured radial concentration gradient was observed by McGuffin and co-workers in their examination of the Z-configuration flow cell to form a dynamic lens.[1] Synovec, Hancock, and Renn developed a detector which utilizes a collimated laser probe beam, a Z-configuration flow cell, and a position-sensitive

---

(1) Evans, C. E.; Shabushnig, J. G.; McGuffin, V. L. *J. Chromatogr.* 1988, *459*, 119–138.
(2) Renn, C. N.; Synovec, R. E. *Anal. Chem.* 1990, *62*, 558–564.
(3) Renn, C. N.; Synovec, R. E. *Anal. Chem.* 1988, *60*, 1188–1193.
(4) Renn, C. N.; Synovec, R. E. *Appl. Spectrosc.* 1989, *43*, 1393–1398.
(5) Hancock, D. O.; Synovec, R. E. *Anal. Chem.* 1988, *60*, 1915–1920.
(6) Hancock, D. O.; Synovec, R. E. *Anal. Chem.* 1988, *60*, 2812–2818.
(7) Hancock, D. O.; Synovec, R. E. *J. Chromatogr.* 1989, *464*, 83–91.
(8) Hancock, D. O.; Renn, C. N.; Synovec, R. E. *Anal. Chem.* 1990, *62*, 2441–2447.
(9) Pawliszyn, J. *Anal. Chem.* 1986, *58*, 243–246.
(10) Pawliszyn, J. *Anal. Chem.* 1986, *58*, 3207–3215.
(11) Renn, C. N.; Synovec, R. E. *Anal. Chem.* 1991, *63*, 568–574.
(12) Renn, C. N.; Synovec, R. E. *J. Chromatogr.* 1991, *536*, 289–301.
(13) Renn, C. N.; Synovec, R. E. *Proc. SPIE—Int. Soc. Opt. Eng.* 1991, *1435*, 128–139.
(14) Taylor, G. *Proc. R. Soc. London* 1953, *A219*, 186–203.
(15) Golay, M. J. E.; Atwood, J. G. *J. Chromatogr.* 1979, *186*, 353–370.
(16) Atwood, J. G.; Golay, M. J. E. *J. Chromatogr.* 1981, *218*, 97–122.
(17) Ruzicka, J.; Hansen, E. H. *Anal. Chim. Acta* 1986, *179*, 71–89.
(18) Vanderslice, J. T.; Stewart, K. K.; Rosenfeld, A. G.; Higgs, D. J. *Talanta* 1981, *28*, 11–18.
(19) Vanderslice, J. T.; Rosenfeld, A. G.; Beecher, G. R. *Anal. Chim. Acta* 1986, *179*, 119–129.
(20) Tjissen, R. *Anal. Chim. Acta* 1980, *114*, 71–89.
(21) Deelder, R. S.; Kroll, M. G. F.; Beeren, A. J. B.; Van Den Berg, J. H. M. *J. Chromatogr.* 1978, *149*, 669–682.
(22) Katz, E. D.; Scott, R. P. W. *J. Chromatogr.* 1983, *270*, 29–50.
(23) Grushka, E.; Kitka, E. J. *J. Am. Chem. Soc.* 1976, *98*, 643–648.

0003-2700/93/0365-0128$04.00/0

detector (PSD) to examine this radial concentration gradient for detection of analytes in HPLC.[2-7] This detector has demonstrated an effective refractive index detection of 4 × 10^{-9} RI units by 3× root mean square determination[6] and has been reported as being 2–3 orders of magnitude more sensitive than detectors which probe the axial concentration gradient.[8] The optimal probe beam position for maximum optical sensitivity for refractive index gradient (RIG) measurements and a simple model which relates RIG sensitivity to the volumetric flow rate and to the translational diffusion coefficient of the observed analyte were also reported.[8] In conjugation with FIA, the radial measurement of the concentration gradient is a promising technique for rapid molecular weight determinations.[6,24-26] Previous reports have demonstrated that a temporal shift in the radial concentration profile is observed as a function of radial probe beam position. This experimental observation supports the existence of a Poiseuille flow profile and the presence of hydrodynamic convection within the flow cell.[26]

We expand upon this model to demonstrate the effects of convection and analyte translational diffusion on RIG measurement sensitivity as a function of flow rate and temperature at low Reynolds number, $Re < 10$, using the Z-configuration flow cell. An objective of this work is to more fully characterize the behavior of RIG detection as a function of flow rate and temperature. Another goal is to demonstrate the applicability of the RIG detector as a sensitive, universal detector for use with high-temperature liquid chromatography (HTLC) and thermal gradient liquid chromatography (TGLC). It is shown that the detection sensitivity of a particular analyte depends on the extent to which it migrates radially while within the flow cell. This dependence will be examined as a function of flow rate and temperature to develop a characterization of baseline and noise behavior as well as test the fitness of the proposed model.

In addition, this proposed model of RIG detector behavior is shown to be fully consistent with the work presented in our previous reports.[2-8,11-13] Examination of a series of polystyrenes showed that sensitivity remained constant for these high molecular weight species for the full range of flow rates tested and for the flow cell used.[5] It is now understood that these analytes, with relatively small diffusion coefficients, should exhibit constant sensitivity because the extent to which they diffuse within the flow cell is not significant enough to appreciably alter the probed radial concentration gradient profile. A characteristic diffusional distance is presented for our flow cell which describes when diffusion begins to cause observable changes in the probed radial concentration profile in relation to the empirically determined constant effect of hydrodynamic convection which determines the optimum RIG peak-to-peak signal for a given flow cell. The coupled nature of diffusion and convection is demonstrated and discussed in relation to the analogous model developed by Giddings for the relation of theoretical plate height to diffusion and flow in packed columns.[27] However, this is the first report in which the effects of diffusion and convection are experimentally uncoupled and individually determined. Examination of the changes in the radial concentration gradient within the well-defined space of the flow cell has allowed for the experimental decoupling of diffusion and convection.

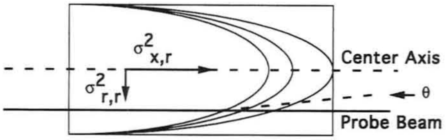

Figure 1. Illustration of the direction of the effects of the radial dispersion-induced length $\sigma_{x,r}^2$ (eq 1) and radial $\sigma_{r,r}^2$, (eq 3) variances upon an analyte concentration profile. Θ, defined by eq 11, showing typical analyte-induced beam deflection (exaggerated).

THEORY

In typical liquid-phase experiments slow radial mass transport, analogous to the C term in the van Deemter equation, dominates the dispersion of the axial concentration profile.[14] The radial dispersion-induced length variance, $\sigma_{x,r}{}^2$, as determined from the description of the Poiseuille flow-determined radial concentration profile for a long tube and in the case of slow mass transport dominated dispersion is given by[14,28]

$$\sigma_{x,r}{}^2 = R^2Lu/24D_m \qquad (1)$$

where R is the flow cell radius, L is the length of the flow tube, u is the average linear flow velocity, and D_m is the translational diffusion coefficient of the analyte. This dominance by the radial dispersion-induced length variance establishes a radial concentration gradient, $dC(r)/dr$, orthogonal to the probe beam, given by

$$\frac{dC(r)}{dr} = \frac{u}{2D_m}\left(r - \frac{r^3}{R^2}\right)\frac{dC(0)}{dx} \qquad (2)$$

where r is the radial distance as measured from the center of the flow cell, $C(0)$ is the analyte concentration at the center of the flow cell, and $dC(0)/dx$ is the axial concentration gradient along the flow cell center in the direction of the flow. Experimentally, r is the average radial position of the collimated laser probe beam and it has been demonstrated that the optimum radial probe position is at $R/\sqrt{3}$. Figure 1 illustrates the direction of the effects described by eqs 1 and 2 on an analyte plug in Poiseuille flow. Note that in terms of the flow cell, $\sigma_{x,r}{}^2$ is a measure of the additional axial band broadening experienced by the analyte while the coefficient $u/2D_m$ is a measure of the magnitude of the change in the concentration gradient caused by diffusion. This diffusion effect is defined as a radial dispersion-induced radial variance, $\sigma_{r,r}{}^2$, given by

$$\sigma_{r,r}{}^2 = D_mL/u \qquad (3)$$

where L is now the length of the flow cell. Because the probe beam observes the entire flow cell length at any one instant, $\sigma_{r,r}{}^2$ is calculated using half of the analyte residence time within the flow cell, i.e., half the flow cell length.

Convection also affects the radial concentration profile. Golay and Atwood have shown that the convection-induced axial variance is $L^2/3$.[15,16] Similarly, a convection-induced radial variance $\sigma_{conv,r}{}^2$ has been described,[26] but not explicitly derived, as a function of both flow cell length and radius. The magnitude of this effect can be determined empirically and, in terms of a physical description, takes the form

$$\sigma_{conv,r}{}^2 = kR^4/L^2 \qquad (4)$$

where k is a constant that must be determined experimentally. This convection-induced radial variance will effect a change in the radial concentration profile. However, this convection-

---

(24) Murugaiah, V.; Synovec, R. E. *Anal. Chim. Acta* **1991**, *246*, 241–249.

(25) Murugaiah, V.; Synovec, R. E. *SOQUE Lasers '90 Conference Proceedings: Lasers in Chemistry* **1991**, *13*, 763.

(26) Murugaiah, V.; Synovec, R. E. *Anal. Chem.*, in press.

(27) Giddings, J. C. *Unified Separation Science*; Wiley-Intersicence: New York, 1991; Chapter 11, pp 259–266.

(28) Hupe, K. P.; Jonker, R. J.; Rozing, G. *J. Chromatogr.* **1984**, *285*, 253–265.

induced radial variance, unlike the diffusion-induced radial variance, is flow rate independent and therefore has a constant effect on $\mathrm{d}C(r)/\mathrm{d}r$. Note that $\sigma_{r,r}{}^2$, $\sigma_{\mathrm{conv},r}{}^2$, and their effects on $\mathrm{d}C(r)/\mathrm{d}r$ are orthogonal to the flow and the probe beam.

If it can be assumed that $\mathrm{d}C(r)/\mathrm{d}r$ is constant at any given instant within the flow cell, or more precisely, an average $\mathrm{d}C(r)/\mathrm{d}r$ exists, then Synovec, Hancock, and Renn have shown that[8]

$$\Theta = \pm 0.0146 \left(\frac{V_\mathrm{i} C_\mathrm{i} L}{R n_\mathrm{o}}\right)\left(\frac{1}{\sigma_\mathrm{x}{}^2}\right)\left(\frac{F}{D_\mathrm{m}}\right)\left(\frac{\mathrm{d}n}{\mathrm{d}C}\right) \tag{5}$$

where Θ is the angular deflection of the probe beam, V_i is the injected volume, C_i is the injected volume fraction of analyte, F is the volumetric flow rate, and $\sigma_\mathrm{x}{}^2$ is the sum of all chromatographic and extracolumn broadening. For HPLC, $\sigma_\mathrm{x}{}^2$ is given by

$$\sigma_\mathrm{x}{}^2 = (\sigma_\mathrm{LC}/\pi R^2)^2 + \sigma_{\mathrm{x,r}}{}^2 \tag{6}$$

where σ_LC is the volume standard deviation of the peak prior to the flow cell. Note that $\sigma_{\mathrm{x,r}}{}^2$ describes the increase in band broadening due to the flow cell (eq 1). Given a worst case scenario for the experiments performed in this investigation, a peak for poly(ethylene glycol) (PEG) 12 600, where 12 600 is the weight average molecular weight of the polymer, with a width at the base of 280 μL, σ_LC is 70 μL, and given $R = 390$ μm, $L = 6$ mm, and $u = 4.48$ mm/s in the flow cell (corresponding to a volumetric flow rate of 130 μL/min for this system) then $\sigma_\mathrm{x}{}^2$ is 214.6 cm² without $\sigma_{\mathrm{x,r}}{}^2$ and 240.3 cm² including the flow cell contribution. Thus, under these conditions, only 6% additional band broadening is introduced, so, as an approximation

$$\sigma_\mathrm{x}{}^2 = (\sigma_\mathrm{LC}/\pi R^2)^2 \tag{7}$$

If one then modifies eq 5 using the definitions of $\sigma_{\mathrm{x,r}}{}^2$ (eq 1) and $\sigma_{\mathrm{conv,r}}{}^2$ (eq 4) to account for the effects of diffusion and convection, the observed RIG signal is described by

$$\Theta \propto \pm 0.0146 \left(\frac{V_\mathrm{i} C_\mathrm{i} L}{R n_\mathrm{o}}\right)\left(\frac{1}{\sigma_\mathrm{x}{}^2}\right)\left(\frac{1}{\sigma_{\mathrm{r,r}}{}^2 + \sigma_{\mathrm{conv,r}}{}^2}\right)\left(\frac{\mathrm{d}n}{\mathrm{d}C}\right) \tag{8}$$

By this, it is asserted that for cases in which diffusion dominates over convection, and therefore causes an appreciable change in $\mathrm{d}C(r)/\mathrm{d}r$ from the optimum convection-dominated conditions, the observed signal described by eqs 7 and 8 becomes

$$\Theta = \pm 0.144 \left(\frac{V_\mathrm{i} C_\mathrm{i} L R^3}{n_\mathrm{o}}\right)\left(\frac{1}{\sigma_\mathrm{LC}{}^2}\right)\left(\frac{1}{\sigma_{\mathrm{r,r}}{}^2}\right)\left(\frac{\mathrm{d}n}{\mathrm{d}C}\right) \tag{9}$$

whereas if translational diffusion does not significantly affect the radial concentration profile, as may occur at higher flow rates, the system lies in a convection-dominated region, and the observed RIG sensitivity will remain constant as given by

$$\Theta \propto \pm 0.144 \left(\frac{V_\mathrm{i} C_\mathrm{i} L R^3}{n_\mathrm{o}}\right)\left(\frac{1}{\sigma_\mathrm{LC}{}^2}\right)\left(\frac{1}{\sigma_{\mathrm{conv,r}}{}^2}\right)\left(\frac{\mathrm{d}n}{\mathrm{d}C}\right) \tag{10}$$

Note that a proportionality is used here and in eq 8, because the exact value of k in eq 4 is not theoretically known.

Because the refractive index of both solvent and analyte depends on temperature, the behavior of RIG measurements should correspondingly be temperature dependent. The dependence of the refractive index gradient $\mathrm{d}n/\mathrm{d}r$ on temperature is given by

$$\frac{\mathrm{d}n}{\mathrm{d}r} = \frac{\mathrm{d}n}{\mathrm{d}T}\frac{\mathrm{d}T}{\mathrm{d}r} \tag{11}$$

where $\mathrm{d}n/\mathrm{d}T$ is a constant term representing the effects of temperature on the mobile-phase refractive index. For RIG experiments using the Z-configuration flow cell, $\mathrm{d}T/\mathrm{d}r$ is the temperature dependence of radial position within the flow cell as a function of flow rate and temperature. This relationship has not been modeled for the Z-configuration flow cell,[11,29] and the exact solution of $\mathrm{d}T/\mathrm{d}r$, which accounts for the loss of heat to the flow cell walls, the changing flow cell wall temperature, and the change in radial thermal gradient shape as a function of flow cell length, for similar tubular systems is not given here for the sake of brevity and clarity.[30-33] As a good approximation the radial thermal gradient takes the form

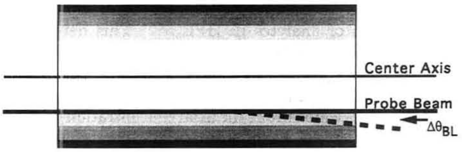

Figure 2. Illustration of the deflection of the laser probe beam due to temperature-induced refractive index gradients (shading), caused by the Poiseuille flow profile, within the unheated flow cell. The mobile-phase refractive index decreases with increasing temperature, deflecting the beam slightly toward the cooler walls. ($\Delta\Theta_\mathrm{BL}$ is shown exaggerated).

$$\mathrm{d}T/\mathrm{d}r = qF(T - T_\mathrm{r}) \tag{12}$$

where q is a system-dependent constant in which the mobile-phase heat capacity, density, viscosity, thermal diffusivity, radial probe position, and the local heat-transfer coefficients are incorporated. T is the temperature to which the column is heated, and T_r is room temperature.

The baseline position Θ_BL of RIG measurements is temperature dependent and described by

$$\Theta_\mathrm{BL} = \frac{L}{n_\mathrm{o}}\frac{\mathrm{d}n}{\mathrm{d}T}\frac{\mathrm{d}T}{\mathrm{d}r} \tag{13}$$

Figure 2 illustrates the effects of temperature on $\mathrm{d}T/\mathrm{d}r$ and, ultimately, the baseline behavior of RIG measurements. Heat loss at the walls results in the development of a thermal gradient within the flow cell. The steepness of this gradient is dependent on the temperature to which the solvent was initially heated and upon flow rate, as suggested by eq 12. The hotter solvent at the flow cell center will possess an inherently lower refractive index than the cooler solvent near the flow cell walls. This results in the formation of a thermal lens which causes a deflection of the probe beam compared to its position at room temperature.

Translational diffusion is also temperature dependent and therefore temperature should affect $\sigma_{\mathrm{r,r}}{}^2$ (eq 3). It is our intent to report an examination of the effects of temperature on RIG baseline behavior and to demonstrate that as the translational diffusion coefficient of an analyte increases with increasing temperature, RIG sensitivity becomes increasingly dominated by $\sigma_{\mathrm{r,r}}{}^2$. This increase in the contribution of diffusion will be examined as a function of flow rate and temperature. The results will lead to a better understanding of the hydrodynamic relationships in small-volume measurements as well as an improved range of applicability for the RIG detector in microbore HPLC (μLC). Enhanced sensitivity for large molecules, with correspondingly small diffusion coefficients, is demonstrated. Note that one of the

---

(29) Smith, R. *J. Fluid Mech.* **1981**, *105*, 469–485.

(30) Schlichting, H.; Kestin, J. *Boundary Layer Theory*; McGraw-Hill: New York, 1960; Chapter 14, pp 306–311.

(31) Shah, R. K.; London, A. L. *Laminar Flow Forced Convection in Ducts*; Academic Press: New York, 1978; Chapters 2–4, pp 37–152.

(32) Incropera, F. P.; DeWitt, D. P.; *Fundamentals of Heat Transfer*; John Wiley & Sons: New York, 1981; Chapter 8, pp 375–426.

(33) Giehdt, W. H.; *Principles of Engineering Heat Transfer*; D. Van Nostrand Co., Inc.: Princeton, NJ, 1957; Chapter 7, pp 134–160.

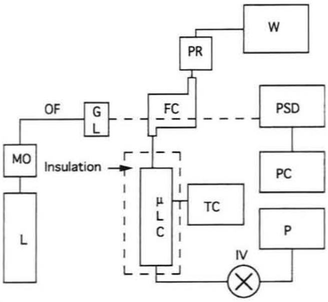

Figure 3. Experimental apparatus: L, HeNe Laser; MO, microscope objective; OF, optical fiber; GL, GRIN lens; FC, flow cell; PSD, position sensitive detector; PC, personal computer; P, syringe pump; IV, injection valve; μLC, microbore column with surrounding thermal insulation; TC, temperature controller; PR, pressure restrictor; W, waste.

primary goals of this work was to study the temperature dependence, and not to minimize temperature effects, until their influence was determined. Because of this, the flow cell in these experiments was not heated and used intentionally as a heat sink to allow for the adequate examination of the expected temperature gradient. In practical applications, the flow cell could also be heated to minimize these temperature effects.

EXPERIMENTAL SECTION

The apparatus used in this study is similar to that used in previous reports and is shown in Figure 3 with modifications.[5-8] The 633-nm, 5-mW CW output from a HeNe laser (Uniphase, 1305P, Sunnyvale, CA) was focused by a 20× microscope objective (Newport, Corp., M-20X, Fountain Valley, CA) onto an optical fiber (6-μm core, 125-μm clad, 175-μm jacket) that was designed for single-mode operation at 633 nm (Fujikura, Ltd., SM 6/125 Al coated, Tokyo, Japan). The optical fiber output was interfaced to a graded refractive index (GRIN) lens that was quarter pitch at 633 nm (NSG America Inc., Somerset, NJ) to produce a collimated probe beam. Measurement of the beam intensity profile indicated that the full probe beam divergence was 3.5 mrad, with an initial diameter of 110 μm, defined as 95% of the beam intensity, at the GRIN lens output face and having a diameter of 200 μm at the flow cell. Modeling of the beam and flow profile interaction suggests that although a 10% loss in relative sensitivity results, the parabolic shape of the sensitivity profile is maintained when a 200-μm-diameter beam is used as compared to using an infinitely narrow source. Changes in observed sensitivity can therefore not be attributed to an optics averaging effect. The probe beam was directed through the Z-configuration flow cell (made in-house) mounted on a high-precision x–y–z translational stage (Newport Corp., 460-X-Y-Z, Fountain Valley, CA) with a 2-cm distance separating the flow cell and GRIN lens. The flow cell was constructed of poly(ether ether ketone) (PEEK) with a 6-mm optical path length and a 780-μm internal diameter. The total flow cell internal volume was 2.9 μL, with flow entering and exiting in the vertical plane. Polished quartz windows were placed over the ends of the flow cell and sealed with a metal coverslip which was bolted into the flow cell body. The probe beam was positioned at the previously determined optimum radial position of 225 μm from the flow cell center on the horizontal radius of the flow cell to avoid possible flow perturbations at the inlet and outlet positions. The collimated probe beam, after it passed through the flow cell, was incident on a position-sensitive detector (PSD) (Hamamatsu, S1352, Hamamatsu, Japan) with dimensions of 33 mm × 2 mm, placed a distance of 0.83 m from the flow cell. PSD sensitivity is along the long, horizontal, axis, in line with the path of deflections predicted for the probe beam.

Table I. Analytes Examined Using Size Exclusion Chromatography

analyte	symbol	mol wt	D_m[a]
poly(ethylene glycol)	PEG 23 000	23000	4.99
poly(ethylene glycol)	PEG 12 600	12600	6.95
poly(ethylene glycol)	PEG 8000	8000	8.92
poly(ethylene glycol)	PEG 900	900	29.7
poly(ethylene glycol)	PEG 400	400	46.3
ethylene glycol	EG	72	118

[a] $\times 10^{-7}$ cm^2/s, as calculated according to eq 14.[24]

For all studies involved an eluent of 100% HPLC grade water was used. Analytes consisted of a series of poly(ethylene glycol)s (PEGs) with a molecular weight range of 72 for ethylene glycol up to 23 000, as shown in Table I. Analytes were dissolved in water to concentrations on the order of 2–100 mmol/L and introduced to the system using an injection valve (Rheodyne, 7520, Cotati, CA) fitted with a 1-μL injection disk. A small-bore LC column was connected to the injection valve via a 5-cm length of $^1/_{16}$-in.-o.d. by 0.005-in.-i.d. PEEK tubing (Upchurch, Oak Harbor, WA) and to the flow cell with a similar piece of tubing. A 2-mm × 250-mm column with 9-μm Asahipak (Keystone Scientific Inc., Asahipak, Bellefonte, PA) packing was used for all separations. For the temperature studies, the column was placed upon a heating strip (Wellman, SS281, Shelbyville, IN) with thermal contact to the heater accomplished via thermal joint compound and the column and connecting tubing wrapped in pipe insulation. Heating was controlled using an Eppendorf controller (Eppendorf, TC-50, Madison, WI). The flow cell was not insulated and therefore could act as a heat exchanger.

After exiting the flow cell, the column effluent passed through a 250 psig pressure restrictor (Upchurch, Oak Harbor, WA) and then passed to waste. A syringe pump (ISCO, LC-2600, Lincoln, NE) was used to deliver the mobile phase and to control flow rates. A flow rate range of 10–130 μL/min and a temperature range of 25–125 °C was examined, with all measurements performed in duplicate. The molecular weights of the PEG standards examined did not exceed the size exclusion limits of the column. A slight shift in retention volume for a given molecular weight was noted, as temperature was increased due to a minor change in analyte hydrodynamic radius and stationary phase pore size distribution.

The convection contribution to the radial concentration gradient was determined by using eq 8 to ratio experimentally determined $\theta\sigma_{LC}^2$ values for a single analyte at varying flow rates. Using the known diffusion coefficient for the analyte examined, the value of $\sigma_{conv,r}^2$ is the only undetermined quantity and therefore can be extracted. This ratio method was used on each analyte and for a variety of flow rate pairings to determine an average value for $\sigma_{conv,r}^2$ and an estimate of its uncertainty.

RESULTS AND DISCUSSION

According to eqs 3 and 8 the sensitivity of RIG measurements depends on the effects that translational diffusion of the analyte and convection have upon the probed radial concentration gradient. These independent, yet coupled, dependencies are examined here to establish that under conditions of adequate analyte residence time within the flow cell RIG sensitivity is proportional to $(\sigma_{r,r}^2)^{-1}$ and reaches a maximum constant term proportional to $(\sigma_{conv,r}^2)^{-1}$ when the effects of diffusion are minimal. Convection is a systematic phenomenon based upon the physical dimensions of the flow cell. As such, it is not dependent upon the velocity of the flow stream and, therefore, is a constant effect as a function of flow rate. Translational diffusion of an analyte, however, can only affect the *probed* radial concentration gradient during its time within the flow cell. The Stokes–Einstein equation predicts the average diffusional distance for an analyte within the flow cell based upon residence time. Residence time is inversely proportional to flow rate, and as a result the effects of the translational diffusion of an analyte increase with decreasing flow rate. Diffusion results in a flattening of the steep concentration gradient, resulting in a decrease in RIG sensitivity, as predicted by eq 8. It is asserted that if an analyte concentration profile within the flow cell diffuses, as described by eq 3, to an extent such that the change in the radial concentration gradient caused by diffusion is substantially larger than the constant change caused by convection ($\sigma_{\mathrm{r,r}} \gg \sigma_{\mathrm{conv,r}}$), then the sensitivity of the RIG measurement shall be proportional to $(\sigma_{\mathrm{r,r}}^2)^{-1}$. Similarly, when diffusion does not appreciably alter the probed radial concentration gradient, then RIG sensitivity will approach a maximum, constant, convection-dominated value proportional to $(\sigma_{\mathrm{conv,r}}^2)^{-1}$.

The validity of these assertions was examined through the chromatographic analysis of a series of poly(ethylene glycol)s (PEGs), given in Table I, of varying molecular weights, therefore varying translational diffusion coefficients as given by[24]

$$D_{\mathrm{m,PEG}} = 1.25 \times 10^{-4}(\mathrm{MW})^{-0.55} \qquad (14)$$

where MW is the weight average molecular weight of the polymer. After chromatographic separation, experimental data consisted of a measure of the height difference, Θ, as taken from peak top to peak bottom of the characteristic derivative-shaped RIG peak, and a measure of peak width from which σ_{LC}^2 was calculated. The chromatographic analysis was then performed over a range of flow rates and temperatures for each analyte. Each analysis was repeated to assure data quality. The data, Θ and σ_{LC}^2 values, were then normalized to remove the individual contributions of V_i, C_i, R, L, and $\mathrm{d}n/\mathrm{d}C$. Figure 4A,B shows the results of this series of chromatographic analyses and a comparison of the data to the proposed model for PEG 12 600 ($D_{\mathrm{m}} = 6.95 \times 10^{-7}$ cm^2/s) and ethylene glycol ($D_{\mathrm{m}} = 1.18 \times 10^{-5}$ cm^2/s), respectively. The data points represent the experimental product, $\Theta\sigma_{\mathrm{LC}}^2$, and include the value for the chromatography-induced variance value to normalize the effects of band broadening in the column for the various analytes. This allows for the specific examination of the diffusion and convection effects upon the radial concentration gradient caused by the flow cell. Similar experiments were performed using PEG 8000 and PEG 900 which resulted in sensitivity response curves similar to those shown in Figure 4A,B, but of intermediate slope, and which are not shown for clarity. PEG 12 600 and ethylene glycol were used to present the extreme values observed. The sloping lines in each figure represent the theoretical sensitivity (eq 9) for each analyte if sensitivity were exlusively dependent upon diffusion, as determined by calculating the expected radial variance using the Stokes–Einstein-based diffusional distance distribution. The contribution of convection to the radial concentration gradient, $\sigma_{\mathrm{conv,r}}$, was determined, as described in the Experimental Section, to be 43.34 ± 4.26 μm for this system. Using this experimentally determined value, the horizontal line at 1.15×10^{-3} μm^{-2} was determined and represents the theoretical sensitivity (eq 10) for all analytes if sensitivity were exclusively dependent upon convection. The sloping curves combine the two independent effects to describe the sensitivity predicted by eq 8. The data presented consistently follow the behavior predicted by eq 8, and Table II shows that a good fit is observed for the analytes examined. Measurements were determined to be convection dominated if RIG sensitivity is within 2 standard deviations of the sensitivity predicted by $\sigma_{\mathrm{conv,r}}$. Based upon this definition, the transition between convection- and diffusion-dominated sensitivity regions occurs at $\sigma_{\mathrm{r,r}}$ values greater than 20 μm. The transition is defined to show that the sensitivity behavior for an analyte at a particular temperature and flow rate can be predicted prior to the experiment, so that experimental conditions may be tuned in order to minimize or enhance the diffusional effect. As expected, at lower flow rates RIG sensitivity is dominated by diffusion. The effect is more pronounced for smaller analytes with large diffusion coefficients, as predicted by eq 4. Sensitivity reaches a maximum constant value, given by eq 10, when convection dominates the changes in the probed radial concentration gradient. These results suggest that maximum RIG sensitivity can be achieved by utilizing larger flow rates, which will additionally reduced analysis time. At smaller flow rates diffusional information can be obtained if the convectional effects of the system are well characterized.

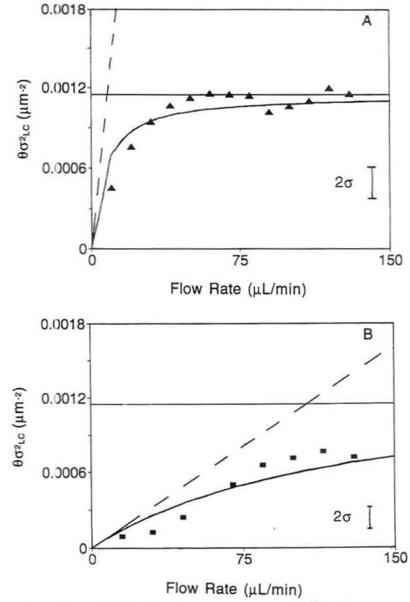

Figure 4. Normalized experimentally obtained $\Theta\sigma_{\mathrm{LC}}^2$ values for (A) PEG 12 600 and (B) ethylene glycol as a function of volumetric flow rate. The sloping line (dashed) represents the theoretical diffusion-dominated response (eq 9) for the specific analyte and the horizontal line represents the theoretical convection-dominated response (eq 10). The sloping curve represents the diffusion and convection based model (eq 8) for the analyte shown. Experimental uncertainty was fairly random, so average error bars of two standard deviations (2σ) are shown for the experimental data.

Table II. Measure of the Fit of the Experimental Data to the Proposed Hydrodynamic Convection and Analyte Diffusion Based Model (eq 8)

analyte	corr coeff (r)[a]	analyte	corr coeff (r)[a]
PEG 12 600	0.97	PEG 900	0.99
PEG 8000	0.96	EG	0.97

[a] Data used to obtain r values for PEG 12 600 and EG are shown in Figure 4A,B.

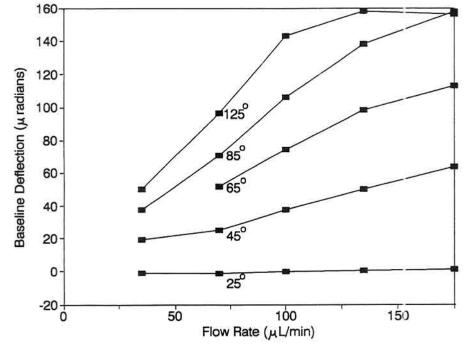

Figure 5. Relative baseline position, $\Delta\Theta_{BL}$, as a function of flow rate and temperature, characterizing the expected baseline drift in the presence of a radial thermal gradient.

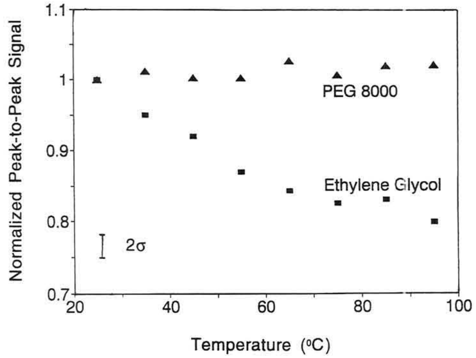

Figure 6. Normalized RIG peak-to-peak signal values for PEG 8000 (triangles) and ethylene glycol (squares) as a function of temperature. Average error bars of two standard deviations (2σ) are shown.

Table III. Baseline Noise as a Function of Baseline Temperature, with Data Averaged to 1 point/s

temp (°C)	σ (μrads)	temp (°C)	σ (μrads)
25	0.34	85	0.70
45	0.37	125	0.93
65	0.68		

Next, the effects of temperature on the baseline behavior of RIG baseline measurements were examined. The Reynolds number, which describes the nature of the flow, is given by[34]

$$Re = 2\rho F/\pi R\eta \tag{15}$$

where ρ and η are the solvent density and viscosity, respectively, for the experimental system as a function of flow rate and temperature. It has been suggested previously that a Reynolds number of 10 or less implies the presence of laminar flow in similar flow cell dimensions.[12] Turbulence would be characterized by larger Reynolds numbers and a complete degradation of the RIG signal. Previous studies have shown that baseline deflection in RIG detection increases with elevated flow rates for high-temperature experiments.[13] Figure 5 illustrates the shifts in detected probe beam angle observed by the PSD for a baseline position as compared to that of room temperature for a range of temperatures as a function of flow rate. The shift in baseline position was determined by comparing baseline positions at room temperature and at an elevated temperature, as given by

$$\Delta\Theta_{BL} = \Theta_T - \Theta_{T_r} \tag{16}$$

where Θ_T and Θ_{T_r} are the relative baseline positions at the elevated and room temperatures, respectively. The temperatures refer to the level to which the column was heated and maintained while the flow cell was not heated and remained exposed to the lab environment. Examining the proportionality of Reynolds number to F/η, one expects the Reynolds number to increase with temperature as mobile-phase viscosity correspondingly decreases. RIG baseline measurements were determined to show a linear increase in relative position as a function of temperature for a constant flow rate, given by

$$d\Theta/dF = 0.095(T - T_r) \tag{17}$$

with a correlation coefficient of $r = 1.00$. The results shown in Figure 5 are in agreement with the baseline behavior predicted by eqs 13 and 14, and the linear dependence of the baseline position on temperature demonstrates that the RIG measurement baseline behavior is stable over the range of flow rates and temperatures examined. In addition, the constant term for the change in baseline position as a function of flow rate and temperature derived experimentally (eq 17) is consistent with the behavior predicted by eq 12. An example of unstable RIG baseline behavior is shown in Figure 5 in the 125 °C isotherm at flow rates above 130 μL/min. Here, the expected baseline shift as a function of flow rate and temperature becomes nonlinear. The calculated Reynolds number of above 10 beginning at 130 μL/min for the 125 °C isotherm may suggest that the flow is becoming turbulent. Note that a pressure restrictor is used, so the mobile phase is still a liquid at this elevated temperature. Extensions of the other isotherms on Figure 5, not shown for clarity, reveal a similar collapse of the expected linear baseline position shift with temperature and flow rate as the Reynolds number for the flow exceeds 10. At this point, the behavior of the baseline becomes erratic, suggesting that the flow has become turbulent. The range of temperatures and flow rates which demonstrate stable baseline behavior is quite large and should be suitable for most chromatographic needs in the flow range useful for 1–2-mm-i.d. columns.

Table III shows the effects of temperature on baseline noise. Noise readings were determined by first observing the angle of deflection for the temperature measurement and then repositioning the detector to the electronic null. This process removes the noise which exists as a function of absolute angle of deflection for the PSD to extract the purely temperature-induced noise. Noise levels were averaged using a 1 point/s time constant. The noise levels and the observed increase are quite small and should not affect chromatographic performance.

Baseline drift for thermal gradient (TG) work is defined by the Θ_{BL} range given in Figure 5 for a given flow rate. At low flow rates and/or temperature changes this baseline shift may not be significant while at higher values the drift may be quite large.[13] As an example, refer to Figure 5 and Table II and note that a thermal gradient experiment run at 50 μL/min from room temperature to 85 °C will result in a 40-μrad baseline shift. A typical signal of 100 μrad would still be easily observed over the sloping baseline. But if the same experiment were run at 150 μL/min, where the baseline is expected to shift nearly 150 μrad, the same 100-μrad signal may be more difficult to measure. Noise increases slightly with temperature, so the limit of detection for the system increases as well. It is important, therefore, to fully characterize the behavior of the baseline and baseline noise in

---

[34] Kachel, V.; Menke, E. In *Flow Cytometry and Sorting*; Melamed, M. R., Mullaney, P. F.; Mendelsohn, M. L., Eds.; John Wiley & Sons: New York, 1979; Chapter 3, pp 41–59.

order to distinguish baseline phenomenon from an analytical signal. This baseline drift has been shown to be directly dependent on the presence of a thermal gradient within the flow cell. Use of a long uninsulated piece of connecting tubing would diminish the severity of the induced thermal gradient and reduce the baseline shift caused as a function of temperature but will introduce additional band broadening. In addition, it would seem that this temperature-induced baseline shift might result in a shift in the net position in the probe beam away from the previously determined[8] optimal radial probe position. However, even an extreme deflection of 100 μrad over the 6-mm optical path length of the flow cell results in only a 0.6-μm shift in the net probe beam position. This shift is negligible compared to the 390-μm radius of the flow cell.

With the stability of the baseline as a function of temperature adequately characterized, the effects of temperature on analyte sensitivity were examined. Figure 6 shows the effects of temperature on the normalized peak-to-peak signal for two of the analytes examined. In this case, initial normalization accounted for differences in chromatographic variance, which is also sensitive to diffusion coefficient differences. It is observed that the signal for PEG 8000 remains constant as a function of temperature while ethylene glycol demonstrates a reduction in sensitivity. To explain this observation, one must return to the examination of eq 8 and the diffusion mechanism which occurs within the flow cell. In each case, the translational diffusion coefficient increases; however, returning to Figure 4 we note that at 70 μL/min RIG sensitivity for PEG 12 600 is convection dominated while for ethylene glycol diffusion still affects the probed radial concentration profile appreciably. A similar determination for PEG 8000 reveals that the analyte, which is very similar to PEG 12 600 ($D_m = 6.95 \times 10^{-7}$ cm^2/s vs 8.92×10^{-7} cm^2/s), is convection dominated in the same flow rate region. The increase in D_m for PEG 8000 as a result of the increase in temperature was not significant enough to appreciably change $\sigma_{r,r}$ and therefore the radial concentration profile. Thus, the sensitivity for PEG 8000 predicted by eq 8 should remain constant, as is observed. The RIG sensitivity for ethylene glycol is diffusion sensitive at 70 μL/min, so a temperature-induced increase in its diffusion coefficient should decrease RIG sensitivity. This is consistent with the observed results.

The implications for liquid chromatography with the RIG detector are that high temperatures may be used without a corresponding loss in sensitivity for analytes if high flow rates are utilized or if the eluent is allowed to cool before entering the RIG detection system. This suggests that the RIG detector can be used in high-temperature liquid chromatography without substantial temperature-based sensitivity losses. As such, the benefits of decreased back-pressure and shortened analysis time achieved with HTLC and TGLC may be coupled with increased sensitivity obtained from radial concentration gradient detection.

RECEIVED for review July 13, 1992. Accepted October 15, 1992.

Anal. Chem. **1993**, *65*, 135–140

Experimental Determination of the Number of Trapped Ions, Detection Limit, and Dynamic Range in Fourier Transform Ion Cyclotron Resonance Mass Spectrometry

Patrick A. Limbach, Peter B. Grosshans,[†] and Alan G. Marshall*,[‡]

Department of Chemistry, 120 West 18th Avenue, The Ohio State University, Columbus, Ohio 43210

Determination of the number of ions that produce a detected time-domain signal in Fourier transform ion cyclotron resonance mass spectrometry is fundamental in establishing (a) the detection limit for a single data acquisition, (b) the maximum number of trapped ions, and (c) the mass spectral dynamic range obtained as the ratio of (b)/(a). Moreover, the ability to monitor ion absolute abundances throughout various experimental event sequences provides a direct measure of (e.g.) ionization efficiency, collisional-induced dissociation efficiency, and ion trapping efficiency. In this paper, we determine the absolute number of trapped ions by comparing the experimentally observed signal voltage to that calculated for a single ion orbiting at the (measured) ICR orbital radius of the ion packet, assuming that all ions orbit in a tight coherent packet in the trap midplane. The effects of relaxing these assumptions are estimated. In this way, we determine a detection limit (undamped signal acquired for 1 s, magnitude-mode mass spectral peak height to baseline standard deviation noise ratio of 3:1 measured at a frequency of 600 kHz, excited ICR orbital radius of 50% of the maximum possible cubic trap radius) of ~177 singly charged ions and a dynamic range of 32 000 at 3.0 T in a cubic trap. Various assumptions, the detection circuit model, and proposed applications for the determination of the number of trapped ions are discussed.

INTRODUCTION

Fourier transform ion cyclotron resonance mass spectrometry (FT/ICR/MS) has recently been combined with a very wide variety of analytically useful ionization techniques in which ions are initially formed outside the ion trap: e.g., laser desorption,[1] matrix-assisted laser desorption,[2] Cs$^+$ secondary ionization,[3,4] dc glow discharge,[5] electrospray,[6] fast neutral beam,[7] entrainment of ions in a supersonic jet,[8] continuous-flow fast atom bombardment,[9] supercritical fluid chromatography,[10] high-pressure ion source,[11] field desorption,[12] ^{252}Cf plasma desorption,[13] metal vapor vacuum arc,[14] and surface-induced dissociation.[15] The theoretical aspects of ion behavior in the ICR trap are now well understood, and recent advances in techniques for ion trapping and ICR excitation and detection have been comprehensively reviewed.[16,17] The groundwork is now in place for the increased use of FT/ICR/MS as a powerful analytical technique. With the rapid expansion in FT/ICR/MS analytical applications comes an increased need for a direct and accurate measure of the number of ions that contribute to the detected time-domain ICR signal, in particular the smallest and largest number of ions that may be detected.

The *minimum* detection limit for FT/ICR/MS is presently defined empirically as the minimum amount of sample which produces a specified mass spectral peak height-to-noise ratio under some sort of standard conditions.[18,19] However, such a definition represents a composite measure of the sample volatility, ionization efficiency, ion trapping efficiency, ion stability toward collisions or reactions, ICR orbital radius, trap size and shape, detection circuit equivalent resistance and capacitance, etc. In practice, these effects have not proved easy to separate, so that there is at present no good measure of the number of ions detected in an FT/ICR/MS experiment.

At the other end of the scale, it is important to establish the *maximum* number of detectable ions, in order to determine the *dynamic range* (ratio of largest to smallest observable signal in a single spectrum). Whereas the maximum number of ions that may be trapped can be estimated from space charge considerations,[20–22] the actual maximum number of

---

* To whom correspondence should be addressed.

[†] Present address: Analytical Sciences Lab, Corporate Research, Exxon Research & Engineering Co., Clinton Township, Rt. 22-East, Annandale, NJ 08801.

[‡] Also a member of the Department of Biochemistry.

(1) *Lasers in Mass Spectrometry*; Lubman, D. M., Ed.; Oxford University Press: New York, 1990.

(2) Hettich, R. L.; Buchanan, M. V. *J. Am. Soc. Mass Spectrom.* **1991**, *2*, 22–28.

(3) Castro, M. E.; Russell, D. H. *Anal. Chem.* **1984**, *56*, 578–581.

(4) Amster, I. J.; Loo, J. A.; Furlong, J. J. P.; McLafferty, F. W. *Anal. Chem.* **1987**, *59*, 313–317.

(5) Barshick, C. M.; Eyler, J. R. *J. Am. Soc. Mass Spectrom.* **1992**, *3*, 122–127.

(6) Henry, K. D.; Williams, E. R.; Wang, B.-H.; McLafferty, F. W.; Shabanowitz, J.; Hunt, D. F. *Proc. Natl. Acad. Sci. U.S.A.* **1989**, *86*, 9075–9078.

(7) Hill, N. C.; Limbach, P. A.; Shomo, R. E., II; Marshall, A. G.; Appelhans, A. D.; Delmore, J. E. *Rev. Sci. Instrum.* **1991**, *62*, 2612–2617.

(8) Smalley, R. E. *Anal. Instrum.* **1988**, *17*, 1–21.

(9) Watson, C. H.; Kruppa, G.; Wronka, J.; Laukien, F. H. *Rapid Commun. Mass Spectrom.* **1991**, *5*, 249–251.

(10) Baumeister, E. R.; West, C. D.; Ijames, C. F.; Wilkins, C. L. *Anal. Chem.* **1991**, *63*, 251–255.

(11) Kofel, P.; McMahon, T. B. *Int. J. Mass Spectrom. Ion Processes* **1990**, *98*, 1–24.

(12) Ipezsa, I.; Knoll, H.; Wanczek, K.-P.; Linden, H. B. *Proceedings of the 36th American Society for Mass Spectrometry Annual Conference on Mass Spectrometry and Allied Topics*, San Francisco, CA, 1988; American Society for Mass Spectrometry: East Lansing, MI, 1988; pp 618–619.

(13) Williams, E. R.; McLafferty, F. W. *J. Am. Soc. Mass Spectrom.* **1990**, *1*, 427–430.

(14) Wang, B. H.; Amster, I. J.; McLafferty, F. W.; Brown, I. B. *Int. J. Mass Spectrom. Ion Processes* **1990**, *100*, 51–61.

(15) Ijames, C. F.; Wilkins, C. L. *Anal. Chem.* **1990**, *62*, 1295–1299.

(16) Marshall, A. G.; Grosshans, P. B. *Anal. Chem.* **1991**, *63*, 215A–229A.

(17) Marshall, A. G.; Schweikhard, L. *Int. J. Mass Spectrom. Ion Processes* **1992**, *118*/*119*, 37–70.

(18) Comisarow, M. B. In *Ion Cyclotron Resonance Spectrometry II*; Hartmann, H., Wanczek, K.-P., Eds.; Springer-Verlag: Berlin, 1982; pp 484–513.

(19) Sack, T. M.; McCrery, D. A.; Gross, M. L. *Anal. Chem.* **1985**, *57*, 1290–1295.

(20) Ledford, E. B., Jr.; Rempel, D. L.; Gross, M. L. *Anal. Chem.* **1984**, *56*, 2744–2748.

(21) Wang, T.-C. L.; Marshall, A. G. *Int. J. Mass Spectrom. Ion Processes* **1986**, *68*, 287–301.

0003-2700/93/0365-0135$04.00/0

trapped ions that contribute to the detected cyclotron signal is unknown.

Finally, a direct measure of the *absolute* number of ions contributing to the ICR signal is vital to such fundamental measurements as ionization efficiency, trapping efficiency (particularly for external ion injection), mechanisms for damping of the time-domain ICR signal, etc. Prior attempts to determine the number of detectable ions in an ICR ion trap include applying a dc voltage to one trapping plate to attract positive ions where the resultant ion current is measured with an electrometer;[23] calculating the number of ions of known electron ionization cross-section from measured electron beam duration, emission current, and ionization volume;[24,25] and applying a dc voltage to either the excitation or trapping electrodes of a cubic trap to induce ions to drift toward the detector electrodes, where their deposited charge is measured.[20,25] However, all of these methods at best determine the number of ions trapped *before* excitation and give no direct indication of the extent of ion loss or dephasing during and after the excitation process. In this paper, we offer a determination of ion number based directly on the observed ICR signal. We obtain the number of coherently orbiting ions simply by dividing the observed signal by the signal calculated for one ion at the same (measured) ICR orbital radius. The method requires only the (one-time) determination of the equivalent resistance and capacitance of the ICR trap and knowledge of the trap geometry. We begin by defining the detection limit and then proceed to review the theory and signal model for the method.

Detection Limit. In sector, quadrupole, and time-of-flight mass spectrometry, the preferred method of signal detection is simply ion counting,[26] so that determination of the detection limit is straightforward. In contrast, an FT/ICR mass spectrum is obtained from a time-domain voltage signal resulting from an image current induced by a coherently orbiting ion packet.[27-31] For an ionized sample containing ions of a single mass-to-charge ratio, m/q, the time-domain ICR signal is directly proportional to the number of ions. Thus, establishment of the absolute number of ions in an FT/ICR measurement requires four steps: (a) separation of the signals from ions of different m/q values; (b) determination of the proportionality factor between the number of ions of a given m/q and the observed voltage signal at their ICR orbital frequency; (c) determination of the noise level; (d) consideration of imprecision resulting from the discrete nature of the time-domain data. Separation of the signals from ions of different m/q is accomplished by discrete Fourier transformation to generate a frequency-domain spectrum.[32] Moreover, the theoretical nature[33,34] and experimental determination of FT/ICR mass spectral magnitude-mode noise are well-understood, as is the relation between spectral precision (in this case, with respect to mass spectral peak height or area) and the number of discrete data points per spectral peak width.[34-36] In this paper, we present the solution to the remaining step, (b), namely, determination of the voltage signal for a known number of ions orbiting in a coherent packet at a known ICR orbital radius.

A suitable definition of detection limit should be as independent as possible of instrumental parameters (e.g., type or size of ion trap, excitation amplitude or duration, and collisional damping of the time-domain ICR signal). Collisional damping may be minimized by choosing a data acquisition period that is short compared to the time-domain exponential damping time constant for the signal; FT/ICR mass spectral peak width is then a function only of acquisition period.[37] On the other hand, since frequency-domain signal-to-noise ratio increases as the square root of acquisition period,[37] the acquisition period should be as long as possible, consistent with the need to avoid signal damping as noted above. As a compromise, we suggest a 1-s acquisition period, at which the time-domain signal should remain undamped at the readily attainable sample pressure of $\sim 10^{-9}$ Torr. ICR time-domain signal strength increases approximately proportional to ICR orbital radius;[29,31,38] however, nonlinear effects introduce complications as the ICR orbital radius approaches the detection electrodes. Again, as a working compromise, we suggest a standard ICR orbital radius equal to half the maximum radius of the trap [e.g., half the inner radius of the ring electrode for cylindrical or hyperbolic traps or half the (lesser of the) excitation or detection plate-to-plate separation in an orthorhombic trap]. Finally, the signal-to-noise ratio should be measured from the frequency-domain FT spectrum, not the time-domain signal, because only the FT spectrum separates signals from ions of different m/q values. The above criteria may be summarized in the following definition of detection limit for FT/ICR mass spectrometry. *The detection limit of an FT/ICR/MS instrument is the minimum number of ions, in a single scan, required to produce a signal whose FT magnitude-mode peak height is 3 times the noise level (defined as the standard deviation of the magnitude-mode baseline noise) for a 1-s observation period of an ICR time-domain signal whose exponential decay time constant is at least 10 s (i.e., negligible signal damping during the detection period), for ions at an initial average postexcitation ICR orbital radius of half the maximum allowed radius.* Because the signal-to-noise ratio in FT/ICR/MS may depend on frequency,[27] we have specified 600 kHz (ion cyclotron orbital frequency to the benzene molecular ion at 3.0 T) as a reference frequency.

Dynamic Range. The dynamic range of FT/ICR mass spectrometry has been variously estimated to be in the 10^3–10^5 range for a single time-domain data acquisition,[23,24] with substantial extension by use of stored-waveform selective ejection of the ions of highest relative abundance.[39] Knowledge of the dynamic range is obviously important for detecting minor constituents in a spectrum. However, present estimates

---

(22) Ledford, E. B., Jr.; Rempel, D. L.; Gross, M. L. *Anal. Chem.* **1984**, *56*, 2744–2748.

(23) Hunter, R. L.; Sherman, M. G.; McIver, R. T., Jr. *Int. J. Mass Spectrom. Ion Phys.* **1983**, *50*, 259–274.

(24) McIver, R. T., Jr.; Hunter, R. L.; Ledford, E. B., Jr.; Locke, M. J.; Francl, T. J. *Int. J. Mass Spectrom. Ion Phys.* **1981**, *39*, 65.

(25) Elling, J. W.; Farrar, T. C.; Campana, J. E. *Proceedings of the 39th American Society for Spectrometry Annual Conference on Mass Spectrometry and Allied Topics*, Nashville, TN, 1991; American Society for Mass Spectrometry: East Lansing, MI, 1991; pp 457–458.

(26) White, F. A.; Wood, G. A. *Mass Spectrometry Applications in Science and Engineering*; John Wiley & Sons: New York, 1986, Chapter 5.

(27) Comisarow, M. B. *J. Chem. Phys.* **1978**, *69*, 4097–4104.

(28) Marshall, A. G.; Wang, T.-C. L.; Cottrell, C. E.; Werbelow, L. G. *J. Am. Chem. Soc.* **1982**, *104*, 7665–7666.

(29) Rempel, D. L.; Huang, S. K.; Gross, M. L. *Int. J. Mass Spectrom. Ion Processes* **1986**, *70*, 163–184.

(30) Nikolaev, E. N.; Gorshkov, M. V. *Int. J. Mass Spectrom. Ion Processes* **1985**, *64*, 115–125.

(31) Grosshans, P. B.; Shields, P. J.; Marshall, A. G. *J. Chem. Phys.* **1991**, *94*, 5341–5352.

(32) Marshall, A. G.; Verdun, F. R. *Fourier Transforms in NMR, Optical, and Mass Spectrometry: A User's Handbook*; Elsevier: Amsterdam, 1990; 460 pp.

(33) Hanna, D. A. *Proceedings of the 33rd American Society for Mass Spectrometry Annual Conference on Mass Spectrometry and Allied Topics*, San Diego, CA, 1985; American Society for Mass Spectrometry: East Lansing, MI, 1985; pp 435–436.

(34) Liang, Z.; Marshall, A. G. *Appl. Spectrosc.* **1990**, *44*, 766–775.

(35) Chen, L.; Cottrell, C. E.; Marshall, A. G. *Chemom. Intell. Lab. Syst.* **1986**, *1*, 51–58.

(36) Liang, Z.; Marshall, A. G. *Anal. Chem.* **1990**, *62*, 70–75.

(37) Marshall, A. G. *Anal. Chem.* **1979**, *51*, 1710–1714.

(38) Grosshans, P. B.; Marshall, A. G. *Int. J. Mass Spectrom. Ion Processes* **1990**, *100*, 347–379.

(39) Wang, T.-C. L.; Ricca, T. L.; Marshall, A. G. *Anal. Chem.* **1986**, *58*, 2935–2938.

of dynamic range suffer from lack of knowledge both of the maximum number of detectable ions and of the detection limit (see above). For example, even if a large number of ions can be trapped, space charge (Coulomb repulsion) effects may tend to spread them out in the trap, reducing the coherence of the excited ICR signal and resulting in axial and radial ion loss as well as loss of signal due to charge induced on the trap electrodes rather than the detector electrodes.

Dynamic range in FT/ICR experiments is limited by both *analog* and *digital* stages. Digital dynamic range is limited (for a single data acquisition of a noiseless signal) by the word length in the analog-to-digital conversion (ADC) step. For typical 10–12-bit ADC's used for FT/ICR/MS, the digital dynamic range per acquisition is thus limited to 1000–4000. Dynamic range may exceed the number of bits per ADC word by use of signal-averaging[32] of multiple acquisitions of noisy signals (e.g., electron ionization), because the signal accumulates as the number of acquisitions whereas the noise accumulates only as the square root of the number of acquisitions.[37] Thus, we shall here be concerned mainly with *analog* dynamic range for a signal accumulated for many acquisitions.

THEORY

Detection Circuit Model. The general theory of detection in the FT/ICR experiment has been described previously.[27,29–31] The detection circuit is shown in Figure 1. A coherently orbiting ion packet induces a differential signal current between the receiver plates and can be modeled as a current source (S in Figure 1). The receiver plates may be modeled as an equivalent capacitor (C in Figure 1) and resistor (R in Figure 1) in parallel which pass this charge to the preamplifier depending on the frequency of the induced charge. To this point, we have followed Comisarow's prior treatment.[27]

In the interest of simplicity and in an effort to draw a parallel with NMR, Comisarow formulated his theory in terms of a dipole moment per unit volume, P, which, generally speaking, does not apply to localized gas-phase ions interacting with finite-dimension receiver electrodes. The Comisarow model gives a correct result for infinite parallel plate receiver electrodes and a symmetrical charge distribution but fails to account for a number of other effects. A consequence of the model is that the induced surface charge density on the detection plates is independent of position. In fact, the surface charge density varies with position.[31] The Comisarow model also neglects dependence of signal on ion axial position, fails to account for harmonic signals, and predicts a linear (rather than approximately linear, reduced by a factor of 0.721 67 for a cubic trap) dependence of ICR signal on ICR orbital radius.[31] Finally, the original Comisarow treatment does not apply to geometries/detection circuits in which even harmonics do not cancel by symmetry (e.g., single-electrode detection[40]) or where magnetron/trapping motion is present (as in all actual ICR ion traps). The more recent model on which the present development is based[31] accommodates all of the above issues. To determine the induced charge on the receiver plates, we therefore proceed as follows:

Let a charge source S induce a differential charge, ΔQ, between the two detect electrodes. The induced charge can be expanded in a Fourier series with coefficients [$A_{2m+1}(2r/a)$, scaled according to the trap geometry] corresponding to the amplitude of the induced charge component at each odd integral multiple ($m = 0, 1, 2, \ldots$) of the ICR orbital frequency, ω_+, in which r is the ICR orbital radius and a is the distance between the centers of the two detector electrodes. Specifically

$$-\Delta Q/q = \sum_{m=0}^{\infty} A_{2m+1}(2r/a) \cos\,[(2m+1)\omega_+ t] \tag{1}$$

or

$$\Delta Q = -q\sum_{m=0}^{\infty} A_{2m+1}(2r/a) \cos\,[(2m+1)\omega_+ t] \tag{2}$$

Since electrical current, $i(t)$, is simply the time rate of change of (induced) charge on the detector electrode(s)

$$i(t) = \frac{\mathrm{d}}{\mathrm{d}t}\frac{\Delta Q}{2} = \frac{\mathrm{d}}{\mathrm{d}t}\left[\frac{-q}{2}\sum_{m=0}^{\infty} A_{2m+1}\left(\frac{2r}{a}\right) \cos\,[(2m+1)\omega_+ t]\right] \tag{3}$$

The factor of $^1/_2$ on the right-hand side of eq 3 is introduced to avoid counting the current twice (once for current flowing out of one detector plate and once for current flowing into the other detector plate). Since current flows either through the resistor [$i(t) = V(t)/R$] or through the capacitor [$i(t) = C\mathrm{d}V(t)/\mathrm{d}t$] of the equivalent circuit of Figure 1[27]

$$i(t) = C\left[\frac{V(t)}{RC} + \frac{\mathrm{d}V(t)}{\mathrm{d}t}\right] \tag{4}$$

in which $V(t)$ is the differential voltage corresponding to the induced differential charge, ΔQ, and R is resistance. Multiplying eq 4 by $\exp(t/RC)$ to create an exact differential, we obtain

$$i(t) = \exp(-t/RC)C\frac{\mathrm{d}}{\mathrm{d}t}(\exp(t/RC)V(t)) \tag{5}$$

so that

$$\frac{q\omega_+}{2C}\sum_{m=0}^{\infty}(2m+1)A_{2m+1}\left(\frac{2r}{a}\right)\exp(t/RC)\sin\,[(2m+1)\omega_+ t] = \frac{\mathrm{d}}{\mathrm{d}t}(\exp(t/RC)V(t)) \tag{6}$$

or

$$\frac{q\omega_+}{2C}\sum_{m=0}^{\infty}(2m+1)A_{2m+1}\left(\frac{2r}{a}\right)\int_{-\infty}^{t}\sin\,[(2m+1)\omega_+ t'] \exp(t'/RC)\,\mathrm{d}t' = \exp(t/RC)V(t) \tag{7}$$

$$\frac{V(t)}{\frac{q\omega_+}{2C}} = \exp(-t/RC)\sum_{m=0}^{\infty}(2m+1)A_{2m+1}\left(\frac{2r}{a}\right)\times \left\{\left[\exp(t'/RC)\frac{1}{RC}\sin\,[(2m+1)\omega_+ t'] - (2m+1)\omega_+\cos\,[(2m+1)\omega_+ t']\right]\Big/\left[\frac{1}{R^2C^2} + (2m+1)^2\omega_+{}^2\right]\right\}\Bigg|_{-\infty}^{t} \tag{8}$$

$$V(t) = \frac{q\omega_+ R}{2}\sum_{m=0}^{\infty}(2m+1)A_{2m+1}(\bar{r})\times \{[\sin\,[(2m+1)\omega_+ t] - (2m+1)RC\omega_+\cos\,[(2m+1)\omega_+ t]]/[1 + [(2m+1)\omega_+ RC]^2]\} \tag{9}$$

in which $\bar{r} = r/(a/2)$ = the ICR orbital radius measured as a fraction of the radius from the center of the trap to the center of either detector electrode. In order to exploit the trigonometric identity, $\sin A \cos B - \cos A \sin B = \sin (A - B)$, we find it useful to define $\theta_m = \tan^{-1}[(2m+1)\omega_+ RC]$, so that

---

(40) Allemann, M.; Kellerhals, H.-P.; Wanczek, K.-P. *Chem. Phys. Lett.* **1981**, *84*, 547–551.

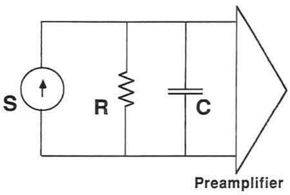

Figure 1. Diagram of the equivalent circuit representation of the detection model used in this paper: signal current source (S), detection circuit equivalent capacitance (C) and resistance (R), and preamplifier. The signal model of this figure is equivalent to a prior model for differential detection.[27]

$$V(t) = \frac{q\omega_+R}{2}\sum_{m=0}^{\infty}\frac{(2m+1)A_{2m+1}(\tilde{r})}{\sqrt{1+[(2m+1)RC\omega_+]^2}}\sin\,[(2m+1)\omega_+ - \theta_m] \tag{10}$$

or

$$V(t) = \frac{q}{2C}\sum_{m=0}^{\infty}A_{2m+1}(\tilde{r})\sin\,(\theta_m)\sin\,[(2m+1)\omega_+t-\theta_m] \tag{11}$$

Keeping only the first term of the sum in eq 11 (i.e., neglecting third and higher-order harmonic signal components), we arrive at

$$V(t) \approx \frac{q}{2C}A_1(\tilde{r})\sin\,(\theta_0)\sin\,[\omega_+t-\theta_0] \tag{12}$$

$$V(t) = \frac{q}{2C}A_1(\tilde{r})\frac{\omega_+RC}{\sqrt{1+(\omega_+RC)^2}}\sin\,[\omega_+t-\theta_0] \tag{13}$$

For $\omega_+RC \gg 1$ (i.e., for $R \approx 1$ MΩ and $C \approx 40$ pf, $m/q \leq 4000$ u/e at 3.0 T) and

$$\theta_0 = \tan^{-1}\,[\omega_+RC] \approx \pi/2 \tag{14}$$

$$V(t) \approx \frac{q}{2C}A_1(\tilde{r})\cos\,(\omega_+t) \tag{15}$$

Equation 15 gives the voltage signal for a single ion. For N identical ions of charge q

$$V(t) = \frac{Nq}{2C}A_1(\tilde{r})\cos\,(\omega_+t) \tag{16}$$

or

$$N = 2CV(t)/qA_1(\tilde{r})\cos\,(\omega_+t) \tag{17}$$

$$N = 2C\frac{V_{\text{p-p}}}{2}/qA_1(\tilde{r}) \tag{18}$$

$$N = CV_{\text{p-p}}/qA_1(\tilde{r}) \tag{19}$$

In order to determine the number of ions contributing to the detected signal, the capacitance, C, of the detection circuit must be determined, the peak-to-peak voltage corresponding to a measured FT/ICR mass spectral peak amplitude must be known, and the radius, r, must be determined. $A_1(\tilde{r})$, which is approximately proportional to $\tilde{r}$, may be determined graphically.[38] The capacitance of the detection circuit and the calibration of the peak-to-peak voltage/spectral peak amplitude may both be determined once for a given instrument. The radius determination has been described previously.[41]

Signal-to-Noise Ratio. If the noise is modeled as a detection-limited (Johnson) noise source and amplifier noise is neglected,[42] then the time-domain rms noise voltage, V_{noise}, takes the form

$$V_{\text{noise}} = \sqrt{\frac{4kT\delta\omega/R}{1+(\omega_+RC)^2}} \tag{20}$$

in which $\Delta\omega$ is the detection bandwidth, T is absolute temperature, and k is Boltzmann's constant. From eqs 13 and 20, the ratio of the signal peak-to-peak amplitude-to-noise ratio then becomes

$$V_{\text{peak-to-peak signal}}/V_{\text{noise}} = NqA_1(\tilde{r})\omega_+R/4\sqrt{kT\delta\omega/R} \tag{21}$$

independent of whether the detection circuit is predominantly capacitive (i.e., $\omega_+RC \gg 1$) or predominantly resistive ($\omega_+RC \ll 1$): in the capacitive limit, the signal is independent of frequency whereas the noise varies inversely with frequency; in the resistive limit, the signal varies directly with frequency and the noise is independent of frequency. Equation 21 shows that the signal-to-noise ratio is frequency-dependent; thus, any definition of the detection limit must account for that frequency dependence. Equation 21 also shows that signal-to-noise ratio is proportional to ICR orbital frequency (and thus to magnetic field strength).

Note that eq 21 is valid only if the noise is dominated by Johnson noise. In that case, the current noise is frequency-independent, but the voltage noise (in the capacitive limit) varies inversely with frequency. Experimentally, except at quite low ICR frequency (<10 kHz), predominantly capacitive detection circuits typically yield frequency-independent voltage noise.[18] In that case, the present method for determining the number of ions remains valid, and signal-to-noise ratio is independent of ICR frequency. Finally, at sufficiently low frequency, detection becomes predominantly resistive (i.e., $\omega_+RC \ll 1$), and the signal varies directly with frequency. Thus, signal-to-noise ratio is expected to be independent of frequency both at high frequency (predominantly capacitive detection, voltage noise independent of frequency) and at very low frequency (predominantly resistive detection, Johnson noise dominant).

EXPERIMENTAL SECTION

Detection Circuit Capacitance. The capacitance calibration was performed by leaking benzene (at a pressure of 5×10^{-7} Torr measured on the source trap ion gauge) into the vacuum chamber. A variable-capacitance bridge was designed and inserted in parallel to the detection circuit. A variety of capacitors was added to the capacitance bridge for each experiment, and the FT/ICR magnitude-mode peak height for the molecular ion of benzene was determined by three-point quadratic interpolation. The conventional experimental event sequence was employed: trap quenching for 1 ms to remove ions, electron beam duration of 500 μs at an emission current of 4.38 μA (measured just behind the electron filament) to form new ions, single-frequency on-resonance excitation (24 $V_{\text{p-p}}$), and direct-mode broad-band detection (4K data points, 2-MHz bandwidth). Each time-domain signal was padded with 15 × 4K zeroes before fast Fourier transformation and magnitude calculation. The event sequence was repeated 2000 times to acquire a spectrum with a magnitude-mode spectral peak height-to-noise ratio of ~25:1.

Signal Level Calibration. To determine the signal level from a known voltage source, a frequency generator was added in parallel to the trap at the detection preamplifier. The experi-

---

[41] Grosshans, P. B.; Marshall, A. G. *Int. J. Mass Spectrom. Ion Processes* **1992**, *115*, 1–19.

[42] Comisarow, M. B. *Int. J. Mass Spectrom. Ion Phys.* **1981**, *37*, 251–257.

mental event sequence was the same as for the trap cross capacitance measurements except that single transients were recorded and the excitation was broadband (although single-frequency excitation could as easily be used). Single-scan magnitude-mode spectral peak heights were measured as described above as a function of the input voltage at various frequencies to determine the response of the preamplifier over the detection bandwidth. The rf voltage of the input from the frequency generator was attenuated to 181.8, 90.90, 19.80, and 9.901 μV_{p-p} for the input voltage level. The signal amplification was set to ×1, ×10, and ×100 for each of the frequencies and voltages investigated to determine the linearity of the analog-to-digital converter amplifier and its effects on the detected peak heights.

Ion Cyclotron Orbital Radius Determination. The average ion cyclotron orbital radius of the ion packet was found by measuring the magnitude ratio of the $C_6H_6^+$ signal at the third harmonic to that at the fundamental ICR orbital frequency. The experimental event sequence consisted of quench period; formation of the ions at 25-V electron beam energy at 4.32-μA emission current, 10-ms electron beam duration; single-frequency on-resonance excitation (14-V_{p-p} excitation amplitude) for 500 μs; 100-ms delay; broad-band detection (4K data points, 2-MHz bandwidth). For each measurement, 100 scans were coadded, padded with 15 × 4K zeroes, apodized with a Blackman-Harris apodization function, fast Fourier transformed, and displayed in magnitude mode. The magnitudes of the signals at the third and first harmonic frequencies were determined from their respective magnitude-mode FT/ICR mass spectral peak heights.[43] Because first and third harmonic signals may decay exponentially at different rates,[44] we set the time-domain acquisition period to be short compared to the exponential damping time constant, so that the frequency-domain relative areas of the two peaks[36] could be well-approximated by the relative frequency-domain peak heights at the first and third harmonic frequencies. The ICR orbital radius was then determined from the ratio of the third-to-first harmonic signal peak heights as described previously.[41,45] The measurement was performed five times, and the average ICR orbital radius was found to be 57% of the maximum allowed trap radius.

Ion Number Determination: Detection Limit. The number of ions contributing to the detected signal was determined as follows. All experiments were performed in heterodyne detection mode, with single-frequency excitation (14 V_{p-p}) for 500 μs and a detection period of 1 s. The number of trapped ions was varied by changing the gas pressure at constant electron beam duration (10 ms) and emission current (4.32 μA). The gas pressure at the source side of the dual trap was held to less than 2×10^{-8} Torr to ensure that the signal remained constant (i.e., undamped) throughout the detection period. Peak heights were measured exactly as before, and the noise level was determined from a software command which fits magnitude-mode baseline noise to a Rayleigh distribution histogram, for a signal-free baseline segment.[33] The noise level is reported as the standard deviation of magnitude-mode baseline noise, which is half the magnitude-mode root-mean-square baseline noise.[46] The signal level is reported as the maximum interpolated magnitude-mode peak height, based on a three-point quadratic fit to the largest three data points per peak. The above-determined signal and noise then define the experimental signal-to-noise ratio for each experiment.

RESULTS AND DISCUSSION

Calibration of the Detection Circuit Capacitance. The detection circuit capacitance arises from the coaxial feedthroughs to and from the trap, the detection plates, and the preamplifier circuit. To obtain a measurement of this capacitance, we added known capacitors to the capacitance bridge and measured the magnitude-mode FT/ICR mass spectral peak height. Because the capacitance bridge was inserted in parallel to the detection circuit, the data should follow the functional form

$$C_x = \frac{\text{constant}}{\text{ion signal}} - C_0 \qquad (22)$$

in which C_x is the measured capacitance with the capacitance bridge inserted into the detection circuit, the ion signal magnitude is determined by the software (see Experimental Section), and C_0 is the capacitance of the detection circuit. From eq 22, it is clear that the ICR signal decreases as capacitance, C_x, is added to the detection circuit. Thus, the y intercept of a plot of $(\text{signal})^{-1}$ vs the measured capacitance, C_x, yields C_0 = 51.7 pF. That value was then used in all subsequent calculations of the number of ions from a given detected signal voltage. The error in the measurement of the detection circuit capacitance is ~±10%, as determined by multiple measurements under identical conditions and statistical analysis of the linear least squares fit of eq 22.

Calibration of the Detector Response to a Known Signal Level Input. The calibration of the detection circuit to a known voltage input was performed at a variety of frequencies for several amplification levels and for several input voltages (see Experimental Section). The calibration curves at 500 kHz (not shown) for ×1, ×10, and ×100 amplification were fitted to straight lines with slightly different slopes:

$$\text{voltage} = 4.23 \times 10^{-5}(\text{magnitude-mode peak max}) \quad (\times 1 \text{ amplification}) \qquad (23)$$

$$\text{voltage} = 4.20 \times 10^{-6}(\text{magnitude-mode peak max}) \quad (\times 10 \text{ amplification}) \qquad (24)$$

$$\text{voltage} = 4.35 \times 10^{-7}(\text{magnitude-mode peak max}) \quad (\times 100 \text{ amplification}) \qquad (25)$$

The generally good agreement between these values indicates that the amplifier chain is essentially linear for this instrument. The slopes from eqs 23–25 were then used to determine the signal voltage in the following three sections.

Detection Limit. Equation 19 gives the formula for calculating the number of ions in a detected signal. The ion cyclotron orbital radius and trap cross capacitance are determined as noted above. The calibration curve of the previous section allows for the determination of the voltage level. The resulting detection limit is shown in Figure 2, in which we plot the number of detected ions as a function of the observed magnitude-mode spectral peak height-to-noise ratio. The data are described by

$$\text{no. of ions} = 59(\text{signal-to-noise ratio}) \qquad (26)$$

Extrapolating to a signal-to-noise ratio of 3:1, we find that the detection limit defined as the number of singly charged ions that produce this signal-to-noise ratio is ~177 for a 1-s time-domain data acquisition period.

Equation 16 is based on the assumption that the induced differential signal voltage arises from a point charge centered on the z-axis of the trap. If ions are in fact distributed along the z-axis, then the actual number of trapped ions will be higher than the above-listed estimate, since the induced signal voltage decreases with increasing z-distance away from the trap center.[47] Thus, the stated detection limit of ~177 singly-charged ions represents a *minimum* number of detectable

---

(43) Serreqi, A.; Comisarow, M. B. *Appl. Spectrosc.* **1987**, *41*, 288–295.

(44) Grosshans, P. B.; Marshall, A. G. *Int. J. Mass Spectrom. Ion Processes* **1991**, *107*, 49–81.

(45) Grosshans, P. B.; Shields, P. J.; Marshall, A. G. *J. Am. Chem. Soc.* **1990**, *112*, 1275–1277.

(46) Williams, C. P.; Marshall, A. G. *Anal. Chem.* **1992**, *64*, 916–923.

(47) Chen, R.; Grosshans, P. B.; Marshall, A. G. Unpublished results, 1992.

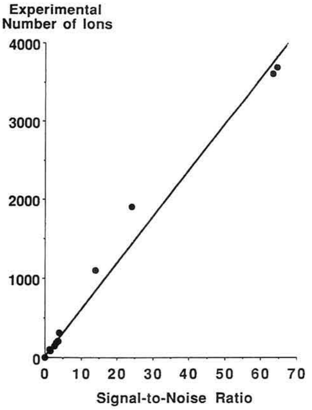

Figure 2. Plot of number of $C_6H_6^+$ ions at 3.0 T ($\sim$600-kHz ICR orbital frequency) contributing to the detected signal as a function of FT/ICR/MS magnitude-mode signal-to-noise ratio. Extrapolated to a magnitude-mode peak height-to-baseline standard deviation noise ratio of 3:1; the detection limit is 177 ions, for a 1-s detection period for ions excited to half their maximum possible ion cyclotron orbital radius in a 1.875-in.-diameter cubic trap.

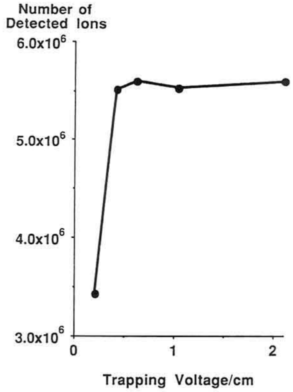

Figure 3. Plot of the maximum number of $C_6H_6^+$ ions that can be detected as a function of trapping voltage. Note that the maximum ion number is constant at $\sim 5.6 \times 10^6$ over a trapping voltage range of 0–2 V/cm. The ratio of the maximum number of trapped ions (Figure 3) to the detection limit (Figure 2) yields a dynamic range of $\sim$32 000:1.

trapped ions in a 1.875-in. cubic trap at an ion cyclotron orbital frequency of 600 kHz.

Maximum Number of Ions and Dynamic Range. The maximum number of detected trapped ions at various trapping voltages is shown in Figure 3. Under the ionization conditions for these experiments, the number of trapped ions reaches a maximum at $\geq$2-V trapping potential (1.875-in. separation between trapping electrodes). The maximum number of trapped ions is $\sim 5.6 \times 10^6$ ions. From that number and the detection limit of $\sim$177 ions, the dynamic range of the technique is $\sim 3.2 \times 10^4$. Of course, a large number of ions leads to space charge effects[22,48,49] such as Coulomb broadening of the peaks,[50–52] but in some applications it may be desirable to trap as many ions as possible when bulk samples that have minor constituents are analyzed. The number of trapped ions may be increased by elongating,[23] screening,[53] or widening the trap or by use of parametric excitation/detection[54] of ions initially formed off-axis. Minor constituent ion abundances may also be built up by ejecting all unwanted species by SWIFT[55,56] or other multiple resonance techniques.

Multiply-Charged Ions. The induced ICR signal magnitude is proportional to the number of charges per ion. Therefore, in light of the recent electrospray FT/ICR/MS work by several research groups[6,57,58] on multiply-charged proteins, it is interesting to note that the detection limit for a signal-to-noise ratio of 3:1 for a detection period of 1 s reduces to just 9 ions which carry ±20 elementary charges. Thus, FT/ICR/MS sensitivity for electrosprayed ions approaches single-ion detectability.

ACKNOWLEDGMENT

This work was supported by grants (to A.G.M.) from the National Science Foundation (CHE-90-21058) and The Ohio State University.

RECEIVED for review March 5, 1992. Accepted October 5, 1992.

---

(48) Jeffries, J. B.; Barlow, S. E.; Dunn, G. H. *Int. J. Mass Spectrom. Ion Processes* **1983**, *54*, 169–187.

(49) Rempel, D. L.; Grese, R. P.; Gross, M. L. *Int. J. Mass Spectrom. Ion Processes* **1990**, *100*, 381–395.

(50) Chen, S.-P.; Comisarow, M. B. *Rapid Commun. Mass Spectrom.* **1991**, *5*, 450–455.

(51) Chen, S.-P.; Comisarow, M. B. *Rapid Commun. Mass Spectrom.* **1992**, *6*, 1–3.

(52) Hendrickson, C. L.; Beu, S. C.; Laude, D. A., Jr. *Proceedings of the 40th American Society for Mass Spectrometry Annual Conference on Mass Spectrometry and Allied Topics*, Washington, DC, 1992; American Society for Mass Spectrometry: East Lansing, MI, 1992; pp 723–724.

(53) Wang, M.; Marshall, A. G. *Anal. Chem.* **1989**, *61*, 1288–1293.

(54) Rempel, D. L.; Ledford, E. B., Jr.; Huang, S. K.; Gross, M. L. *Anal. Chem.* **1987**, *59*, 2527–2532.

(55) Marshall, A. G.; Wang, T.-C. L.; Ricca, T. L. *J. Am. Chem. Soc.* **1985**, *107*, 7893–7897.

(56) Marshall, A. G.; Wang, T.-C. L.; Chen, L.; Ricca, T. L. In *ACS Symposium Series*; Buchanan, M. V., Ed.; American Chemical Society: Washington, DC, 1987; Vol. 359, pp 21–33.

(57) Henry, K. D.; Quinn, J. P.; McLafferty, F. W. *J. Am. Chem. Soc.* **1991**, *113*, 5447–5449.

(58) Hofstadler, S. A.; Laude, D. A., Jr. *Proceedings of the 39th American Society for Mass Spectrometry Annual Conference on Mass Spectrometry and Allied Topics*, Nashville, TN, 1991; American Society for Mass Spectrometry: East Lansing, MI, 1991; pp 1538–1539.

Numerical Analysis of Elution Behaviors of Substituted Benzoate Anions in Ion Chromatography

Naoki Hirayama* **and Tooru Kuwamoto**

Department of Chemistry, Faculty of Science, Kyoto University, Sakyo-ku, Kyoto 606-01, Japan

The influence of sample ion structures on the elutions of the sample ions in ion chromatography was studied for effective separation. In this study, the differences in the retention times of varied substituted benzoate anions were analyzed numerically by dividing the substituent effect into three terms: an *LFER-applicable effect term*, a *steric effect term*, and a *positional effect correction term*. The LFER-applicable effect term was introduced by putting the theory of linear free energy relationships (LFERs) into the relationship between the anion-exchange equilibrium constants (K_{ex}) and the dissociation constants (K_a) of the sample anions. The steric effect term was introduced by considering the influence of the hydrated sizes of the anions, which depend on the kind and number of the introduced substituents. It is expressed by using newly defined invariable *steric effect indices*. The positional effect correction term was introduced to correct the specific effect caused by the position of the substituents and expressed by using newly defined *positional effect correction indices*. Furthermore, the numerical calculation of the retention times of these anions was done.

INTRODUCTION

Ion chromatography (IC)[1] is a very effective analytical method for the separation and simultaneous determination of many ions in an aqueous solution. It is widely used in the fields of environmental, clinical and food analyses, etc.[2-4]

The numerical analysis of the retention times of sample ions is very important in order to fix the optimum chromatographic condition. Several workers[5-31] have reported on the model and the method for the numerical analysis and prediction of the retention times.

In the numerical analysis, it is the most important to consider the factors regulating the retention times of the sample ions, such as the concentration of the eluent ion or the ion-exchange equilibrium constant (K_{ex}) between the sample ion and the eluent ion.[32]

On the other hand, it is well-known that a series of equilibrium constants in one reaction of the chemical species having similar structures can often be expressed as the function of that of another reaction of an analogous species by using the theory of linear free energy relationships (LFERs).[33,34] Therefore, it is possible to treat a series of K_{ex} as the function of a series of the dissociation constants (K_a) of the sample species.

Furthermore, an *ion pair* is formed between the sample ion and the functional group in the ion exchanger. It was previously reported that K_{ex} increases with the decrease in the hydrated size of the sample ion.[35-38] From this fact, the hydrated (solvated) size of the sample ion seems to be a very important factor in the numerical analysis.

In this paper, the authors investigated the method for the numerical calculation of the retention times by using substituted benzoate anions, to which the LFERs are easily applicable,[33,34] as samples. It was found that the substituent effect of the retention times of these anions can be divided into three terms: an "LFER-applicable effect term", a "steric effect term", and a "positional effect correction term". The first is expressed as the function of the pK_a, the second as that of the kind and number of the substituents, and the last as that of the position of the substituents.

THEORY

The authors applied Leffler and Grunwald's theory of extrathermodynamic relationships[33] to numerically analyze

---

(1) Small, H.; Stevens, T. S.; Baumann, W. C. *Anal. Chem.* **1975**, *47*, 1801–1809.
(2) Gjerde, D. T.; Fritz, J. S. *Ion Chromatography*; 2nd ed.; Hüthig: Heidelberg, 1987.
(3) Tarter, J. G., Ed. *Ion Chromatography*; Marcel Decker: New York, Basel, 1987.
(4) Haddad, P. R.; Jackson, P. E. *Ion Chromatography*; Elsevier: Amsterdom, 1990.
(5) Gjerde, D. T.; Fritz, J. S. *J. Chromatogr.* **1979**, *176*, 199–206.
(6) Van Os, M. J.; Slanina, J.; De Ligny, C. L.; Hammers, W. E.; Agterdenbos, J. *Anal. Chim. Acta* **1982**, *144*, 73–82.
(7) Haddad, P. R.; Cowie, C. E. *J. Chromatogr.* **1984**, *303*, 321–330.
(8) Diop, A.; Jardy, A.; Caude, M.; Rosset, R. *Analusis* **1986**, *14*, 67–73.
(9) Jardy, A.; Caude, M.; Diop, A.; Curvale, C.; Rosset, R. *J. Chromatogr.* **1988**, *439*, 137–149.
(10) Hoover, T. B. *Sep. Sci. Technol.* **1982**, *17*, 295–305.
(11) Jenke, D. R.; Pagenkopf, G. K. *J. Chromatogr.* **1983**, *269*, 202–207.
(12) Jenke, D. R.; Pagenkopf, G. K. *Anal. Chem.* **1984**, *56*, 85–88.
(13) Jenke, D. R.; Pagenkopf, G. K. *Anal. Chem.* **1984**, *56*, 88–91.
(14) Jenke, D. R. *Anal. Chem.* **1984**, *56*, 2674–2681.
(15) Baba, Y.; Yoza, N.; Ohashi, S. *J. Chromatogr.* **1985**, *348*, 27–37.
(16) Baba, Y.; Yoza, N.; Ohashi, S. *J. Chromatogr.* **1985**, *350*, 119–125.
(17) Baba, Y.; Fukuda, M.; Yoza, N. *J. Chromatogr.* **1988**, *458*, 385–394.
(18) Baba, Y.; Ito, M. K. *J. Chromatogr.* **1989**, *485*, 647–655.
(19) Baba, Y.; Kura, G. *J. Chromatogr.* **1991**, *550*, 5–14.
(20) Rounds, M. A.; Regnier, F. E. *J. Chromatogr.* **1984**, *283*, 37–45.
(21) Rojas, J.; Ballesteros, L.; Valcarcel, M. *Microchem. J.* **1986**, *34*, 92–102.
(22) Stout, R. W.; Sivakoff, S. I.; Ricker, R. D.; Snyder, L. R. *J. Chromatogr.* **1986**, *353*, 439–463.
(23) Drager, R. R.; Regnier, F. E. *J. Chromatogr.* **1986**, *359*, 147–155.
(24) Parente, E. S.; Wetlaufer, D. B. *J. Chromatogr.* **1986**, *355*, 29–40.
(25) Rocklin, R. D.; Pohl, C. A.; Schibler, J. A. *J. Chromatogr.* **1987**, *411*, 107–119.
(26) Senyavin, M. M.; Venitsianov, E. V.; Dolgonosov, A. M. *Zh. Anal. Khim.* **1987**, *42*, 82–88.
(27) Hodges, R. S.; Robert Parker, J. M.; Mant, C. T.; Sharma, R. R. *J. Chromatogr.* **1988**, *458*, 147–167.
(28) Sasagawa, T.; Sakamoto, Y.; Hirose, T.; Yoshida, T.; Kobayashi, Y.; Sato, Y.; Koizumi, K. *J. Chromatogr.* **1989**, *485*, 533–540.
(29) Whiteley, R. D.; Berninger, J. A.; Rouhana, N.; Wang, N. H. L. *Biotechnol. Prog.* **1991**, *7*, 544–53.
(30) Maruo, M.; Hirayama, N.; Kuwamoto, T. *J. Chromatogr.* **1989**, *481*, 315–322.
(31) Hirayama, N.; Kuwamoto, T. *J. Chromatogr.* **1990**, *508*, 51–60.
(32) Gjerde, D. T.; Schmuckler, G.; Fritz, J. S. *J. Chromatogr.* **1980**, *187*, 35–45.
(33) Leffler, J. E.; Grunwald, E. *Rates and Equilibria of Organic Reactions*; John Wiley & Sons: New York and London, 1963.
(34) Inamoto, N. *Hammett Rule*; Maruzen: Toyko, 1983.
(35) Marcus, Y.; Kertes, A. S. *Ion Exchange and Solvent Extraction of Metal Complexes*; John Wiley & Sons: London, 1969.
(36) Gregor, H. P. *J. Am. Chem. Soc.* **1948**, *70*, 1293.
(37) Gregor, H. P. *J. Am. Chem. Soc.* **1951**, *73*, 642–650.
(38) Reichenberg, D. In *Ion Exchange*; Marinsky, J. A., Ed.; Marcel Dekker: New York, 1966; Vol. 1.

0003-2700/93/0365-0141$04.00/0

the elution behavior of substituted benzoate anions in IC. In this theory, the aromatic species (RY) is divided into the zone (R) containing the substituent and that (Y) containing the reaction cite. Each of these zones is regarded as contributing an additive term to the free energy and also as interacting with the other zone. The standard free energy ($\bar{G}^{\circ}_{\mathrm{RY}}$) of RY is expressed by using the independent additive terms (G_{R}, G_{Y}) and the term ($I_{\mathrm{R,Y}}$) having the dimension of energy and resulting from the interaction between R and Y as follows:

$$\begin{aligned}\bar{G}^{\circ}_{\mathrm{RY}} &= G_{\mathrm{R}} + G_{\mathrm{Y}} + I_{\mathrm{R,Y}} \\ &= G_{\mathrm{R}} + G_{\mathrm{Y}} + I_{\mathrm{R}}I_{\mathrm{Y}} \qquad (1)\end{aligned}$$

where I_{R} and I_{Y} are obtained by the assumption that $I_{\mathrm{R,Y}}$ is factorable into two terms related to R and Y.

On the dissociation of substituted benzoic acid (RCOOH)

$$\mathrm{RCOOH} \rightleftharpoons \mathrm{H^+} + \mathrm{RCOO^-} \qquad (2)$$

the change ($\Delta\bar{G}^{\circ}_{\mathrm{R,a}}$) of the free energy is shown by using eq 1 as follows:

$$\begin{aligned}\Delta\bar{G}^{\circ}_{\mathrm{R,a}} &= (\bar{G}^{\circ}_{\mathrm{RCOO^-}} + \bar{G}^{\circ}_{\mathrm{H^+}}) - \bar{G}^{\circ}_{\mathrm{RCOOH}} \\ &= (G_{\mathrm{R}} + G_{\mathrm{COO^-}} + I_{\mathrm{R}}I_{\mathrm{COO^-}}) + \bar{G}^{\circ}_{\mathrm{H^+}} - (G_{\mathrm{R}} + \\ &\qquad G_{\mathrm{COOH}} + I_{\mathrm{R}}I_{\mathrm{COOH}}) \\ &= \bar{G}^{\circ}_{\mathrm{H^+}} + G_{\mathrm{COO^-}} - G_{\mathrm{COOH}} + I_{\mathrm{R}}(I_{\mathrm{COO^-}} - I_{\mathrm{COOH}}) \qquad (3)\end{aligned}$$

where subscript "a" denotes the dissociation reaction. Therefore, the substituent effect ($\delta_{\mathrm{R}}\Delta\bar{G}^{\circ}_{\mathrm{a}}$) on the dissociation reaction of RCOOH is shown as follows:

$$\begin{aligned}\delta_{\mathrm{R}}\Delta\bar{G}^{\circ}_{\mathrm{a}} &= \Delta\bar{G}^{\circ}_{\mathrm{R,a}} - \Delta\bar{G}^{\circ}_{\mathrm{R_0,a}} \\ &= (I_{\mathrm{R}} - I_{\mathrm{R_0}})(I_{\mathrm{COO^-}} - I_{\mathrm{COOH}}) \qquad (4)\end{aligned}$$

where subscript "$\mathrm{R_0}$" shows the unsubstituted species.

On the other hand, in the following anion-exchange equilibrium in the anion-exchange column of IC

$$\mathrm{E{-}FG} + \mathrm{RCOO^-} \rightleftharpoons \mathrm{E^-} + \mathrm{RCOO{-}FG} \qquad (5)$$

where $\mathrm{E^-}$ denotes the eluent anion having a charge of −1, and FG denotes the functional group on the anion-exchanger, the standard free enegy ($\bar{G}^{\circ}_{\mathrm{RCOO-FG}}$) of the retained anion (RCOO–FG) cannot be expressed by using eq 1 because the equation has no term for the hydrated size of the anion which governs the stability of the ion pair.[39,40] For the accurate analysis of $\bar{G}^{\circ}_{\mathrm{RCOO-FG}}$, eq 1 has to be corrected by adding terms to estimate the steric effect, peculiar to an *ion pair*, governed by the hydrated size.

In the theory of extrathermodynamic relationships,[33] when there is more than one mechanism of interaction between two zones of the species, the use of separate interaction terms corresponding to respective mechanisms is allowable. Accordingly, in this paper, the two interaction terms independent of $I_{\mathrm{R,COO-FG}}$ ($=I_{\mathrm{R}}I_{\mathrm{COO-FG}}$) were added to eq 1 as follows:

$$\begin{aligned}\bar{G}^{\circ}_{\mathrm{RCOO-FG}} &= G_{\mathrm{R}} + G_{\mathrm{COO-FG}} + I_{\mathrm{R,COO-FG}} + I'_{\mathrm{R,COO-FG}} + \\ &\qquad I''_{\mathrm{R,COO-FG}} \\ &= G_{\mathrm{R}} + G_{\mathrm{COO-FG}} + I_{\mathrm{R}}I_{\mathrm{COO-FG}} + I'_{\mathrm{R,COO-FG}} + \\ &\qquad I''_{\mathrm{R,COO-FG}} \qquad (6)\end{aligned}$$

where $I'_{\mathrm{R,COO-FG}}$ (called the steric effect term) is used to estimate the steric effect caused by the hydration and decided only by the kind and the number of the substituents. $I''_{\mathrm{R,COO-FG}}$ (called the positional effect correction term) is used to correct the steric effect caused specifically by the position of the substituents. On the other hand, $I_{\mathrm{R,COO-FG}}$ (called the LFER-applicable effect term) shows the inductive and resonance effects usually considered in LFERs. The effects are regarded as independent of the steric effect.

By using eq 6, the change ($\Delta\bar{G}^{\circ}_{\mathrm{R,ex}}$) of the free energy in the anion-exchange reaction is shown as follows:

$$\begin{aligned}\Delta\bar{G}^{\circ}_{\mathrm{R,ex}} &= (\bar{G}^{\circ}_{\mathrm{E^-}} + \bar{G}^{\circ}_{\mathrm{E-FG}}) + G_{\mathrm{COO-FG}} - G_{\mathrm{COO^-}} + \\ &\qquad I_{\mathrm{R}}(I_{\mathrm{COO-FG}} - I_{\mathrm{COO^-}}) + I'_{\mathrm{R,COO-FG}} + I''_{\mathrm{R,COO-FG}} \qquad (7)\end{aligned}$$

where subscript "ex" denotes the anion-exchange reaction.

By defining

$$I'_{\mathrm{R_0,COO-FG}} \equiv 0 \qquad (8)$$

$$I''_{\mathrm{R_0,COO-FG}} \equiv 0 \qquad (9)$$

the substituent effect ($\delta_{\mathrm{R}}\Delta\bar{G}^{\circ}_{\mathrm{ex}}$) on the anion-exchange reaction is expressed from eqs 4 and 7 as follows:

$$\begin{aligned}\delta_{\mathrm{R}}\Delta\bar{G}^{\circ}_{\mathrm{ex}} &= \Delta\bar{G}^{\circ}_{\mathrm{R,ex}} - \Delta\bar{G}^{\circ}_{\mathrm{R_0,ex}} \\ &= (I_{\mathrm{R}} - I_{\mathrm{R_0}})(I_{\mathrm{COO-FG}} - I_{\mathrm{COO^-}}) + I'_{\mathrm{R,COO-FG}} + \\ &\qquad I''_{\mathrm{R,COO-FG}} \\ &= \frac{I_{\mathrm{COO-FG}} - I_{\mathrm{COO^-}}}{I_{\mathrm{COO^-}} - I_{\mathrm{COOH}}}\delta_{\mathrm{R}}\Delta\bar{G}^{\circ}_{\mathrm{a}} + I'_{\mathrm{R,COO-FG}} + \\ &\qquad I''_{\mathrm{R,COO-FG}} \qquad (10)\end{aligned}$$

Since $I'_{\mathrm{R\,COO-FG}}$ is determined by the kind and number of the substituents (X), the term can be expressed as I'_{X}. The steric effect of each substituent is considered to be independent, as follows:

$$I'_{\mathrm{X}} = \sum_j n_{\mathrm{X}_j}\mathbf{i}'_{\mathrm{X}_j} \qquad (11)$$

where $\mathbf{i}'_{\mathrm{X}_j}$ denotes steric effect factor of X_j and n_{X_j} is the number of X_j.

On the other hand, $I''_{\mathrm{R,COO-FG}}$ is determined by the position of the substituents. If the steric effect of a meta substituent is used as the standard, the substituent effects of the ortho substituent, para substituent, and neighboring substituents have to be corrected. In other words, this term is divided into an "ortho-effect correction term" ($I''_{o\text{-}\mathrm{X}}$), a "para-effect correction term" ($I''_{p\text{-}\mathrm{X}}$) and a "neighboring-effect correction term" ($I''_{\mathrm{X\text{-}X'}}$), as follows:

$$I''_{\mathrm{R,COO-FG}} = I''_{o\text{-}\mathrm{X}} + I''_{p\text{-}\mathrm{X}} + I''_{\mathrm{X\text{-}X'}} \qquad (12)$$

The correction of each substituent(s) is considered to be independent, as follows:

$$I''_{o\text{-}\mathrm{X}} = \sum_j n_{o\text{-}\mathrm{X}_j}\mathbf{i}''_{o\text{-}\mathrm{X}_j} \qquad (13)$$

$$I''_{p\text{-}\mathrm{X}} = \sum_j n_{p\text{-}\mathrm{X}_j}\mathbf{i}''_{p\text{-}\mathrm{X}_j} \qquad (14)$$

$$I''_{\mathrm{X\text{-}X'}} = \sum_j n_{\mathrm{X}_j\text{-}\mathrm{X}_j'}\mathbf{i}''_{\mathrm{X}_j\text{-}\mathrm{X}_j'} \qquad (15)$$

where $\mathbf{i}''_{o\text{-}\mathrm{X}_j}$, $\mathbf{i}''_{p\text{-}\mathrm{X}_j}$, and $\mathbf{i}''_{\mathrm{X}_j\text{-}\mathrm{X}_j'}$ denote positional effect correction factors and $n_{o\text{-}\mathrm{X}_j}$, $n_{p\text{-}\mathrm{X}_j}$, and $n_{\mathrm{X}_j\text{-}\mathrm{X}_j'}$ are the numbers of respective substituent(s). By substituting eqs 11–15 into

---

(39) Kay, R. L.; Evans, D. F.; Matesich, S. M. F. In *Solute-Solvent Interactions*; Coetzec, J. F., Ritchie, C. D., Eds.; Marcel Decker: New York, 1976; Vol 2, Chapter 10.

(40) Okazaki, S.; Sakamoto, I. *Solvents and Ions*; San-ei: Kyoto, 1990.

eq 10

$$\delta_R\Delta\bar{G}^\circ{}_{ex} = \frac{I_{COO\text{-}FG} - I_{COO\text{-}}}{I_{COO\text{-}} - I_{COOH}}\delta_R\Delta\bar{G}^\circ{}_a + I'_X + I''_{o\text{-}X} + I''_{p\text{-}X} + I''_{X\text{-}X'}$$

$$= \frac{I_{COO\text{-}FG} - I_{COO\text{-}}}{I_{COO\text{-}} - I_{COOH}}\delta_R\Delta\bar{G}^\circ{}_a + \sum_j n_{X_j}\mathbf{i}_{X_j} + \sum_j n_{o\text{-}X_j}\mathbf{i}''_{o\text{-}X_j} + \sum_j n_{p\text{-}X_j}\mathbf{i}''_{p\text{-}X_j} + \sum_j n_{X_j\text{-}X_j'}\mathbf{i}''_{X_j\text{-}X_j'} \quad (16)$$

From the thermodynamic relationships

$$\Delta\bar{G}^\circ{}_{R,a} = -RT_1 \ln K_a(R) \quad (17)$$

$$\Delta\bar{G}^\circ{}_{R,ex} = -RT_2 \ln K_{ex}(R) \quad (18)$$

where T_1 and T_2 show the temperatures, and from the following ion-chromatographic relationship[32]

$$t_R'(R) = k'(R)t_0 = K_{ex}(R)\frac{\text{Cap}}{[E^-]}\frac{w}{v_0}t_0 \quad (19)$$

where $t_R'(R)$ is the retention time of sample $RCOO^-$ anion, $k'(R)$ is the capacity factor of $RCOO^-$, Cap is the column capacity, w is the weight of anion exchanger in column, v_0 is the column dead volume, and t_0 is the void time, the following equation is obtained for the fixed eluting condition:

$$\log t_R'(R) - \log t_R'(R_0) = \log K_{ex}(R) - \log K_{ex}(R_0) = \frac{T_1}{T_2}\frac{I_{COO\text{-}FG} - I_{COO\text{-}}}{I_{COOH} - I_{COO\text{-}}}\{pK_a(R) - pK_a(R_0)\} - \frac{1}{2.303RT_2}\left(\sum_j n_{X_j}\mathbf{i}'_{X_j} + \sum_j n_{o\text{-}X_j}\mathbf{i}''_{o\text{-}X_j} + \sum_j n_{p\text{-}X_j}\mathbf{i}''_{p\text{-}X_j} + \sum_j n_{X_j\text{-}X_j'}\mathbf{i}''_{X_j\text{-}X_j'}\right) \quad (20)$$

By defining the "LFER–applicable effect constant" ($-\rho'$), the "adjusted steric effect factors" (i'_{X_j}), and the "adjusted positional effect correction factors" ($i''_{o\text{-}X_j}$, $i''_{p\text{-}X_j}$, and $i''_{X_j\text{-}X_j'}$) as follows

$$-\rho' = \frac{T_1}{T_2}\frac{I_{COO\text{-}FG} - I_{COO\text{-}}}{I_{COOH} - I_{COO\text{-}}} \quad (21)$$

$$i'_{X_j}\ (\text{or } i''_{o\text{-}X_j}, i''_{p\text{-}X_j}, i''_{X_j\text{-}X_j'}) = -\frac{1}{2.303RT_2}\mathbf{i}'_{X_j}\ (\text{or } \mathbf{i}''_{o\text{-}X_j}, \mathbf{i}''_{p\text{-}X_j}, \mathbf{i}''_{X_j\text{-}X_j'}) \quad (22)$$

where the symbol of $-\rho'$ having a minus sign corresponds to the Hammett $\rho\sigma$ relationship, and by substituting them into eq 20, the following equation is obtained:

$$\log t_R'(R) - \log t_R'(R_0) = (-\rho')\{pK_a(R) - pK_a(R_0)\} + \left(\sum_j n_{X_j}i'_{X_j} + \sum_j n_{o\text{-}X_j}i''_{o\text{-}X_j} + \sum_j n_{p\text{-}X_j}i''_{p\text{-}X_j} + \sum_j n_{X_j\text{-}X_j'}i''_{X_j\text{-}X_j'}\right) \quad (23)$$

In practice, the values of i'_{X_j}, $i''_{o\text{-}X_j}$, $i''_{p\text{-}X_j}$, and $i''_{X_j\text{-}X_j'}$ are changed by changing the eluent condition, such as the kind or concentration of the eluent anion or the pH, which influences the ionic strength of the mobile phase or the solvation of the sample anions in the column. However, these values are proportional to each other. Therefore, the invariable "steric effect indices" (j'_{X_j}) and the "positional effect correction indices" ($j''_{o\text{-}X_j}$, $j''_{p\text{-}X_j}$, $j''_{X_j\text{-}X_j'}$) are defined as follows:

$$j'_{X_j}\ (\text{or } j''_{o\text{-}X_j}, j''_{p\text{-}X_j}, j''_{X_j\text{-}X_j'}) = \frac{i'_{X_j}\ (\text{or } i''_{o\text{-}X_j}, i''_{p\text{-}X_j}, i''_{X_j\text{-}X_j'})}{i'_{X_I}} \quad (24)$$

where X_I denotes the fixed substituent. (In this paper, Cl was selected as X_I.) In this case, eq 23 is rewritten as follows:

$$\log t_R'(R) - \log t_R'(R_0) = (-\rho')\{pK_a(R) - pK_a(R_0)\} + i'_{X_I}\left(\sum_j n_{X_j}j'_{X_j} + \sum_j n_{o\text{-}X_j}j''_{o\text{-}X_j} + \sum_j n_{p\text{-}X_j}j''_{p\text{-}X_j} + \sum_j n_{X_j\text{-}X_j'}j''_{X_j\text{-}X_j'}\right) \quad (25)$$

EXPERIMENTAL SECTION

Apparatus. A Tosoh Model HLC-601 ion chromatograph system made up of a computer-controlled pump, a sample injector (100 μL), and an oven was used. For the retentions of substituted benzoate anions, two columns (50-mm × 4.6-mm i.d.) packed with different anion exchangers were used. One of them was a Tosoh Model TSKgel IC-Anion-PW (polymethacrylate gel base, particle size 10 μm, capacity 0.03 mequiv/g), and the other was a Tosoh Model TSKgel IC-Anion-SW (silica gel base, particle size 5 μm, capacity 0.4 mequiv/g). The flow rate was maintained at 1.0 mL/min under a pressure of 30–60 kg/cm². The column was placed in the oven regulated at 30 °C. The peaks were detected by a Tosoh Model UV-8 Model II ultraviolet detector at a wavelength of 254 nm and recorded by a Shimadzu Model Chromatopack C-R1A.

Eluents. Each stock solution of 1 M hydrochloric acid (HCl), 100 mM perchloric acid ($HClO_4$), 1 M sulfuric acid (H_2SO_4), and 1 M acetic acid (HOAc) was prepared by diluting the concentrated acid. Each stock solution of 1 M oxalic acid (H_2Ox) and 1 M tris(hydroxymethyl)aminomethane (Tris) was prepared by dissolving the reagent in distilled water.

Each eluent was prepared by mixing the acid stock solution and the Tris stock solution and by diluting the mixed solution with distilled water after which the eluent was deaerated.

Standard Sample Solutions. Table I shows the substituted benzoates used in this study.[41–43] The stock solutions (50 mM) of substituted benzoates were prepared by dissolving each sodium salt in distilled water or by mixing each acid and equivalent sodium hydroxide and then diluting the mixed solution with distilled water. Working standard solutions (0.2 mM) were prepared by diluting the stock solutions with distilled water.

Calculation of the Factors and the Indices. When the substituents of the sample anions are only one kind (X), eq 23 is simplified as follows:

$$\log t_R'(R) = \{\log t_R'(R_0) - (-\rho')pK_a(R_0)\} + (-\rho')pK_a(R) + n_X i'_X + n_{o\text{-}X}i''_{o\text{-}X} + n_{p\text{-}X}i''_{p\text{-}X} + n_{X\text{-}X}i''_{X\text{-}X}$$
$$= A + (-\rho')pK_a(R) + n_X i'_X + n_{o\text{-}X}i''_{o\text{-}X} + n_{p\text{-}X}i''_{p\text{-}X} + n_{X\text{-}X}i''_{X\text{-}X} \quad (26)$$

where A is a constant determined by the experimental condition.

The values of $-\rho'$ and A were regressively calculated from the retention times of unsubstituted and X_S-substituted benzoate anions by using the following equation:

$$\log t_R'(R) = A + (-\rho')pK_a(R) + n_{X_S}i'_{X_S} \quad (27)$$

where X_S is the substituent in which all the values of $i''_{o\text{-}X_S}$, $i''_{p\text{-}X_S}$, and $i''_{X_S\text{-}X_S}$ are negligible. (In this paper, Cl was selected as X_S.) After that, i'_X, $i''_{o\text{-}X}$, $i''_{p\text{-}X}$, and $i''_{X\text{-}X}$ on arbitrary X were regressively calculated by using eq 26 with substituting the calculated values of $-\rho'$ and A. Finally, j'_X, $j''_{o\text{-}X}$, $j''_{p\text{-}X}$, and $j''_{X\text{-}X}$ were determined by using eq 24.

---

(41) Dean, J. A., Ed. *Lange's Handbook of Chemistry*, 13th ed.; McGraw-Hill: New York, 1985.

(42) Buckingham, J., Ed. *Dictionary of Organic Compounds*, 5th ed.; Chapman and Hall: New York, 1982.

(43) Davis, M. M.; Hetzer, H. B. *J. Phys. Chem.* **1957**, *61*, 123–125.

Table I. Substituted Benzoic Acids Used in This Study and Their Retention Times (t_R')

				column			
				IC-Anion-PW		IC-Anion-SW	
no.	substituent	name	pK_a (25 °C)[41]	t_R'/min[c]	log t_R'	t_R'/min[c]	log t_R'
1	(H)	benzoic acid	4.20	2.42	0.384	3.80	0.580
2	2-Cl	*o*-chlorobenzoic acid	2.88	2.14	0.330	3.03	0.481
3	3-Cl	*m*-chlorobenzoic acid	3.83	9.87	0.994	7.18	0.856
4	4-Cl	*p*-chlorobenzoic acid	3.99	9.43	0.975	6.36	0.803
5	2,4-Cl_2	2,4-dichlorobenzoic acid	2.68[a]	7.11	0.852	4.59	0.662
6	2,5-Cl_2	2,5-dichlorobenzoic acid	2.47[a]	6.83	0.834	4.54	0.657
7	2,6-Cl_2	2,6-dichlorobenzoic acid	1.59[a]	2.69	0.430	3.05	0.484
8	3,4-Cl_2	3,4-dichlorobenzoic acid	3.64[b]	34.74	1.541	12.39	1.093
9	2-NO_2	*o*-nitrobenzoic acid	2.18	1.69	0.228	2.63	0.420
10	3-NO_2	*m*-nitrobenzoic acid	3.46	6.83	0.834	3.92	0.593
11	4-NO_2	*p*-nitrobenzoic acid	3.44	7.03	0.847	3.06	0.486
12	2,4-$(NO_2)_2$	2,4-dinitrobenzoic acid	1.43	4.69	0.671	2.05	0.312
13	3,4-$(NO_2)_2$	3,4-dinitrobenzoic acid	2.82	30.89	1.490	4.82	0.683
14	3,5-$(NO_2)_2$	3,5-dinitrobenzoic acid	2.85	15.49	1.190	2.59	0.413
15	2-OCH_3	*o*-anisic acid	4.09	1.03	0.013	2.24	0.350
16	3-OCH_3	*m*-anisic acid	4.08	3.62	0.559	5.07	0.705
17	4-OCH_3	*p*-anisic acid	4.49	3.28	0.516	5.07	0.705
18	3,4-$(OCH_3)_2$	3,4-dimethoxybenzoic acid	4.44	2.31	0.364	4.57	0.660
19	2-CH_3	*o*-methylbenzoic acid	3.90	1.59	0.201	2.39	0.378
20	3-CH_3	*m*-methylbenzoic acid	4.27	3.91	0.592	5.26	0.721
21	4-CH_3	*p*-methylbenzoic acid	4.36	3.85	0.585	5.54	0.744
22	3,4-$(CH_3)_2$	3,4-dimethylbenzoic acid	4.41	6.39	0.806	8.19	0.913
23	2-NH_2	anthranilic acid	4.79	3.01	0.479	4.19	0.622
24	3-NH_2	*m*-aminobenzoic acid	4.79	1.66	0.220	3.33	0.522
25	4-NH_2	*p*-aminobenzoic acid	4.85	1.67	0.223	3.31	0.520
26	3,5-$(NH_2)_2$	3,5-diaminobenzoic acid	5.30	1.13	0.053	3.15	0.498
27	2-I	*o*-iodobenzoic acid	2.86	3.64	0.561	3.84	0.584
28	3-I	*m*-iodobenzoic acid	3.86	24.08	1.382	13.08	1.117
29	4-I	*p*-iodobenzoic acid	4.00	24.58	1.391	11.83	1.073
30	2-OH	salicylic acid	2.98	15.62	1.194	9.74	0.989
31	3-OH	*m*-hydroxybenzoic acid	4.08	3.40	0.531	4.65	0.667
32	4-OH	*p*-hydroxybenzoic acid	4.58	3.03	0.481	4.48	0.651
33	2,4-$(OH)_2$	β-resorcylic acid	3.29	17.06	1.232	13.54	1.132
34	2,6-$(OH)_2$	γ-resorcylic acid	1.30	92.89	1.968	23.52	1.371
35	3,4-$(OH)_2$	protocatechuic acid	4.48	3.29	0.517	NE[d]	
36	3,5-$(OH)_2$	α-resorcylic acid	4.04	4.99	0.698	6.77	0.831
37	3,4,5-$(OH)_3$	gallic acid	4.19	3.71	0.569	NE[d]	

[a] Reference 42. [b] Reference 43. [c] Eluent: 40 mM HCl–Tris, pH 7.0. [d] Not eluted.

RESULTS AND DISCUSSION

Table I shows the measured retention times of the substituted benzoate anions in 40 mM HCl–Tris (pH 7.0) as eluent. From these data, it was found that the log $t_R'(R)$ is not obtained as a simple function of the pK_a(R) and that none of the Hammett $\rho\sigma$, $\rho\sigma^+$, $\rho\sigma^-$, and $\rho\sigma^0$ relationships are applicable to log $t_R'(R)$ on IC. Therefore, it was necessary to consider the steric effect.

Selection of X_S. The selection of X_S is necessary for the linear regression calculation of eq 27. In this paper, Cl was selected as X_S because the substituent is relatively small and does not form hydrogen bonding and because the pK_a values of many Cl-substituted benzoates are easily available.

By using data nos. 1–8 in Table I, the regression calculation of eq 27 was performed. The results and correlation coefficients (r) were as follows:

For IC-Anion-PW

$$\log t_R'(R) = -1.961 + 0.562\mathrm{p}K_a(R) + 0.710 n_{Cl} \quad (28)$$

$$r = 0.986$$

For IC-Anion-SW

$$\log t_R'(R) = -0.693 + 0.305\mathrm{p}K_a(R) + 0.314 n_{Cl} \quad (29)$$

$$r = 0.963$$

Figure 1 shows the comparison of the regressively calculated values with the measured values on the IC-Anion-PW column. From the facts, it was found that the selection of the Cl substituent as X_S is valid for the regression calculation.

Calculation of the Factors and the Indices. The values of i'_X, $i''_{o\text{-}X}$, $i''_{p\text{-}X}$, and $i''_{X\text{-}X}$ were regressively calculated by using eq 26. After that, j'_X, $j''_{o\text{-}X}$, $j''_{p\text{-}X}$, and $j''_{X\text{-}X}$ were calculated by using eq 24 and the value of i'_{Cl} ($=i'_{X_I}$). Table II shows the calculated values. Several adjusted positional effect correction factors ($i''_{o\text{-}X}$, $i''_{p\text{-}X}$, $i''_{X\text{-}X}$) and positional effect correction indices ($j''_{o\text{-}X}$, $j''_{p\text{-}X}$, $j''_{X\text{-}X}$) were neglected because these calculated values were very small.

Constancy of the Indices. Table III shows the results of the linear regression calculations of the indices calculated from the data in several eluents vs those indices in the standard eluent, 40 mM HCl–Tris (pH 7.0). The indices were invariable in arbitrary eluent conditions, as shown in the table.

Indices in Various Corrections. (a) Steric Effect Indices (j'_X). The steric effect term is determined by the kind and number of substituents. As shown in Table II, the value of j'_X on X = NH_2 (hydrophilic substituent) was negative because the hydrated size of this substituent is large. On the contrary, that on X = I (hydrophobic substituent) was relatively large because the hydrated size of this substituent is small. From these results, it was found that the values of j'_X are mainly determined by the hydration of X.

(b) Positional Effect Correction Indices ($j''_{o\text{-}X}$, $j''_{p\text{-}X}$, $j''_{X\text{-}X'}$). Although the steric effect term does not contain the effect caused by the position of the substituents, the hydrated size or the charge distribution of the anion is affected by the

Table II. Calculated Values of Adjusted Steric Effect Factors i'_X, Adjusted Positional Effect Correction Factors $i''_{o\text{-}X}$, $i''_{p\text{-}X}$, $i''_{X\text{-}X'}$, Steric Effect Indices j'_X, and Positional Effect Correction Indices $j''_{o\text{-}X}$, $j''_{p\text{-}X}$, $j''_{X\text{-}X'}$ (Eluent: 40 mM HCl–Tris, pH 7.0)

substituent (X)	i'_X	$i''_{o\text{-}X}$	$i''_{p\text{-}X}$	$i''_{X\text{-}X}$	j'_X	$j''_{o\text{-}X}$	$j''_{p\text{-}X}$	$j''_{X\text{-}X}$
Column: IC-Anion-PW ($A = -1.961$, $-\rho' = 0.562$)								
Cl	0.710	0^a	0^a	0^a	1.000^c	0^a	0^a	0^a
NO_2	0.808	0.183	0^a	0.249	1.138	0.258	0^a	0.351
OCH_3	0.227	−0.552	−0.273	−0.351	0.320	−0.777	−0.385	−0.494
CH_3	0.138	−0.168	0^a	0^a	0.194	−0.237	0^a	0^a
NH_2	−0.497	0.245	0^a	*b*	−0.700	0.345	0^a	*b*
I	1.139	−0.224	0^a	*b*	1.604	−0.315	0^a	*b*
OH	0.188	1.381	−0.384	0^a	0.265	1.945	−0.541	0^a
Column: IC-Anion-SW ($A = -0.693$, $-\rho' = 0.305$)								
Cl	0.314	0^a	0^a	0^a	1.000^c	0^a	0^a	0^a
NO_2	0.138	0.302	0^a	0.240	0.439	0.962	0^a	0.764
OCH_3	0.154	−0.358	−0.125	−0.184	0.490	−1.140	−0.398	−0.586
CH_3	0.124	−0.243	0^a	0^a	0.395	−0.774	0^a	0^a
NH_2	−0.227	0.081	0^a	*b*	−0.723	0.257	0^a	*b*
I	0.590	−0.185	0^a	*b*	1.879	−0.589	0^a	*b*
OH	0.140	0.686	−0.187	*b*	0.446	2.185	−0.596	*b*

[a] Neglected. [b] Cannot be calculated. [c] Defined as unity.

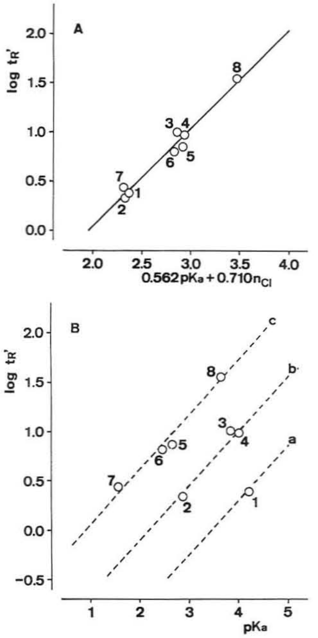

Figure 1. Comparison of the regressively calculated log t_R'(R) of Cl-substituted benzoate anions with the measured values. Eluent, 40 mM HCl–Tris, pH 7.0. Column, TSKgel IC-Anion-PW. (A) Relationship between log t_R'(R) and (0.562pK_a(R) + 0.710n_{Cl}). (B) Relationship between log t_R'(R) and pK_a(R). Key: (open circles) measured data (sample, shown in Table I); (solid line, A) the regressively calculated result (eq 28); (broken lines, B) the result obtained by substituting n_{Cl} = (a) 0, (b) 1, and (c) 2, respectively, into eq 28.

steric interaction specifically caused by the position. Therefore, the positional effect correction term has to be carried out as a function of the position of the substituents.

(i) Correction of the Ortho Effect ($j''_{o\text{-}X}$). When substituent X is situated in the ortho position of benzoate, some specific effects between X and COO^-, such as steric repulsion, steric inhibition of resonance, and intramolecular hydrogen bonding, are considered. These effects cause a change in the hydrated size or the charge distribution.

Table III. Relationship between the j'_X, $j''_{o\text{-}X}$, $j''_{p\text{-}X}$, and $j''_{X\text{-}X'}$ Values in Several Eluents and Those in the Standard Eluent Using a Linear Regression Calculation (Standard Eluent: 40 mM Cl^- (pH 7.0))

$$j'_X \text{ (or } j''_{o\text{-}X}, j''_{p\text{-}X}, j''_{X\text{-}X'}) = B + Cj'_X \text{ (or } j''_{o\text{-}X}, j''_{p\text{-}X}, j''_{X\text{-}X'}) \text{ (standard)}$$

	column					
	IC-Anion-PW			IC-Anion-SW		
eluent[a]	*B*	*C*	r^b	*B*	*C*	r^b
10 mM ClO_4^-	0.031	0.973	0.998	0.027	0.970	0.996
100 mM OAc^-	−0.006	1.007	1.000	0.009	0.986	0.999
50 mM Ox^{2-}	−0.009	1.011	1.000	0.006	0.987	1.000
60 mM SO_4^{2-}	−0.013	1.019	0.999	0.000	0.992	0.999
20 mM Cl^-	0.005	0.987	1.000	0.016	0.984	0.999
80 mM Cl^-	−0.005	1.006	1.000	0.007	0.995	1.000
40 mM Cl^- (pH 8.0)[c]	−0.001	0.998	1.000			
40 mM Cl^- (pH 9.0)[c]	0.002	0.998	1.000			

[a] pH = 7.0 except where specifically mentioned. [b] Correlation coefficient. [c] Calculated without using j'_{OH}, $j''_{o\text{-}OH}$, and $j''_{p\text{-}OH}$ values.

The value of $j''_{o\text{-}OH}$ was positive and very large because the intramolecular hydrogen bonding between OH and COO^- interferes with the hydration of the anion and results in the small hydrated size of the anion, as shown in Table II. The value of $j''_{o\text{-}NH_2}$ was positive but relatively small because the intramolecular hydrogen bonding between NH_2 and COO^- is weaker than the bonding between OH and COO^-.

When X is relatively small and does not result in hydrogen bonding with COO^- or COOH, such as Cl, the value of $j''_{o\text{-}X}$ is very small and negligible.

(ii) Correction of the Para Effect ($j''_{p\text{-}X}$). In general, the steric effect of the *p*-X substituent is similar to that of the *m*-X substituent. $j''_{p\text{-}X}$, which is used for the correction of the steric effect of *p*-X obtained by defining that of *m*-X as standard, is very small and negligible. However, when X is an electron-releasing substituent, such as OCH_3 and OH, the value of $j''_{p\text{-}X}$ is not negligible, as shown in Table II.

The para-electron-releasing-substituted benzoic acid has a dipolar resonance structure in water[33] and is stabilized. The dissociation of the acid is depressed by the stability. As shown in Table I, the pK_a values[41] of *p*-anisic acid and *p*-hydroxybenzoic acid are actually 0.4–0.5 higher than those of the meta-substituted acids.

On the other hand, the structure of the *ion pair* between the para-substituted benzoate anion and the functional group

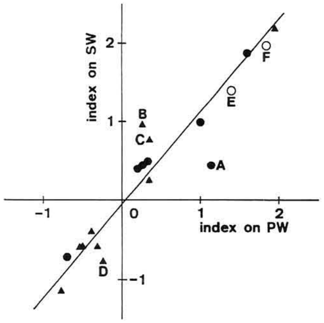

Figure 2. Relationship between the indices of the IC-Anion-SW column and those of the IC-Anion-PW column. The eluent is the same as in Figure 1. Data: (●) j'_X (A, j'_{NO_2}); (▲) $j''_{o\text{-}X}$, $j''_{p\text{-}X}$, j''_{X-X} (B, $j''_{o\text{-}NO_2}$; C, $j''_{NO_2-NO_2}$; D, $j''_{o\text{-}CH_3}$); (○) E, ($j'_{NO_2} + j''_{o\text{-}NO_2}$) and F, ($2j'_{NO_2} + j''_{NO_2-NO_2}$). The line is regressively calculated result (except for data A–F, eq 30).

in the anion exchanger is not a dipolar resonance structure. Therefore, for the expression of K_{ex} using K_a, it is necessary to correct the effect related to the dipolar resonance structure by using $j''_{p\text{-}X}$.

(iii) Correction of the Neighboring Effect ($j''_{X\text{-}X'}$). When the two neighboring substituents, X and X′, are relatively large, steric repulsion often occurs between them. This phenomenon is similar to the case of an ortho-substituted benzoate. Therefore the values of $j''_{NO_2-NO_2}$ and $j''_{OCH_3-OCH_3}$ were not negligible, as shown in Table II.

Indices of Different Ion Exchangers. In the two anion exchangers, IC-Anion-PW and IC-Anion-SW, having the same functional group, the diethylmethylammonium cation, the elution behaviors of sample anions are estimated to be similar to each other.

Figure 2 shows the relationship between the indices of IC-Anion-SW and those of IC-Anion-PW. The line was regressively calculated, except for j'_{NO_2}, $j''_{o\text{-}NO_2}$, $j''_{NO_2-NO_2}$, and $j''_{o\text{-}CH_3}$, as follows:

$$j'_X \text{ (or } j''_{o\text{-}X}, j''_{p\text{-}X}, j''_{X\text{-}X'}) \text{ (IC-Anion-SW)} = 1.159 j'_X \text{ (or } j''_{o\text{-}X}, j''_{p\text{-}X}, j''_{X\text{-}X'}) \text{ (IC-Anion-PW)} - 0.018 \quad (30)$$

$$r = 0.991$$

And it was found that the indices of the two anion exchangers are generally similar to each other.

However, the data for j'_{NO_2}, $j''_{o\text{-}NO_2}$, and $j''_{NO_2-NO_2}$ were not near the line. It seems that the distribution of π-electrons in the benzene ring is changed by the resonance between NO_2 and the ring on the same plane. Accordingly, the electrostatic interaction between the anion exchanger and benzene ring is changed.

However, with o-NO_2 or two neighboring NO_2, the change in this distribution of π-electrons is interfered with by the steric inhibition of resonance. The sums of the steric effect index and the positional effect correction indices, ($j'_{NO_2} + j''_{o\text{-}NO_2}$) and ($2j'_{NO_2} + j''_{NO_2-NO_2}$), were near the line, as shown in the figure.

The reason for the unfitness of $j''_{o\text{-}CH_3}$ is not known.

Numerical Calculation of Retention Times. From the above, it was found that the retention times of the sample (substituted benzoate) anions in any eluent condition can be numerically calculated by substituting the values of A, $-\rho'$, and i'_{Cl} ($=i'_{X_1}$) and the indices of j'_X, $j''_{o\text{-}X}$, $j''_{p\text{-}X}$, and $j''_{X\text{-}X'}$ into eq 25.

Figure 3 and Table IV show the comparison between the calculated and the observed retention times of substituted benzoate anions in 5 mM NaOH eluent (pH 11.7) on the IC-Anion-PW column. The correlation coefficients (r) of log t_R'(R) and t_R'(R) were 0.997 and 0.994, respectively. It was found that this method is very effective in the numerical calculation of the retention times of substituted benzoate anions.

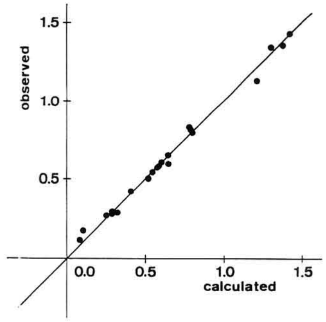

Figure 3. Relationship between the calculated and observed log t_R'(R) of substituted benzoate anions. Conditions: eluent, 5 mM NaOH; pH 11.7; column, TSKgel IC-Anion-PW.

Table IV. Comparison of the Calculated and Observed Retention Times of the Substituted Benzoate Anions (Eluent: 5 mM NaOH, pH 11.7. Column: IC-Anion-PW)

		calcd		obsd	
no.	substituent	t_R'/min	log t_R'	t_R'/min	log t_R'
1	(H)			2.65	0.423[a]
2	2-Cl			2.33	0.367[a]
3	3-Cl			9.26	0.967[a]
4	4-Cl			8.91	0.950[a]
5	2,4-Cl_2			6.71	0.827[a]
6	2,5-Cl_2			6.40	0.806[a]
7	2,6-Cl_2			2.78	0.444[a]
8	3,4-Cl_2			30.73	1.488[a]
9	2-NO_2	1.93	0.286	1.89	0.277
10	3-NO_2	6.14	0.788	6.47	0.811
11	4-NO_2	6.00	0.778	6.65	0.823
12	2,4-$(NO_2)_2$	4.38	0.641	4.47	0.650
13	3,4-$(NO_2)_2$	26.30	1.420	26.82	1.428
14	3,5-$(NO_2)_2$	16.14	1.208	13.47	1.129
15	2-OCH_3	1.21	0.082	1.30	0.114
16	3-OCH_3	3.81	0.581	3.76	0.575
17	4-OCH_3	3.52	0.546	3.43	0.535
18	3,4-$(OCH_3)_2$	2.55	0.407	2.63	0.420
19	2-CH_3	1.79	0.252	1.83	0.262
20	3-CH_3	3.97	0.599	3.98	0.600
21	4-CH_3	4.43	0.646	3.95	0.597
22	3,4-$(CH_3)_2$	6.30	0.799	6.19	0.792
23	2-NH_2	3.27	0.515	3.16	0.500
24	3-NH_2	1.95	0.291	1.97	0.294
25	4-NH_2	2.10	0.322	1.94	0.288
26	3,5-$(NH_2)_2$	1.27	0.103	1.50	0.176
27	2-I	3.73	0.572	3.69	0.567
28	3-I	19.95	1.300	21.75	1.337
29	4-I	23.60	1.373	22.32	1.349

[a] Used for the calculation of the values of A (−1.760), $-\rho'$ (0.523), and i'_{Cl} (0.649) by using eq 27.

CONCLUSION

In this paper, the authors found that the retention times of substituted benzoate anions in IC can be explained by dividing the substituent effect into three terms: an LFER-applicable effect term expressed by using the pK_a values of the species, a steric effect term expressed by using the steric effect indices (j'_X), and a positional effect correction term expressed by using the positional effect correction indices ($j''_{o\text{-X}}$, $j''_{p\text{-X}}$, $j''_{\text{X-X}'}$).

LFERs are applicable not only to substituted benzoates but also to other aromatic or aliphatic compounds.[33,34] By applying the LFERs, it is expected that the theory in this paper will be valid for the analysis of the retention times of other organic ions in IC.

ACKNOWLEDGMENT

This work was financially supported by the Murata Science Foundation and the Nippon Life Insurance Foundation, No. C88110012.

RECEIVED for review March 18, 1992. Accepted September 30, 1992.

Expert System for Data Acquisition To Achieve a Constant Signal-to-Noise Ratio: Application to Imaging of DNA Sequencing Gels

Lance B. Koutny and Edward S. Yeung*

Department of Chemistry and Ames Laboratory-USDOE, Iowa State University, Ames, Iowa 50011

Normally, data acquisition and processing in chemical measurements are based on equal time (effort) for each data point. This leads to uneven signal-to-noise ratios (S/N) for each point. We present an expert system which decides in real time whether adequate S/N has been achieved for each point. If so, that data point will be omitted in all further acquisition or processing operations, greatly increasing the overall efficiency. The special case of analyzing DNA sequencing gels is tested with this scheme. A factor of 7.6 reduction in effort is demonstrated for a data set of 384 × 250 pixels, which normally would require 6 million sequential operations (64 frames).

In chemical analysis, parallel or multiplexed data acquisition and data treatment are often the rule rather than the exception. For information that is inherently multidimensional, such a mode of operation is essential for handling the large volume of data. Even in the case of one-dimensional information, parallel processing allows substantial savings in the total measurements or computation time.

Traditionally, each data point in parallel measurements is treated with equal weight. The total data acquisition or data processing time is therefore evenly divided among all the data points. This allows processing in the absence of any knowledge about the data set of interest. In the end, some data points will acquire a higher signal-to-noise ratio (S/N) than others. Universally, however, the criterion for satisfactory measurement is to achieve a certain minimum S/N for each every data point. The minimum S/N will be different depending on whether identification or quantitation is desired and the level of quantitative precision needed. It is in fact wasteful to consider a given data point further once the minimum S/N level has been achieved. The data acquisition or data processing time for that data point could be more beneficially used to enhance the S/N of other data points. There is therefore a need for expert systems that will allow data acquisition to achieve constant S/N rather than constant time (effort) for the individual data points.

Certain common measurement schemes are readily modified to provide constant S/N over the data set, although we were not aware of any literature precedents of such a mode of operation. In scanning spectrophotometry, very often the system is shot-noise (photon statistics) limited. A constant scan rate will result in data points with varying S/N levels. It should however be straightfoward to integrate at each wavelength interval until a certain total count (photocurrent) is accumulated. One can then move on to the next wavelength interval and start integrating again. The scan will become asymmetric in time, but constant in S/N. It is obvious that the total scan time will be reduced. In emission spectrometry, for example, one can further impose a requirement that each wavelength interval will only be integrated for a certain maximum period. This will allow one to quickly skip over regions with little useful information. The gain in efficiency will depend on the amount of useful information versus the amount of useless information and on the range of data values within the set. The spectrometer will have to be controllable interactively, e.g. stepping motor drive, and a resident algorithm must be available to make decisions in real time.

Not all analytical measurements can directly take advantage of this concept. In chromatography, for example, where time is dictated by the separation and not the measurement process, interactive data acquisition is typically not possible. An exception is in pulsed-field gel electrophoresis.[1] In multiplexed spectroscopy such as Fourier transform variants, all data points must be acquired before a valid transform is allowed. The distribution of S/N in the resulting spectrum does not follow a simple dependence on the S/N of the individual points in the interferogram. Even if the mirrors can be asynchronously scanned, one would not necessarily want to implement constant S/N data acquisition.

With the ultimate goal of the human genome inititative being to sequence all 3×10^9 base pairs in human DNA, it is clear that computers must be involved in all steps of the detection and interpretation of sequencing data. Traditional human methods simply cannot complete the task in the time frame desired, and human operation is severely prone to errors due to fatigue and misjudgment. One step in this automation process is imaging electrophoretic gels and storing the information in a format the computer can easily analyze later. Many approaches have been used,[2-8] including single-point densitometers[9,10] and two-dimensional detectors.[11-19] The algorithm described here is applicable to systems in which

---

(1) McGregor, D. A.; Yeung, E. S. *Anal. Chem.* **1992,** *64,* 1–5.
(2) Komaromy, M.; Goven, H. *Nucleic Acid Res.* **1984,** *12,* 675–678.
(3) Staden, R. *Nucleic Acid Res.* **1984,** *12,* 499–503.
(4) Taylor, P. *J. Biomed. Biophys. Methods* **1987,** *14,* 71–83.
(5) Sanders, J. Z.; Petterson, A. A.; Hughes, P. J.; Connell, C. R.; Raff, M.; Menchen, S.; Hood, L. E.; Teplow, D. B. *Electrophoresis* **1989,** *11,* 3–11.
(6) Elder, J. K.; Southern, E. M. In *Nucleic Acid and Protein Sequence Analysis: A Practical Approach*; Bishop, M. J., Rawlings, C. J., Eds.; IRL Press: Oxford, U.K., 1987; pp 219–229.
(7) Ehrhardt, W.; Englisch, U.; Neuhorr, V. *Electrophoresis* **1989,** *10,* 265–266.
(8) Elder, J. K. *Electrophoresis* **1990,** *11,* 440–444.
(9) Galat, A. *Electrophoresis* **1989,** *10,* 659–667.
(10) Autran, J. C.; Abbal, P. *Electrophoresis* **1988,** *9,* 205–213.
(11) Elder, J. K.; Green, D. K.; Southern, E. M. *Nucleic Acid Res.* **1986,** *14,* 417–424.
(12) Chan, K. C.; Koutny, L. B.; Yeung, E. S. *Anal. Chem.* **1991,** *63,* 746–750.
(13) Freeman, S. E.; Larcom, L. L.; Thompson, B. D. *Electrophoresis* **1990,** *11,* 425–431.
(14) Boniszewski, Z. A. M.; Comley, J. S.; Hughes, B.; Read, C. A. *Electrophoresis* **1990,** *11,* 432–440.
(15) Sutherland, J. C.; Sutherland, B. M.; Emrick, A.; Monteleone, D. C.; Ribeiro, E. A.; Trunk, J.; Son, M.; Serwer, P.; Poddar, S. K.; Maniloff, J. *BioTechniques* **1991,** *10,* 492–497.
(16) Gray, A. J.; Beecher, D. E.; Olson, M. V. *Nucleic Acid Res.* **1984,** *12,* 473–491.
(17) Toda, R.; Fujita, T.; Ohashi, M. *Electrophoresis* **1984,** *5,* 42–47.
(18) Prehm, J.; Jungblut, P.; Klose, J. *Electrophoresis* **1987,** *8,* 562–572.
(19) Gray, A. J.; Beecher, D. E.; Olson, M. V. *Nucleic Acid Res.* **1984,** *12,* 473–491.

0003-2700/93/0365-0148$04.00/0

individual picture elements (pixels) can be interrogated and read in any order desired, with the goal being to significantly reduce the number of pixels that must be read and analyzed to absolutely identify and locate all of the signal bands. Bands in sequencing gels often vary in intensity and thus require varying degrees of interrogation by the imaging device before they can be absolutely confirmed. Previous techniques[20] simply scan all areas repeatedly until the S/N is such that all bands are detectable, and thus much time and effort is wasted scanning areas that are more readily decipherable.

One detector that our technique will be especially well suited for is the charge injection device (CID) based imaging systems. Complete systems with operational software will be commercially available soon. These systems will be quite similar to the scientific-grade cooled charged couple device (CCD) based imaging systems that first appeared in 1987, except that one will be able to read the pixel intensities in any pattern desired, even nondestructively.[21] One limitation of these devices is that each detector element can only hold a certain amount of charge before it becomes saturated. This so-called full-well capacity is typically less than 250 000 electrons. Thus, even though these are integrating devices, the data may need to be read out well before enough photons have been detected to assure an adequate S/N to positively identify the image features. This is especially true in absorption-based detection methods such as the ultraviolet absorption method for DNA demonstrated by these authors previously.[12] Because the bands appear as very small decreases in the large background signal, the initial image that was read before detector saturation was always shot-noise limited. Although some bands were clearly detectable, other bands required as many as 64 frames of images to be acquired and averaged before positive identification. Since the images were shot-noise limited, this provided a factor of 8 improvement in detection limit.

Another limitation in CCD imaging is the data acquisition rate. To assure an accurate reading of the charge in these elements, readout must be performed in a slow-scan mode. Typical readout rates are on the order of 200 000 elements/s. Since typical devices now contain 250 000 to 4 million picture elements, full image readout can take several seconds. Thus, a constant S/N mode of data acquisition for signal averaging will significantly reduce the amount of time spent and the amount of computation required. Even if the formation allows binning before readout, a proportional amount of time and storage can be saved.

EXPERIMENTAL SECTION

In any process that mimics human vision it may at first seem complex, but when properly broken down into smaller tasks using appropriate assumptions, vision algorithms need not be sophisticated or require state-of-the-art programming techniques or prohibitively expensive computer hardware. The present image analysis algorithm can be broken down into several simple steps as follows.

Preliminary Feature Recognition. Before the features of interest can be analyzed, the expert system must first identify the general features. The first step toward this goal is to acquire one full image and perform image analysis to describe and record these features. Defining the expected orientations of the gel features will greatly simplify this task. The algorithm will assume that the gel is oriented such that the "starting wells" are situated in a horizontal manner and that the direction of electrophoresis is vertical. In the selected convention, pixel rows are horizontal and pixel columns are vertical. The only general features that need to be located are the lanes. At this point, it is assumed that the lanes are straight and of uniform width or that lane wandering due to heating and gel inhomogeneities has been corrected for using an appropriate algorithm.[11] Lanes are easily identified and their positions recorded by simply searching for groups of pixel columns that have closely related sets of features, as reported by Elder.[8] This can be accomplished at a low S/N level. After this step, the imaged area corresponding to the empty lane boundaries as well as the region preceding the "starting wells" can be omitted from further processing.

Specific Feature Recognition. Once these lane boundaries are defined, recognition of specific features can begin, which in this case are the DNA fragment bands inside of each lane. At this point, it is assumed that the bands are fairly straight and horizontal or that an automated algorithm has been applied to straighten them, such as the one previously described by us.[22] That algorithm would be ideal in this situation because it does not require that all bands be visible and it requires no time-consuming human intervention. It is also assumed that the bands are correctly ordered and do not significantly overlap in their pixel row locations. Again, by applying the algorithm previously described by us, one assures such a condition.

With straight lanes and bands, the information contained in the image is essentially four related one-dimensional arrays, with each array being composed of the average intensities of the pixel columns that make up each lane versus the corresponding row locations. Bands in each lane can then be identified with any peak-finding algorithm. For this work a simple threshold method was implemented based on the intensity and statistics of the background noise. The noise is assumed to conform to a Gaussian or normal distribution, and its magnitude is determined by calculating the standard deviation, which is simply the root-mean-square (rms) fluctuation of the pixel intensities in the nonlane area.[23] This is commonly referred to as the rms noise. The rms noise of the data in the one-dimensional arrays will be this value divided by the square root of the number of columns averaged to produce it. The threshold is then set as this value multiplied by an appropriate factor. The magnitude of this factor will determine the probability of locating false signals. A search is then conducted for groups of data points in the one-dimensional arrays that exceed this threshold. Any group is considered a band if the number of consecutive row locations exceeds the full width at half-maximum (in pixels) expected for the data. This is easy for DNA sequencing gels. Band locations are then recorded to a file as a data pair consisting of the lane number and the centroid of the pixel row locations of the groups of data points identified as a band.

Decision Making. At this point, the expert system must use the information already gained to make decisions regarding the areas that should be read again and those regions that can be skipped. Obviously, the pixel columns between lanes need not be probed anymore. The only information contained in these areas is the rms noise, and it can be assumed that the noise will accumulate as the square root of the number of times an area is read, while the signal will accumulate proportional to this number.[20] The next step is to decide which pixel rows no longer need to be probed. This is quite easily performed if one assumes that once a band is found, no other bands will be found in the same pixel row locations in the other three lanes. This is quite significant as it allows the algorithm not only to mark the area in which the band was found as inactive but also to mark three more equally sized areas in other lanes where it can be concluded that no bands reside. By the time most of the bands have been located, this assumption will have allowed the expert system to mark nearly all of the image as inactive versus only one-fourth without utilizing this assumption. A convenient method of programming this information is to create a Boolean data array with one entry for each row. The array is initially set to all true, which is defined to mean that all pixels in that row, which are also in lane areas, are active. When a band is located, a block of row locations in the Boolean array centered at the band location and equal in number to the expected width of a band in pixels is marked false, or becomes inactive.

---

[20] Baxes, G. A. *Digital Processing: A Practical Primer*; Prentice Hall: Englewood Cliffs, NJ, 1984; p 167.

[21] Sweedler, J. V.; Bilhorn, R. B.; Epperson, P. M.; Sims, G. R.; Denton, M. B. *Anal. Chem.* **1988**, *60*, 282–291.

[22] Koutny, L. B.; Yeung, E. S. *Appl. Spectrosc.* **1992**, *46*, 136–141.

[23] Ingle, J. D.; Crouch, S. R. *Spectrochemical Analysis*; Prentice Hall: Englewood Cliffs, NJ, 1988; pp 543–546.

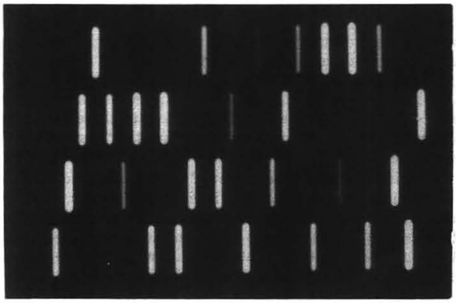

Figure 1. DNA sequencing test image prior to noise addition.

Signal Accumulation. Once the initial image has been fully analyzed, a reasonable approach must be found for continuation of the search. Instead of performing the above methods after each pass of the image, it is more prudent to do so only after the S/N has increased significantly for the bands not yet located. For simplicity a square root of 2 improvement in S/N was chosen. Thus, each pass must double the total number of previous reads of each active pixel before band location and decision making occurs again. Since noise accumulates at a rate of the square root of number of reads, the threshold must be increased by a factor of the square root of 2 each pass. The signal however will double each pass, resulting in the enhanced S/N that can be exploited to locate bands not found in previous passes. The advantage of choosing this square root of 2 improvement is easily demonstrated. If, for example, 64 reads are needed to locate the last band, the program will only make seven passes through the band location and decision-making portions of the algorithm, which are the most complex. Although not every band will be located at the earliest possible time, computations will be reduced by a factor of 9.

Termination. Since DNA sequencing data consist of a series of bands that are fairly evenly distributed in the direction of electrophoresis, it is quite simple for the expert system to determine when the reading process is complete. The distances between neighboring bands versus band number should be fairly monotonic as one moves down the gel image, and if this is not the case, the process should continue.

Test System. The expert system was implemented on a 80486-based IBM compatible personal computer running at 33 MHz and operating under DOS 5.0 (Microsoft). Programming was performed using Turbo BASIC (Borland), which is a compilable version of BASIC that incorporates many PASCAL structures. The 64 simulated images were stored on the hard disk, and pixel intensities were passed on to resident memory (simulated data acquisition) as necessary.

To demonstrate the technique, data were artificially created that would mimic what a detector would report if it were reading a DNA sequencing gel that followed all of the assumptions listed earlier. The data were created starting with a noiseless image data array of 28 bands randomly distributed in 4 lanes. The dimensions of this image are 384 × 250 pixels and therefore contain 96 000 pixels. Each band is 13 by 52 pixels and is Gaussian along the pixel column direction. Band intensities vary from 40 to 580 counts in steps of 20 counts. The full width at half-maximum value for these bands is approximately 5 pixels. The maximum intensities of a band are constant over the middle 40 pixel columns and decrease in a Gaussian manner on each of the ends which consist of six columns each. This is a good approximation of the results that occur due to diffusional broadening as a signal band travels through a gel. Pixel resolution is appropriate to avoid blurring due to the detector resolution. The spacing between lanes is 5 pixels. This image was superimposed (added) upon 64 similarly sized images of artificial noise which were Gaussian in nature with an average intensity of zero and root-mean square variation of 290. The noise in all 64 frames is independent of that in the other frames. Figure 1 is a visual representation of the image before noise was added. Figure 2 is the same with one of the 64 frames of noise added. The images were formatted so that they could be read into and displayed on a Photometrics CC200 Imaging System (Photometrics Ltd., Tucson, AZ). The expert system therefore "reads" and uses these frames as if they are real gel images obtained from a CCD camera in real time.

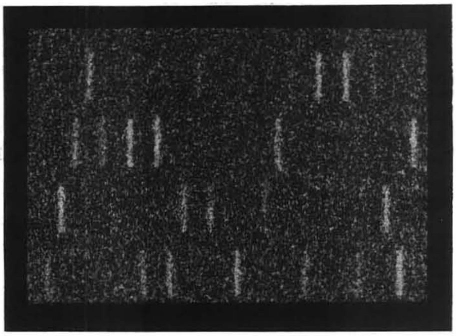

Figure 2. DNA sequencing test image superimposed on one frame of noise.

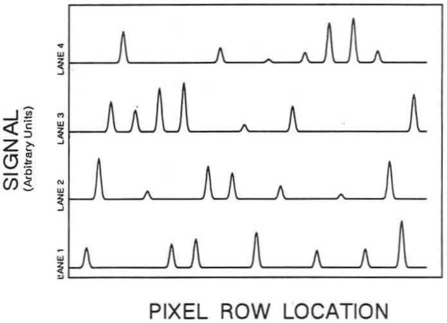

Figure 3. One-dimensional representation of lanes in the noiseless image, as shown in Figure 1.

RESULTS AND DISCUSSION

Since the lanes are 52 pixels across, and the noise is random, the data stored in a one-dimensional array for a given lane as described earlier have a rms noise of approximately 40 pixel counts after one reading. Thus, after "accumulating" one image, the bands have a S/N ranging from approximately 1 to 16. The one-dimensional representation of the lanes, created by binning together pixel columns, for the noiseless image is shown in Figure 3. Figure 4 shows the same representation for a single image with noise added. The S/N will increase by a factor of the square root of the number of frames accumulated until, after 64 frames, the range is 8–96, as shown in Figure 5. It is clear that some bands can be positively identified earlier than others.

The expert system itself is quite simple yet elegant. By reducing the data as it is read, the computer program only requires a few variables such as lane locations, threshold parameters, and five one-dimensional arrays and contains no time-consuming multidimensional array calculations.

The most important figure of merit of the present approach is the factor by which the amount of data acquisition is reduced. The threshold chosen for this study was 3 times the RMS noise, and all bands were located in seven passes with a maximum number of reads for any area of 64. Sixteen of the 28 bands were located in the first pass, and between one and three in each subsequent pass. Table I presents a

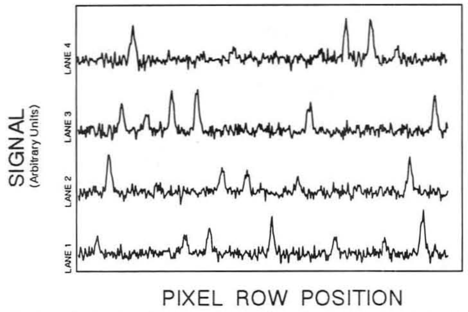

Figure 4. One-dimensional representation of lanes in the image with noise added, as shown in Figure 2.

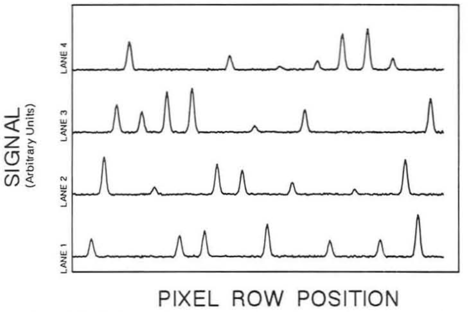

Figure 5. One-dimensional representation of lanes in the image after accumulating 64 frames.

Table I. Some Important Operating Parameters and Results for Each Pass Excuted by the Expert System on the Sample Data Set

pass no.	1	2	3	4	5	6	7
no. of frames accumulated	1	2	4	8	16	32	64
threshold (3 times rms noise)	120	170	240	340	480	679	960
no. of bands located	16	3	3	2	1	2	1
S/N of bands located	6.5 and up	7–10	7–11	8.5–11.5	10	8.5–11.5	8
percentage of areas marked inactive	54	64	74.5	81	84.5	91.5	95

summary of some of the important operating parameters and results for each pass. Bands were located when their cumulative S/N ranged from 6.5 to 11.5. The lower value of this range is explained by the fact that five pixels must exceed the threshold which is equal to 3 times the rms noise. Since five pixels is the full width at half-maximum of a band and band shapes are Guassian, one would expect positive identification of a band when the maximum intensity exceeded twice the threshold, or 6 times the noise intensity. The upper value is due to the fact that feature recognition and decision making does not occur after every frame, and accumulation may proceed up to twice that required for positive identification, which would result in a S/N of 12.

The last row of Table I reports the cumulative percentage of the lane areas marked as inactive after each pass. These values can be used to calculate the most important figure of merit of the system, which is the factor by which data acquisition and processing is reduced. Only 806 944 pixels were read versus the 6 144 000 that would have been read if all 64 frames had been accumulated in their entirety, resulting in the factor of 7.6 reduction in data points read. Depending on the distribution of band intensities, this value could be significantly higher or lower but will never drop below 1, as it would be in the unlikely case that all bands were of the same intensity or when all bands were located in one pass. This factor could be increased by performing analysis after each set of selective accumulations of pixel intensities at the expense of computational load.

Figure 6. One-dimensional representation of lanes with selective accumulation as prescribed by the expert system. Peaks are smaller in rows with fewer frames of data accumulated, but S/N is constant for each recognized feature in the image.

Figure 6 is a plot of the four one-dimensional arrays after data frames were selectively accumulated by the expert system. When any given band was detected, data acquisition and processing was terminated for those pixel row locations for each lane. Thus, the noise in the other lanes at those positions is representative of the noise used to determine the threshold. The weaker bands accumulate to a larger total signal because they must overcome a larger accumulated noise. Figure 6 is an unfamiliar looking plot because S/N is constant throughout the data set. However, it represents the most efficient treatment of data for feature recognition.

Single-point densitometers that allow random access would see the full effect of this reduced data acquisition factor, since the entire detection time is spent acquiring data. In CID detection schemes worthwhile benefit would only be seen when the signal is bright enough that much more time is spent reading the pixels than is spent integrating signal.

Another performance figure that must be mentioned is computational overhead time. Presently, while the computer is performing peak location and making decisions, data acquisition cannot proceed. This is another reason why a simple method with minimal variables and data arrays is advantageous. As written in Turbo BASIC and without careful optimization, the program required only 1.2 s to execute all but the data acquisition part of the algorithm on a 33-MHz 80486-based computer operating under DOS 5.0. This value could easily be significantly improved with more appropriate programming techniques or hardware.

In any automated DNA sequencing procedure, absolute accuracy is required. Since a statistical method is used in this method to determine the cutoff threshold used, precise error rates for the algorithm can be calculated. In Gaussian statistics, the probability of a given noise element exceeding 3 times the rms value is one in 770,[23] and the chance of five points in a row exceeding this threshold is one in 2.7×10^{14}. Since the data actually read contained approximately 800 000 possible combinations of five pixels in a row and 28 bands were successfully located, the chances of a false peak in this example was 1 in every 924 million peaks found. This error rate is quite acceptable and can be increased or decreased in a predictable manner by altering the cutoff threshold.

Another important aspect of any automated image analysis process is the elimination or reduction of human interaction and judgment. This expert system does quite well in this respect. The only input required from the human operator is the expected dimensions of the bands, and this information is quite easily determined by observing past runs and should remain constant for a given experimental setup. Beyond requiring this information, the algorithm executes completely independently.

Finally, it should be emphasized that not all limiting noise can be reduced by repeated measurements. Time-independent background spatial variations, e.g. gel inhomogeneities, can only be corrected for by flat-fielding.[12] This is in contrast with the measurement of absorbance, such as that simulated in Table I. These are generally shot-noise or flicker-noise limited and will benefit from the present scheme.

ACKNOWLEDGMENT

The Ames Laboratory is operated by Iowa Sate University for the U.S. Department of Energy under Contract W-7405-Eng-82. This work was supported by the Director of Energy Research, Office of Health and Environmental Research.

RECEIVED for review May 27, 1992. Accepted October 21, 1992.

Anal. Chem. **1993,** *65,* 153–157

Native Fluorescence Detection of Nucleic Acids and DNA Restriction Fragments in Capillary Electrophoresis

Robert E. Milofsky† and Edward S. Yeung*

Department of Chemistry and Ames Laboratory-USDOE, Iowa State University, Ames, Iowa 50011

A sensitive laser-induced fluorescence (LIF) detection scheme for native nucleic acids and DNA restriction fragments separated by capillary electrophoresis (CE) has been developed. The 275.4-nm line from an argon ion laser or the 248-nm line from a waveguide KrF laser is used to excite native fluorescence. Detection limits for guanosine and adenosine monophosphate (1.5 $\times 10^{-8}$ and 5 $\times 10^{-8}$ M, respectively) are up to 3 orders of magnitude lower than UV detection. Sensitivity for native fluorescence of DNA restriction fragments in gel-filled capillaries rivals that of UV absorption. The decrease in performance in gel-filled separations using LIF detection is caused by the high background associated with gel fluorescence, as well as gel quenching of the fluorescence emission. The development of gels exhibiting lower background fluorescence or off-column coupling should lead to significant improvements in sensitivity over UV detection. This novel and practical system enables, for the first time, the sensitive detection of nucleic-acid-containing compounds without the need for fluorescence labeling.

INTRODUCTION

The development of capillary zone electrophoresis, capillary gel electrophoresis, and micellar electrokinetic capillary chromatography (MEKC) has revolutionized the field of bioanalytical separations.[1–6] The high efficiency of CE results in rapid separations with theoretical plates routinely approaching 1 million.[7–11]. To date, the most common mode of detection has been the UV–vis absorbance detector due to its near-universal application and relative ease of fabrication. However, due to the size constraints associated with the capillaries used in modern CE instrumentation, the sensitivity of UV detection is severely limited.[12] Without sufficient detection power, high efficiency separations found in CE are of limited utility. CE thus presents a serious challenge to modern detector technology, due to the constraints of nanoliter analyte volumes and micrometer detection path lengths.

Laser-induced fluorescence (LIF) detection can outperform UV–absorbance detection by as much as 6 orders of magnitude for highly efficient fluorophores.[13] Unfortunately, many biomolecules have relatively low fluorescence quantum yields and have been detected only after pre- or postcolumn derivatization with highly luminescent tags. While the use of fluorescent probes can greatly improve limits of detection,[14–17] they suffer from limited shelf life and a decrease in separation efficiency and can be complicated by slow kinetics or incomplete reaction. Furthermore, the extension of HPLC derivatization techniques becomes problematic when sample sizes are at or below the microliter level. Postcolumn reaction schemes represent a more serious challenge in CE than HPLC due to the larger effect of band broadening.[18–20] Finally, chemically altering biomolecules via labeling may be detrimental if further assays are desired or if the chemical activity of the molecule needs to be preserved. While the use of fluorescence detection in CE has been demonstrated for analytes tagged with highly fluorescent molecules, little work has been done on the native fluorescence of biomolecules. This lag in native detection is 2-fold, consisting of a lack of deep-UV lasers, as well as an inhibition to take advantage of the fluorescence signal from molecules that possess adequate chromophores but have low quantum yields for fluorescence. Traditionally, in HPLC separations, UV absorbance is the method of choice for detection due to the relatively long path length of the detector cell. In CE, where path lengths may be as small as 10 μm, fluorescence detection can often lead to significant improvements in sensitivity even for analytes with relatively poor fluorescence quantum yields. For example, Lee and Yeung have illustrated a large enhancement in sensitivity for the LIF detection of native proteins over detection by UV absorbance.[21]

The application of CE for the analysis of nucleosides and nucleotides has been well documented.[22–30] Detection by UV absorbance,[30] radiolabeling,[27] and indirect detection[28] have

---

† Present address: Department of Chemistry, Fort Lewis College, Durango, CO 81301.

(1) Jorgensen, J. W.; Lukacs, K. D. *Science* **1983,** *222,* 266–272.

(2) Hjerten, S. *J. Chromatogr.* **1985,** *347,* 191–198.

(3) Wallingford, R. A.; Ewing, A. G. *Anal. Chem.* **1987,** *59,* 1762–1766.

(4) Gordon, M. J.; Huang, X.; Pentoney, S. L., Jr.; Zare, R. N. *Science* **1988,** *242,* 224–228.

(5) Karger, B. L. *Nature* **1989,** *339,* 641–642.

(6) Ewing, A. G.; Wallingford, R. A.; Olefirowicz, T. M. *Anal. Chem.* **1989,** *61,* 292A–303A.

(7) Cohen, A. S.; Najarian, D. R.; Paulus, A.; Guttman, A.; Smith, J. A.; Karger, B. L. *Proc. Natl. Acad. Sci. U.S.A.* **1988,** *85,* 9660–9663.

(8) Guttman, A.; Cohen, A. S.; Heiger, D. N.; Karger, B. L. *Anal. Chem.* **1990,** *62,* 137–141.

(9) Luckey, J. A.; Drossman, H.; Kostichka, A. J.; Mead, D. A.; D'Cunha, J.; Norris, T. B.; Smith, L. M. *Nucleic Acid Res.* **1990,** *18,* 4417–4421.

(10) Swerdlow, H.; Gesteland, R. *Nucleic Acid Res.* **1990,** *18,* 1415–1419.

(11) Baba, Y.; Matsura, T.; Wakamoto, K.; Tsuhako, M. *J. Chromatogr.* **1991,** *558,* 273–284.

(12) Wahlbroehl, Y.; Jorgensen, J. W. *J. Chromatogr.* **1984,** *315,* 135–143.

(13) Kuhr, W. G. *Anal. Chem.* **1990,** *62,* 403r–414r.

(14) Green, J.; Jorgensen, J. *J. High Resolut. Chromatogr. Chromatogr. Commun.* **1984,** *7,* 529–531.

(15) Kaspar, T.; Melera, M.; Gozel, P.; Brownlee, R. *J. Chromatogr.* **1988,** *458,* 303–312.

(16) Gassman, E.; Kuo, J.; Zare, R. *Science* **1985,** *230,* 813–814.

(17) Cheng, Y.-F.; Dovichi, N. J. *Science* **1989,** *242,* 562–564.

(18) Pentoney, S.; Huang, X.; Burgi, D.; Zare, R. *Anal. Chem.* **1988,** *60,* 2625–2629.

(19) Tsuda, T.; Kobayashi, Y.; Hori, A.; Matsumato, T.; Suzuki, O. *J. Chromatogr.* **1988,** *456,* 375–381.

(20) Nickerson, B.; Jorgensen, J. *J. Chromatogr.* **1989,** *480,* 157–168.

(21) Lee, T. T.; Yeung, E. S. *J. Chromatogr.* **1992,** *595,* 319–325.

(22) Burton, D.; Sepaniak, M.; Maskarinec, M. *Chromatographia* **1986,** *21,* 583–586.

(23) Liu, J.; Banks, J. F. J.; Novotny, M. *J. Microcolumns Sep.* **1989,** *1,* 136–141.

(24) Cohen, A.; Terabe, S.; Smith, J.; Karger, B. L. *Anal. Chem.* **1987,** *59,* 1021–1027.

(25) Tsuda, T.; Nakagawa, G.; Sato, M.; Yogi, K. *Appl. Biochem.* **1983,** *5,* 330–336.

(26) Sustacek, V.; Foret, F.; Bocek, P. *J. Chromatogr.* **1989,** *480,* 271–276.

(27) Pentoney, S.; Zare, R.; Quint, J. *Anal. Chem.* **1989,** *61,* 1642–1647.

(28) Kuhr, W. G.; Yeung, E. S. *Anal. Chem.* **1988,** *60,* 2642–2646.

(29) Gross, L.; Yeung, E. S. *J. Chromatogr.* **1989,** *480,* 169–178.

0003-2700/93/0365-0153$04.00/0

been reported and exhibit moderate success. While detection limits using radiolabeling are quite impressive,[27] radiochemical labeling requires handling and disposing of hazardous materials with short shelf lives. More recently, Lee et al. have achieved impressive detection limits following fluorescence labeling with dansyl chloride.[31] Separation was achieved using MEKC. Although the work by Lee et al. represents a substantial improvement over previous detection schemes, it requires a relatively complex assay for the derivatization step and leaves the analytes permanently altered.

During the past 5 years, there has been an explosion in the field of capillary gel electrophoresis (CGE) for the separation of DNA restriction fragments (ref 32 and references within). The resolving power and speed of CGE has been shown to be much better than the traditional slab gel techniques[33-36] and HPLC,[11] making CGE an attractive alternative for automated DNA sequencing.[37] Numerous reports have been made of separations involving over 300 bases in less than 1 h.[33-35] Dovichi et al. have demonstrated yoctomole sensitivity for DNA fragments labeled with highly fluorescent tags.[34] However, the procedure requires the use of derivatization, which affects the electrophoretic mobility of the fragments. Others have used UV absorbance to detect DNA fragments separated in gel-filled capillaries.[38] These approaches sacrifice detection sensitivity but have the advantage of leaving the DNA in its "natural" state.

In this paper, we demonstrate high-sensitivity detection of native nucleotide fluorescence. The method takes advantage of the shift in fluorescence quantum efficiency associated with a change in the pH of the analyte's environment.[39,40] By moving above or below the pK_a of fluorescence activation, a significant enhancement in detection limits can be realized. The deep UV lines from an argon-ion laser or a KrF laser provide excellent overlap with the absorption spectra of nucleic acids and DNA and can be extremely stable sources (dynamic reserve > 200). This work illustrates, for the first time, the use of native fluorescence for detection of nucleic acids and DNA restriction fragments in capillary electrophoresis separations.

EXPERIMENTAL SECTION

Materials. Reagent grade adenosine, guanosine, thymine, and cytidine 5′-monophosphate nucleic acids and electrophoretic grade tris(hydroxymethyl)aminomethane (Tris), boric acid, *N,N,N′,N′*-tetramethylethylenediamine (TEMED), ammonium persulfate, and ethylenediaminetetraacetic acid (EDTA) were obtained from Sigma (St. Louis, MO). [3-(Methacryloxy)propyl]-trimethoxysilane was purchased from Kodak and used without purification. Electrophoretic grade acrylamide was a product of BioRad and electrophoretic grade sodium dodecyl sulfate (SDS) was purchased from Fluka and purified by recrystallization three times from ethanol. Citric acid and disodium phosphate (Fisher) were used as received. *Hin*dIII digest of λDNA and the *Hae*III digest of ϕX174 DNA were obtained from International Biotechnologies, Inc. (New Haven, CT). Poly(deoxyadenylic acid) [poly(dA)] was obtained from Aldrich (Milwaukee, WI) at a concentration of 5 units/mL. The oligonucleotides were dissolved in 2 mL of water and then diluted as needed in the running buffer.

CE Instrumentation. The fluorescence detection apparatus has been described in detail elsewhere.[21] Briefly, a prism was used to isolate the 275.4-nm line from a Spectra Physics Model 2045 argon ion laser after optimization for deep UV operation. Alternatively, the 248-nm line of a Potomac Photonics Model GX-1000 waveguide laser (Lanham, MD) operated in the KrF mode (repetititon rate = 500 Hz) was used as the excitation source. A 1-cm focal length quartz lens was used to focus the laser beam into the capillary, and the fluorescence image from the sample was collected using a 10× microscope objective, passed through two UG-1 band-pass filters (Schott Glass Technologies, Duryea, PA), and detected by a RCA 1P28 photomultiplier tube. The output current from the PMT was monitored by a Keithley Model 4170 picoammeter. Finally, an IBM PC computer equipped with an A/D board (Chromperfect, Justice Innovation, Palo Alto, CA) was used for data collection. The data were acquired at 5 Hz and smoothed using the procedure described by Savitsky–Golay.[41] Scattering artifacts due to submicron particles passing through the laser beam were digitally removed by a spike filter. A 65-point cubic smooth was applied for gel separations with broad peaks and a 15- or 21-point smooth was used for the MEKC separations with sharper peaks. A positive polarity Glassman (Whitehouse, NJ) MJ series high-voltage power supply (+30 kV, 400 μA) was used to generate the potential across the capillary. Injections were made electrokinetically at either the positive (MEKC) or ground (CGE) end or hydrodynamically by lifting the analyte reservoir 5 cm above the exit buffer for 30 s. For MEKC, injection was carried out at 7.5 kV for 1 s (unless noted otherwise) and a running potential of 20 kV was applied. For CGE, injection was at 3.5 kV for 3 s and a running potential of 6 kV was used. An electronic timing circuit was used to control the time of injection.[28] For UV-absorbance comparisons, an Isco (Lincoln, NE) Model 3140 CE system operating at an absorption wavelength of 260 nm was used. All experimental parameters were identical for both the fluorescence and UV measurements. Polyimide-coated fused-silica capillaries (360-μm o.d., 50- and 75-μm i.d., 40–110-cm total length) were purchased from Polymicro Technologies (Phoenix, AZ). For MEKC, 50-μm-i.d., 360-μm-o.d. DB-1 GC capillary columns (J&W Scientific) having a 5-μm film thickness were used. The DB-1 columns were conditioned for 5 h with the running buffer prior to use. All analytes were made up in the running buffers which, for the MEKC experiments, consisted of 10 mM citric acid at pH 2.7 or 10 mM disodium phosphate brought to pH 10.7 with 1 M NaOH, and 10 mM SDS.

Preparation of Acrylamide Gel-Filled Capillaries. Linear polyacrylamide gel-filled capillaries were prepared as follows: A 3% T bis(acrylamide) solution was polymerized outside the capillary by adding 5 μL of TEMED as a catalyst and approximately 1 mg of ammonium persulfate (APS) as the initiator to 20 mL of a 3% T aqueous buffer solution of acrylamide. The buffer was composed of either 5 mM boric acid, 5 mM Tris, and 0.5 mM EDTA at pH 10.7 (the pH was adjusted with 1 M NaOH) or 50 mM boric acid, 50 mM Tris, and 1 mM EDTA at pH 8.3. All buffer solutions were filtered with a 0.2-μm filter (Alltech, Deerfield, IL) prior to polymerization. The polymerization was complete after 1 h. Fused-silica columns (360-μm o.d. and 75-μm i.d., 60-cm total length, 22-cm effective length) were treated prior to use by filling with a 1% solution of [(methacryloxy)-propyl]trimethoxysilane in 50:50 acetone:water. After a 1-h reaction period, the columns were pressure flushed with water for 10 min. A window was then burned in the polyimide coating, 22 cm from the injection (ground) end, using hot sulfuric acid. The detection zone was cleaned with methanol before use. The coated columns were pressure filled with the polymerized acrylamide gel for a 30-min period. Shorter fill times for the gels resulted in poor separation efficiencies, possibly due to bubbles remaining in the gel.[32] Once the column was filled, it was allowed

---

(30) Wang, T.; Hartwick, R. A.; Champlin, J. *J. Chromatogr.* **1989**, *462*, 147–154.

(31) Lee, T.; Yeung, E. S.; Sharma, M. *J. Chromatogr.* **1991**, *565*, 197–206.

(32) Baba, Y.; Matsura, T.; Wakamoto, K.; Morita, Y.; Nishitusu, Y.; Tsuhako, M. *Anal. Chem.* **1992**, *64*, 1221–1225.

(33) Drossman, H.; Luckey, J. A.; Kostichka, A. J.; D'Cunha, J.; Smith, L. M. *Anal. Chem.* **1990**, *62*, 900–903.

(34) Swerdlow, H.; Wu, S.; Harke, H.; Dovichi, N. J. *J. Chromatogr.* **1990**, *516*, 61–67.

(35) Cohen, A. S.; Najarian, D. R.; Karger, B. L. *J. Chromatogr.* **1990**, *516*, 49–60.

(36) Brennan, T.; Chakel, J.; Bente, P.; Field, M. *Biological Mass Spectrometry*; Elsevier: Amsterdam, 1990; pp 159–177.

(37) Trainor, G. L. *Anal. Chem.* **1990**, *62*, 418–426.

(38) Heiger, D. N.; Cohen, A. S.; Karger, B. L. *J. Chromatogr.* **1990**, *516*, 33–48.

(39) Udenfriend, S.; Zaltzman, P. *Anal. Biochem.* **1962**, *3*, 49–59.

(40) Börresen, H. C. *Acta Chem. Scand.* **1963**, *17*, 921–929.

(41) Savitsky, A.; Golay, M. E. *Anal. Chem.* **1964**, *36*, 1627–1639.

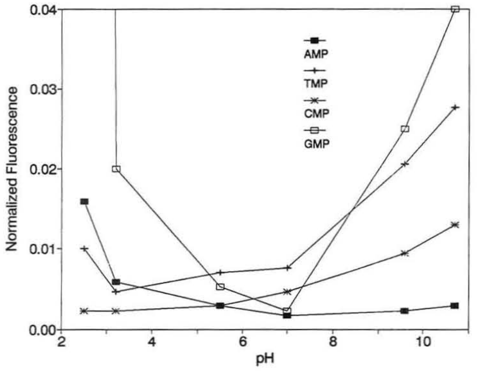

Figure 1. Effect of pH on fluorescence emission intensity. Analytes were present at 0.1 mM. All other conditions are given in the text. Fluorescence intensity is normalized to a value of 1 for GMP at pH 2.7. The data point for GMP at pH 2.7 having a value of 1 is not shown.

to equilibrate by electrophoresis for 30 min at 6 kV. At a running potential of 6 kV, the current was 8 μA.

pH Effects. The effect of pH on fluorescence intensity was examined by flow injection analysis. The pH of the running buffer (disodium phosphate) was adjusted using either 1 M sodium hydroxide or 0.5 M phosphoric acid. An Isco Model 314 syringe pump provided the bulk flow of buffer solution, and a Valco microbore injection valve (60 nL) was used to introduce the analyte onto the capillary. Valco capillary fittings were used to connect the microbore injector to the capillary column. A Potomac Photonics Model GX-1000 waveguide laser (Lanham, MD) operated in the KrF mode ($\lambda = 248$ nm) replaced the argon ion laser as the excitation source. The experimental setup for fluorescence detection was the same as described above. A Linear 1200 chart recorder was used to record the output voltage from the picroammeter. All injections were made in triplicate.

RESULTS AND DISCUSSION

Although little work has been done concerning the native fluorescence of nucleic acids or DNA, early reports suggest that at very acidic or alkaline pH, purine residues become highly fluorescent.[39,40] Confirmation of the work by Udenfriend and Zaltzman[39] and Börresen[40] led to the application of native fluorescence detection of nucleic acids and DNA in CE. The peak heights for each analyte, obtained by the flow injection method (see Experimental Section) with LIF at λ_{ex} 248 nm, were measured at pH values ranging from 2.7 to 10.7 in order to determine the optimal pH for fluorescence detection. Figure 1 illustrates the drastic effect that pH has on the emission intensity of guanosine (GMP), adenosine (AMP), thymine (TMP), and cytidine (CMP) monophosphate. The scale has been normalized to a value of 1 for the fluorescence signal of GMP at pH 2.7, indicating the large enhancement in fluorescence for GMP under acidic conditions. Detection limits (LOD) at acidic pH, as illustrated in Figure 1 and in Table I, are quite impressive for both GMP and AMP. While the sensitivity for AMP and GMP detection decreased at pH 10.7 (compared to pH 2.7), the detection limits for CMP and TMP improved (see Table I) under basic conditions. Table I also compares the detection limits for the four monophosphate nucleotides using native LIF at λ_{ex} 275 nm, at λ_{ex} 248 nm, and UV absorbance. It is of particular interest to note that detection limits using the KrF excimer laser are only slightly worse than those when the argon ion laser is used as the excitation source. Waveguide lasers require little maintenance, are rugged and compact, and are available at low cost. The loss in sensitivity is due to the decrease in stability of the 248-nm source, as well as an increase in the fluorescence background of the quartz capillary with 248-nm excitation (the analytes have nearly the same molar absorptivities at 248 and 275 nm). Although the LOD for native fluorescence is still worse than that of fluorescently tagged nucleotides,[31] the purine bases show a significant enhancement over conventional UV absorbance at both pH extremes. Figure 2 is an electropherogram of 5×10^{-8} M GMP showing the impressive sensitivity of LIF for purine-base nucleic acids.

Table I. Limits of Detection for Nucleic Acids, Oligonucleotides, and DNA Restriction Fragments by LIF and UV Absorption (1–5 nL Injected)

analyte	UV[a]	LIF[a]	LIF[b]	LIF[c]
AMP (M)	1.6×10^{-5}	5×10^{-8}	8×10^{-8}	8×10^{-6}
GMP (M)	1.2×10^{-5}	1.5×10^{-8}	6×10^{-8}	8×10^{-7}
CMP (M)	1.5×10^{-5}	5×10^{-5}	8×10^{-5}	7×10^{-6}
TMP (M)	1.5×10^{-5}	2×10^{-6}	4×10^{-6}	1×10^{-6}
λ*Hin*dIII[d] (μg/mL)	26.4	0.4		
Hae ϕx174[d] (μg/mL)	26.4	0.4		
A_2 (μg/mL)	27.0	0.035		
A_6 (μg/mL)	9.9	0.10		
A_9[e] (μg/mL)	60	0.39		

[a] MEKC at pH 2.7, λ_{ex} 275 nm. [b] MEKC at pH 2.7, λ_{ex} 248 nm. [c] pH 10.7, λ_{ex} 248 nm. [d] Detection limit based on single peak of unresolved fragments. [e] Detection limits based on the largest peak (electrophoresis gave rise to multiple peaks for our sample).

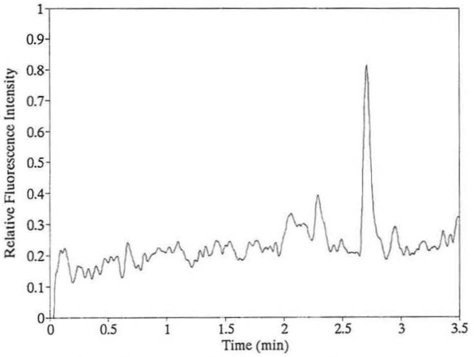

Figure 2. Electropherogram of 5×10^{-8} M GMP using λ_{ex} 275 nm. A 50-μm-i.d., 360-μm-o.d., 40-cm total length DB-1 column with 20-cm effective length was used. The running buffer was 10 mM SDS and 5 mM citric acid at pH 2.7. Injection was performed electrokinetically for 5 s at 10 kV, and the running potential was 20 kV. The data were smoothed with a 15-point cubic Savitsky–Golay procedure.

In order to extend the application of native nucleotide fluorescence to DNA mapping, detection limits for oligonucleotides and DNA restriction fragments were also determined using fluorescence and UV absorbance. Table I lists the detection limits for various poly(dA) oligonucleotides, *Hin*dIII digest of λDNA and the *Hae*III digest of ϕX174 DNA in free zone electrophoresis at pH 2.7. The concentration detection limits per unit mass for the various oligonucleotides are again substantially better than UV measurements and are approximately constant, indicating that the mode of fluorescence quenching in gel separations (see discussion below) is not an intramolecular event between base pairs, but rather quenching by the polyacrylamide gel.

Although the mobilities of these analytes are almost identical below pH 3.0,[42] the addition of 10 mM SDS results in baseline resolution of the four monophosphate nucleotides.

---

(42) Hirokawa, T.; Kobayashi, S.; Kiso, Y. *J. Chromatogr.* **1985**, *318*, 195–210.

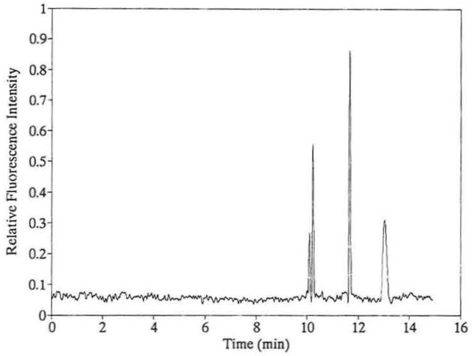

Figure 3. Electropherogram of a mixture of CMP, AMP, GMP, and TMP with concentrations of 2×10^{-4}, 5×10^{-7}, 1×10^{-7}, and 2×10^{-5} M, respectively, using λ_{ex} 248 nm. A 105-cm DB-1 column having an 85-cm effective length and 50-μm i.d. was used. The buffer concentration was the same as in Figure 2. Injection was at 7.5 kV for 1 s, and the running potential was 20 kV. The data were smoothed with a 21-point cubic Golay–Savitsky procedure.

Figure 3 is an electropherogram illustrating the MEKC separation of CMP, AMP, GMP, and TMP at pH 2.7, using a 105-cm column, 85 cm to the detector (360-μm o.d., 50-μm i.d.). The first two are fully resolved despite digital smoothing. It is interesting to note that the separation was not complete at column lengths shorter than 85-cm effective length or at running potentials greater than 20 kV. Addition of up to 10% acetonitrile was found to enhance separation, while excess organic modifier (>10%) resulted in a decrease in separation efficiency. Although concentrations of SDS greater than the 10 mM used in Figure 3 resulted in greater separation efficiency, the larger fluorescence background associated with the surfactant limited sensitivity. The rigorous purification of SDS (see Experimental Section) was critical, decreasing the fluorescence background from several microamperes to 100 nA. Separations attempted in bare silica columns were hindered by severe peak broadening. This problem was overcome by switching to a DB-1 coated GC column, as well as by controlling the amount of surfactant used in the separation. The DB-1 columns were found to be extremely stable at low pH's.

Figure 4 illustrates the linear acrylamide gel separation of the *Hae*III digest of ϕX174 DNA at pH 8.3 and 10.7. Although similar separations with higher resolution have been achieved previously[38] (at pH 8.3), this report is believed to be the first illustration of native fluorescence detection of DNA restriction fragments in conjunction with CGE. The peak width of the smaller fragments indicates that digital smoothing did not contribute significantly to the overlap of the larger fragments. The S/N for LIF was roughly the same as for UV detection (UV detection not shown). Note the apparent loss in sensitivity for the higher molecular weight fragments when the separation is carried out at pH 10.7 (Figure 4b). It is not clear whether this decrease in signal is due to cleavage of the larger restriction fragments or is caused by a fluorescence quenching phenomena. Interestingly, the background emission from the gel was found to be 10 times greater at pH 10.7 than at pH 8.3. The decrease in background at lower pH permitted the use of higher PMT voltages. Note that the concentration of the DNA was 2 times greater at pH 8.3 than at pH 10.7. Dilution of the sample at the higher pH was necessary since the samples were made up in a high ionic strength buffer at pH 8.0. Figure 4a shows a monotonic increase in peak heights and peak areas for the larger fragments, confirming that intramolecular quenching is not important. This of course is necessary for applications to large DNA fragments.

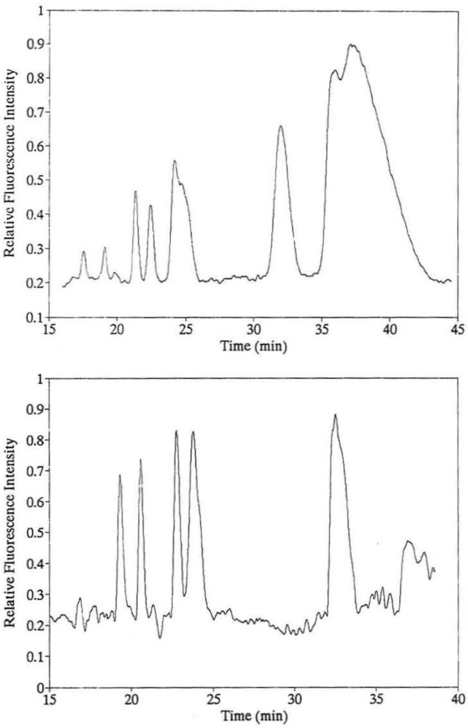

Figure 4. PAGE separation of the *Hae*III ×174 DNA restriction fragments using λ_{ex} 275 nm. (a, Top) 50 mM borate, 50 mM Tris, 1 mM EDTA, pH 8.3, 3% T acrylamide. Injection was at 3.5 kV for 3 s, and the running potential was 6 kV. The DNA concentration was 255 μg/mL. All other conditions are given in the text. (b, Bottom) same as above but the buffer solution was 5 mM borate, 5 mM Tris, 0.5 mM EDTA, pH 10.7. The DNA concentration was 125 μg/mL. The data were smoothed with a 65-point cubic Golay–Savitsky procedure.

As suggested by the comparison of S/N for LIF vs absorbance detection in CE and CGE, the extension of native fluorescence detection to gel-filled separations was associated with a loss in sensitivity, relative to free zone detection limits. For example, the detection limit of the *Hae*III digest of ϕX174 DNA was approximately 15 times worse in CGE as compared to the free zone CE detection limit. There are several possibilities for this phenomena. First, the separation media required for the resolution of large molecular weight species, having similar free-solution electrophoretic mobilities, are known to have significant fluorescence backgrounds. The background emission from such media as polyacrylamide (PAG) and hydroxymethylcellulose (HMP) lie in the same spectral region as the emission of DNA (300–400 nm) and thus cannot be spectroscopically isolated. Therefore, high background levels limit sensitivity. Second, the PAG appears to quench the fluorescence signal by some sort of gel–fluorophore interaction. As mentioned earlier, the signal is not quenched by an intramolecular phenomena, as evidenced by the fact that the sensitivity for all the oligonucleotides was roughly the same (per weight). Thirdly, low-pH conditions (pH < 3.0) result in a huge decrease in the mobility of the DNA, as the purine and pyrimidine rings become protonated. Decreases in electrophoretic mobilities diminish

DNA's ability to swim upstream through the PAG. This separation constraint prohibited the application of native fluorescence detection at low pH. Since pH values less than 3.0 were needed to provide the highest fluorescence yields, so far we were not able to work in the most sensitive pH region. One may be able to eventually use extremely acidic conditions, where DNA fragments are multiply positively charged, for CE separations. Off-column coupling by, e.g., sheath flow will also avoid problems associated with the separation media.[34] It is also possible that the development of new separation media may permit the sensitive detection of DNA restriction fragments by native LIF. For example, Cohen et al. have reported the rapid separation of DNA restriction fragments using 0.1% SDS and 7 M urea.[43] However, a fluorescent background of several microamperes from contaminants in urea prevented us from using a separation scheme similar to that of Cohen et al. We have demonstrated (vide supra) the high sensitivity of native LIF in MEKC for the determination of monophosphate nucleotides using SDS as the surfactant. Those results suggest that the use of LIF for detection in separation schemes similar to the ones already illustrated by Cohen et al.[43] should be feasible.

CONCLUSIONS

This work indicates that LIF detection of native nucleic acids, oligonucleotides, and DNA restriction fragments provides a significant enhancement over conventional UV absorbance in both free zone electrophoresis and MEKC. Our comparison with UV-absorbance detection is based on identical separation conditions, where band broadening, capillary diameter, and noise spikes due to submicron particles are similar. There have been recent developments in enhancing absorbance detection by rectangular cells,[44] Z-shaped cells,[45] and multiple reflection.[46] The first and the last types are not readily commercially available. Also, the last two introduces band broadening because of the longer axial path length. The high sensitivity for AMP suggests the possible application to the measurement of AMP, ADP, and ATP in single cells. The concentration of these nucleotides are on the order of 10^{-17} mol/cell.[47] With nanoliter injection volumes and detection limits approaching 10^{-8} M, we have demonstrated here the sensitivity necessary to do single-cell analysis using native fluorescence detection. The excellent sensitivity of native fluorescence for GMP suggests the application to the study of DNA damage. However, since these samples are not commercially available and are difficult to synthesize, they were not included in the present study. Previous work has required the use of labeling assays to assess radiation damage to DNA.[48] The bulky derivatized nucleotides are difficult to separate under free zone conditions in CE but have been separated via MEKC.[31] Since 8-OHdGmp is one of the major modified nucleotides identified when DNA is exposed to ionizing radiation, native fluorescence detection may prove sensitive enough for such assays without the need for the complex manipulations for tagging nucleotides. Also, modified nucleic acids and nucleotides could be determined in their "free state", allowing further analysis after separation. In this manner, native LIF appears to be well suited for the detection of modified nucleotides in the presence of normal nucleotides at the attomole level. Finally, the development of new separation media for DNA restriction fragments may result in significant improvements in analysis time due to the sensitivity enhancement of LIF over UV absorbance and the elimination of the need for precolumn derivatization and may have applications in genetic mapping and DNA sequencing. The absence of a fluorescent tag will eliminate variations in migration rates among the sequencing lanes and will simplify front-end manipulation in DNA sequencing.

ACKNOWLEDGMENT

Ames Laboratory is operated for the U.S. Department of Energy by Iowa State University under Contract No. W-7405-Eng-82. This work was supported by the Director of Energy Research, Office of Health and Environmental Research. We would like to thank David McGregor and King Chan for discussions in the area of capillary gel separations.

RECEIVED for review July 2, 1992. Accepted October 16, 1992.

---

(43) Cohen, A. S.; Najarian, D.; Smith, D.; J. A.; Karger, B. L. *J. Chromatogr.* **1988**, *458*, 323–333.

(44) Tsuda, T.; Sweedler, J. V.; Zare, R. N. *Anal. Chem.* **1990**, *62*, 2149–2152.

(45) Chervet, J. P.; van Soest, R. E. J.; Meijvogel, C. J. *J. High Resolut. Chromatogr.* **1989**, *12*, 278–281.

(46) Wang, T.; Aikin, J. H.; Huie, C. W.; Hartwick, R. A. *Anal. Chem.* **1991**, *63*, 1372–1376.

(47) Pennell, R. B. In *The Red Blood Cell*; Sergenor, D. M., Ed.; Academic Press: New York, 1974; pp 125–126.

(48) Kelman, D. J.; Lilga, K. T.; Sharma, M. *Chem.-Biol. Interact.* **1988**, *77*, 85–100.

Quantification of Polymerase Chain Reaction Products in Agarose Gels with a Fluorescent Europium Chelate as Label and Time-Resolved Fluorescence Spectroscopy

Alex Chan, Eleftherios P. Diamandis,* and Mel Krajden

Departments of Clinical Biochemistry and Microbiology, The Toronto Hospital, Toronto Western Division,
399 Bathurst Street, Toronto, Ontario M5T 2S8, Canada, and Department of Clinical Biochemistry and Microbiology,
University of Toronto, 100 College Street, Toronto, Ontario M5G 1L5, Canada

We have 5′-end-labeled one polymerase chain reaction (PCR) primer with the europium chelator 4,7-bis(chlorosulfophenyl)-1,10-phenanthroline-2,9-dicarboxylic acid (BCPDA). After performing PCR in the presence of another unlabeled primer, we separated the 362 bp PCR product with 2% low melting point agarose gel electrophoresis. The gel was then immersed into a Eu^{3+} solution. During soaking, Eu^{3+} diffuses into the gel and associates with BCPDA to form a fluorescent complex of long fluorescence lifetime. This complex can be quantified by scanning the gel with a time-resolved fluorometric reader. Because BCPDA and Eu^{3+} are not fluorescent by themselves, background signals are very low. The detection limit was about 5 ng of DNA. We have also shown that the BCPDA-labeled product could be blotted and detected on the membrane by using an anti-BCPDA antibody. These two technologies may find applications other than in PCR, e.g. in fluorescence-based DNA sequencing and in solution hybridization.

INTRODUCTION

The polymerase chain reaction, PCR, has gained wide acceptance as an exponential nucleic acid amplification technique and is used very frequently for research and clinical applications.[1,2] PCR is currently used mainly as a qualitative tool. However, for certain applications, there is a need for obtaining semiquantitative or even quantitative information. Although quantitative PCR has been described,[3,4] it is not used frequently because of its relative complexity. As a compromise, many are using semiquantitative approaches. In these protocols, PCR products become radioactive by incorporating either radioactive primers or radioactive nucleotides.[5,6] Similarly, others have incorporated biotin or digoxigenin.[7,8] These haptens can be detected by linking them to detection systems, e.g. enzymes, through streptavidin or antibodies, respectively. More recently, high-performance liquid chromatography has been used to quantify the PCR products.[9,10] Within a relatively narrow working range, it can be shown that the amount of PCR product generated is roughly proportional to the amount of the initial template concentration.[10]

Ethidium bromide staining is currently the standard method for the qualitative assessment of DNA in agarose gels, including PCR products.[11] Glazer et al. have quantified DNA embedded in agarose gels using fluorometric measurements. Their method is based on the ability of double-stranded DNA to form stable fluorescent complexes with ethidium homodimer. Background readings remain low because the fluorescent complex is formed before electrophoresis; excess dye and stained DNA move in opposite directions during electrophoresis.[12]

In this paper, we describe a new method for the quantitative assessment of PCR products directly in agarose gels. The method involves labeling of the 5′-end of one PCR primer with the europium chelator 4,7-bis(chlorosulfophenyl)-1,10-phenathroline-2,9-dicarboxylic acid, BCPDA.[13] After PCR, the products are separated by agarose gel electrophoresis. The gel is then immersed into an aqueous Eu^{3+} solution. During soaking, Eu^{3+} diffuses into the gel and associates with BCPDA to form a fluorescent complex of long fluorescence lifetime.[14,15] This complex can be quantified in the gel with scanning time-resolved fluorometry.[16] A feature of this method is that neither BCPDA nor Eu^{3+} are fluorescent by themselves and thus, background readings are very low. Additionally, native short-lived fluorescence from the gel or other sources and scattered light are eliminated by using pulsed-excitation time-resolved measurements.[15] This newly devised method has been successfully applied in a model system.

We have also shown that BCPDA-labeled PCR products can be blotted to nylon membranes and subsequently visualized by using anti-BCPDA antibodies and an alkaline phosphatase-based detection system. These results suggest that BCPDA may be a useful hapten for DNA labeling and may find applications similar to those of digoxigenin, a hapten that is detected in diverse applications using labeled antibodies.[17]

---

* To whom correspondence may be addressed at Department of Clinical Biochemistry, Toronto Western Hospital, 399 Bathurst Street, Toronto, Ontario M5T 2S8, Canada.

(1) Saiki, R. K.; Gelfand, D. H.; Stoffel, S.; Scharf, S. J.; Higuchi, R.; Horn, G.-T.; Mullis, K. B.; Erlich, H. A. *Science* **1988,** *239,* 487–491.

(2) Gibbs, R. A. *Anal. Chem.* **1990,** *62,* 1202–1214.

(3) Wang, A. M.; Doyle, M. V.; Mark, D. F. *Proc. Natl. Acad. Sci. U.S.A.* **1989,** *86,* 9717–9721.

(4) Gilliland, G.; Perrin, S.; Blanchard, K.; Bunn, F. H. *Proc. Natl. Acad. Sci. U.S.A.* **1990,** *87,* 2725–2729.

(5) Hayashi, K.; Orita, M.; Suzuki, Y.; Sekiya, T. *Nucleic Acids Res.* **1989,** *17,* 3605.

(6) Abbott, M. A.; Poiesz, B. J.; Byrne, B. C.; Kwok, S.; Sninsky, J. J.; Ehrlich, G. D. *J. Infect. Dis.* **1988,** *158,* 1158–1169.

(7) Lo, Y.-M. D.; Mehal, W. Z.; Fleming, K. A. *Nucleic Acids Res.* **1988,** *16,* 8719.

(8) Lion, T.; Haas, O. A. *Anal. Biochem.* **1990,** *188,* 335–337.

(9) Katz, E. D.; Dong, M. W. *BioTechniques* **1990,** *8,* 546–555.

(10) Warren, W.; Wheat, T.; Knudsen, P. *BioTechniques* **1991,** *11,* 250–255.

(11) Sambrook, J.; Fritsch, E. F.; Maniatis, T. *Molecular Cloning. A Laboratory Mannual,* 2nd ed.; Cold Spring Harbor Laboratory Press: Cold Spring Harbor, 1989.

(12) Glazer, A. N.; Peck, K.; Mathies, R. A. *Proc. Natl. Acad. Sci. U.S.A.* **1990,** *87,* 3851–3855.

(13) Evangelista, R. A.; Pollak, A.; Allore, B.; Templeton, E. F.; Morton, R. C.; Diamandis, E. P. *Clin. Biochem.* **1988,** *21,* 173–178.

(14) Diamandis, E. P. *Clin. Biochem.* **1988,** *21,* 139–150.

(15) Diamandis, E. P.; Christopoulos, T. K. *Anal. Chem.* **1990,** *62,* 1149A–1157A.

(16) Christopoulos, T. K.; Diamandis, E. P.; Wilson, G. *Nucleic Acids Res.* **1991,** *19,* 6015–6019.

0003-2700/93/0365-0158$04.00/0

MATERIALS AND METHODS

Instrumentation. We have used the CyberFluor 615 immunoanalyzer, a time-resolved fluorometer available from CyberFluor Inc., Toronto, Canada. A special software was written which transforms this instrument from a microplate reader to a high-resolution time-resolved fluorometric scanner. This special software is also available through CyberFluor. The performance of this scanner was previously described.[16] Absorbance measurements were carried out with a Model UV160U UV–vis double-beam spectrophotometer from Shimadzu Corp., Kyoto, Japan. PCR experiments were performed with a thermal cycler from Perkin-Elmer Corp., Norwalk, CT 06859. Electrophoresis was performed with equipment from Pharmacia, Piscataway, NJ 08855. High-performance liquid chromatography (HPLC) was performed with equipment from Shimadzu and a DEAE-TSK weak anion-exchange column (4.6 mm × 3.5 cm) from Perkin-Elmer. On-line detection was with a UV monitor at 260 nm.

Materials. The PCR primers used in this study were described by Hsia et al.[18] In addition to these primers, we also synthesized primers of the same sequence which contain a free amino group at their 5′-ends. This was accomplished with the TFA–amino linker amidite, available from Pharmacia LKB Biotechnology. The amino linker was added after the final 5′-nucleotide of each primer and the 6*N*-(trifluoroacetyl) moiety was removed by treatment with concentrated ammonia. After ammonia evaporation, the 5′-amino-containing primers were purified with gel filtration chromatography on Sephadex G-25 with 0.01 mol/L sodium borate as the mobile phase. The primer-containing fractions were combined and evaporated to dryness. BCPDA was synthesized as previously described.[13] As PCR target, we used a pUC19 plasmid containing a cytomegalovirus DNA isert of 2260 base pairs (bp). The insert was cloned with use of Eco RI and Kpn I restriction enzymes. Additionally, we inserted a 210 bp sequence from the ϕX174 phage with use of the Bal I restriction enzyme. This plasmid, when amplified with the primers of Hsia et al.[18] gives a PCR product of 362 bp. All chemicals used were molecular biology grade or reagent grade. Europium chloride hexahydrate was from Aldrich Chemical Co., Milwaukee, WI.

Labeling and Purification of PCR Primers with BCPDA. The 5′-amino-containing primers were dissolved in a 0.01 mol/L borate buffer, pH 9.1, at a concentration of 2 mg/mL. To this solution, we added a 10-fold molar excess of a freshly prepared ethanolic solution of BCPDA. The volume of the BCPDA ethanolic solution added was less than 10% of the total reaction volume. The labeling reaction was allowed to proceed at room temperature for 2 h. The reaction mixture was then loaded on a PD-10 disposable gel filtration column (Pharmacia) which was equilibrated and eluted with 0.1 mol/L sodium bicarbonate solution. Eluate fractions of 0.5 mL were collected. The fractions were checked by absorbance measurements at 260 and 325 nm (where BCPDA absorbs) and also by time-resolved fluorometry as follows: Ten-microliter fractions were added in microtiter wells and mixed with 100 μL of a 10^{-5} mol/L solution of $EuCl_3$ in a 0.1 mol/L Tris buffer, pH 7.80. The fluorescence of the solution, which is due to the formation of the BCPDA–Eu^{3+} complex, was then measured by time-resolved fluorometry with the 615 immunoanalyzer.

Fractions containing BCPDA-labeled primers eluted near the void volume of the column, and they were pooled, evaporated to dryness with a vacuum centrifuge (Savant Instruments, Farmingdale, NY 11735), reconstituted in distilled water, and used for the PCR experiments.

Assessment of the Extent of BCPDA Labeling of Primers. The extent of labeling of the BCPDA-derivatized primers was assessed by absorbance measurements at 325 nm. At this wavelength, BCPDA, with an extinction coefficient of 1.5×10^4 mol^{-1}·L cm^{-1} [19] is the only absorbing species.

Polymerase Chain Reaction Experiments. PCR experiments were carried out in a 100-μL total reaction volume. Ninety microliters was comprised of primers (500 ng each), buffer (50 mmol/L KCl, 10 mmol/L Tris, pH 8.3), nucleotides (200 μmol/L) and Taq polymerase (2.5 units). The sample volume was 10 μL. The PCR mixture was preheated at 94 °C for 6 min before adding the primers (hot start protocol). The cycling was as follows: denaturation at 94 °C for 1 min, annealing at 55 °C for 2 min, extension at 72 °C for 2 min. The number of cycles was 30.

Detection of BCPDA-Labeled Primers and PCR Products in Agarose Gels. We have constructed a special gel casting tray which is identical in size to a microtiter plate with dimensions of 8 × 12.5 cm. On this casting tray we marked lines corresponding to the positions of the eight rows of the plate and used a special plastic comb which creates wells in each row of the casting tray.

We used 70 mL of a 2% agarose solution in Tris–acetate buffer to cast the gels and loaded between 1- and 25-μL sample volumes. PCR products generated with unlabeled primers were stained with ethidium bromide as suggested.[11] PCR products generated with BCPDA-labeled primers were best detected in 2% low melting point agarose gels. Gels were stained with Eu^{3+} solution as follows. After electrophoretic separation, the gel is immersed into a $EuCl_3$ solution (10^{-4} mol/L in 10^{-2} mol/L HCl) for 30 min at room temperature. Subsequently, the gel is washed twice with distilled water. BCPDA-labeled primers were detected on agarose gels with the same staining procedure.

Detection of PCR Products by High-Performance Liquid Chromatography. The PCR product was spiked with 40 ng of a HindIII-linearized pUC 19 plasmid as an internal control, and 20 μL of the sample was then injected into the HPLC system with an autosampler. The HPLC gradient elution system used was as follows: Buffer A was a 0.025 mol/L Tris buffer, pH 9.0, containing 1 mol/L NaCl. Buffer B was a 0.025 mol/L Tris buffer, pH 9.0. The HPLC column was equilibrated with 50% each of buffers A and B before injection. Starting at injection time (0 min), buffer A was increased linearly to 68% in 6 min. At 6.1 min, buffer A was increased to 100%. At 9 min, the buffer composition returned to 50% each. The next injection was at 15 min, allowing column re-equilibration for 6 min.

The absorbance of the eluent was continuously monitored at 260 nm. Data processing and quantitative area calculation of each peak was automatic.

Development of Polyclonal Antibodies to BCPDA. Rabbits were immunized withe a BCPDA–thyroglobulin conjugate prepared as previously described.[19] Injections with complete and incomplete Freund's adjuvant were given following standard protocols as described.[20] Good titers of antibodies were obtained after about 4 months. The BCPDA antiserum was used without prior purification.

Southern Blot Experiments. PCR products were separated by electrophoresis on 2% agarose gels. Gels were blotted to Hybond-N nylon membranes (Amersham) using standard procedures.[11] After UV fixing of the nucleic acids to nylon, membranes were processed in one of two ways: (a) The membrane was washed with water and then immersed into a $EuCl_3$ solution, 10^{-4} mol/L, in 10^{-3} mol/L HCl for 10 min. After washing with water, the membrane was dried in an air-oven (45 °C) and scanned with the time-resolved fluorometer. (b) The membrane was incubated in a blocking solution, commercially available from Boehinger-Mannheim, for 1 h at room temperature and then immersed into a solution containing rabbit anti-BCPDA antiserum diluted 8000-fold in the blocking solution.

After 30 min, the membrane was washed twice with a wash solution (100 mmol/L Tris, 150 mmol/L NaCl, pH 7.5) and incubated by shaking in a solution containing alkaline phosphatase-labeled goat anti-rabbit antibody (from Jackson Immunoresearch, West Grove, PA 19390) diluted 5000-fold in the blocking solution. After a 30-min incubation and subsequent membrane washing as above, the membrane was immersed into a developing solution containing bromochloroindolyl phosphate (BCIP) and nitroblue tetrazolium (NBT) as described.[11] After color development for 15–30 min or longer as required, the reaction was stopped by removing the membrane.

Extraction and Quantification of PCR Products in Microtiter Wells. PCR products generated with BCPDA-labeled primers were separated in 2% agarose gels. The bands

---

(17) Martin, R.; Hoover, C.; Grimme, S.; Grogan, C.; Holtke, J.; Kessler, C. *BioTechniques* **1990**, *9*, 762–768.

(18) Hsia, K.; Spector, D. H.; Lawrie, J.; Spector, S. A. *J. Clin. Microbiol.* **1989**, *27*, 1802–1809.

(19) Diamandis, E. P.; Morton, R. C. *J. Immunol. Methods* **1988**, *112*, 43–52.

(20) Harlow, E.; Lane, D. *Antibodies. A Laboratory Manual*; Cold Spring Harbor Laboratory Press: Cold Spring Harbor, 1988.

Table I. Labeled and Unlabeled Primers Used in This Study

primer	stock solution, $\mu g/mL$	absorbance ratio A_{260}/A_{280}	molar ratio, BCPDA/primer	base sequence
1401	68.9	1.83		5′-GGCAGCTATCGTGACTGGGA-3′
1401*[a]	34.6	1.61[b]	0.86	
1402	66.0	1.81		5′-GATCCGACGACCCATTGTCTAAG-3′
1402*	61.2	1.62[b]	1.05	

[a] Asterisk indicates primers labeled with BCPDA. [b] Ratio decreases due to the presence of BCPDA.

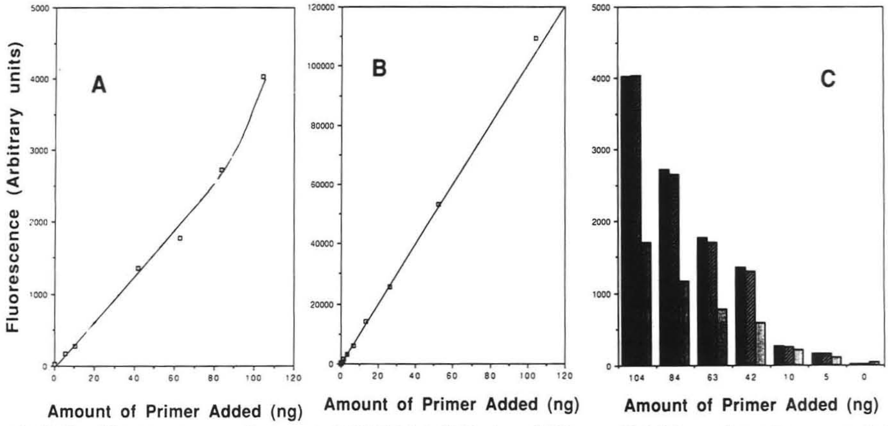

Figure 1. (A) Plot of fluorescence versus the amount of BCPDA-labeled PCR primer 1402* present in 2% low melting point agarose gels. These gels were stained with Eu^{3+} and scanned with the time-resolved fluorometer. The reproducibility of each point between various experiments was 10–15%. (B) The same amount of primer was measured in microtiter wells in the presence of excess Eu^{3+}. Each point is a mean of three replicates with CV's between 2 and 3%. (C) Effect of washing the gels containing BCPDA-labeled PCR primer after staining with Eu^{3+}. First bar: no wash. Second bar: 15-min soaking. Third bar: 2-h soaking.

were visualized by ethidium bromide staining, excised from the gels and DNA extracted as follows: (a) From agarose gels with the Geneclean kit (Bio 101, Inc., La Jolla, CA 92038-2284) which utilizes glass beads as the solid-phase. (b) From low melting point agarose gels using the enzyme gelease (Epicentre Technologies, Madison, WI 53713) to digest the agarose. In both cases, the manufacturer's instruction were followed. The final extract from a, 10–20 μL, was transferred to white opaque microtiter wells (from Dynatech laboratories), and 100 μL of a 10^{-4} mol/L Eu^{3+} solution in 0.1 mol/L Tris buffer, pH 7.80, was added. The final extract from b, about 100 μL, was also transferred to microtiter wells and the Eu^{3+} solution added as above.

In both cases, the fluorescence of the solutions, which is directly proportional to the amount of BCPDA present in the sample, was quantified with the 615 immunoanalyzer working as a microplate time-resolved fluorometric reader.

RESULTS AND DISCUSSION

The unlabeled and BCPDA-labeled primers used in this study are described in Table I. The sequences have been described elsewhere.[18] Figure 1 shows data for the detection of labeled primer 1402* in 2% low melting point agarose gels. For this experiment, we used a stock 1402* solution of 5 μg/mL and loaded sample volumes of 1–20 μL (5–100 ng). After a short electrophoresis for 5 min, to allow entrance of the primers into the gel, we stained the gel with Eu^{3+} solution as described. The gel was then scanned at various times to assess the stability of the signal. During this period the gel was stored at 4 °C. Detectable changes, presumably due to diffusion effects, appear after 6 h of storage or longer. The detection limit for primer 1402*, defined as the amount of primer that could be distinguished from zero with 95% confidence, was about 0.3–0.5 ng. When we constructed a calibration curve by plotting fluorescence readings versus amount of primer loaded, we obtained the plot shown in Figure 1A. A direct relation exists, but the response is not linear with loadings greater than 80 ng.

When the same amounts of primer were added in microtiter wells and measured in the presence of excess Eu^{3+}, the response was linear and the fluorescence readings were much higher (Figure 1B). This finding is expected for various reasons (a). In microtitration wells, about 50–60% of the measured fluorescence is reaching the detector through reflections at the sites of the wells; this signal is not collected in gel scanning measurements (b). The excitation of the band in the gel is not optimal. Because of its linear shape, part of the band is not excited at all. With measurements in microtitration wells, the excitation beam is optimized to focus in the center of the well (c). The presence of the gel above the fluorescent band poses a barrier to both excitation and emission radiation and may also contribute to scattering.

The effect of washing the gels after staining with Eu^{3+} was studied with gels containing labeled primer 1402*. Unwashed gels and gels soaked in water for up to 15 min show similar readings. Extensively soaked gels (2 h or more) start to lose fluorescence, presumably through leakage of Eu^{3+} from the complex (dissociation) (Figure 1C). Unwashed and briefly washed gels have similar backrounds which are 15–20 arbitrary fluorescence units.

Preliminary PCR experiments with labeled primers which were not purified from excess unreacted BCPDA have shown that no PCR products were obtained. Presumably, this is due to Mg^{2+} chelation by the excess BCPDA. Excess BCPDA was removed with gel filtration chromatography on PD-10 disposable columns (Pharmacia) as shown in Figure 2. Free BCPDA has affinity for the Sephadex matrix[19] and elutes much later in comparison to BCPDA-labeled primers. The primer-containing fractions were pooled and concentrated by vacuum centrifugation.

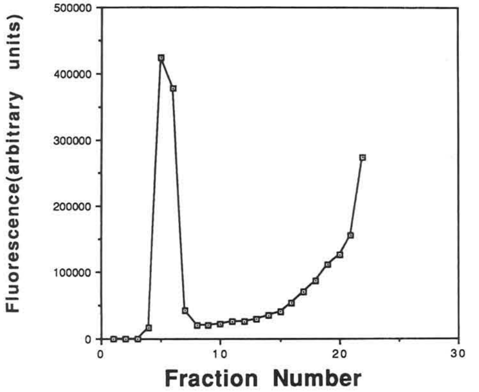

Figure 2. Elution of BCPDA-labeled primer 1402* and unreacted free BCPDA from a disposable PD-10 Sephadex column. The column was eluted with a 0.1 mol/L sodium bicarbonate solution. Pure BCPDA-labeled primer elutes near the void volume of the column (fractions 4–7, 0.5 mL each). Each fraction was measured in triplicate in microtiter wells in the presence of excess Eu^{3+}·CV's were between 2 and 3%.

The molar ratio of BCPDA to primer was calculated with absorbance measurements at 325 nm where only BCPDA absorbs[19] and at 260 nm where both components absorb. The calculated molar ratio was close to the theoretically expected (Table I).

The effect of soaking time with Eu^{3+} on the fluorescence readings was studied with gels containing labeled primer 1402* at varying amounts. Soaking time ranged from 5 to 75 min. It was found that plateau in fluorescence is obtained with soaking times of about 20–30 min. No backround increase was observed after extensive soaking (75 min) with Eu^{3+}.

In Figure 3 we present data for various PCR reactions using different combinations of labeled and unlabeled primers. We used 1 ng of plasmid target in all cases. Specific PCR product, 362 bp long, was obtained when unlabeled primers were used (lane 2) or when unlabeled primer 1401 was used in combination with labeled primer 1402* (lane 5).

No products were detected when labeled primer 1401* was used either with unlabeled (lane 3) or labeled (lane 4) primer 1402. For all subsequent experiments, we used the primer combination 1401–1402*. The reasons for the absence of PCR products when labeled primer 1401* was used were not examined further.

Figure 4 shows time-resolved fluorometric scans of PCR products generated with primers 1401–1402*, separated on agarose gels as shown in Figure 3 and stained with Eu^{3+}. The two peaks of Figure 4A correspond to the 362 bp PCR product and the excess primers, respectively. The ratio of signal/background for the first peak is about 27 (3220/120). The same PCR product was run on a 2% low melting point agarose gel and scanned as above (Figure 4B). The scan is qualitatively similar to that of Figure 4A, but the resolution is improved and the backround signal was reduced to almost undetectable levels (less than 30 arbitrary fluorescence units). Thus, low melting point agarose gel electrophoresis is the preferred separation method for the proposed application. Scanning of gels stained with Eu^{3+}, containing PCR products generated with unlabeled primers or molecular weight standards, give no appreciable fluorescence or peak patterns.

The quantitative nature of the proposed method was established by separating varying amounts of a PCR product generated with primers 1401–1402* on 2% agarose gels and scanning, after Eu^{3+} staining. Figure 5 is an ethidium bromide-stained gel which is loaded with varying amounts of a PCR product generated with 1401–1402*. The gel was stained with Eu^{3+} and scanned with the proposed method. There is a direct relationship between fluorescence and sample volume, but as also shown in Figure 1, the response is not linear.

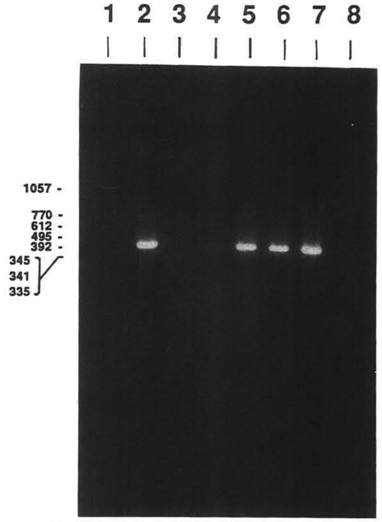

Figure 3. Ethidium bromide-stained 2% agarose gel containing PCR products generated from 1 ng of plasmid target, in the presence of various combinations of PCR primers described in Table I. Lane 1: Molecular weight markers ϕX174, Hinc II digest. The length of the markers in bp is shown on the left side. Lane 2: Primers 1401–1402. Lane 3: 1401*–1402. Lane 4: 1401*–1402*. Lane 5: 1401–1402*. Lanes 6 and 7 are repeats of lanes 2 and 5, respectively. Lane 8: Negative control without PCR target. The primers with an asterisk after the number are labeled at their 5′-end with BCPDA.

Figure 6 shows PCR products generated from varying amounts of the plasmid template and stained with ethidium bromide. The 1401–1402* primer set was used. Some data, with target plasmid amounts less than 100 pg, are not shown because the PCR product was not visible on ethidium bromide gels. The same gels were stained with Eu^{3+} and the lanes scanned with the time-resolved fluorometer. The peak heights, plotted against the initial target plasmid amount, are shown in Figure 6B. There is a direct relationship between signal and target up to about 1 ng of target plasmid. Above that level, the plateau effect of PCR is evident. A PCR product, generated with primers 1401–1402*, was quantified by using high-performance liquid chromatography with a weak anion-exchange column. This product was used to calculate the detection limit of the scanning method in gels which is about 3–5 ng of PCR products. This detection limit is similar to that achieved by HPLC and about 5–10-fold better in comparison to ethidium bromide staining with visual inspection.

Sets of PCR products were quantified by HPLC and by the gel scanning method. The signals observed, in arbitrary units, correlated well with each other (Figure 7).

We also made efforts to extract BCPDA-labeled PCR products from gels and quantify them in microtiter wells. For these experiments, we used two different strategies: (a) After cutting the gel containing the PCR band, we dissolved the gel with enzyme digestion using the Gelease technique. (b) We used the Geneclean kit. These methods exhibited high backround signals and lower signal to backround ratios in comparison to the direct gel scanning technique and for this reason were not examined further.

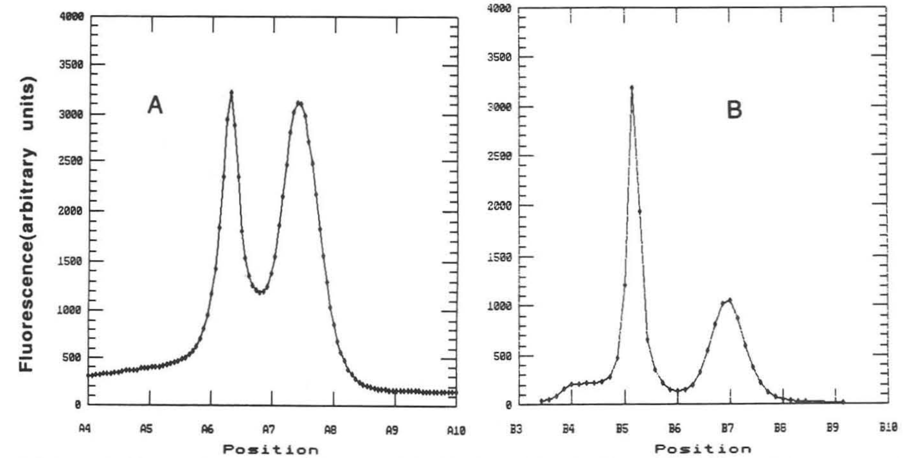

Figure 4. Time-resolved fluorometric scan of a 2% gel containing BCPDA-labeled PCR product (first peak) and BCPDA-labeled unreacted primers (second peak). The gel was stained with Eu^{3+}. (A) Regular agarose gel. (B) Low melting point agarose gel. The relative position of each peak is printed by reference to microtiter well row (A and B) and well number.

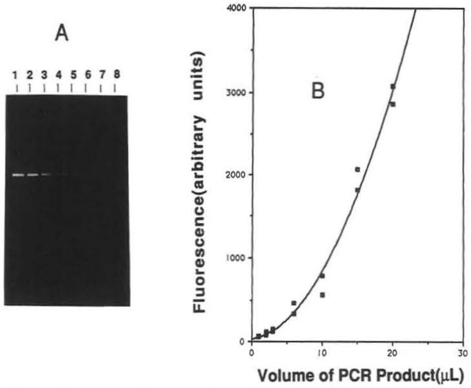

Figure 5. (A) Ethidium bromide-stained 2% agarose gel containing varying amounts of a PCR product generated with primers 1401–1402*. Volume loaded was 20, 15, 10, 6, 3, 2, 1, and 0 µL in lanes 1–8, respectively. The same gel was stained with Eu^{3+} and scanned with the time-resolved fluorometer. The peak height was plotted as a function of volume loaded as shown in B. Each volume was loaded in duplicate.

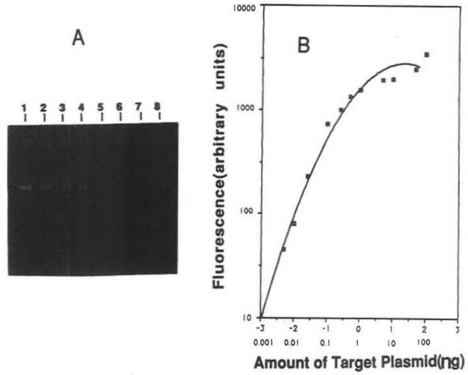

Figure 6. (A) Ethidium bromide-stained 2% agarose gel containing PCR products generated with primers 1401–1402*. The amount of target plasmid DNA used (ng) was 100 (lane 1), 50 (lane 2), 10 (lane 3), 5 (lane 4), 1 (lane 5), 0.5 (lane 6), 0.25 (lane 7), 0.1 (lane 8). Lower amounts down to 5 pg were also used but are not shown. (B) The gel was stained with Eu^{3+} and scanned with the time-resolved fluorometer. The fluorescence of each lane (peak height, singleton measurements) was plotted against the target plasmid amount used, in a double logarithmic plot. The plateau effect is evident at target concentrations above 1 ng.

We have also examined the possibility of using the Southern blot technique to transfer the BCPDA-labeled PCR products to nylon membranes and subsequently stained them with Eu^{3+}, by immersing the membranes in Eu^{3+} solutions. The membranes could then be scanned with the time-resolved fluorometer.

Some data are shown in Figure 8. Higher fluorescence readings are observed with the membrane scanning methods but backround readings were also higher in comparison to direct gel scanning (1500 vs less than 30 arbitrary fluorescence units, respectively). Moreover, saturation effects appear relatively quickly presumably due to membrane saturation at higher levels of DNA blotted. Comparatively, gel staining and scanning is the preferred method because the detection limits and dynamic range are better and the method is less time-consuming.

We have used the BCPDA-labeled PCR products immobilized on nylon membranes to devise another new method for their detection, using polyclonal antibodies against BCPDA. These antibodies were raised in rabbits using a BCPDA–thyroglobulin conjugate as immunogen. The immobilized PCR product was reacted with the BCPDA antibodies. Subsequently, a goat anti-rabbit secondary antibody, labeled with alkaline phosphatase was added. The alkaline phosphatase activity was then detected with the BCIP/NBT substrate. Obviously, other substrates for alkaline phosphatase could also be used. Some results are shown in Figure 9. Lane 2 contains a PCR product generated with unlabeled 1401 and 1402 primers. No peak is detected with the proposed method. Lanes 3, 4, 5, 6, and 7 contain PCR products labeled with BCPDA through primer 1402*. With ethidium bromide staining the PCR product is seen up to lane 6. With the immunological procedure, which utilizes anti-BCPDA antibodies, the PCR product in lane 7 is easily detectable. The detection limit of the immunological procedure is about 100 pg of specific PCR product, which is superior to the method of direct gel scanning and HPLC.

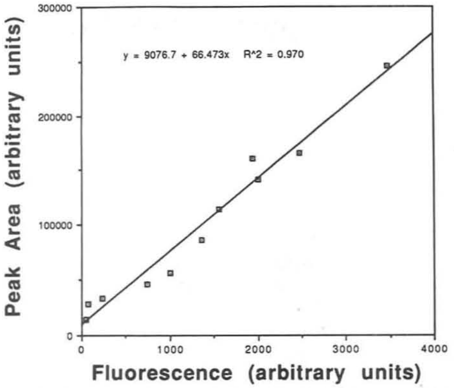

Figure 7. Correlation of signals obtained with high-performance liquid chromatography (*y*) and fluorometric scanning in agarose gels (*x*). PCR products were analyzed by both methods at varying dilutions. For more details see text.

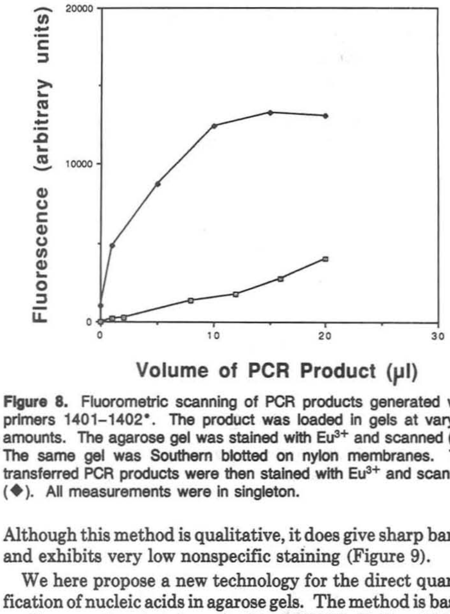

Figure 8. Fluorometric scanning of PCR products generated with primers 1401–1402*. The product was loaded in gels at varying amounts. The agarose gel was stained with Eu^{3+} and scanned (◻). The same gel was Southern blotted on nylon membranes. The transferred PCR products were then stained with Eu^{3+} and scanned (◆). All measurements were in singleton.

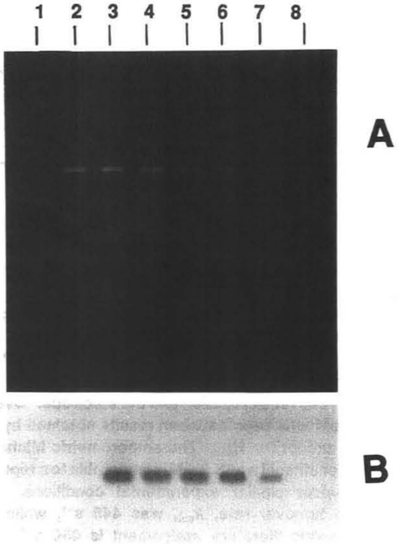

Figure 9. (A) Ethidium bromide-stained gel containing a PCR product generated with unlabeled primers 1401–1402 (lane 2) or with 1401–1402* (BCPDA-labeled 1402 primer) (lanes 3–7). The PCR product was loaded at varying amounts as follows. Lane 1: molecular weight markers, now shown. Lane 2: 20 μL. Lane 3: 20 μL. Lane 4: 15 μL. Lane 5: 10 μL. Lane 6: 5 μL. Lane 7: 1 μL. In lane 8 no target was added (negative control). The gel in A was blotted to nylon by the Southern method and stained with use of anti-BCPDA antibodies. (B) No signal was obtained in lane 2 as expected. The band in lane 7 is not visible with ethidium bromide staining but is easily detectable with the proposed method.

Although this method is qualitative, it does give sharp bands and exhibits very low nonspecific staining (Figure 9).

We here propose a new technology for the direct quantification of nucleic acids in agarose gels. The method is based on the use of a europium chelate, BCPDA–Eu^{3+}, which is fluorescent and can be quantified with microsecond scanning time-resolved fluorometry. In the proposed method, BCPDA is covalently bound to nucleic acids, i.e. at the 5′-end of a PCR primer.

The fluorescent complex can be formed by the diffusion of Eu^{3+} ions into the gel from an aqueous solution. In this case, neither BCPDA nor Eu^{3+} are fluorescent by themselves. Thus, the backround signal observed due to the reagents used is minimal. Additionally, any other backround signal due to scattering or short-lived fluorescence from other chemicals present is eliminated by using the time-resolved fluorometric principle.[14] This technology could find applications other than PCR. For example, 5′-end fluoresceinated primers are used for automated DNA sequencing.[21] BCPDA-labeled primers could also be similarly used. We are currently investigating the possibility of synthesizing BCPDA-labeled nucleotides for general molecular biology applications. These reagents could be detected in gels or after blotting to membranes. In addition to using the time-resolved fluorometric scanner described here, a time-resolved camera recently constructed, (available by Kronem Systems, Toronto, Canada) could also be applicable in obtaining gel or filter pictures.

The development of a BCPDA antibody that recognizes BCPDA on blots and in microtiter well assays makes BCPDA an attractive hapten similar to digoxigenin for DNA applications.[17] In this regard, BCPDA could be used as one of two haptens in systems employing solution hybridization strategies. In such systems, one hapten is used to link the hybrid to a solid phase and another one to link the hybrid to a detection system. These possibilities are currently under investigation.

ACKNOWLEDGMENT

This work was supported by grants to E.P.D. from the Medical Research Council of Canada, The Van Slyke Society of the American Association for Clinical Chemistry, CyberFluor Inc., and the Ontario Ministry of Colleges and Universities.

RECEIVED for review August 6, 1992. Accepted October 16, 1992.

---

[21] Voss, H.; Zimmerman, J.; Schwager, C.; Erfle, H.; Stegemann, J.; Stucky, K.; Ansorge, W. *Nucleic Acids Res.* **1990**, *18*, 1066.

Anal. Chem. **1993**, *65*, 164–168

Comparison of Spectrophotometric and Amperometric Rate Parameters of Enzymatic Reactions

Marguerite K. Ciolkosz* and Joseph Jordan†

The Pennsylvania State University, Chemistry Department, University Park, Pennsylvania 16802

In the context of current interest in electroanalytical sensors for biomedical applications, enzyme kinetic parameters obtained amperometrically were compared with those determined spectrophotometrically for ethanol oxidation catalyzed by alcohol dehydrogenase. The amperometry was conducted at a platinum rotated disk electrode, utilizing hexacyanoferrate(III/II) as an electron shuttle between the enzyme-catalyzed redox reaction and the electrode. Overall good agreement was seen between results obtained by the two methods except for V_{max}. The amperometric Michaelis constant, K_M, for ethanol was 3.2 mM, comparable to a reported value of 3 under similar experimental conditions. The amperometric turnover rate, k_{cat}, was 448 s^{-1}, while the spectrophotometric literature assignment is 450 s^{-1}. The amperometric K_M for cosubstrate NAD was 0.80 mM versus spectrophotometric literature values ranging from 0.1 to 1 mM. On the other hand, the amperometric maximum initial reaction velocity, V_{max}, was 15% lower than its spectrophotometric counterpart.

INTRODUCTION

Amperometric sensors have seen extensive biomedical application in recent years due to the ease with which they can be coupled to biologically important enzymatic redox reactions. Such oxidoreductase-catalyzed reactions invariably involve an electron-transfer step which can be transduced, by a suitably designed amperometric sensor, into a current which may serve to monitor substrate and/or product concentrations. X-ray crystallographic studies[1] and indirect evidence from mediator-modified enzymes[2,3] suggest that catalytic sites of redox enzymes are often deeply embedded, minimizing the possibility of direct charge transfer from the site of the reaction to an electrode surface. In the large group of redox enzymes which depends on the soluble pyridine nucleotide cofactor, $NAD(P)^+/NAD(P)H$, this limitation could, in principle, be overcome because the cofactor serves as a soluble charge carrier and is capable of electron transfer at an electrode. However the process

$$\mathrm{NAD(P)H} = \mathrm{NAD(P)^+} + 2\,\mathrm{e^-} + \mathrm{H^+} \qquad (1)$$

entails a large anodic overpotential at all known electrode materials and may result in decreased selectivity when other electrooxidizable species are present in solution. Moreover, NADH adsorbs strongly at platinum electrodes and proceeds through a complicated radical mechanism.[4] These difficulties can be circumvented through the use of an amperometric couple capable of homogeneous redox reaction, in aqueous solution, with the pyridine nucleotide moiety and having facile heterogeneous electron-transfer kinetics at the electrode surface. A generalized three-step sequence may consist, for instance, of the reactions

$$\text{enzymatic} \qquad \text{s-H} + \mathrm{NAD(P)^+} = \text{s} + \mathrm{NAD(P)H} \qquad (2)$$

$$\text{chemical} \qquad \mathrm{NAD(P)H} + \text{ox.} = \mathrm{NAD(P)^+} + \text{red.} \qquad (3)$$

$$\text{electrochemical} \qquad \text{red.} = \text{ox.} + \mathrm{e^-} \qquad (4)$$

where *s-H* and *s* represent the reduced and oxidized forms of the substrate, respectively, and *ox.* and *red.* represent the oxidized and reduced forms of the amperometric couple.

The ADH-catalyzed oxidation of alcohols is a bireactant, biproduct reaction involving a ternary alcohol–NAD–ADH complex.[5] This is similar to the enzyme mechanism proposed for alcohol oxidase-catalyzed oxidation of ethanol we have discussed in an earlier publication.[6] Conventional single-substrate enzyme kinetics rely on the assumption that the overall process

$$\mathrm{S} \overset{\mathrm{E}}{\rightleftharpoons} \mathrm{P} \qquad (5)$$

proceeds from the *s*ubstrate (S) to the *p*roduct (P) in the presence of the *e*nzyme (E) via the sequence

$$\mathrm{E} + \mathrm{S} \underset{k_{-1}}{\overset{k_1}{\rightleftharpoons}} \mathrm{ES} \qquad (6)$$

$$\mathrm{ES} \xrightarrow{k_2} \mathrm{E} + \mathrm{P} \qquad (7)$$

where ES is a binary substrate–enzyme complex (the "Michaelis–Menten" intermediate). This model leads to the well-known relationship

$$V_0 = \frac{V_{max}[\mathrm{S}]}{K_M + [\mathrm{S}]} \qquad (8)$$

where V_0 is the initial velocity of reaction 7 whose rate-determining step is reaction 9, V_{max} denotes the limiting maximal velocity that would be observed if all the enzyme is present as the complexed ES form, [S] is the substrate concentration, and K_M is the so-called Michaelis–Menten constant. The parameter K_M expresses the relationship between the steady-state concentrations of reactants and intermediates,[7] and it can be shown that

$$K_M = \frac{k_2 + k_{-1}}{k_1} = \frac{[\mathrm{E}][\mathrm{S}]}{[\mathrm{ES}]} \qquad (9)$$

When the substrate concentration equals the value of K_M,

---

* Corresponding author. Permanent address: 121 Old Mill Rd., State College, PA 16801.

† Deceased.

(1) Eklund, H.; Plapp, B. V.; Samama, J.; Brändén, C. *J. Biol. Chem.* **1982**, *25*, 14349–14358.

(2) Degani, Y.; Heller, A. *J. Phys. Chem.* **1987**, *91*, 1285–1289.

(3) Bartlett, P. N.; Whitaker, R. G.; Green, M. J.; Frew, J. *J. Chem. Soc., Chem. Commun.* **1987**, 1603–1604.

(4) Samec, Z.; Elving, P. J. *J. Electroanal. Chem. Interfacial Electrochem.* **1983**, *144*, 217–234.

(5) Brändén, C.; Jörnvall, H.; Eklund, H.; Furugren, B. In *The Enzymes*, 3rd ed.; Boyer, P. D., Ed.; Academic Press: New York, 1975; Vol. XI, pp 103–190.

(6) Jordan, J.; Ciolkosz, M. *J. Solution Chem.* **1991**, *20*, 995–1000.

(7) Segel, I. H. *Enzyme Kinetics*; John Wiley & Sons: New York, 1975; Chapter 6.

0003-2700/93/0365-0164$04.00/0

the initial velocity, V_0, is half of the saturation velocity, or $^1/_2 V_{max}$.

Multisubstrate systems such as reaction 2 of the type

$$A + B \overset{E}{\rightleftharpoons} P + Q \qquad (10)$$

may proceed via ternary intermediate complexes through a sequential mechanism such as

$$E + A = EA \quad \text{or} \quad E + B = EB \qquad (11)$$

$$EA + B = EAB \quad \text{or} \quad EB + A = EAB \qquad (12)$$

$$EAB \rightarrow E + \text{product(s)} \qquad (13)$$

Reaction sequence 11–13 is characterized by the feature that both the substrate (A) and the cosubstrate (B) first bind with the enzyme (E) in a ternary complex (EAB) before any products are released. If the transformation of the ternary complex into products is relatively slow and that of complex formation is rapid, the following simplified velocity equation may be obtained for such a system:[8]

$$V_0 = \frac{V_{max}}{1 + \frac{(K_M)_A}{[A]} + \frac{(K_M)_B}{[B]} + \frac{(K_M)_{AB}}{[A][B]}} \qquad (14)$$

where two Michaelis–Menten constants, $(K_M)_A$ and $(K_M)_B$, and corresponding substrate (A) and cosubstrate (B) concentrations are implicated, and the last term of the denominator relates to the mutual interaction of A and B at the binding site. Under conditions where the concentration of substrate A is much greater than its Michaelis constant, $[A] \gg (K_M)_A$, velocity eq 14 can be reduced to

$$V_0 = \frac{V_{max}}{1 + (K_M)_B/[B]} = \frac{V_{max}[B]}{(K_M)_B + [B]} \qquad (15)$$

A similar approach with $[B] \gg (K_M)_B$ will result in a velocity equation in terms of substrate A and $(K_M)_A$. Such equations correspond to the velocity equation of a single-substrate reaction and allow simplified Michaelis constant evaluation.

As the reaction proceeds, substrate concentrations gradually decrease and, as the product concentration builds up, the unidirectionality of the reaction no longer exists. This invalidates the assumptions used to derive the V_0 equations. Hence, it is essential to make measurements within the time interval during which reaction conditions do not deviate significantly from those required for the velocity equations.

A variety of approaches have been used to monitor the progress of pyridine nucleotide-dependent enzymatic reactions. Spectrophotometric absorption of ultraviolet radiation by the reduced form of the cofactor, NAD(P)H, is the most commonly accepted method. However, few published studies have intercompared amperometrically and spectrophotometrically obtained enzyme kinetic parameters. Talbott[9] found good agreement between spectrophotometrically determined values reported in the literature and his electrochemically determined Michaelis constant, K_m, for the substrate β-D-glucose but not for the cosubstrate of glucose oxidase, a bisubstrate, biproduct enzyme which does not involve a ternary complex. Other researchers have noted discrepancies as well. It is of general interest to compare results obtained spectrophotometrically and amperometrically, both for analytical purposes and as a way of probing the possibility that mediators effect changes in the kinetic mechanism of the "natural" enzymatic reaction.

EXPERIMENTAL SECTION

Apparatus. Electrochemical experiments were performed in a water-jacketed, thermostated cell at a platinum rotated disk electrode (Pt-RDE, area = 3.2×10^{-6} m^2) with a platinum wire auxiliary electrode and saturated calomel reference electrode (SCE). Constant-potential chronoamperometric experiments were carried out with an IBM EC/225 voltametric analyzer set at the desired potential. Data were acquired with a Rapid Systems 4 × 4 digital oscilloscope and/or a Yokogawa XYT recorder.

Reagents. All solutions were prepared with distilled water in which the conductivity was determined to be less than 11 $\mu\Omega^{-1}$. Potassium hexacyanoferrate(III) (Baker), ethanol (Pharmco), β-nicotinamide adenine dinucleotides (NAD$^+$ and NADH, Sigma), and yeast alcohol dehydrogenase, EC 1.1.1.1 (Sigma), were used without further purification. The supporting electrolyte was 0.2 M KCl in pH 8.8, 0.05 M pyrophosphate buffer.

Procedure. Unless otherwise stated, experiments were performed at 298 K under anaerobic conditions. Yeast alcohol dehydrogenase (Y-ADH) in concentrations appropriate to the experimental design (100 pM for initial velocity experiments, 400 nM for ethanol concentration determinations) was added to the electrochemical cell which held 10 mL of a buffered solution of ethanol and NAD$^+$. Ethanol concentrations of 0.01–300 mM (100K_M) and NAD concentrations of 0.02–8 mM (10K_M), were used. Except as noted, the $K_3Fe(CN)_6$ concentration was kept at 50 mM. Prior to each recording the working electrode was polished 3 min with 0.05-μm γ alumina (Buehler), rinsed in distilled water, and sonicated 10 s in distilled water. The cell was covered, and its contents were sparged prior to and blanketed during each experiment with N_2. The Pt-RDE was rotated at 900 or 1600 rpm with a Pine Instrument Co. analytical rotator. The potentiostat was set to maintain a potential difference of +500 mV vs SCE (a potential at which the anodic current was limited by mass transport of hexacyanoferrate from bulk solution to the electrode surface), and the anodic current was recorded as a function of time. Experiments to determine enzyme kinetic parameters were patterned after the initial velocity studies described by Segel.[7] Slope measurements were made on the steepest part of the current–time response, representing the first 10–30 s of the reaction.

RESULTS AND DISCUSSION

Relationship of Current–Time Behavior to Hexacyanoferrate(II) Concentration. The ternary reaction sequence for the ADH-catalyzed oxidation of ethanol was

enzymatic

$$C_2H_5OH + NAD^+ = CH_3CHO + NADH + H^+ \qquad (16)$$

chemical

$$NADH + 2Fe(CN)_6^{3-} = NAD^+ + 2Fe(CN)_6^{4-} + H^+ \qquad (17)$$

electrochemical

$$Fe(CN)_6^{4-} = Fe(CN)_6^{3-} + e^- \text{ (anodic current)} \qquad (18)$$

Reactions 16 and 17 are homogeneous reactions occurring in aqueous solution, while reaction 18 is heterogeneous, with electron transfer across the electrode–solution interface. Oxidation of ethanol, indicated by the forward direction of reaction 16, proceeds to virtual completion at pH 8.8. Reaction 18 is fast compared to reactions 16 and 17 at the applied potential (500 mV vs SCE) where the rate is mass transport limited. Figure 1 shows the relative concentration profile of the reactants and products in this sequence. Note that the $Fe(CN)_6^{4-}$ concentration increases at twice the rate of ethanol depletion and that, after an initial decrease, the

---

[8] Michal, G. In *Principles of Enzymatic Analysis*; Bergmeyer, H. U., Ed.; Verlag Chemie: New York, 1978; pp 29–34.

[9] Talbott, J. L. Enzymatic Amperometry of Glucose. Ph.D. Thesis, The Pennsylvania State University, 1987.

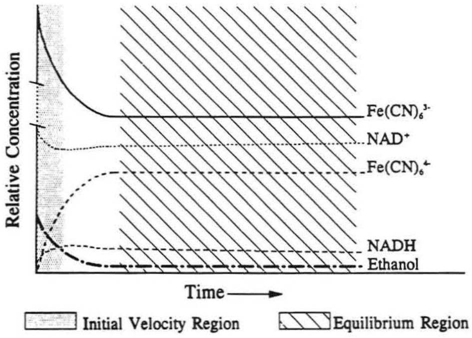

Figure 1. Relative concentration profile of reactants and products in ADH-catalyzed ethanol oxidation coupled to the electrode by hexacyanoferrate(II/III) (not to scale).

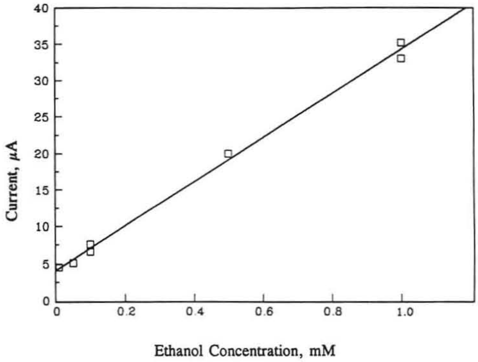

Figure 2. Linear range for amperometric ethanol concentration determination. Plot of i_l for hexacyanoferrate(II) oxidation at times corresponding to the equilibrium region of Figure 1.

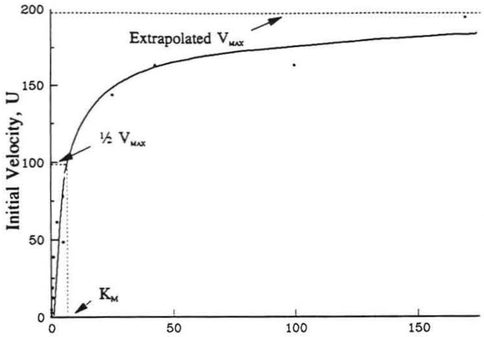

Figure 3. Michaelis plot showing initial reaction velocity in enzyme units. 1.0 unit of enzyme activity transforms 1.0 μmol of substrate/min at 298 K.

NAD^+ concentration remains constant since virtually all NADH produced is immediately reoxidized by $Fe(CN)_6^{3-}$ via reaction 17.

Hexacyanoferrate(II/III) meets many of the criteria for desirable redox couples, as listed by Coury et al:[10] well-defined, reversible voltammetry, adequate aqueous solubility, availability in high purity, sufficient chemical stability, lack of cross-reactivity with the enzymatic substrate, and ability to accept electrons from the reduced enzyme or the reduced cofactor. In addition, at moderate concentrations $Fe(CN)_6^{3-}$ does not significantly affect the activity of the enzyme itself. The two-reaction sequence (reactions 17 and 18) has been studied at glassy carbon and carbon paste electrodes and applied to lactate dehydrogenase assays in serum.[11] Hexacyanoferrate(III) has been employed as a mediator or amperometric couple by other researchers with flavin enzymes.[12,13] At a platinum electrode, hexacyanoferrate(II) ($E_{1/2}$ = 220 mV vs SCE) is oxidized at a potential several hundred millivolts less anodic than NADH, significantly reducing the probability that side reactions (electrooxidation of other biological components which may be present in the sample) will occur. Nevertheless, some side reactions do occur. Analysis of the steady-state current obtained for these experiments which were allowed to proceed to virtual completion (equilibrium region of Figure 1) revealed an anodic current 2–9% in excess of the current predicted for 100% efficiency according to the Levich equation. The percent current excess is greatest for experiments using high enzyme concentrations and amounts to 0.6 μA/mg of ADH. It is possible that impurities in the crystalline Y-ADH preparation, such as residual ethanol and NADH, are partly responsible for the observed current excess. On the other hand, some oxidation of ADH by hexacyanoferrate(III) may account for the excess current, which is proportional to the amount of enzyme present. We have encountered high oxidation currents and loss of enzyme activity with another enzyme, alcohol oxidase, in the presence of hexacyanoferrate(III) (unpublished data), and Durliat et al.[13] have reported loss of enzyme activity with hexacyanoferrate(III) concentrations greater than 10 mM with lactate dehydrogenase. However, this effect with ADH is small and does not invalidate determination of ethanol concentration or kinetic parameters discussed below. Initial reaction rates were determined from the slope of the current–time graph during the first 30 s of the reaction (initial velocity region of Figure 1), using the Levich equation:

$$i_l = 0.620nFAD^{2/3}\omega^{1/2}\nu^{-1/6}C^*$$

in which D, the diffusion coefficient of $Fe(CN)_6^{4-}$, is 6.5 × 10^{-10} m²/s at 298 K (Adams[14]), ν, kinematic viscosity, is 1.0 × 10^{-6} m²/s, A is the area of the Pt-RDE, C^* is the bulk concentration of $Fe(CN)_6^{4-}$, $n = 1$ is the number of electrons transferred in the electrooxidation of $Fe(CN)_6^{4-}$, and F is the Faraday constant. Since the amount of $Fe(CN)_6^{4-}$ generated in reaction 17 is stoichiometrically related to the amount of ethanol reacted

$$\Delta C^*_{\mathrm{Fe(CN)_6^{4-}}} = -2\Delta C^*_{\mathrm{ethanol}}$$

i_l represents a measure of the amount of ethanol that has been oxidized. The rate of change of the limiting current then gives the rate of change of concentration, i.e., the reaction rate:

$$\frac{\Delta i_l}{\Delta t} = 0.620nFAD^{2/3}\omega^{1/2}\nu^{-1/6}\frac{\Delta C^*}{\Delta t}$$

Initial rate analysis of experiments in which concentrations of $Fe(CN)_6^{3-}$ or NADH were varied while the other was held

---

(10) Coury, L. A., Jr.; Oliver, B. N.; Egekeze, J. O.; Sosnoff, C. S.; Brumfield, J. C.; Buck, R. P.; Murray, R. W. *Anal. Chem.* **1990**, *62*, 452–458.

(11) Thomas, L. C.; Christian, G. D. *Anal. Chim. Acta* **1976**, *82*, 265–272.

(12) Talbott, J.; Jordan, J. *Microchem. J.* **1988**, *37*, 5–12.

(13) Durliat, H.; Comtat, M.; Mahenc, J. *Anal. Chim. Acta* **1976**, *85*, 31–40.

(14) Adams, R. N. *Electrochemistry at Solid Electrodes*; Marcel Dekker, Inc.: New York, 1969.

Table I. Comparison of Spectrophotometric and Amperometric Kinetic Parameters

kinetic param	spectrophotometric value	electrochemical value	method of data analysis[7]
V_{max}	100% of specified ADH assay value[a]	85% of specified ADH assay value	Eadie–Hofstee
K_M(ethanol), mM	3	3.2[b]	Eadie–Hofstee
K_M(NAD^+), mM	0.1–1	0.80[c]	Eadie–Hofstee
k_{cat}, s^{-1}	450	448[d]	Δ[NADH, μM]/Δt per μM enzyme

[a] Information supplied by manufacturer. [b] Sample standard deviation, $s_x = \sqrt{[n\Sigma x^2 - (\Sigma x)^2]/n(n-1)} = 0.5$, $n = 16$. [c] $s = 0.08$, $n = 10$. [d] $s = 42$, $n = 14$.

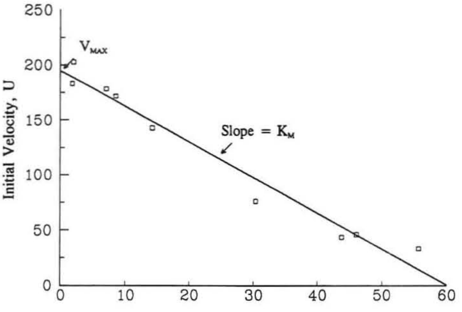

Figure 4. Eadie–Hofstee plot of initial reaction velocity versus initial velocity to ethanol concentration ratio. The Michaelis constant, K_M, for ethanol here is seen to be 3.2 mM.

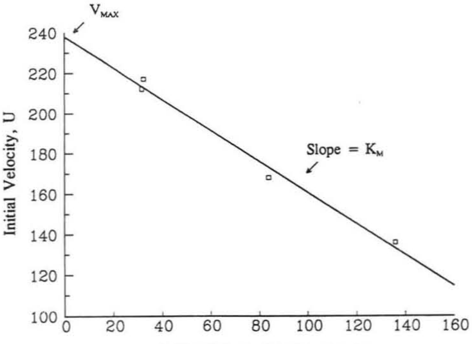

Figure 5. Eadie–Hofstee plot of initial reaction velocity versus velocity to NAD concentration ratio. The Michaelis constant, K_M, for NAD here is seen to be 0.8 mM.

constant clearly indicated that reaction 17 was first order with respect to both NADH and $Fe(CN)_6^{3-}$. This is in agreement with the work of Carlson et al.[15] who used ferrocenium salts as their 1-electron amperometric couple and found the reaction to be first order in both NADH and the amperometric couple. The rate constants for reaction 17 were determined from initial reaction rates to be 1.0 and 0.234 $M^{-1}\,s^{-1}$ at 298 and 279 K, respectively. An Arrhenius plot of these values, under the assumption that linearity prevails within this temperature range (not documented), indicates an activation energy barrier on the order of 50 kJ mol^{-1}.

The initial velocity of the ternary reaction sequence 16–18 was directly proportional to $Fe(CN)_6^{3-}$ concentrations up to approximately 25 mM. At $Fe(CN)_6^{3-}$ concentrations above 25 mM the velocity approached a maximum determined primarily by the rate at which NADH was produced in reaction 16. Thus the rate-determining reaction in the sequence is reaction 16 and $\Delta i/\Delta t$ is a valid measure of the rate of enzyme-catalyzed ethanol oxidation under the prevailing experimental conditions. Concentration-dependent enzyme activity inhibition could not be discerned up to 150 mM $Fe(CN)_6^{3-}$.

Enzyme Kinetic Parameters. Ethanol concentrations between 0.01 and 1 mM show an excellent linear current response ($R = 0.9982$), as can be seen from Figure 2. The current was measured 30 min after enzyme was added to the reaction mixture, at which time the reaction had nearly gone to completion (the so-called "equilibrium region" of Figure 1). This linearity is further documented in the Michaelis plot of initial reaction velocities (Figure 3). The maximum initial reaction velocity, V_{max}, seen in Figure 3 was lower than the value determined spectrophotometrically with comparable NAD, ADH, and ethanol concentrations. The primary experimental difference was the presence of various concentrations of $Fe(CN)_6^{3-}$ in the reaction mixture of the electrochemical experiments. Possibly, hexacyanoferrate(III) interacts with the enzyme in a concentration-independent manner and limits the maximum reaction velocity. The enzyme activity (V_{max}) specified on the assay data sheet accompanying the Y-ADH purchased from Sigma was confirmed by spectrophotometric analysis (by the method of Hoch and Vallee as described in ref 21) in our laboratory. Electrochemical determination, however, consistently gave V_{max} values approximately 15% lower than spectrophotometric determination.

Kinetic parameters determined amperometrically in our laboratory are summarized in Table I, together with spectrophotometric literature values. Michaelis constants, K_M, for ethanol and NAD were determined from initial reaction rates at the Pt-RDE. Analysis by Eadie–Hofstee plots and Lineweaver–Burk plots yielded similar values. A survey of the literature shows that these have been extensively studied spectrophotometrically. Dickinson and Monger,[16] working at pH 7.05, obtained $K_M(NAD^+) = 0.109$ mM and K_M(ethanol) = 21.7 mM. Hayes and Velick[17] determined the Michaelis constants, K_M, at pH 7.9 to be 0.17 mM (NAD^+) and 18 mM (ethanol). Burstein et al.[18] reported K_M values of 1 and 3 mM for NAD^+ and ethanol, respectively, for ADH in pH 9.2 buffer solution. The considerable variability of the Michaelis constants reported above appears to be at least partially related to pH. A comparison of kinetic parameters determined spectrophotometrically with those determined electrochemically thus must take this factor into consideration. Albery[19] worked out the steady-state kinetic equations for a conducting organic salt-membrane electrode and applied it to ADH-catalyzed alcohol oxidation.[20] He lists an "electrochemical Michaelis constant", K_{ME}, for ethanol of 2.7 mM at

---

(15) Carlson, B. W.; Miller, L. L.; Neta, P.; Grodkowski, J. *J. Am. Chem. Soc.* **1984**, *106*, 7233–7239.

(16) Dickinson, F. M.; Monger, G. P. *Biochem. J.* **1973**, *131*, 261–270.

(17) Hayes, J. E.; Velick, S. F. *J. Biol. Chem.* **1954**, *207*, 225–244.

(18) Burstein, C.; Ounissi, H.; Legoy, M. D.; Gellf, G.; Thomas, D. *Appl. Biochem. Biotechnol.* **1981**, 329–338.

(19) Albery, W. John; Bartlett, P. N. *J. Electroanal. Chem. Interfacial Electrochem.* **1985**, *194*, 211–222.

(20) Albery, W. J.; Bartlett, P. N.; Cass, A. E. G.; Sim, K. W. *J. Electroanal. Chem. Interfacial Electrochem.* **1987**, *218*, 127–134.

pH 9.0. This is in good agreement with our results (K_M(ethanol) = 3.2 mM at pH 8.8) as determined from Eadie–Hofstee plots (Figure 4), in spite of experimental differences. The research reported here differs from the Albery experiment in that neither the enzyme nor the mediator were physically immobilized near the electrode surface. Thus, our system is dependent only on the well-documented diffusion coefficient of $Fe(CN)_6{}^{4-}$ in water and is not affected by diffusion through membrane material. It is apparent that at pH closer to 7, the Michaelis constant for ethanol is much greater than in basic solution. This suggests that the enzyme has greater affinity for ethanol in basic solution, as anticipated from the fact that ethanol oxidation is optimal at pH 8.8 while equilibrium is strongly shifted in favor of aldehyde reduction[21] at pH 7. The reverse trend for NAD^+ is difficult to explain but may in fact reflect variation due to experimental design. For many dehydrogenases the K_M for NAD^+ falls in the range 0.1–1 mM.[22] As pH increased from 7.05 to 9.2, the reported K_M(NAD) increased from 0.109 to 1 mM. The K_M(NAD) = 0.80 mM value obtained amperometrically at pH 8.8 in our laboratory (Figure 5) is in general agreement with this pattern of pH dependency. Our amperometrically determined catalytic constant, k_{cat}, also known as the turnover number, was in excellent agreement with spectrophotometrically determined values.[16,17]

The averaged kinetic results of more than a dozen experiments are presented in Table I alongside spectrophotometrically determined parameters. Literature values used in this table are referenced in the discussion and were selected from research conducted at pH 9 ± 0.2 whenever available.

CONCLUSIONS

A comparison of amperometrically (in the presence of an artificial mediator) and spectrophotometrically determined enzyme kinetic parameters shows overall good agreement between the two methods. We feel that the concordance between available spectrophotometric measurements in the literature and electrochemical measurements is generally so satisfactory that it indicates that the relevant enzymatic mechanisms of the natural enzymatic reaction and the one occurring in the presence of the mediator are the same. Only the maximum reaction velocity, V_{max}, determinations showed differences in excess of 10% which warrant further investigation.

ACKNOWLEDGMENT

Financial support was provided by the Ben Franklin Partnership of the Commonwealth of Pennsylvania and by Med-Chek Laboratories of Pittsburgh. M.K.C. is grateful for sabbatical leave granted by the State College (PA) Area School District.

RECEIVED for review April 17, 1992. Accepted October 20, 1992.

---

[21] *Worthington Enzyme Manual*; Worthington, C. C., Ed.; Worthington Biochemical Corp.: Freehold, NJ, 1988.

[22] Fersht, A. *Enzyme Structure and Mechanism*; W. H. Freeman and Co.: San Francisco, 1977.

Anal. Chem. **1993,** *65,* 169–175 **169**

Photoelectrochemical Sensor for Catalase Activity Based on the in Situ Generation and Detection of Substrate

Claudia B. Cohen and Stephen G. Weber*

Department of Chemistry, University of Pittsburgh, Pittsburgh, Pennsylvania 15260

A device for the in situ generation and detection of hydrogen peroxide is presented for application to the automation of enzyme immunoassay and application to biosensors. The device is fabricated from a gold-coated optical fiber. It photochemically generates and electrochemically detects H_2O_2 in aqueous, buffered solutions. The electrochemical signal is attenuated in the presence of the enzyme catalase (EC 1.11.1.6), for which H_2O_2 is a substrate. The quantum efficiency of the peroxide-producing reaction (0.20%), the collection efficiency of the gold ring electrode ($(3.8 \pm 0.5) \times 10^{-3}$), and the sensitivity of the photocurrent to catalase have been evaluated. The sensor's photosignal is reduced by 50% in the presence of 25 nM catalase. Detection limits of 76 pM catalase have been obtained using FIA.

INTRODUCTION

Enzyme immunoassay (EIA) is an invaluable tool for the specific and sensitive determination of a host of chemical species.[1-3] In fact, EIA is often the method of choice for the identification and quantitation of analytes of clinical and environmental significance. The EIA is at once simple, sensitive, and robust, and sensors based on the principles of EIA would be a natural technological evolution. Aizawa,[4] Ikarayama,[5] and Hill[6] have each made contributions toward the design of such devices; however, to date, they cannot be elevated to the status of "sensor" because the manual addition of substrate to the sample is necessary once the device is in place. The requirement of substrate addition is a significant impediment to the successful development of EIA-inspired sensors.[7,8]

There are several possible approaches to this obstacle. Enzyme substrate could be released in a regulated way using coulometric control over modified electrodes.[9] Less controlled, but simpler, is the slow leak approach of Walt[10] in which a reservoir of substrate passively releases its contents by diffusion. In addition to these approaches there are electrochemical and photochemical reactions that may be used to create substrate on demand from a plentiful precursor. The advantage of the latter approach is that substrate can be generated indefinitely if the precursor is ubiquitous; however, the substrate generation reaction must be chosen carefully since few ubiquitous substrate precursors exist. A sensor based on the latter principle must generate substrate and then detect it or detect the product of the enzyme reaction. A change in the detected signal signifies the presence of the enzyme-labeled analyte. Recently, enzyme electrodes which incorporated horseradish peroxidase were shown to be sensitive to cyanide[11] and Mn^{2+}.[12] These devices generated hydrogen peroxide electrochemically.

This paper describes a device that generates and detects hydrogen peroxide, which is a substrate for catalase and peroxidases. The hydrogen peroxide is generated from the photochemical reduction of the ubiquitous substrate precursor, oxygen. The photoreduction is mediated by tris(2,2′-bipyridine)ruthenium, $Ru(bpy)_3^{2+}$, by an as yet incompletely understood mechanism.[13-15] The peroxide is detected amperometrically. The basis for the device is the gold-coated optical fiber[16] which conveniently illuminates an area inside of a circular, gold ring electrode. The optical fiber makes it possible to photoexcite $Ru(bpy)_3^{2+}$ in oxygen-containing samples. Peroxide, generated as a result of the quenching reaction, can diffuse to the gold ring working electrode. The $Ru(bpy)_3^{3+}$ generated from the quenching reaction can be rapidly reduced back to the dication by reductants that are present in serum and urine, the most important of which is uric acid.[17] The cationic $Ru(bpy)_3^{2+}$ can be isolated on the device in an ion-exchange membrane such that the sensor is truly reagentless.

We have determined the sensitivity of peroxide-containing solutions to catalase, the quantum efficiency of the peroxide-producing reaction as it occurs in solution, and we have estimated the quantum efficiency of the same reaction as it occurs in the device. We have also attempted to estimate the collection efficiency of the ring electrode, that fraction of the peroxide produced at the face of the optical fiber that is detected at the surrounding gold ring. Finally the device's sensitivity to catalase has been determined, and some clues as to the influence of the spatial arrangement of the source of the peroxide and the detector of the peroxide have been obtained.

EXPERIMENTAL SECTION

Probe Construction. *Materials.* A number of devices were constructed at various points throughout the development of the sensor. Gold-coated fused-silica fiber from Fiberguide was used (SFS400/440G). The fiber consists of a 400-μm diameter pure fused-silica core, a 20-μm-thick fluorine-doped fused-silica

---

* To whom correspondence should be addressed.

(1) Munroe, D. *Anal. Chem.* **1984,** *56,* 920A–931A.

(2) Rubenstein, K. E.; Schneider, R. S.; Ullman, E. F. *Biochem. Biophys. Res. Commun.* **1972,** *47,* 846.

(3) Nakamura, R. M.; Robbins, B. A. *J. Clin. Lab. Anal.* **1988,** *2,* 51–61.

(4) Aizawa, M. In *Chemomeasuring by High Performance Chemical Sensor Systems, Final Report of Special Project Research,* Chairman Tanaka, S.; 1986–1988; pp 217–222.

(5) Ikariyama, Y.; Furuki, M.; Aizawa, M. *Anal. Chem.* **1985,** *57,* 496–500.

(6) Hill, H. A. O.; Klein, N. A.; Psalti, I. S. M.; Walton, N. J. *Anal. Chem.* **1989,** *61,* 2200–2206.

(7) Anderson, F. P.; Miller, M. G. *Clin. Chem.* (*Winston-Salem*) **1988,** *37,* 1417.

(8) Meyerhoff, M. E. Personal Communication, 1992.

(9) Miller, L. L.; Smith, G. A.; Chang, A. C.; Zhou, Q. X. *J. Controlled Release* **1987,** *6,* 293.

(10) Barnard, S. M.; Walt, D. R. *Science* **1991,** *251,* 927.

(11) Smit, M. H.; Cass, A. E. G. *Anal. Chem.* **1990,** *62,* 2429.

(12) Smit, M. H.; Rechnitz, G. A. *Anal. Chem.* **1992,** *64,* 245.

(13) Demas, J. N.; Diemente, D.; Harris, E. W. *J. Am. Chem. Soc.* **1973,** *95,* 6864.

(14) Winterle, J. S.; Klinger, D. S.; Hammond, G. S. *J. Am. Chem. Soc.* **1976,** *98,* 3719.

(15) Ismail, K. Z.; Weber, S. G. *Biosens. Bioelectron.* **1991,** *6,* 699–705.

(16) Kuhn, L. S.; Weber, A.; Weber, S. G. *Anal. Chem.* **1990,** *62,* 1631.

(17) Weber, S. G.; Morgan, D. M.; Elbicki, J. M. *Clin. Chem.* (*Winston-Salem*) **1983,** *29,* 1665.

0003-2700/93/0365-0169$04.00/0

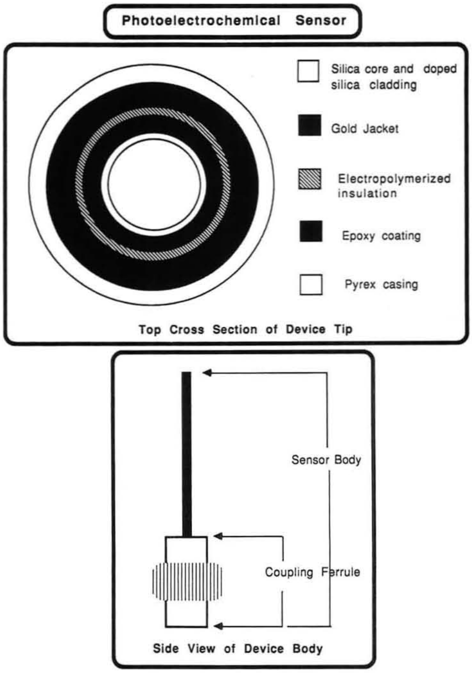

Figure 1. Schematic of the sensing device.

cladding, and a 35-μm-thick gold jacket. In some cases a smaller diameter fiber was used in which case all the dimensions were halved. Ensign Bickford Optics Co. couplers (CC-430-3.0) were used to link the sensor to the fiber optic from the light source. An air-cooled multiline argon ion laser, Cyonics (Model 2201-30BL), provided 458–515-nm light for all the experiments except the enzymatic determination of the quantum efficiency of peroxide production. Epoxy, Epotek 353ND (Billerica, MA), was used as an insulating adhesive.

Electrochemical polymerization of 2-allylphenol[18] on the gold part of the fiber was performed with ammonium hydroxide (Fisher), ethylene glycol monobutyl ether (Aldrich), and 98% 2-allylphenol (Aldrich) in methanol (Fisher)/water (doubly deionized and distilled). The monomer was electropolymerized at +0.40 V vs a silver wire reference with a silver wire auxiliary electrode for 30 min. The poly(oxyphenol) coating on the fiber was cured overnight (12–15 h) at 160 °C. SEM observations are consistent with the deposition of an insulating, continuous thin film along the length of the gold-coated fiber.

Fabrication Procedure. Various fabrication procedures were implemented throughout the development of the construction of the sensor. The most recent version of the device is depicted in Figure 1. Sections of the coated fiber, approximately 5 cm in length, were cleaved with a hand-held scoring device. The gold was rinsed with flux (W. Harris Co.), rosin flux remover (Archer), and water. Several millimeters of gold were stripped from one end of the fiber by running it through a bead of hot solder. The remaining gold and solder were removed by exposure of the stripped part of the fiber to aqua regia for approximately 15 min at room temperature. The exposed cladding was etched in concentrated hydrofluoric acid for 3–5 min until the fiber fit snugly into the coupling ferrule. An electrical connection between the ferrule and gold was made by soldering 100-μm copper wire to the exposed gold and the coupler. In some instances the 100-μm wire was in turn attached to a 0.75-mm copper lead.

The poly(oxyphenol)-insulated fiber was covered with 353ND epoxy for rigidity and to protect the polymer film. The device was polished in a series of slurries: 7-μm silicon carbide (Buehler) and 0.3-, 0.1-, and 0.05-μm alumina (Leco), on a Leco VP-50 polishing wheel with the aid of an in-house-made electrode holder. In some experiments the device was coated with approximately 5-μL of Nafion solution as received (5 wt % solution in a mixture of lower molecular weight alcohols and 10% water). The droplets air-dried. The Nafion-coated fibers were then soaked in an aqueous solution of 1 mM $Ru(bpy)_3^{2+}$ for 15 min and rinsed with water.[19]

Characterization of the Device. *Reagents.* Tris(2,2′-bipyridine)ruthenium(II) chloride hexahydrate, ($Ru(bpy)_3^{2+}$), from Strem Chemicals was used as obtained for photochemical experiments. Ferrocene and ferrocenecarboxylic acid (Aldrich) were used as received for electrochemical characterization. Potassium phosphate, monobasic (EM Sciences), sodium hydroxide and hydrogen peroxide (30% in water) (Mallinckrodt), hydrofluoric acid (J. T. Baker), hydrochloric acid (Fisher Scientific), and triethanolamine (Aldrich) were all used as received. Purified catalase (11 000 units/mg protein) from bovine liver was obtained from Sigma. All water was doubly deionized and distilled.

Quantum Efficiency of Peroxide Production. The quantum efficiency for the photochemical production of hydrogen peroxide was evaluated enzymatically. Hydrogen peroxide was generated from the quenching by oxygen of photoexcited $Ru(bpy)_3^{2+}$ in aqueous solutions of 5 μM $Ru(bpy)_3^{2+}$, 10 mM EDTA. The solutions were irradiated for 5 min with 50-mW, 458-nm light from a Spectra Physics Model 164-09 argon ion laser (Spectra-Physics, Inc., Mountain View, CA). An excess of horseradish peroxidase (HRP) and tetramethylbenzidine (TMB) were then added. TMB is oxidized by H_2O_2 in the presence of HRP to a colored product (λ_{max} = 655 nm, ϵ_{max} = 5400).[20,21] The quantity of photogenerated H_2O_2 was evaluated from a calibration curve of TMB absorbance as a function of peroxide concentration. The calibration curve was constructed from various H_2O_2-spiked solutions in which the H_2O_2 concentration was determined by titration with standardized potassium permanganate solution.[22]

Photovoltammetry. Photovoltammograms were constructed from chronoamperometric data. The working electrode was either the gold microring exposed at the end of the optical fiber or a 10-μm gold disk embedded in a glass sleeve (BAS) for the chronoamperometric experiments. Two-electrode, constant-potential experiments were conducted with a Ag/AgCl (3 M NaCl) reference/auxiliary electrode (FIA/ECD experiments), or with a silver wire. NaCl (10 mM) was present in solutions when a silver wire was used. The device was housed in a light-tight aluminum box within a Faraday cage.

Laser light for the photovoltammetric experiment was focused with an inverted 10× microscope objective to a coupling fiber via a Newport Model F-19-Cl-T fiber optic coupler. The power emanating from the fiber tip of the device was 6 mW. Voltages were applied with an LC-4 Bioanalytical Systems amperometric detector. Signals were recorded on an Allen Datagraph XY recorder. Oxidation currents were recorded as a function of time in the dark and then during irradiation. The signals increased monotonically following the onset of illumination until they reached a stable current plateau. Steady-state responses were reached 25–35 s after the light was turned on. No change in response was observed for 500 s after plateau values were achieved. Three to six replicate photocurrents at the plateau value after about 50–100 s were averaged. Replicate measurements within samples and between samples were conducted. Errors reported here are standard deviations. Figure 2 shows a typical chronoamperometric response to light for a 200-μm core diameter fiber in a 10-μL sample of 0.2 mM $Ru(bpy)_3^{2+}$ in 0.1 M phosphate buffer, 10 mM NaCl, 25 mM triethanolamine. Note that the magnitude of the photogenerated current can be controlled by

---

[18] Potje-Kamloth, K.; Janata, P.; Janata, J.; Josowicz, M. *Sens. Actuators* **1989**, *18*, 415–425.

[19] Szentirmay, M. N.; Martin, C. R. *Anal. Chem.* **1984**, *56*, 1898–1902.

[20] Holland, V. R.; Saunders, B. C. *Tetrahedron* **1974**, *30*, 3299–3302.

[21] Lijana, R. C.; Williams, M. C. *J. Lab. Clin. Med.* **1974**, *92* (2), 266–276.

[22] Braun, R. D.; Walters, F. H. *Applications of Chemical Analysis*; McGraw-Hill, Inc.: New York, 1982; p 86.

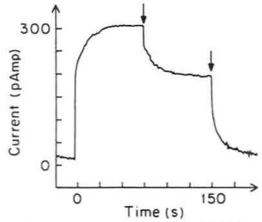

Figure 2. Current response as a function of light intensity. Oxidation currents for a 0.2 mM $Ru(bpy)_3^{2+}$ solution in 0.1 M phosphate buffer, 10 mM NaCl, 25 mM triethanolamine at pH 7.0 are shown. A 10-μL sample was irradiated with blue light through a 200-μm core diameter optical fiber. The current was collected at a 230-μm-diameter gold ring electrode poised at +0.500 V vs a silver wire reference/auxiliary electrode. The abscissa is 25 s/division, and the sensitivity is 50 pA/division. At time zero, the light (6 mW) was turned on. The first arrow corresponds to the time at which the light intensity was approximately halved by turning the rotating power dial of the laser power supply. The second arrow indicates the time at which the laser light was turned off.

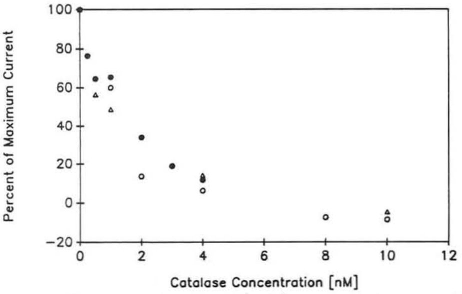

Figure 3. Current as a function of catalase concentration at a gold ring electrode in a flow cell (gold ring working electrode (230-μm i.d.) in a flow cell vs Ag/AgCl (3.0 M NaCl) with a steel auxiliary electrode). Samples (100 μL) of peroxide in 0.1 M phosphate buffer, 10 mM NaCl, pH 7.0, contained (○) 20 μM, (●) 20 μM, and (△) 40 μM hydrogen peroxide. Each symbol represents data obtained on different days.

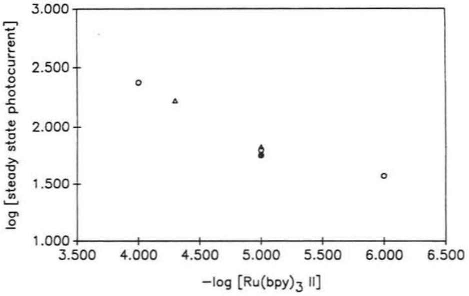

Figure 4. Current as a function of $Ru(bpy)_3^{2+}$ concentration for the electrochemical sensor. Steady-state oxidation currents at +0.500 V were observed with a 200-μm core diameter fiber and a 15-μm-thick gold ring. Samples (10 μL) of $Ru(bpy)_3^{2+}$ in 0.1 M phosphate buffer, 10 mM NaCl, 25 mM triethanolamine, pH 7.0, were irradiated for 60 s with 5 mW of blue light. Different symbols denote data obtained on various days.

controlling the light intensity. The signal decays to its baseline value when the light is turned off.

Characterization of the gold ring working electrode and its sensitivity to catalase in the presence of hydrogen peroxide was investigated with flow injection analysis using a stainless steel flow cell with a Teflon floor. A Narishige MN-100N joystick manipulator facilitated the placement of the gold electrode directly over the entry aperture of the flowing buffer. The stainless steel wall of the cell served as an auxiliary electrode in three-electrode experiments. The buffer was pumped with a Laboratory Data Control Constametric III pump modified with a low flow rate pump. The flow stream from the pump was connected with Teflon tubing to the Teflon floor of the flow cell.

RESULTS AND DISCUSSION

In order to assure ourselves that the gold ring electrode was responsive to H_2O_2, that the H_2O_2 concentration was responsive to catalase at low catalase concentrations and that the catalase does not foul the electrode at the concentration used, we performed FIA experiments. In these experiments, there was no photochemical production of peroxide, and peroxide solutions were used. To the peroxide solutions, catalase was added 30 s before injection into the FIA system. The gold ring working electrode was poised at +0.500 V vs a silver/silver chloride (3.0 M NaCl) reference electrode with a steel auxiliary electrode in the flow cell. Figure 3 contains the data for the enzymatic attenuation of peroxide oxidation current. Note that the current generated by the oxidation of the enzyme substrate, peroxide, is sensitive to catalase. Exposure of the substrate to the enzyme results in depletion of the peroxide and a corresponding decrease in the measured current. As little as 1 nM catalase reduces the oxidation current by 40%. The catalase sensitivity does not appear to be a function of peroxide concentration; the substrate concentration does not alter the activity beyond that due to day to day variability. The FIA signals depend only on the catalase concentration, not on the order in which they were injected. We infer from this that catalase does not foul the electrode at the concentrations used.

The quantum efficiency for the photochemical production of hydrogen peroxide by oxygen quenching of $Ru(bpy)_3^{2+}$ in aqueous solution was determined enzymatically in a cuvette by irradiating aqueous samples directly with laser light. The rate of peroxide production for a 5 μM $Ru(bpy)_3^{2+}$ solution in 0.1 M phosphate buffer at pH 7.0 in the presence of 50-mW, 458-nm blue light was 4.7×10^{-11} mol s^{-1}. The efficiency of peroxide production based on the moles of peroxide produced per moles of photons absorbed is 0.17%.

The latter experiment shows that the ubiquitous substrate precursor O_2 can be used to generate H_2O_2 with photochemistry. The former experiment has shown that electrochemical detection of micromolar levels of peroxide is sensitive to nanomolar levels of catalase in a 30-s period. In the remainder of the experiments discussed, various attempts will be made to carry out both functions simultaneously in a small volume.

In all of the experiments in which peroxide was generated from the illumination of $Ru(bpy)_3^{2+}$, it has been necessary to add a reductant, triethanolamine. The photoexcited $Ru(bpy)_3^{2+}$ reduces oxygen to peroxide and triethanolamine serves as a sacrificial electron donor to regenerate $Ru(bpy)_3^{2+}$. This would seem to defeat the purpose of the device, which is to obviate the need for the addition of reagent to the analyzed solution. However, we have shown in previous work[15] that there is a significant concentration of reductants in serum capable of reducing the oxidized ruthenium complex. Thus, for applications in that medium or in urine, no addition of electron donors ought to be required. Because the following experiments were all performed in buffers, there is a need to add a reductant.

A series of solutions of varying concentrations of $Ru(bpy)_3^{2+}$ was illuminated in order to see that the ring electrode was sensitive to the production of an electroactive species in the illuminated volume of the solution in front of the fiber. The steady-state photocurrent from the oxidation of peroxide

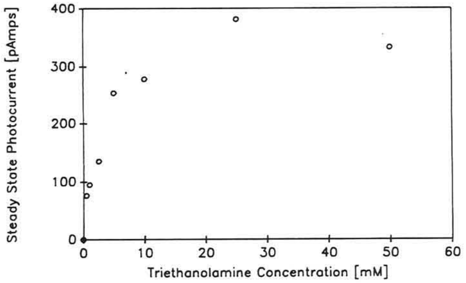

Figure 5. Current as a function of tertiary amine concentration. Steady-state oxidation currents at +0.500 V were assessed with a 200-μm core diameter gold-coated optical fiber vs a silver wire reference/auxiliary electrode. Samples (10 μL) of 0.02 mM $Ru(bpy)_3^{2+}$ in 0.1 M phosphate buffer, 10 mM NaCl, pH 7.0, with various triethanolamine concentrations were irradiated with 6 mW of blue light.

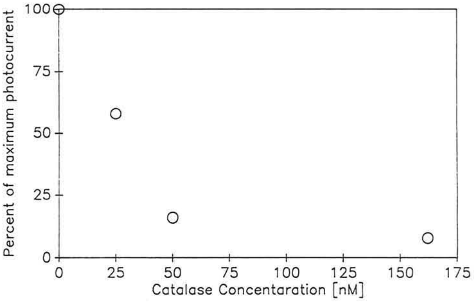

Figure 6. Current as a function of catalase concentration for the $Ru(bpy)_3^{2+}$/Nafion-coated device. Steady-state oxidation currents at +0.500 V were observed for the gold ring electrode (440-μm i.d.) vs a silver wire reference/auxiliary electrode. Samples (5 μL) of 25 mM triethanolamine, 10 mM NaCl, pH 7.0, in 0.1 M phosphate buffer were irradiated for 50 s with 6 mW of blue light.

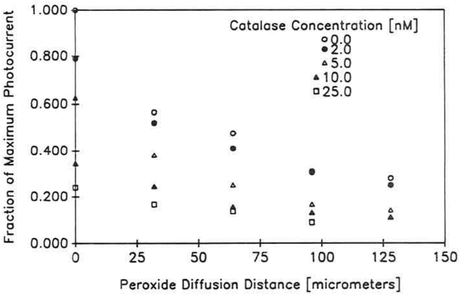

Figure 7. Current as a function of catalase concentration and H_2O_2 diffusion distance between a $Ru(bpy)_3^{2+}$/Nafion-coated optical fiber and a gold microelectrode. Samples (5 μL) of 25 mM triethanolamine, 10 mM NaCl, pH 7.0, in 0.1 M phosphate buffer were irradiated for 60 s with 6 mW of blue light. The oxidation currents were observed at +0.500 V applied to the gold microelectrode (10-μm diameter) vs a silver wire reference/auxiliary electrode.

generated in the quenching reaction in 10-μL aliquots of each solution was recorded. These data are plotted as Figure 4. The light power at the tip of the device was 6 mW, the applied potential was +0.500 V, and the optical fiber diameter was 200 μm. The dependence of the photocurrent on the concentration of $Ru(bpy)_3^{2+}$ indicates that the current is from the expected source, the reaction of oxygen with $^*Ru(bpy)_3^{2+}$. The data were acquired over several days; the day to day reproducibility is evidently satisfactory.

Figure 5 shows the steady-state photocurrent for the oxidation of H_2O_2 as a function of the tertiary amine reductant concentration. The steady-state photocurrents are generated in 10-μL samples of 0.2 mM $Ru(bpy)_3^{2+}$ in 0.1 M phosphate buffer at pH 7.0. A 200-μm core diameter gold-coated fiber vs a silver wire reference/auxiliary electrode was used in these constant-potential experiments (+0.500 V applied). An increase in steady-state photosignals is observed up to approximately 25 mM triethanolamine. It was not possible to distinguish a photosignal above the background current in the absence of triethanolamine. As little as 2 nM triethanolamine gave oxidation currents on the order of 50% of the maximum signal. These data emphasize the requirement for the sacrificial electron donor in order to regenerate $Ru(bpy)_3^{2+}$. It is appropriate to mention that the mechanism for the regeneration of $Ru(bpy)_3^{2+}$ is not clear. One possibility is that the excited $Ru(bpy)_3^{2+}$ is quenched by triplet diatomic oxygen which yields singlet oxygen. Then, the sacrificial electron donor reduces singlet oxygen to superoxide, $O_2^{\bullet -}$. Alternately, electron-transfer quenching of $^*Ru(bpy)_3^{2+}$ by oxygen may produce $Ru(bpy)_3^{3+}$ and superoxide directly, followed by the reduction of $Ru(bpy)_3^{3+}$ to $Ru(bpy)_3^{2+}$ by the tertiary amine.[23]

Use of the Device To Determine Catalase. The oxidation current should be attenuated by catalase in the sample to a degree that corresponds to the concentration of the enzyme present. The reduction in photocurrent as a function of catalase concentration for the $Ru(bpy)_3^{2+}$/Nafion–coated device is shown in Figure 6. Samples (5 μL) of 25 mM triethanolamine, 10 mM NaCl, pH 7.0, in 0.1 M phosphate buffer were irradiated for 50 s with 6 mW of blue light. The oxidation currents were observed from the gold ring electrode (440-μm i.d.) at +0.500 V vs a silver wire reference/auxiliary electrode in the two-electrode chronoamperometric experiments. The maximum photosignal is reduced by almost 50% in the presence of 25 nM catalase as compared to a 50% signal reduction in the presence of only a few nanomolar catalase for the FIA experiments. This difference may be due to a difference in exposure time of the enzyme to the substrate in the static vs flow experiments. In the static experiment the measured response results from a balance between the rate of H_2O_2 production and the rate of catalytic H_2O_2 consumption. In the flow experiment, peroxide was incubated with the enzyme for a constant time and the remaining peroxide is responsible for the response. An estimate of the minimum residence time of H_2O_2 in the sample can be made from the quantity r^2/D, where $r = r_{\text{inner ring}} - r_{\text{fiber}}$ and D is the peroxide diffusion coefficient. From this relationship it follows that increasing the distance between the optical fiber and the electrode will increase the exposure time of H_2O_2 to catalase in solution. In the static experiments this variable may afford a means for achieving a higher sensitivity of the photocurrent to catalase.

In order to investigate the dependence of the photocurrent on the peroxide diffusion distance it was necessary to physically separate the peroxide generation site from the detection element. The optical fiber was coated with a $Ru(bpy)_3^{2+}$-impregnated Nafion layer. This served as the source of the H_2O_2. A gold disk working electrode (10-μm diameter), poised at +0.500 V vs a silver wire auxiliary/reference electrode, was placed in a movable stage opposite the $Ru(bpy)_3^{2+}$/Nafion layer; this served as the peroxide sink or detection element. By moving the gold working electrode in the stage, the peroxide oxidation current could be monitored as a function of the diffusion distance between the peroxide

---

[23] Miller, S. S.; Zahir, K.; Haim, A. *Inorg. Chem.* **1985**, *24*, 3978.

Table I. Photocurrents for the Detection Systems Studied in the Absence of Catalase and Catalase Detection Limits

detection element	electrode dimension[a] (μm)	i^b (pA)	SNR	sensitivity[c] to catalase (nM)	detection Limit (nM catalase)
Au ring electrode in flow cell	230	280 ± 10	28	0.010	0.076
Au ring electrode in static system	230	40 ± 3	13	2.1	33
Ru(byp)$_3^{2+}$/Nafion-coated Au ring electrode	440	21 ± 4	5	0.66	25
Au disk microelectrode	10	29 ± 3	10	0.10	2

[a] Dimension is the internal diameter of the ring and the diameter of the disk. [b] All currents are background-subtracted values in the absence of catalase with estimated standard deviations. [c] Concentration required to decrease the current by 1% from the value recorded in the absence of catalase.

source and sink. As well, the sensitivity of the oxidation current to catalase concentration could be investigated as a function of peroxide diffusion distance or exposure time of the enzyme to its substrate. Figure 7 is a plot of the reduction in photocurrent as a function of catalase concentration and peroxide diffusion distance. It is apparent that the concentration of the peroxide detected decreases with increasing distance between the gold electrode and the source of the peroxide photogeneration. However, at each distance the fraction of the photocurrent attenuated by the catalase remains relatively constant.

From the experiments described above, we could not observe a peroxide diffusion distance dependence of the sensitivity of the working electrode to catalase. This is surprising since we might have expected a distance-dependent sensitivity. Assuming a peroxide diffusion coefficient on the order of 10^{-5} cm^2 s^{-1}, the time scale corresponding to the distances studied (10–100 μm) is 0.1–10 s. The mechanism of catalase activity at short times and low peroxide concentration is complex. While at steady state the overall reaction is first order in peroxide concentration, the steady-state kinetics may not be established in the foregoing experiment.[24] This complicates attempts to uncover theoretically the distance dependence of the sensitivity. This issue will require further investigation in future studies.

The successful design of a reagentless sensor for the in situ generation and detection of enzyme substrate must take into account the geometry of the substrate source and sink elements, the exposure time of substrate to enzyme, the production efficiency of substrate, and the collection efficiency of the detection element. While we cannot directly compare the collection efficiencies of each construct at every stage of the device development, we can make a simple comparison of the current response and detection limits of each experimental setup to get a sense of which system embodies the best design features (Table I). Although it was not our intention to develop a series of comparable devices and compare their responses in a controlled experiment, some information results from a comparison of results from the four methods used. Table I describes the four systems briefly and shows three figures of merit for each: the signal to noise ratio (SNR) for the measurement of current from physically (line 1) or photochemically (lines 2–4) added peroxide, the sensitivity in the initial portion of the catalase calibration curve, and a detection limit based on a sensitivity to noise ratio of 2.

The SNR of the FIA system, line 1, cannot be compared to that of any of the other systems because we do not know the peroxide concentration for lines 2–4. There is not a dramatic difference in SNR for lines 2–4. There is a dramatic difference in the sensitivity to catalase for each system. The flow system, line 1, is 10 times more sensitive than the system in line 4, which is about 10 times more sensitive than the systems in lines 2 and 3, which incorporate the monolithic devices. This variation in sensitivity is in parallel with a similar trend in detection limit. Thus we can attribute improvements in the detection limit of a system to improved sensitivity rather than to better SNR. This offers some insight about where to focus our efforts for improving future sensing systems.

We note that the exposure time of enzyme to substrate was longest for the system in line 1, and shortest for lines 2 and 3. Intuitively, we expect that the sensitivity to catalase is a function of exposure time. Although we did not see this time dependence of current response reflected in our distance studies, this may be due to some experimental artifact. Recall that the distance dependence experiments were performed in order to control the mean residence time of H_2O_2 in the sample. The residence time is related to the distance traveled by diffusion. However, in our experiments there must be a considerable thermal gradient which will induce convection in the drop. Furthermore, as convection is inhibited by viscous coupling of the fluid to the walls surrounding it, a smaller volume typically will demonstrate less fluid motion due to a thermal gradient than a larger volume because the surface area to volume ratio is larger in the former, small-volume, case. In the distance study, the surface area to volume ratio would have been smaller at larger distances. The convection would have increased mass transport the most when the distance was the largest. This convection would have decreased the peroxide residence time the most effectively when the time should have been the longest. That simple steady-state Fickian diffusion is not occurring can be appreciated by noting that the photocurrent is not as strongly dependent on distance (Figure 7) as would be expected.

Collection Efficiency of the Device. In electrochemical generator-collector experiments such as the rotating ring disk,[25] series electrodes in a laminar flow cell,[26] or interdigitated arrays,[27] one figure of merit is the collection efficiency. It is the fraction of the material produced by the generator that is collected at the collector. Because our experiment has a photochemical generator, we are not in a position to know the generation rate as accurately as we would if there were a disk electrode and we could measure the current. Nonetheless, with assumptions that will be made clear, we can approximate it.

It would be ideal if we could estimate the collection efficiency in the reagentless device that will be used to determine catalase. This device has a Nafion coating on its surface in which the counterion to the material's bound anionic charges is Ru(bpy)$_3^{2+}$.[19,28] The coating covers the ring electrode as well as the optical fiber surface, and it is applied by an admittedly crude method: simple dip coating. As a consequence, although such devices are fully functional, their

---

(24) Nicholls, P.; Schonbaum, G. R. *The Enzymes*; Academic Press: New York, 1963; Vol. 8, p 147.

(25) Albery, W. J.; Bruckenstein, S. *Trans. Faraday Soc.* **1966**, *62*, 1920.

(26) Matsuda, H. *J. Electroanal. Chem. Interfacial Electrochem.* **1967**, *15* (4), 325–336.

(27) Sanderson, D. G.; Anderson, L. B. *Anal. Chem.* **1985**, *57*, 2388.

(28) Martin, C. R.; Rubinstein, I.; Bard, A. J. *J. Am. Chem. Soc.* **1982**, *104* (8), 4817–4824.

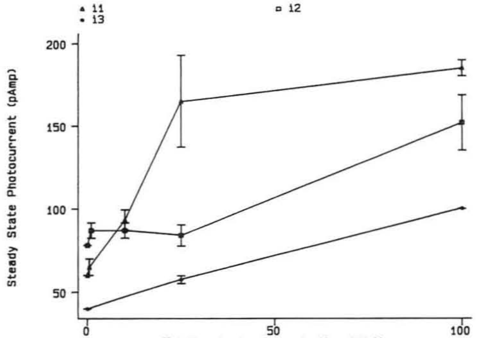

Figure 8. Current as a function of triethanolamine concentration for the $Ru(bpy)_3^{2+}$/Nafion-coated sensor. Samples (10 μL) of 0–100 mM triethanolamine, 10 mM NaCl, pH 7.0, in 0.1 M phosphate buffer were irradiated for 50 s with 6 mW of blue light. The oxidation currents were observed at +0.500 V applied to the gold ring electrode (440-μm i.d.) vs a silver wire reference/auxiliary electrode. The symbols Δ and □ represent data obtained with two different sensors and the blank, O, was done with a Nafion-coated device, without $Ru(bpy)_3^{2+}$.

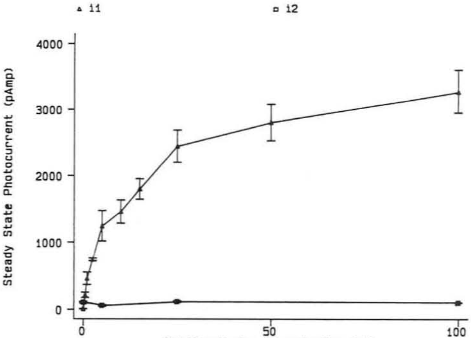

Figure 9. Current as a function of tertiary amine concentration. Steady-state oxidation currents at +0.500 V were assessed with a 400-μm core diameter gold-coated optical fiber vs a silver wire reference/auxiliary electrode. Samples (10 μL) of 10^{-2} M $Ru(bpy)_3^{2+}$ in 0.1 M phosphate buffer, 10 mM NaCl, pH 7.0, with 0–100 mM triethanolamine concentrations were irradiated with 6 mW of blue light. The data, Δ, represent the averages of six replicates made with two devices on two days. The error bars indicate the estimated standard deviation of each measurement. Blanks (□) were measured in the absence of $Ru(bpy)_3^{2+}$.

response to the concentration of triethanolamine is not very reproducible from device to device (see Figure 8). As well, the current response with no $Ru(bpy)_3^{2+}$ in the film is troubling and not well understood. It is preferable to evaluate the collection efficiency from a more reproducible system.

The requirement of the experimental system in which the collection efficiency is measured is that the peroxide be generated near the face of the fiber as it is in the model device when the fiber is coated with the $Ru(bpy)_3^{2+}$-containing polymer. We achieve this by photolyzing a solution that is 10 mM in $Ru(bpy)_3^{2+}$. The depth of solution at which the light intensity reaches 50% of its value at the face of the fiber, corresponding to an optical absorbance of 0.3, is on the order of 20 μm. Since the space between the edge of the fiber and the inner edge of the ring electrode is of the same order of magnitude, this is a reasonable experimental approximation to the ideal surface generation of peroxide.

Before the data are presented, some theoretical development is necessary so that the approximations are clearly defined and the analysis of the data is clarified. The basic idea is to measure the current due to peroxide at the gold ring as a function of the triethanolamine concentration. The peroxide production rate depends on the rates of two reactions which occur in series, the quenching of the excited state of $Ru(bpy)_3^{2+}$ by oxygen and a followup reaction: either the reaction of singlet oxygen with triethanolamine or the reaction of $Ru(bpy)_3^{2+}$ with triethanolamine, depending on the mechanism. The peroxide oxidation rate is related to the measured current. If we can determine the production rate at the fiber face, then, because we know the oxidation rate at the ring, we can determine the collection efficiency.

The overall flux of peroxide from the fiber face must be the combination of the oxygen and triethanolamine fluxes in series. Each flux is the product of a bulk concentration and a mass-transfer coefficient.

$$J_d = J_o J_t/(J_o + J_t) = C_o M_o C_t M_t/(C_o M_o + C_t M_t) \quad (1)$$

where J_d is the flux to the disk, J_o is the oxygen flux, J_t is the triethanolamine flux, C_o is the bulk concentration of oxygen, C_t is the bulk concentration of the triethanolamine, and M's are mass-transfer coefficients. As C_t approaches zero, the flux to the disk becomes equal to the triethanolamine flux.

The current that is measured at the ring represents a fraction of the equivalent current that is generated at the disk; that fraction is the collection efficiency. We can determine the equivalent current at the disk from the measurement of the triethanolamine flux. At low C_t, J_d is just $C_t M_t$; the slope of a curve of current measured at the ring vs triethanolamine concentration will be the product of M_t and the collection efficiency. Figure 9 shows the data for ring current vs triethanolamine concentration. At low C_t the curve is linear with a slope of 236 pA/mM and a standard deviation of 24 pA/mM. An estimate of M_t can be made from theory. The ratio of current to bulk concentration for the steady-state mass transport controlled flux to a disk[29] is

$$i/C = 4nFDR \quad (2)$$

This ratio is 62 ± 6 nA/mM, for $n = 1$ and a diffusion coefficient for triethanolamine in water of 8.0×10^{-6} cm^2 s^{-1}. The diffusion coefficient was estimated from the limiting ionic conductivity of the tetraethylammonium ion, which we approximate as $30 \pm 3\ \Omega^{-1}$ cm^2 equiv^{-1} in aqueous solution at 298.2 K.[30,31] The value of the ratio for the disk is in agreement with previously published experimental and theoretical results.[32] If we can assume that the photochemical flux is mass transport controlled, then the ratio of these two sensitivities is the collection efficiency. Rate constants for the oxygen quenching of $*Ru(bpy)_3^{2+}$ and the reduction of $Ru(bpy)_3^{3+}$ by amines are known and are consistent with mass transport control on the time scale of our experiments.[33,34]

$$\mathrm{CE} = (0.236\ \mathrm{nA/mM})/(62\ \mathrm{nA/mM}) = (3.8 \pm 0.5) \times 10^{-3} \quad (3)$$

It is now possible to measure the flux of peroxide from the surface, which must be, because of stoichiometry, half of the flux of triethanolamine. When the bulk triethanolamine concentration is 25 mM, the current measured is 2.4 nA (Figure 9). Since the collection efficiency is 0.0038, the equivalent

---

(29) Saito, Y. *Rev. Polarogr.* **1968**, *15*, 178–187.

(30) Burgess, J. *Ions in Solution: Basic Principles of Chemical Interaction*; Ellis Horwood Limited Publishers: Chichester, U.K. 1988; p 33.

(31) Bockris, J.; Reddy, A. *Modern Electrochemistry*; Plenum Press: New York, 1970; Vol. 1, Chapter 4.

(32) Kuhn, L. S.; Weber, A.; Weber, S. G. *Anal. Chem.* **1990**, *62*, 1631.

(33) Prasad, D. R.; Mandal, K.; Hoffman, M. Z. *Coord. Chem. Rev.* **1985**, *64*, 175–190.

(34) Winterle, J. S.; Kliger, D. S.; Hammond, G. S. *J. Am. Chem. Soc.* **1976**, *98*, 3719–3721.

current at the fiber face is 630 nA. The molar production rate is related to the current as (where A is area)

$$dC/dt = JA = i/nF = 6.5 \pm 0.9 \text{ pmol/s} \quad (4)$$

The error in this value is due to the uncertainty associated with the collection efficiency. The light power at the tip of the device is 6 mW, so the quantum yield is 0.20%, in good agreement with the value measured in bulk solution. This agreement lends credibility to our assumptions.

Oxygen Depletion. The peroxide generation in our system is dependent upon the presence of the ubiquitous precursor, molecular oxygen. Since the solubility of dissolved oxygen in aqueous solutions is 1.4 mM at 1 atm and 20 °C, it is necessary to consider the possibility that oxygen pressure limits the sensor's performance. The peroxide production rate is 6.5 pmol^{-1} (eq 4), which we assume is also the rate of O_2 consumption. In the 5-μL samples this corresponds to O_2 depletion at a rate of approximately 1 μM s^{-1}. Since these experiments lasted 100 s, the quantity consumed is only 10% of the oxygen initially available in the aqueous, buffered samples. This is consistent with our experimental observation that there is no diminution in steady-state photocurrent for more than 500 s following the onset of illumination. Thus, it is unlikely that O_2 depletion has had an influence on the experiments described herein. However, as a general issue, the depletion of O_2 must be considered if sensors incorporating this concept are used in other environments or if larger photon fluxes are used. Some further general considerations and how they relate to our experiments follow.

If O_2 is depleted, diffusive mass transport will replenish it. The replenishment rate depends on the local O_2 concentration and diffusion coefficient and on geometry. For the situation encountered in our experiments, viz. a hemispherical droplet of buffer in air, the mass transport limitation will be diffusion within the droplet. The solution of time-dependent diffusion into a sphere with a constant concentration at the surface is well-known.[35] If, at $t = 0$, the concentration of diffusing species is taken uniformly to zero inside the sphere, then the concentration at the center of the sphere becomes 95% of the surface concentration when the dimensionless parameter Dt/a^2 becomes 0.4. Using a diffusion coefficient (D) for oxygen in water[36] of 2.6×10^{-5} cm^2 s^{-1} and a drop radius (a) of 0.134 cm, the 95% diffusional relaxation time is 280 s. This value is of the same order of magnitude as the length of time for each experiment, 100 s. Thus, had we used a larger photon flux to generate peroxide, the effect of diminished O_2 may have been seen.

There are three further ameliorating influences on the depletion of O_2. The detection process, the oxidation of H_2O_2 to O_2, replenishes the O_2 supply. Albeit in the devices described it is an inconsequential quantity, it need not be so. This is a matter of better design. The catalase reaction replenishes the O_2 supply. Finally, Figures 5 and 9 show a limiting plateau in the response vs amine concentration. It is O_2 supply that limits the response at the plateau. Operation under conditions corresponding to the initial linear portion of the curve where amine mass transport limits the response will confer immunity to small fluctuations in oxygen concentration.

Oxygen depletion may be more of a concern when the device is used in situ for whole blood or plasma samples where the diffusion coefficient of O_2 is lower and the partial pressure of oxygen is 0.10–0.13 or 0.039–0.046 atm for arterial or venous blood, respectively.[37] The most important of the ameliorating factors to consider is the amine concentration. The voltammetry of Ru(byp)$_3^{2+}$ in serum[17] shows that the concentration of Ru(bpy)$_3^{2+}$-reducing species is equivalent to about 2 mM (based on the height of the catalytic wave). This is an oversimplication, because the wave height depends on the rate constant as well. However, it is actually the turnover rate of Ru(bpy)$_3^{3+}$ to Ru(bpy)$_3^{2+}$ that is important, so in the absence of detailed knowledge of the species reacting and their reaction rate constants, equivalence to 2 mM of a rapidly reacting species such as oxalate or triethanolamine is helpful information. Note that 2 mM is a relatively low concentration in the context of this work (see Figures 5 and 9). Thus, the rate-limiting step in H_2O_2 production in serum may be diffusion of the reducing substances, not the diffusion of O_2. Before application in serum can be envisioned, more attention to these issues will be needed.

In conclusion, the data presented here support the use of the gold-coated optical fiber as a reagentless sensor for the in situ photogeneration and electrochemical detection of the enzyme substrate hydrogen peroxide. The peroxide oxidation current is sensitive to catalase; about 25 nM catalase can reduce the device's photosignal by 50%. The reduction in photocurrent is fast; steady-state photosignals can be achieved in a matter of minutes. The lower limit of detection is greatly improved over previously reported values for systems in which the enzyme substrate was not generated in situ and had to be added manually to each sample.[4,5] A comparison of the quantum efficiencies for the photochemical production of hydrogen peroxide in bulk solution and at the face of the optical fiber indicates that no loss in the efficiency of substrate production can be expected when Ru(bpy)$_3^{2+}$ is localized on the surface of the device. From the H_2O_2 diffusion distance studies there does not appear to be an obvious improvement in the sensitivity of the photocurrent to catalase concentration as a function of the distance between the peroxide source and sink. However, this observation may be more related to convection than to the diffusion time of peroxide. It might be advantageous to create a well in the face of the device such that the optical fiber core is recessed below the plane of the gold ring working electrode. Further studies with an etched silica fiber should clarify this issue.

The practical advantages of the sensor include the ease of construction and a reagentless design. It is possible to localize the Ru(bpy)$_3^{2+}$ on the silica core of the fiber by using the ion-exchange capabilities of Nafion. Ambient oxygen is a convenient, abundant source of quencher. Due to the catalase activity of many metal ion complexes it should also be possible to develop metal ion sensors based on our device. Studies are currently underway to optimize the utility of the device in human serum and urine.

ACKNOWLEDGMENT

The financial support for this work from the Ben Franklin Partnership of Western Pennsylvania for the Biosensor Development and Modeling Center and the Office of Naval Research is gratefully acknowledged.

RECEIVED for review June 8, 1992. Accepted October 16, 1992.

---

[35] Crank, J. *The Mathematics of Diffusion*; 2nd ed.; Oxford University Press: Oxford, U.K., 1975; p 90–92.

[36] Hoare, J. P. *The Electrochemistry of Oxygen*; John Wiley & Sons, Inc.: New York, 1968; p 170.

[37] Kaplan, L. A.; Pesce, A. J. *Clinical Chemistry: Theory, Analysis and Correlation*; C. V. Mosby Co.: St. Louis, MO, 1984; p 392.

The Use of Tetraalkylammonium Ion-Sensitive Electrodes for the Liposome Marker Release Assay

Takashi Katsu

Faculty of Pharmaceutical Sciences, Okayama University, Tsushima, Okayama 700, Japan

A series of tetraalkylammonium ion-sensitive electrodes was constructed with the aim of finding new ionic markers suitable for use in the permeability assay of liposomal membranes. The series comprised the tetramethyl-, tetraethyl-, tetrapropyl-, tetrabutyl-, and tetraamylammonium ion homologues, and they were compared with tetraphenylphosphonium and K^+ ion-sensitive electrodes. Tetraalkylammonium ions with alkyl chain lengths shorter than that of a propyl group and octanol–water partition coefficients of less than 5×10^{-2} did not significantly permeate liposomal membranes composed of egg phosphatidylcholine and were trapped stably in the inner liposomal aqueous phase. We selected the tetraethylammonium ion for further study and verified its validity for use as a marker by conducting an experiment to determine antibody and complement activities by measuring the immunoreaction-induced liposomal membrane permeability changes. In addition to being suitable for use in such a conventional permeability assay, the tetraalkylammonium ion-sensitive electrodes were used successfully to determine the sizes of channels formed in liposomal membranes.

INTRODUCTION

Liposome permeability measurements are fundamental to investigations of the interactions between biologically active substances and membranes. Rapid changes in liposomal permeability can be brought about by calcium-mediated fusion, interaction with drugs, antibody/complement-mediated lysis of antigen-bearing liposomes, and passage through the phase-transition temperature. When measuring such permeability changes, it is important to choose a marker molecule which neither passes through intact membranes nor associates with membranes in any way that destabilizes or aggregates them and can be separated easily from liposomes by conventional methods.[1] Various markers satisfying these criteria have been developed, for example, glucose, arsenazo-III, and carboxyfluorescein, which can be detected by various spectrometric methods.[1]

Ionic substances also are convenient markers and are detected potentiometrically with the corresponding ion-selective electrodes.[2-5] Potentiometric measurement has some inherent advantages over spectrometric methods, i.e., simpler procedure, low cost, and ease of continuous monitoring of marker ion release from liposomes. Umezawa and coworkers[3,4] prepared liposomes loaded with tetraamylammonium ions (TAA^+) and monitored the immune lysis-induced release of the TAA^+ marker with a TAA^+-sensitive electrode. However, the liposomes had to be freshly prepared for each experiment, because storage for more than about 12 h resulted in scattered data.[3] It is likely that, as a result of its high lipophilicity, TAA^+ is released outside the liposomes spontaneously. Such lipophilic cations are particularly useful for membrane potential measurements[6] which require establishment of a rapid ionic equilibrium across membranes, and the lipophilic tetraphenylphosphonium ion (TPP^+) has been used extensively for such studies.[7,8]

The prime aim of our study was to find a less leaky ionic marker that could be used for liposomal membrane permeability assays. We chose a series of tetraalkylammonium ions, R_4N^+, where R = methyl, ethyl, propyl, butyl, and amyl, abbreviated to TMA^+, TEA^+, TPA^+, TBA^+, and TAA^+, respectively, and compared them with TPP^+ [7,8] and K^+ [5] as marker ions. First, we investigated the relationship between the liposomal permeability to and the octanol–water partition coefficient of each marker ion. We found that permeation of tetraalkylammonium ions with alkyl chain lengths shorter than that of a propyl group through a liposomal membrane composed of egg phosphatidylcholine (PC) was insignificant, which corresponded with their octanol–water partition coefficients of less than 5×10^{-2}. Next, we entrapped TEA^+ in liposomes and proved that it was loaded stably in the liposomes and was superior in this respect to the marker cation, TAA^+, used in a previous study.[3,4] These TEA^+-loaded liposomes were used to determine antibody and complement activities. In addition to the conventional permeability assay, tetraalkylammonium ion markers were used to determine the sizes of channels that formed in the liposomal membranes by utilizing their characteristic subtle size increases with increasing alkyl chain lengths. We determined the size of the channel formed by amphotericin B.[9,10] This channel rendered the membrane permeable to TMA^+, whereas it was impermeable to TEA^+. Therefore, the diameter of the amphotericin B channel was between that of TMA^+ (0.7 nm) and TEA^+ (0.8 nm). This method was useful for the precise determination of the sizes of channels formed in liposomal membranes.

EXPERIMENTAL SECTION

Reagents. The sources of the reagents used were as follows: tetramethylammonium chloride (TMACl), tetraethylammonium chloride (TEACl), tetrabutylammonium chloride (TBACl), di-*n*-octyl phthalate and 1-octanol from Tokyo Kasei Kogyo, Japan; tetrapropylammonium chloride (TPACl) from Alfa Products, USA; tetraamylammonium chloride (TAACl) from Kanto Kagaku, Japan; valinomyin from Boehringer Mannheim, Germany; tetraphenylphosphonium chloride (TPPCl), sodium tetrakis[3,5-bis(trifluoromethyl)phenyl]borate, and 2-fluoro-2′-nitrodiphenyl ether from Dojindo Laboratories, Japan; poly(vinyl chloride)

---

(1) New, R. R. C. In *Liposomes: a Practical Approach*; New, R. R. C., Ed.; IRL Press: Oxford, 1990; pp 105–161.

(2) D'Orazio, P.; Rechnitz, G. A. *Anal. Chem.* **1977**, *49*, 2083–2086.

(3) Shiba, K.; Umezawa, Y.; Watanabe, T.; Ogawa, S.; Fujiwara, S. *Anal. Chem.* **1980**, *52*, 1610–1613.

(4) Umezawa, Y.; Sofue, S.; Takamoto, Y. *Talanta* **1984**, *31*, 375–378.

(5) Katsu, T.; Tanaka, A.; Fujita, Y. *Chem. Pharm. Bull.* **1982**, *30*, 1504–1507.

(6) Rottenberg, H. *Methods Enzymol.* **1979**, *55*, 547–569.

(7) Kamo, N.; Muratsugu, M.; Hongoh, R.; Kobatake, Y. *J. Membrane Biol.* **1979**, *49*, 105–121.

(8) Hosoi, S.; Mochizuki, N.; Hayashi, S.; Kasai, M. *Biochim. Biophys. Acta* **1980**, *600*, 844–852.

(9) De Kruijff, B.; Demel, R. A. *Biochim. Biophys. Acta* **1974**, *339*, 57–70.

(10) Bolard, J. *Biochim. Biophys. Acta* **1986**, *864*, 257–304.

0003-2700/93/0365-0176$04.00/0

(PVC) (degree of polymerization, 1020) from Nacalai Tesque, Japan; dipalmitoylphosphatidylcholine (DPPC), dicetyl phosphate (DCP), cholesterol, amphotericin B, and melittin from Sigma, USA; egg phosphatidylcholine (PC) from The Green Cross Corporation, Japan; preserved sheep blood was purchased from The Japan Lamb Corporation and rabbit anti-sheep hemolysin and guinea pig complement (titer, 182 CH_{50} units/mL) were obtained from Kyokuto Seiyaku Kogyo, Japan. All the other chemicals used were of analytical reagent grade.

Electrode System. Tetraalkylammonium ion-sensitive electrodes were constructed using a PVC-based membrane with the following composition:[11] 0.5 mg of sodium tetrakis[3,5-bis(trifluoromethyl)phenyl]borate, 60 μL of 2-fluoro-2′-nitrodiphenyl ether, and 30 mg of PVC. The materials were dissolved in about 1 mL of tetrahydrofuran and poured into a flat Petri dish (30-mm diameter), and the solvent was allowed to evaporate at room temperature. The resulting membrane was cut and stuck to a PVC tube (4-mm outer diameter, 3-mm inner diameter) with tetrahydrofuran. A TPP^+-sensitive electrode was similarly constructed. A PVC-sensor membrane of a K^+-sensitive electrode contained valinomycin as a neutral carrier and di-*n*-octyl phthalate as a membrane solvent.[12] The electrochemical cell used in this study is represented as follows:[11,12] Ag,AgCl/internal solution/PVC-sensor membrane/sample solution/1 M NH_4NO_3 (salt bridge)/10 mM KCl/AgCl,Ag. Each internal solution comprised a 10 mM solution of the chloride salt of the required marker cation. This electrode system, including the reference electrode,[12] is compact, and therefore, assay sample volumes were decreased down to 0.3–1 mL. The electromotive force between the pair of Ag/AgCl electrodes was measured with an appropriate field-effect transistor operational amplifier (input resistane > 10^{12} Ω) and recorded. The selectivity coefficients of the ion-sensitive electrodes were determined using the separate solution method with the respective chloride salts (10 mM).[13]

Partition Coefficients. The octanol–water partition coefficients of the tetraalkylammonium chloride series, TPPCl, and KCl were determined as follows. Each marker substance was dissolved in water (2 mL), an equal volume of 1-octanol was added, the mixtures were equilibrated by shaking in a capped test tube for 1 h at 37 °C, and the partition coefficient was determined by measuring the concentration of marker ion in the aqueous phase before and after the addition of octanol using the corresponding ion-sensitive electrode. However, the decreases in the marker ion concentrations, except that of TAA^+ in the aqueous phase were too small to determine, which indicates that the tetraalkylammonium ions, except TAA^+, distributed almost exclusively in water. In order to determine the concentrations of the small amounts of marker dissolved in octanol, we took 1 mL of octanol phase, reextracted it with 1 mL of water, and measured the concentration in the water using the appropriate ion-sensitive electrode and used this value as the concentration in 1-octanol. In addition, Gran's plot[14] was used for quantification in some cases to reduce the slight experimental error arising from differences between the electrode calibration curves of pure water and octanol-contaminated water.

Membrane Permeabilities to Marker Ions. The membrane permeability to each marker ion was evaluated by measuring the ion uptake rate into the inner liposomal aqueous phase induced by the membrane potential. It is well-known that lipophilic cations are drawn inside membranes when the inner membrane potential is negative.[7,8] In this study, a negative membrane potential was created by adding valinomycin to K^+-loaded liposomes suspended in a K^+-free medium as follows. Egg PC liposomes were prepared by the reversed-phase evaporation method.[12] Egg PC (10 μmol, 7.7 mg) was dissolved in 1.5 mL of diethyl ether, 1 mL of aqueous solution containing 150 mM KCl/5 mM 4-(2-hydroxyethyl)-1-piperazineethanesulfonic acid (HEPES)–NaOH (pH 7.4) was added, and the mixture was sonicated (Ohtake Works, Japan; Type 5201) for 2 min at 0 °C to obtain a homogeneous emulsion. Then, the diethyl ether solvent was removed completely using a conventional rotary evaporator under reduced pressure (by water aspirator) at 25 °C, after which a homogeneous suspension of liposomes remained. The liposomes were centrifuged (105000*g*, 30 min) and washed twice with 150 mM NaCl/5 mM HEPES–NaOH (pH 7.4) to remove the untrapped K^+ and the final pellet was suspended in 1 mL of 150 mM NaCl/5 mM HEPES–NaOH (pH 7.4). The experiments to determine the marker uptake were carried out at 25 °C as follows. An aliquot of the liposome suspension (0.1 mL) was diluted with 0.2 mL of 150 mM NaCl/5 mM HEPES–NaOH (pH 7.4), and an aqueous solution of the required marker cation (3 μL, final concentration 0.1 mM) was added, followed by addition of an ethanolic solution of valinomycin (0.3 μL, final concentration 0.1 μM), which generated a membrane potential due to the difference between the K^+ concentrations across the liposomal membrane and induced uptake of the lipophilic marker cation into the inner liposomal compartment. The addition of an aqueous solution of melittin[15,16] (3 μL, final concentration 20 μM) abolished this membrane potential and brought about efflux of the accumulated lipophilic cations to the external medium.

Complement-Mediated Immune Lysis. Forssman antigen, incorporated into liposomes, was used as a lipid antigen and a lipid mixture containing it was isolated from sheep erythrocytes, as described by Rose and Oklander.[17] About 50 mg of lipid was extracted from 50 mL of preserved sheep blood, which was stabilized and diluted with Alsever's solution (50%, v/v). Multilamellar TEA^+-loaded liposomes were prepared, using procedures similar to those described previously.[5] The dried thin film of lipid mixture, which contained DPPC (20 μmol, 14.7 mg), cholesterol (15 μmol, 5.8 mg), DCP (2 μmol, 1.1 mg), and the above-described lipid extract (2.0 mg), was swollen in 2 mL of 150 mM TEACl at 55 °C, centrifuged, and washed three times to remove any untrapped marker. The final lipid mixture pellet was dispersed in 2 mL of 0.15 M NaCl solution. Immunoreaction was carried out at 37 °C as follows. An aliquot (0.1 mL) of the liposome suspension was diluted with an appropriate volume of modified veronal buffer, which comprised 3.13 mM barbital, 1.82 mM sodium barbital, 0.15 mM $CaCl_2$, 0.5 mM $MgCl_2$, and 145 mM NaCl.[5] The final reaction volume, including the antiserum and complement that were added later, was 500 μL. In order to determine the antibody activities, the liposomes were sensitized initially with various dilutions of rabbit anti-sheep antiserum for 5 min, guinea pig complement (final dilution 1:50) was added, and the potential change resulting from TEA^+ efflux was recorded 15 min later in a similar manner conducted previously.[5] Similar experiments were carried out to determine the complement activities, in which the final dilution of the antiserum remained constant (1:500) and the dilution of complement varied.

Channel Size Determination. Both TEA^+ and K^+ were incorporated simultaneously into liposomes for the determination of the sizes of the channels formed by amphotericin B. Liposomes were prepared using the reversed-phase evaporation method. Egg PC (10 μmol, 7.7 mg) and cholesterol (2 μmol, 0.77 mg) were dissolved in 1.5 mL of diethyl ether, and 1 mL of an aqueous solution containing 50 mM KCl/50 mM TEACl/100 mM sucrose/5 mM HEPES–NaOH (pH 7.4) was added. Sucrose was added to the inner aqueous liposomal phase, as the reversed-phase liposomes without sucrose floated after the centrifugation procedure, because the density of the TEA^+-containing solution was lower than that of water and the addition of a substance, such as sucrose, with a much greater density was necessary to sediment the liposomes. The final pellet was suspended in 1 mL of 150 mM NaCl/5 mM HEPES–NaOH (pH 7.4), an aliquot (100 μL) of this liposomal suspension was diluted with 400 μL required assay mixture solution at 25 °C to produce final suspension media of either (a) 50 mM NaCl/200 mM sucrose/5 mM HEPES–NaOH (pH 7.4) or (b) 150 mM NaCl/5 mM HEPES–NaOH (pH 7.4), to which amphotericin B dimethyl sulfoxide solution (10 μL, final concentration 200 μg/mL) was added, and the amounts of effluxed markers were recorded 15 min later. The total amounts of marker ions were determined by disrupting liposomes by addition of an aqueous solution of melittin[15,16] (5 μL, final

---

(11) Katsu, T.; Sanchika, K.; Okazaki, H.; Kondo, T.; Kayamoto, T.; Fujita, Y. *Chem. Pharm. Bull.* **1991**, *39*, 1651–1654.

(12) Katsu, T.; Kobayashi, H.; Fujita, Y. *Biochim. Biophys. Acta* **1986**, *860*, 608–619.

(13) Katsu, T.; Kayamoto, T.; Fujita, Y. *Anal. Chim. Acta* **1990**, *239*, 23–27.

(14) Gran, G. *Analyst* **1952**, *77*, 661–671.

(15) Katsu, T.; Kuroko, M.; Morikawa, T.; Sanchika, K.; Fujita, Y.; Yamamura, H.; Uda, M. *Biochim. Biophys. Acta* **1989**, *983*, 135–141.

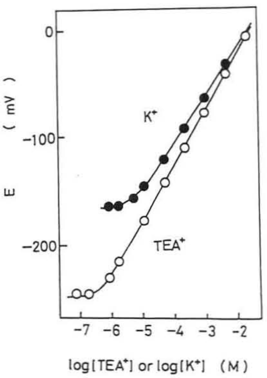

Figure 1. Calibration curves of TEA^+ and K^+ electrodes in 150 mM NaCl/5 mM HEPES–NaOH (pH 7.4) buffer at 25 °C.

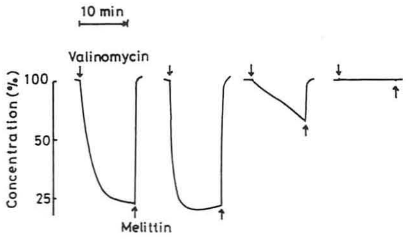

Figure 2. Valinomycin-induced uptake of marker ions into reversed-phase egg PC liposomes at 25 °C. At the time indicated by the first arrow, valinomycin was added; the second arrow indicates the time when melittin was added. The concentration of marker ion before addition of valinomycin was expressed as 100%.

concentration 20 μM). The following diameters of tetraalkylammonium ions were used for estimation of channel size:[18] TMA^+, 0.7 nm; TEA^+, 0.8 nm; TPA^+, 0.9 nm.

RESULTS AND DISCUSSION

Electrode Response Characteristics. The calibration curves of the TEA^+ and K^+ electrodes, in a buffer solution comprising 150 mM NaCl/5 mM HEPES–NaOH (pH 7.4), are shown in Figure 1. The detection limits of the TEA^+ and K^+ electrodes were 0.5 and 5 μM, respectively, which were determined by extrapolating the linear regions and baseline of the calibration curve and the intersection point was defined as the detection limit.[13] The slopes in the linear range were 58 mV/decade for the TEA^+ and 56 mV/decade for the K^+ electrode. The selectivity coefficients of the electrodes are shown in Table I. The K^+ electrode was not subject to serious interference from tetraalkylammonium ions with alkyl chain lengths shorter than that of a propyl group. The TEA^+ electrode was not subject to interference from K^+, although interference from ions with alkyl chain lengths greater than an ethyl group was marked.

Membrane Permeability and Partition Coefficient. The membrane permeability of each marker ion was evaluated by measuring the membrane potential-induced uptake of the ion into the inner liposomal aqueous phase. Valinomycin is known to evoke a membrane potential when there is a K^+ gradient across the liposomal membrane. In our study, liposomes containing KCl solution were suspended in a NaCl-containing medium. When a lipophilic ion, which permeated the membrane freely, was added to this liposome suspension, movement of the ion inside the liposomes occurred immediately. The uptake rates of the various marker cations are shown in Figure 2. The TAA^+ was taken up more rapidly than TPP^+, which is used widely for membrane potential measurements.[7,8] The uptake rate decreased markedly as the alkyl chain length of the quaternary ions became shorter and virtually no TPA^+ was taken up. In order to confirm that the uptake has been induced by the membrane potential, a membrane disrupting agent, melittin,[15,16] was added to the suspension, which abolished the membrane potential and caused efflux of the accumulated lipophilic ions.

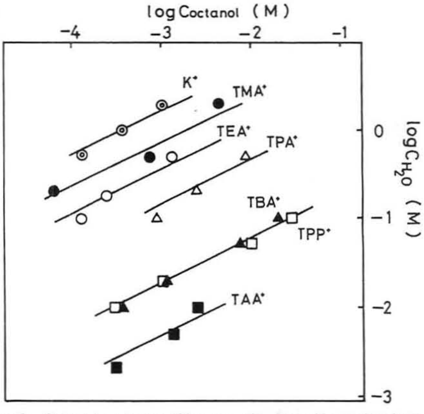

Figure 3. Octanol–water partition experiments with marker ions.

The octanol–water partition coefficients of each marker cation, at various concentrations, were determined, and their equilibrium distributions are shown in Figure 3. The slopes of all the lines were about 0.5, which indicates that all the marker cations bound strongly to their counter anion Cl^- in octanol, as discussed below. The partition coefficient is defined as

$$P = C_o/C_w \tag{1}$$

where C_o is the marker ion concentration in octanol and C_w is that in water. When the marker substance (RX) does not dissociate in octanol, but does so in water ($R^+ + X^-$), we can obtain

$$P = C_o/C_w^{\ 2} \tag{2}$$

because the concentrations [R^+] and [X^-] are equal to [RX]. Therefore, in these circumstances the slope of the plot of log C_o vs log C_w is 0.5. Our results were very close to this value, and the partition coefficients are summarized in Table II. The membrane permeability experiments showed that TPA^+ did not permeate egg PC liposomal membranes appreciably and its octanol–water partition coefficient, expressed as the logarithm, was −1.3. Therefore, it is reasonable to assume that the phospholipid membrane was less permeable to substances with partition coefficients below this value.

Use of Tetraethylammonium Ions for the Marker Release Assay. We selected TEA^+ as a marker ion and used it for the determination of antibody and complement activities. In previous studies,[3-5] TAA^+ and K^+ were used for this assay, but we found that TAA^+ was not particulary suitable

---

(16) Ohhashi, T.; Katsu, T.; Ikeda, M. *Biochim. Biophys. Acta* **1992**, *1106*, 165–170.

(17) Rose, H. G.; Oklander, M. *J. Lipid Res.* **1965**, *6*, 428–431.

(18) Fujishiro, R.; Wada, G.; Tamamushi, R. *Gendai Butsuri-Kagaku Koza*; Tokyo Kagaku Dojin: Tokyo, 1968; Vol. 8, Chapter 4.

Table I. Selectivity Coefficients of TEA$^+$ and K$^+$ Electrodes[a]

	Na$^+$	K$^+$	TMA$^+$	TEA$^+$	TPA$^+$	TBA$^+$	TAA$^+$	TPP$^+$
TEA$^+$ electrode	-4.0	-3.9	-1.8		1.7	3.3	5.0	4.6
K$^+$ electrode	-2.9		-3.0	-3.0	-1.9	-0.2	1.9	1.0

[a] Expressed as the logarithm of the selectivity coefficient, log $K^{\mathrm{Pot}}_{\mathrm{TEA^+,X}}$ or log $K^{\mathrm{Pot}}_{\mathrm{K^+,X}}$.

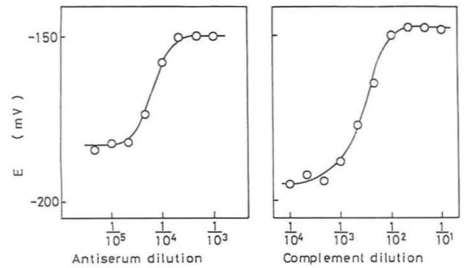

Figure 4. Potential vs concentration graphs of (a) antiserum and (b) complement.

Table II. Octanol-Water Partition Coefficients[a]

K$^+$	TMA$^+$	TEA$^+$	TPA$^+$	TBA$^+$	TAA$^+$	TPP$^+$
-3.4	-2.7	-2.1	-1.3	0.4	1.7	0.4

[a] Expressed as the logarithm of the partition coefficient, log P.

because liposomes were higly permeable to it. As for K$^+$, although it was trapped stably in liposomes, the level of K$^+$ in the antiserum and complement had to be reduced beforehand by dialysis[5] to avoid it contaminating the assay system. These disadvantages could be overcome by using a new marker, TEA$^+$, which did not leak appreciably, even after storage in a refrigerator at 4 °C for 2 weeks. The TEA$^+$-sensitive electrode did not suffer serious interference from Na$^+$, K$^+$, or other cations present in biological fluids, which is evident from the selectivity coefficients of the electrode presented in Table I. The antibody and complement activities, based on the potential changes caused by TEA$^+$ efflux from liposomes as a result of immunoreaction, determined are shown in Figure 4. The amount of TEA$^+$ effluxed was dependent on the dilution of both antiserum and complement; in our system, the immune response could be observed with dilutions as low as 1:5 × 10^5 of antiserum and 1:10^3 of complement. These results demonstrated that the combination of TEA$^+$-loaded liposomes and a TEA$^+$-sensitive electrode is suitable for measuring the activities of immune reagents.

Channel Size Determination. Liposomes loaded with both K$^+$ and TEA$^+$ were prepared and used to determine the sizes of channels formed in the liposomes by monitoring the difference between the rates of K$^+$ and TEA$^+$ effluxes. No cross-interference of the K$^+$ and TEA$^+$ electrodes during the determination process was observed, as discussed above. The amphotericin B-induced K$^+$ and TEA$^+$ effluxes from liposomes suspended in the medium containing 50 mM NaCl/200 mM sucrose/5 mM HEPES-NaOH (pH 7.4) are shown in Figure 5a. The medium contained a high concentration of sucrose to protect the liposomes against osmotic lysis,[19,20] which leads to TEA$^+$ efflux despite formation of small-sized channels. Such osmotic lysis was actually observed in the next experiment (Figure 5b). The amphotericin molecules, which are known to form channels in cholesterol-containing liposomes,[9,10] induced efflux of K$^+$, but not of TEA$^+$. When the liposomal membrane was disrupted by adding melittin,[15,16] a large potential change due to TEA$^+$ efflux was observed, which indicated that TEA$^+$ was trapped in the liposomes and verified that amphotericin B only induced K$^+$ efflux from liposomes.

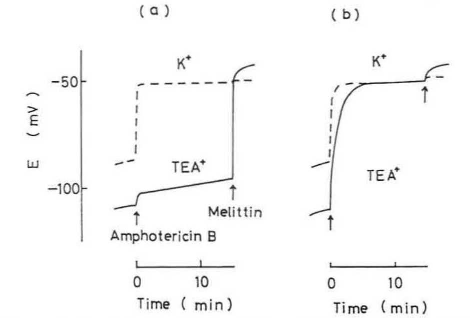

Figure 5. Amphotericin B-induced K$^+$ and TEA$^+$ efflux at 25 °C. Lipsomes were suspended in (a) solution containing 50 mM NaCl, 200 mM sucrose, and 5 mM HEPES-NaOH (pH 7.4) or (b) solution containing 150 mM NaCl and 5 mM HEPES-NaOH (pH 7.4). At the time indicated by the first arrow, amphotericin B was added; the second arrow indicates the time when melittin was added.

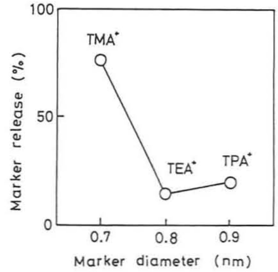

Figure 6. Relationship between the percent efflux induced by amphotericin B and the tetraalkylammonium ion diameters.

Liposomes were also suspended in medium containing 150 mM NaCl/5 mM HEPES-NaOH (pH 7.4). Under these conditions, if the ionophore can open a channel which is large enough to permit the permeation of Na$^+$ present in the external medium, the osmotic pressure of the internal aqueous phase becomes higher than that of outer one and the liposomes burst,[19,20] resulting in TEA$^+$ efflux. Amphotericin induced TEA$^+$ efflux, which was conducted by Na$^+$ influx (Figure 5b). These two experiments with and without sucrose in the medium afforded information that the size of the channels opened by the amphotericin molecules was between that of Na$^+$ and TEA$^+$. In order to determine the channel size more precisely, we prepared liposomes loaded with TMA$^+$ instead of TEA$^+$ and performed the same experiment under conditions of osmotic protection. Simultaneous efflux of TMA$^+$ and K$^+$ was observed clearly. We also prepared liposomes loaded with TPA$^+$, the ionic size of which was larger than that of TEA$^+$, but this ion was not released as we expected. The

---

(19) Katsu, T.; Ninomiya, C.; Kuroko, M.; Kobayashi, H.; Hirota, T.; Fujita, Y. *Biochim. Biophys. Acta* **1988**, *939*, 57-63.

(20) Oku, N.; Nojima, S.; Inoue, K. *Biochim. Biophys. Acta* **1980**, *595*, 277-290.

relationship between the percent efflux and marker ion sizes are shown in Figure 6. It was clear that the diameter of the channels made by the amphotericin molecules was between that of TMA^+ (0.7 nm) and TEA^+ (0.8 nm), which accorded well with the size reported previously.[9] Therefore, this assay can provide detailed information about the sizes of channels formed in liposomal membranes.

Concluding Remarks. In this study, we have shown that the use of a series of tetraalkylammonium ions is suitable for the assay of liposomal membrane permeability, and combining marker ions of various sizes enabled us to determine the precise size of channels formed in liposomal membranes.

ACKNOWLEDGMENT

We wish to thank Ms. Kyoko Ito, who carried out some of the preliminary experiments that were extended in this study, and Ms. Tokiko Kawakami and Mr. Takashi Kayamoto for their technical assistance. This work was supported by a Grant-in-Aid from the Shimadzu Science Foundation and a Grant-in-Aid for Scientific Research from the Ministry of Education, Science and Culture of Japan.

RECEIVED for review July 1, 1992. Accepted October 22, 1992.

Anal. Chem. 1993, 65, 181–182

A New Low Conductivity Standard Solution

Truman S. Light*

4 Webster Road, Lexington, Massachusetts 02173

Edwards S. Atwood and John Driscoll

HNU Systems, Inc., 160 Charlemont Street, Newton Highlands, Massachusetts 02161

Stuart Licht

Department of Chemistry, Clark University, 950 Main Street, Worcester, Massachusetts 01610

A new conductivity standard solution is described that may be used for accurate determination of cell constants. This low-conductivity, high-resistivity solution is particularly applicable for calibration of cells that are used for measurement in the ultrapure water domain (0.0550 μS cm^{-1}, 18.18 MΩ cm, 25 °C). The low conductivity is achieved by the addition of 45–50% sucrose which increases viscosity 10-fold and correspondingly decreases the conductivity. A recommended concentration is 0.010 00 N acetic acid and 45.00% sucrose. The conductivity of this solution is 23.06 ± 0.1 μS cm^{-1} (resistivity of 43 370 Ω cm). The solution is stable for several months and is accurately prepared by common analytical methodology.

INTRODUCTION

The routine measurement of low-conductivity solutions, such as ultrapure water (0.0550 μS cm^{-1}, 18.18 MΩ cm, 25 °C), is important in the semiconductor, power, and nuclear reactor industries as well as in ordinary laboratory practice.[1,2] Slight differences in resistivity from that of pure water may be interpreted as ionic impurities at the fractional parts per billion level.[3,4] For this reason, cell constants need to be accurately calibrated with an accuracy of the order of 0.1%.

Standard solutions for obtaining cell constants are available in the ASTM literature for higher conductivity domains.[5] Employing these commonly used standard solutions, a lack of constancy in cell constants has been demonstrated for cells made of materials other than platinum.[1,3] The difficulty has been attributed to measurement problems inherent in the low electrical resistance of the solutions, the addition of extraneous resistance due to oxide coatings on the electrode surfaces, and other problems ascribed to alternating current errors at low resistance due to cable and electrode capacitances and shielding.[6] Many of these problems are mitigated if low-conductivity, high-resistance standard solutions are made available. Search for reproducible low-conductivity organic liquids has not been successful because of the inability to control the trace concentration of ions and the variability of impurity ions. Special solutions for standardization of cells used in low-conductivity applications have recently been suggested.[3,7] In 1990 NIST (National Institute for Standards and Technology) introduced the 25 μS cm^{-1} standard[7] which is composed of approximately 5.88 × 10^{-5} M hydrochloric acid solution. However, that solution is costly and due to its low concentration is particularly sensitive to environmental and other impurities. A 14.9 μS cm^{-1} standard suggested in 1991,[3] composed of 10^{-4} M KCl, is also quite dilute, is sensitive to environmental impurities, and has a relatively large blank correction.

This paper presents a procedure that permits preparation of standard solutions with unusually low-conductivity, high-resistivity, that are less susceptible to environmental contaminants and have an accuracy suitable for calibration of conductivity cell constants. Aqueous solutions with macro-concentrations of sucrose are utilized. Sucrose substantially increases the viscosity of the solution and, from the relationship illustrated by the Walden product,[8] decreases the diffusion coefficient and, correspondingly, the conductivity.

EXPERIMENTAL SECTION

Apparatus. Conductivity measurements were obtained with Thornton conductivity cells and a conductivity/resistivity meter, Thornton Model 750 LM, with resistance measurements verified with standard 0.1% resistors. A thermometer of 0.1 °C accuracy traceable to NIST was employed.

Reagents. All chemicals were reagent grade. Deionized water was used with a conductivity of less than 1.0 μS cm^{-1} at 25 °C when measured in air. The sucrose employed was tested to give a low blank. The 50% sucrose solution measured 2.0 μS cm^{-1} at 25.0 °C, which corresponds to 9 × 10^{-4}% if sodium chloride is assumed to be the ionic impurity. The 45% sucrose solution blank measured 3.0 μS cm^{-1} at 25 °C. The potassium chloride not only was reagent grade but also was certified with an analysis of 100.0% (NIST, J. T. Baker).

Procedure. Potassium chloride standard conductivity solutions were prepared as defined by ASTM procedures.[5] Acetic acid solutions, 0.010 00 M, were prepared by dilution of stock 1.000 M acetic acid (Aldrich, Catalog No. 31 859.0) and verified by titration of a 100.0-mL sample with standard 0.1000 M NaOH to a pH 8.6 end point with a glass electrode and 10.00-mL buret. Alternatively, appropriate dilution and standardization from glacial acetic acid may be employed. Sucrose solution mixtures were prepared by weight/weight to 0.1% relative error accuracy.

RESULTS AND DISCUSSION

Theory. The approximate relationship between the conductivity, κ, and viscosity, η, is known as the Walden product[8]

---

* To whom correspondence should be addressed.

(1) Thornton, R. D.; Light, T. S. *Ultrapure Water* 1989 (July/August), 14–26.

(2) Light, T. S.; Licht, S. *Anal. Chem.* 1987, *59*, 2327–2330.

(3) Light, T. S.; Thornton, R. D. *Ultrapure Water*, 1991 (April), 59–66.

(4) Pate, K. T. *Ultrapure Water* 1991 (Jan/Feb), 26–33.

(5) American Society for Testing and Materials. *Standard Test Methods for the Electrical Conductivity and Resistivity of Water*; ASTM D1125-91; ASTM: Philadelphia, PA, 1992.

(6) Braunstein, J.; Robbins, G. D. *J. Chem. Educ.* 1971, *48*, 52.

(7) NIST. *Standard Reference Material, SRM 3190* (25 μS cm^{-1} solution, $230/500 mL); National Institute of Standards and Technology: Gaithersburg, MD, 1991.

(8) Nakahara, M.; Ibuki, K. *J. Phys. Chem.* 1986, *90*, 3026–3030.

0003-2700/93/0365-0181$04.00/0

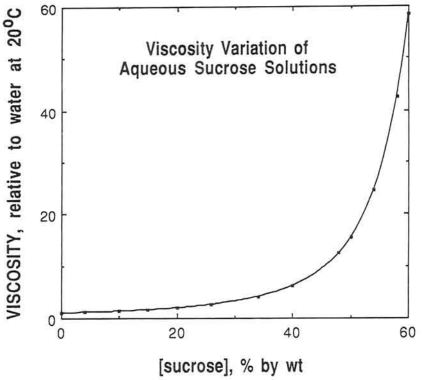

Figure 1. Viscosity variation of aqueous sucrose solutions.[9a,b]

$$\kappa\eta = \text{constant} \tag{1}$$

The inverse relationship between viscosity and the diffusion coefficient or conductivity is a property often used in physical chemical studies of aqueous solutions.[9a,10] The use of sucrose has proved to be a valuable device for substantially altering solution viscosity with a minimum of chemical interference. Figure 1 shows the viscosity variation in water due to the addition of sucrose[9a,b] and illustrates both the increasing magnitude as well as the increasing rate of change of the viscosity at higher concentrations of sucrose. A 45% sucrose solution increases the viscosity of water 9-fold, while a 60% concentration increases the viscosity 58-fold. Although the Walden product is known to be an approximation,[8] similar decreases in conductivity are expected and found.

The relations between cell constant (K, cm^{-1}), resistance (R, Ω), resistivity (ρ, Ω cm), conductance (C, S) and conductivity (κ, S cm^{-1}) is given by

$$\rho = R/K = RC/\kappa \tag{2}$$

Sucrose Standards. Solutions of potassium chloride were selected which corresponded to standard conductivity solutions described by ASTM.[5] These solutions along with acetic acid of similar concentration were studied with and without additions of large amounts of sucrose. Table I shows that for a given concentration of either potassium chloride or acetic acid, the conductivity is decreased by a factor of approximately 10 with the addition of 50% sucrose (weight/weight), and a factor of 7 in the presence of 45% sucrose. Table I also demonstrates that with or without the addition of sucrose, changing the concentration of potassium chloride by a factor of 10 results in a conductivity change a little less than 10, but changing the concentration of acetic acid by a factor of 10, again with or without sucrose, changes the conductivity by slightly more than 3. Both of these results are consistent with the strong and weak electrolyte characteristics of potassium chloride and acetic acid, respectively, and demonstrate that sucrose is essentially electrochemically inert.

A standard conductivity solution in the low-conductivity region is needed to obtain accurate cell constants for the several types of metal employed as electrodes in conductivity cells. Table II illustrates the variation in cell constants when calibration is made with standard solutions of varied resistance.[1,3] Minimum resistivity of several thousand ohm centimeters is apparently required to obtain cell constants which may be used in measurement of ultrapure water at the 18 MΩ cm level.

Table I. Conductivity with and without Sucrose, at 25.0 °C (Values Based on Cell Constants Obtained in Ultrapure Water As Described in Reference 1)

	conductivity[a] (μS cm^{-1})		
concn (M) potassium chloride	aqueous	50.00% sucrose	ratio (aqueous/sucrose)
0.001000	147.0	15.1	9.74
0.01000	1410	146.0	9.66
0.1000	13200	1390	9.50

	conductivity[a] (μS cm^{-1})		
concn (M) acetic acid	aqueous	50.00% sucrose	ratio (aqueous/sucrose)
0.001000	48.3	4.26	11.34
0.01000	164.6	15.7	10.48
0.1000	520	56.6	9.19

	conductivity[a] (μS cm^{-1})		
concn (M) acetic acid	aqueous	45.00% sucrose	ratio (aqueous/sucrose)
0.01000	164.6	23.16	7.11

[a] After subtraction of the conductivity of the water, or water plus sucrose, used to prepare the solutions.

Table II. Measured Variation in Apparent Cell Constants (cm^{-1}) for Conductivity Electrodes of Various Metals

electrode	soln C[a]	soln D[a]	soln E[b]	sucrose[c]	water[d]
titanium	0.1062	0.1031	0.1000	0.1000	0.0999
rhodium	0.1106	0.0995		0.0994	0.0993
platinum	0.1039	0.1012		0.0986	

[a] ASTM solution C (0.001 N KCl) and ASTM solution D (0.01 N KCl).[5] [b] Proposed solution (10^{-4} N KCl).[3] [c] Proposed standard, this paper, 45.00% sucrose + 0.010 00 M acetic acid. [d] As measured in ultrapure water of resistivity 18.18 MΩ cm, 25 °C.[1]

It is suggested that the solution, listed in Table I, which is composed of 0.010 00 M acetic acid with 45.00% sucrose (weight/weight) is suitable as a standard conductivity solution. The conductivity of this solution is 23.06 ± 0.1 μS cm^{-1} (43 370 Ω cm) at 25 °C and is suitable for determining cell constants of 0.1 or 0.01 cm^{-1} used for measurements of ultrapure water. It has proved to be fairly stable, increasing in conductivity, by about 0.2 μS cm^{-1}, following 3 months of storage and showing no discoloration. Another sample of analytical grade sucrose, from a source other than Aldrich, gave less stability and larger blanks and showed more rapid discoloration due to mold growth. Storage in air is not a problem since its acidity inhibits absorption of CO_2. Its conductivity is close to the lowest standard of 25 μS cm^{-1} available from NIST,[7] and the variation of viscosity with concentration is minimal (cf. Figure 1) so that minor errors in sucrose composition would have relatively little effect on the conductivity.

ACKNOWLEDGMENT

The loan of instrumentation by Thornton Associates is appreciated. This paper has been presented at the Pittsburgh Conference on Analytical Chemistry and Applied Spectroscopy in New Orleans, March 9, 1992.

RECEIVED August 10, 1992. Accepted October 21, 1992.

---

(9) (a) Zhang, X.; Yang, H.; Bard, A. J. *J. Am. Chem. Soc.* **1987**, *109*, 1916–1920. (b) Timmermans, J. In *Physico-Chemical Constants of Binary Systems*; Université Libre: Brussels, Belgium, 1960; Vol. 4.

(10) Licht, S.; Cammarata, V.; Wrighton, M. S. *Science* **1989**, *243*, 1176–1178.

Anal. Chem. **1993,** *65,* 183–187

TECHNICAL NOTES

On-Line Detection of Proteins in Gel Electrophoresis by Ultraviolet Absorption and by Native Fluorescence Utilizing a Charge-Coupled Device Imaging System

Lance B. Koutny and Edward S. Yeung*

Department of Chemistry and Ames Laboratory-USDOE, Iowa State University, Ames, Iowa 50011

INTRODUCTION

Slab-gel electrophoresis is the most common technique for the separation of high molecular weight biomolecules such as proteins.[1] Acrylamide gels, as described by Laemmli,[2] are generally the matrix of choice for the separation of SDS-denatured proteins via electrophoresis. Agarose gels, similar to those used for nucleic acids, are also useful for the separation of proteins but have not been widely applied.[3] Agarose gels are advantageous for many reasons including simplicity of gel casting, easy sample recovery, and the fact that it is nontoxic to both the experimenter and the proteins. In the past, agarose was not used because of its poor resolving power at molecular weights below 40 000. New agarose gel systems are available that will resolve proteins ranging from 20 000 to 200 000 with or without SDS denaturing.[4] In this study, agarose gel was chosen for its optical qualities and ability to be cast in an open system that can be imaged as the experiment is running.

The method most commonly used for visualization of the protein bands in the gel matrix is staining with coomassie brilliant blue. This process requires several hours and can only be done postrun. It is desirable to be able to monitor the electrophoresis during the run. There is one system available capable of online detection that is based on Schlieren optics. That system works quite well for acrylamide gels.[5] It is the goal of this paper to demonstrate two additional on-line detection schemes and compare them to traditional coomassie staining.

Of the 20 common amino acids that are the basic units of proteins, tryptophan, phenylalanine, and tyrosine display significant absorption in the ultraviolet region between 250 and 300 nm.[6] This property is the basis of detection of protein in most capillary electrophoresis experiments.[7] Detection of DNA via absorption of 254-nm ultraviolet radiation has been demonstrated in agarose slab gels in a method called ultraviolet shadowing,[8] which was recently improved upon by us utilizing a modern charge-coupled device (CCD) imaging system.[9] This shadowing system should also be capable of on-line detection of proteins in their native form in an agarose matrix, as we will attempt to demonstrate here. Direct UV densitometry should provide comparable detection limits, but that is not a simultaneous multichannel technique.

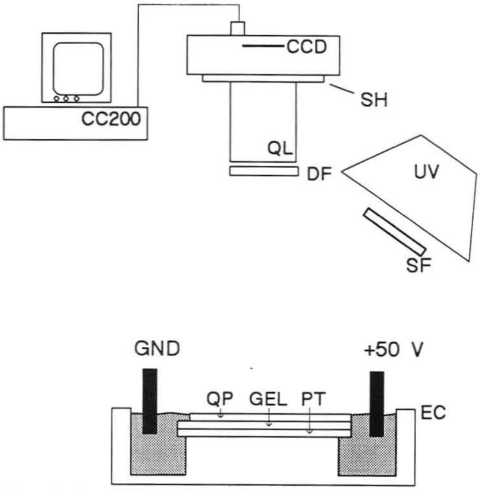

Figure 1. Experimental setup: CCD = charge-coupled device camera, SH = shutter, QL = quartz lens, DF = detection filter, UV = ultraviolet lamp, SF = source filter, EC = electrophoresis cell, QP = quartz plate, GEL = agarose gel, PT = Plexiglas tray, CC200 = data system for camera.

Proteins that contain tryptophan or tyrosine groups are known to fluoresce between 300 and 400 nm when excited with ultraviolet radiation within the absorption band of the three absorbing amino acids.[10] This native fluorescence has been exploited in capillary electrophoresis detection[11,12] but never in slab gels. This native fluorescence will be the basis of the other on-line visualization technique presented here.

EXPERIMENTAL SECTION

Gel Electrophoresis. The running buffer contained only 5 mM sodium phosphate (dibasic) titrated to pH 10.2 using 1 M sodium hydroxide. Both chemicals were analytical grade and were purchased from Sigma (St. Louis, MO). Ultrapure grade agarose was purchased from Bio-Rad (Richmond, CA). The protein standards used, conalbumin type V and chicken egg albumin grade V, were also purchased from Sigma. Both proteins were prepared in solution at 1 μg/μL concentrations in the running buffer. The human serum was derived by centrifugation from

---

(1) Andrews, A. T. *Electrophoresis: Theory, Techniques, and Biochemical and Clinical Applications*; Oxford University Press: New York, 1988.

(2) Laemmli, U. K. *Nature* **1970,** *227,* 680–685.

(3) Moos, M., Jr.; Nguyen, N. Y.; Lin, T.-Y. *J. Biol. Chem.* **1988,** *263,* 6005–6008.

(4) *FMC ProSieve Gel System: The Agarose System for Electrophoretic Separation of Proteins*; FMC BioProducts: Rockland, ME, 1992.

(5) Takagi, T.; Kubota, H. *Electrophoresis* **1990,** *11,* 361–366.

(6) Teale, F. W. J. *Biochem. J.* **1960,** *76,* 381–388.

(7) Jorgenson, J. W.; Wahlbroehl, Y. *J. Chromatogr.* **1984,** *315,* 135–143.

(8) Hassur, S. M.; Whitlock, H. W. *Anal. Biochem.* **1974,** *59,* 162–164.

(9) Chan, K. C.; Koutny, L. B.; Yeung, E. S. *Anal. Chem.* **1991,** *63,* 746–750.

(10) Konev, S. V. *Fluorescence and Phosphorescence of Proteins and Nucleic Acids*; Plenum Press: New York, 1967.

(11) Swaile, D. F.; Sepaniak, M. J. *J. Liq. Chromatogr.* **1991,** *14,* 869–893.

(12) Lee, T. T.; Yeung, E. S. *J. Chromatogr.* **1992,** *595,* 319–325.

0003-2700/93/0365-0183$04.00/0

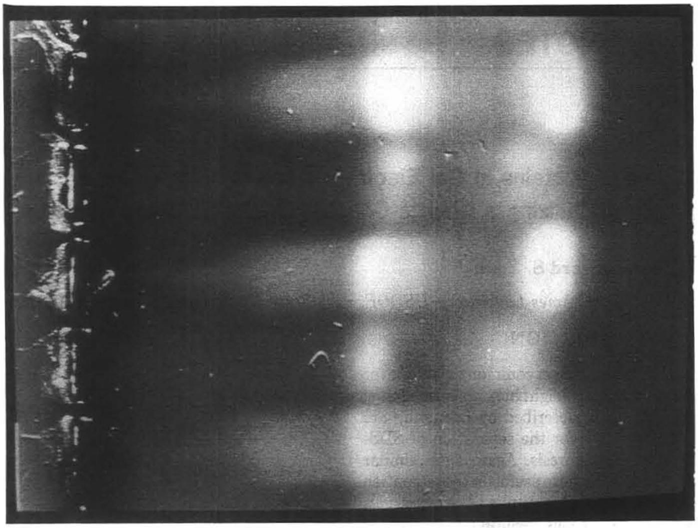

Figure 2. Flat-fielded image of protein native fluorescence in a slab gel after 70 min of electrophoresis. Electrophoresis direction is from left to right.

whole blood obtained from a healthy adult male and was diluted by a factor of 20 in the running buffer.

Agarose gels of 1.5% weight-to-volume in running buffer were cast in one of two sandwichlike manners. For native fluorescence detection, the gel was cast on a clear Plexiglas tray and covered with a 70-mm × 80-mm × 1.5-mm nonfluorescent quartz plate (Quartz Scientific). For ultraviolet absorption detection, the Plexiglas tray was replaced with one made from red fluorescent Plexiglas acquired from Plexiform (Iowa City, IA). In both cases, the gels were 3 mm thick, and the backs of the trays were spray-painted flat black. Sample wells were formed with a 1-mm × 5.5-mm comb and were approximately 2 mm deep. In all cases, 5 μL of sample was loaded in each well.

Electrophoresis was carried out horizontally in a mini sub cell (Bio-Rad) at a constant 50 V. The current measured was 20–25 mA. The running buffer level was adjusted to touch both ends of the gel without running on top of the gel sandwich. This was done to leave good optical access to the gel through the quartz plate.

For the staining detection method, gels were run using on-line detection, removed after completion of electrophoresis, and placed in a staining solution containing 40% methanol, 10% glacial acetic acid, and 0.5% coomassie brilliant blue (Sigma) for 4 h. Destaining, using the above solution minus the coomassie brilliant blue, required 36 h due to the thickness of the gels. The destained gel was then placed on a clear Plexiglas tray that had been spray-painted white for detection.

Detection. Figure 1 shows a schematic of the detection setup used for all three detection modes. A scientific grade cooled CCD digital camera system (PhotoMetrics Ltd., Model CC200, Tucson, AZ) was used to image the gels during electrophoresis. The system was equipped with a thermoelectrically cooled (Thomson TH7882) 384 × 576 pixel CCD. The camera head, with a 105-mm *f*/4.5 UV Nikkor quartz camera lens (Nikon, Japan), was securely mounted 55 cm above the gel. For native fluorescence, a 30-W hand-held UV lamp, operating at 254 nm, was mounted 15 cm above the gel. A 2-in. × 2-in. 10-nm band-pass interference filter centered at 254 nm with 13% transmittance (Melles Griot), was placed on the UV lamp, with the remainder of the light-emitting area masked off. To isolate the detector from the excitation source, a 305-nm glass cutoff filter (Melles Griot) was placed in front of the camera lens. For UV absorption detection, the interference filter was removed, and a 550-nm glass long-pass filter was placed in front of the camera lens. During detection of stained gels, the UV lamp was removed and diffused room light was used for illumination.

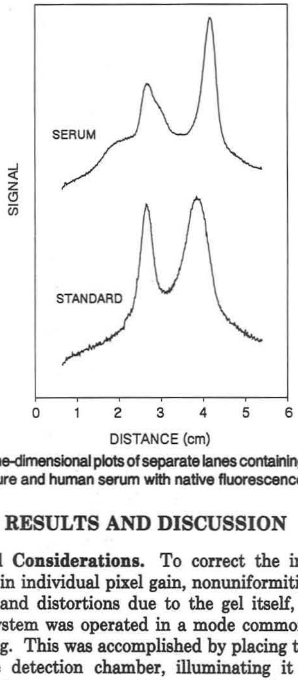

Figure 3. One-dimensional plots of separate lanes containing a standard protein mixture and human serum with native fluorescence detection.

RESULTS AND DISCUSSION

General Considerations. To correct the images for variations in individual pixel gain, nonuniformities in illumination, and distortions due to the gel itself, the CCD imaging system was operated in a mode commonly called flat-fielding. This was accomplished by placing the loaded gel in the detection chamber, illuminating it with the ultraviolet lamp, acquiring a blank image, and storing that digitally prior to application of the running voltage. Then, at desired intervals throughout electrophoresis, images were acquired and flat-fielded by simply dividing the current image by the blank, pixel by pixel, and multiplying the result by a constant factor. These calculations require only a few seconds for our 576 × 384 pixel images. The resulting images can then be displayed immediately and are also stored digitally for later analysis and printing. Flat-fielding was not applied to the staining technique since the gel must be handled, and

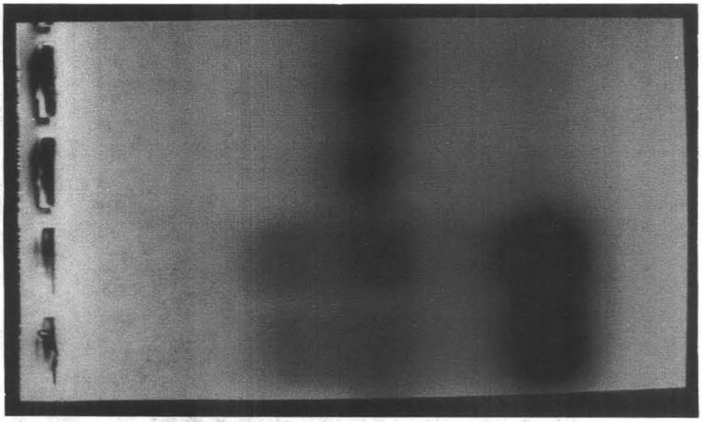

Figure 4. Flat-fielded image of protein ultraviolet absorption in a slab gel after 70 min electrophoresis. Electrophoresis direction is from left to right.

it would have been nearly impossible to place the gel in the exact position it was at prior to electrophoresis.

A major concern in both on-line detection schemes was fluctuations in background signals due to changes in the optical properties, such as fluorescence and scattering, of the gel during electrophoresis. Such fluctuations are not corrected by flat-fielding and, if large enough, tend to obscure the signal bands. Acrylamide gels were found to have very unstable fluorescent and scattering backgrounds that were possibly due to artifacts of the polymerization reaction and the fact that the gels did not adhere well to the quantz coverplate. Even with extensive prerunning of these gels in the horizontal sandwiched configuration, a steady background could not be achieved. Agarose gels have a higher background signal level due to scattering from the more opaque gel, but it is a constant background which is easily normalized during flat-fielding. One problem with our sandwiched agarose gels, however, is that this background changes as the gel heats up to near its melting point (typically 36 °C) and becomes less opaque. During electrophoresis, gels experience Joule heating that is directly related to the electrical current being passed through the gel. To minimize this heating, all gels were run with a 5 mM buffer instead of the 500 mM buffers typically used. This reduced the current from over 100 mA to near 20 mA for all runs, and gel heating was no longer a serious problem. An alternative approach that would allow for normal buffer strengths would be to design a system incorporating backside gel cooling while maintaining front-side optical access.

Many components of the on-line imaging system had to be carefully selected due to the fact that both absorption and fluorescence occur in the ultraviolet. Current CCDs, as manufactured, have an insignificant quantum efficiency below 400 nm. The CCD in our system was coated with MetaChrome II, a proprietary chromophore that is vacuum deposited on the CCD sensor when the imaging system is built.[13] With this coating, a quantum efficiency of 20% is attained for the entire ultraviolet region. To prevent unnecessary background signal, the plate covering the gel was constructed from Suprasil (Heraeus Amersil) fused silica, which does not fluoresce when irradiated with UV light. The optimum excitation and absorption wavelength of proteins is near 280 nm, but there is no convenient and intense broad area illumination source available at this wavelength. Instead, a low-pressure mercury lamp emitting at 254 nm was used. Although this is quite far from the maximum absorption wavelength, enough light was absorbed to demonstrate both on-line techniques. For the UV absorption technique, the use of a more appropriate wavelength would result in larger absorbance signals, thereby increasing the signal-to-noise ratio. For native fluorescence, a wavelength closer to the absorption maximum would shorten the amount of time required for signal accumulation and thus reduce the amount of background accumulated, again resulting in an increased signal-to-noise ratio. The last component of the imaging system subject to the ultraviolet requirement was the camera lens. Normal flint glass lenses do not pass light below 350 nm and are thus not applicable in the native fluorescence scheme. The lens required, which was made with quartz and lithium fluoride optical elements, was quite expensive and had to be custom built. The technology certainly exists to create an equivalent optical system based on reflective components (e.g. catadioptric lens). However, we are not aware of any standard supplier of such optics that will provide similar aberration-free images of the gel area.

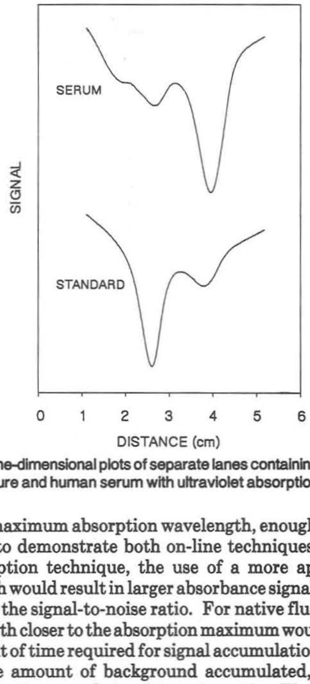

Figure 5. One-dimensional plots of separate lanes containing a standard protein mixture and human serum with ultraviolet absorption detection.

Native Fluorescence. Figure 2 is the flat-fielded image of protein native fluorescence detected after 70 min of

---

[13] Sims, G. R.; Griffin, F. *Proc. SPIE—Int. Soc. Opt. Eng.* **1989**, *1071*, 31–42.

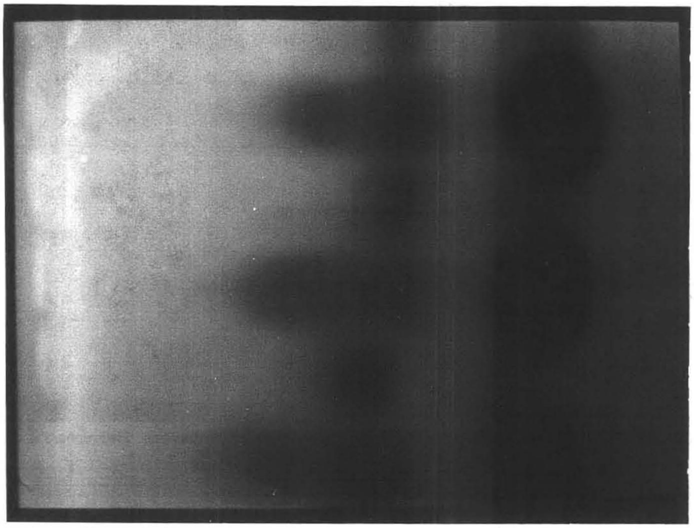

Figure 6. Image of coomassie blue stained protein gel after 70 min of electrophoresis. Electrophoresis direction is from left to right.

electrophoresis. The image was accumulated for 200 s, while electrophoresis was suspended, and flat-fielded with a 200-s blank frame as described earlier. The wells are located at the left side of the image, and electrophoresis proceeded horizontally across the imaged area. Counting from the top, lanes 2 and 4 were loaded with the two protein standards, and lanes 1, 3, and 5 were loaded with diluted human blood serum. Previously,[12] we have found that the fluorescence efficiencies of proteins are substantially higher at pH 10 than at pH 7. This explains our choice of the running buffer to optimize detectability.

Figure 3 presents the information from lanes 2 and 3 in a graphical manner. The plots were generated by averaging the rows of pixels that compose a lane into a one-dimensional chromatogram-like data set versus distance traveled in the gel. For the protein standard mixture, the first band, located 2.5 cm from the starting well, respresents conalbumin with a molecular weight of 68 000, while the second band, at 3.75 cm, is chicken egg albumin at 45 000. In the plot for human blood serum, the unresolved features from 1.5 to 3.0 cm are the four major globulin fractions while the well-resolved band at 4.0 cm is human albumin.[14] These separations are typical of slab gel electrophoresis at typical loadings, in agarose or in acrylamide gels. It can be seen that detectability is more than adequate for these applications. Exposure times under 1 min are clearly sufficient, particularly if more intense lamps are used.

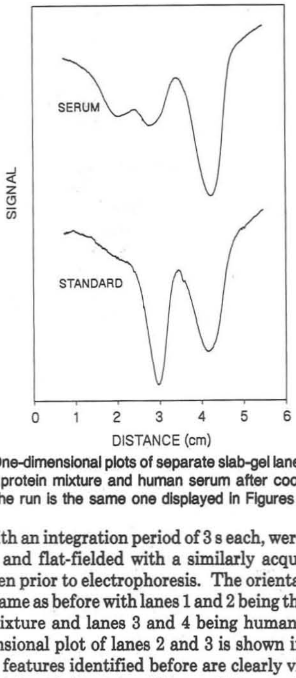

Figure 7. One-dimensional plots of separate slab-gel lanes containing a standard protein mixture and human serum after coomassie blue staining. The run is the same one displayed in Figures 2 and 3.

Ultraviolet Absorption. Figure 4 is the flat-fielded image of an ultraviolet absorption gel image after 70 min of electrophoresis. As before,[9,15] the CCD monitors the fluorescence of the Plexiglas in the visible region rather than the source intensity at 254 nm. This avoids interference from UV fluorescence from the gel, the buffer, or the optical components, and allows a standard CCD chip to be used. Thus, we expect UV absorption to be applicable to polyacrylamide gels as well. Since absorbance measurements using CCDs are inherently shot-noise limited due to the limited integrating capacity of the individual sensor elements,[15] frame averaging was used prior to flat-fielding. In this case, 16 frames, with an integration period of 3 s each, were acquired, averaged, and flat-fielded with a similarly acquired blank image taken prior to electrophoresis. The orientation of the gel is the same as before with lanes 1 and 2 being the standard protein mixture and lanes 3 and 4 being human serum. A one-dimensional plot of lanes 2 and 3 is shown in Figure 5. The same features identified before are clearly visible here, except that the relative intensities are different. This shows that ultraviolet absorption is a viable real-time technique for monitoring protein gel electrophoresis.

Coomassie Blue Staining. To allow a fair evaluation of the two on-line techniques, a coomassie blue stained gel image was run and is shown in Figure 6. This is actually the same gel that is shown in Figure 2 after staining and destaining, as described earlier. Figure 7 shows the one-dimensional plots of lanes 2 and 3, and once again, the same features occur with different relative intensities. It is important to note that Figure 6 provides an exact one-to-one correspondence to

---

(14) Putnam, F. W. *The Plasma Proteins*; Academic Press: New York, 1960; Vo. I, p 56.

(15) McGregor, D. A.; Yeung, E. S. *Anal. Chem.* **1992**, *64*, 1–6.

Figure 2; i.e. the detection techniques described here can directly replace standard visualization methods.

Detection Response. The difference in the relative protein band intensities from method to method is easily explained by examining the signal source in each case. In the traditional staining techniques, quantitative information is not available since the signal intensities are not proportional to the amount of protein present in the band due to inconsistencies in the staining process.[16]

In the direct fluorescence scheme, a proteins response is determined by many factors, of which the most important is the percentage of tryptophan residues.[10] Since not all proteins and peptides contain aromatic amino acids, this detection scheme is not universal. This actually may be advantageous when attempting to detect a small amount of a fluorescing protein in the presence of a large amount of a similarly sized nonfluorescing protein. It should be feasible to some day disperse the fluorescence spectrally, to provide identification based on tryptophan/tyrosine ratios, or to study protein conformations during electrophoresis.

The ultraviolet absorption technique is nearly universal since it only requires that a protein contains any of the three absorbing amino acids. The varying response of proteins depends on a combination of percent absorbers and total mass and is demonstrated clearly in Figure 5. In the standard mixture, both proteins are present at the same total mass as loaded, but the second band (chicken egg albumin) has a lower percentage of absorbers than the first (conalbumin) and thus displays a smaller signal.

Unlike traditional staining methods, both on-line techniques will give quantitative information. Although the signal obtained for different proteins at the same loaded mass varies, any individual protein will give a predictable signal based on concentration and its optical properties. This is assuming that the run conditions are identical so that spectral shifts due to conformations and the local environments are reproduced. The acquistion of an entire image as opposed to single-point densitometry also allows integration of the intensity (signal) over all pixels within a band to further improve quantitation.[17]

CONCLUSION

The CCD camera system is well suited for the on-line detection schemes presented in this paper because of its low noise characteristics and high sensitivity. The ability of the imaging system to perform flat-fielding was essential to both techniques as optical nonuniformities in the gels would have seriously degraded detection. As performed in this study, both on-line techniques appear to be competitive in terms of detectability with conventional staining methods. Silver staining of proteins presently offers better detectability, but there one loses the ability to monitor the separation in real time. It should be noted, however, that both on-line techniques could benefit from a more intense light source and a better spectral match with the absorption bands, as well as longer signal integration times. For this, the Mg arc lamp at 285.2 nm may be a reasonable excitation source.

Both on-line methods are compatible with traditional separation and detection methods. Other than switching to agarose gels and running at lower buffer strengths, both of which are desirable in many cases, the methods impose no restrictions on the operating parameters for slab-gel electrophroesis. Since neither the gel nor the proteins are altered, traditional methods such as staining can be performed after on-line detection, as shown in Figures 2 and 6, if desired. The on-line methods also have the advantage of simplifying protein recovery since no chromophores or radioactive labels must be removed after electrophoresis. In fact, if proteins were to be prestained for absorption or for fluorescence detection, it is likely that the separation will be compromised due to heterogeneity created by derivatization at multiple sites. Finally, the most attractive feature associated with on-line detection is the ability to manipulate the separation interactively during electrophoresis.[15]

ACKNOWLEDGMENT

The Ames Laboratory is operated by Iowa State University for the U.S. Department of Energy under Contract No. W-7405-Eng-82. This work is supported by the Director of Energy Research, Office of Basic Energy Sciences, Division of Chemical Sciences.

RECEIVED for review June 1, 1992. Accepted October 22, 1992.

---

(16) Yamamoto, H.; Nakatani, M.; Shinya, K.; Kim, B.-H; Kakuno, T. *Anal. Biochem.* **1990**, *191*, 58–64.

(17) Ma, Y.; Koutny, L. B.; Yeung, E. S. *Anal. Chem.* **1989**, *61*, 1931–1933.

Anal. Chem. **1993**, *65*, 188–191

Median Filtering for Removal of Low-Frequency Background Drift

Alvin W. Moore, Jr.,* and James W. Jorgenson

CB 3290, Department of Chemistry, University of North Carolina—Chapel Hill, Chapel Hill, North Carolina 27599

INTRODUCTION

We have recently discovered a very simple method of removing low-frequency baseline drift in chromatographic data. The method involves digitally filtering the chromatographic data using a moving median filter. This is a nonlinear filter which gives results quite different from the more common moving average filter. The moving median filter removes impulse characteristics (such as noise spikes) in a signal but preserves large sudden changes of level (i.e. edges) such as baseline shifts and low-frequency changes such as baseline drift.

Median filtering was suggested as a tool for data analyses by Tukey in 1971 and later came to be used in image processing.[1] Typical uses of the moving median filter include removal of noise in scanned images,[2,3] removal of cosmic ray spikes from image data collected with charge-coupled device (CCD) detectors,[4] and cleaning pitches from noise in speech processing.[5,6]

We are using the moving median filter in a manner parallel to an image-processing technique called object extraction.[1] In this case, the median filter is used to help distinguish objects in an image with a varying background. For our purposes, the objects of interest are the chromatographic peaks, while the varying background is the undesirable baseline drift. We first median filter the chromatogram, actually removing the peaks of interest and leaving only the baseline drift. We then subtract this filtered data from the original raw data to give the difference data. The difference data reproduces our original peaks of interest, but now on a flat baseline, with little or no distortion of the original peak shape.

In this note we will explain the nonlinear moving median filtering method and its application in removal of background drift. We will also identify some of the factors controlling its effective use.

EXPERIMENTAL SECTION

All data processing was done on a Macintosh II personal computer, running LabVIEW 2 software (National Instruments Corp., Austin, TX). LabVIEW 2 is a high-level scientific programming language for the Macintosh. It has a graphical user interface and comes with a number of preprogrammed ("canned") routines for digital signal processing. All of the digital filtering described here is done with the prewritten LabVIEW 2 routines. However, implementation of the moving median filter in other programming languages should not be difficult (see mathematical description of filter, below).

Data taken from the literature were scanned into the computer as a bitmap using a Microtek MSF 300GS image scanner and then digitized into numeric data using Flexitrace software (Tree Star, Inc., Campbell, CA).

FILTERING

In image processing, the moving median is used to suppress impulse noise. Here, impulse refers to locally large positive or negative values of short duration. Moving median filters suppress such noise provided the filtering window is at least twice the width of the impulses. Then impulses which are sufficiently separated will be completely deleted by the filter. Impulses lying close to each other may remain, though reduced in intensity. In our case, the "impulses" are not noise but are the chromatographic peaks, actually the part of the signal we wish to keep. The filter rank value controls the width of the window and determines whether peaks will pass through or be eliminated.

The moving median filter processes the input data such that each point in the output data is the median of a subset (window) of points centered on the corresponding point in the input data. The median is the middle value of the subset, after sorting it from high to low values. Chromatographic peaks in the data will always be sorted toward the high end of the subset, while baseline values in the data will always be sorted toward the low end. Thus peaks which span less than half the points in the subset never reach the middle (median) value and are effectively removed from the output data.

Mathematically, the median filter can be explained as follows. The median filter routine accepts as inputs the data array to be filtered, X, of size n, and a value for the filter rank, r, where $n > r \geq 0$. The output of the median filter routine is a filtered data array, Y, of the same dimensions as X. Each point in the output array is the median of a subset of $2r + 1$ points centered on the corresponding point in the input array, that is

X = input array, data to be filtered

Y = output array, filtered data

n = size of input array

r = median filter rank, where $n > r \geq 0$

J_i = subset of input array X, centered about the *ith* element of X, such that

$$J_i = \{x_{i-r}, x_{i-r+1}, ..., x_{i-1}, x_i, x_{i+1}, ..., x_{i+r-1}, x_{i+r}\}$$

and indexed elements outside the range of X are set equal to zero. The elements of Y are calculated by $y_i = \text{median}(J_i)$, for $i = 0, 1, 2, ..., n - 1$.

As mentioned earlier, peaks which make up less than 50% of the points in a subset are removed. The median filter preferentially removes sharper peaks and passes broader features, and its discrimination between sharp and broad is controlled by the value of the filter rank, r. Lower values of r give smaller windows and only remove the sharpest peaks, while higher values of r give larger filtering windows and can result in the removal of even relatively broad peaks from the input data.

BASELINE CORRECTION

We would like to remove the baseline drift which is often a problem in chromatographic data and retain the sharp solute peaks that "ride" on top of the drift. Also, we would like to do this without significantly affecting the areas, heights, or shapes of the peaks of interest.

---

(1) Justusson, B. I. In *Two-Dimensional Digital Signal Processing II, Transforms and Median Filters*; Huang, T. S., Ed.; Springer-Verlag: New York, 1981; pp 161–196.

(2) Franco, M.; Treister, A. *Flexitrace, Automatic Graph to Number Conversion*; Tree Star Inc.: Campbell, CA, 1990.

(3) Wecksung, G. W.; Campbell, K. *Computer* 1974, 7, 63–71.

(4) CSMA Software Manual; Princeton Instruments Inc.: Trenton, NJ, 1990.

(5) Rabiner, L. R.; Sambur, M. R.; Schmidt, C. E. *IEEE Trans. Acoust., Speech, Signal Process.* 1975, 23, 552–557.

(6) Jayant, N. S. *IEEE Trans. Commun.* 1976, 24, 1043–1045.

0003-2700/93/0365-0188$04.00/0

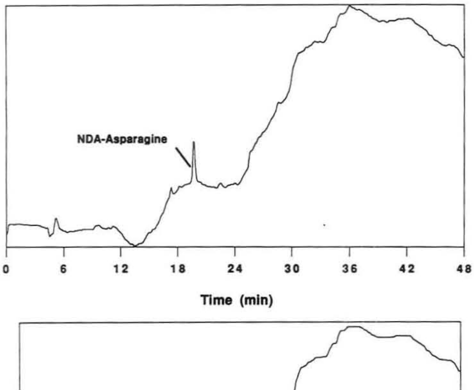

Figure 1. (a, Top) raw data. Chromatographic analysis scanned in from ref 7 and digitized. (b, Middle) median-filtered data. Raw data filtered with a median filter of rank 52. (c, Bottom) raw minus median-filtered data. Background-subtracted (difference) data, raw data from Figure 1a minus median-filtered data from Figure 1b.

Figure 1a is a chromatogram taken from the literature.[7] The data as plotted in the literature were scanned in, digitized, and replotted to give Figure 1a. A total of 2000 points were taken across the x-axis, so the effective sampling rate for the data shown is 0.7 Hz. This is a liquid chromatographic (LC) analysis of naphthalene-2,3-dicarboxaldehyde (NDA) labeled asparagine using an electrochemical detector in the amperometric mode. The y-axis in the original data is electrochemical oxidation current. Since this is a gradient LC run near the detection limit for NDA–asparagine, baseline drift is severe.

Figure 1b is the result of filtering the raw data in Figure 1a with a median filter of rank 52. That is, each point in Figure 1b is the median of a 105-point ($2r + 1 = 105$) subarray centered on the corresponding point in Figure 1a. Notice that the sharp NDA–asparagine peak and most of the other sharp features in Figure 1a are missing in Figure 1b, but most of the characteristics of the baseline drift remain. The information we are interested in, however, is generally in the sharper features. Next we subtract the data in Figure 1b from that in Figure 1a to obtain Figure 1c, the difference data. In Figure 1c, the NDA–asparagine peak is now the largest peak in the chromatogram, on what is now a flat baseline. The other sharp features from Figure 1a are also accurately carried through into Figure 1c, only much more discernible now after removal of the drift.

QUANTITATION

To quantitatively measure the effects of the filtering procedure, we compared peak height and peak area for the asparagine peak in the raw data and the difference data. Peak areas and heights were calculated from the digitized data using a program written in LabVIEW. The peak start and stop times for the asparagine peak in the raw data were arbitrarily chosen by the user. The program then drew a baseline between these two points, and y-axis values for this baseline were subtracted from the peak's values to get corrected y-values. These corrected values were then used in the peak integration and peak height calculation routines, to avoid any additional area or height due to the baseline drift. The same method and the same start and stop times were used in calculating areas and heights for the raw data and the background-subtracted (difference) data. Results of these peak comparisons as a function of the rank of the median filter are shown in Figure 2.

Figure 2a shows the percent area of the filtered peak relative to the unfiltered peak as a function of the rank of the median filter used. Figure 2b is a similar comparison of peak height. Since the results for peak heights follow the same trend as peak areas, the following discussion will consider only peak areas.

In general, the optimum rank value is greater than or equal to the width at the base (measured in the number of data points) of the widest peak of interest. This will ensure that the filtering window for the moving median is over twice the peak width, and the peaks will be completely removed from the filtered data. Since the width is measured in the number of data points rather than time, the data acquisition rate must be considered. A peak 30 s wide sampled at 1 point/s (Hz) will require a rank of 30 (to give a filtering window width of 61 points). This will ensure that the peak will be completely removed in the filtered data. The same peak sampled at 2 Hz would be 60 points wide and require a rank of 60 (a window 121 points wide).

For a given peak, here NDA–asparagine, peak area in the difference data is much less than in the original data if the rank is less than the optimum value for that peak. If the rank is greater than the optimum value for that peak, peak area in the difference data increases slightly.

The asparagine peak is about 80 s wide at the base, and the effective data acquisition rate for this scanned image is 0.7 Hz. This gives 56 points across the peak and an optimum rank for filtering (as defined above) of 56. In practice we find that peak areas are the same in the original and difference data for ranks of 52–64. As shown in Figure 2a, below rank 52, peak area values drop rapidly in the difference data. Above the optimum, peak area in the difference data has risen only 2% by rank 96. This can be explained as follows.

At rank values below the optimum, significant signal from relatively sharp peaks passes through the median filter and is subtracted out in the second step of the procedure. Thus peak areas in the difference data are lower than in the raw data. At some point (for the asparagine peak, at ranks 52–64), the peak area in the difference data exactly equals that in the raw data. This is the ideal rank value to use with the

---

[7] Oates, M. D.; Jorgenson, J. W. *Anal. Chem.* **1989**, *61*, 432–435.

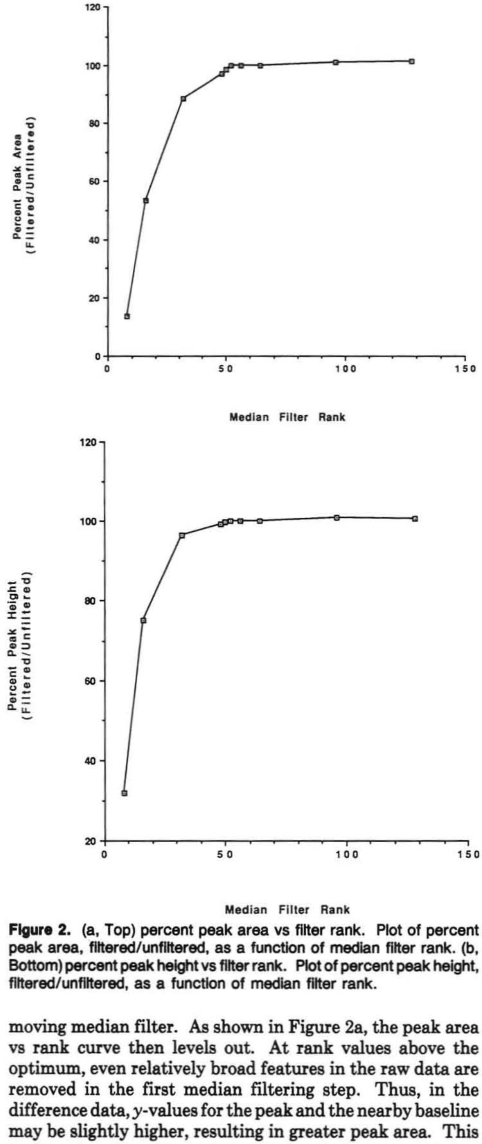

Figure 2. (a, Top) percent peak area vs filter rank. Plot of percent peak area, filtered/unfiltered, as a function of median filter rank. (b, Bottom) percent peak height vs filter rank. Plot of percent peak height, filtered/unfiltered, as a function of median filter rank.

moving median filter. As shown in Figure 2a, the peak area vs rank curve then levels out. At rank values above the optimum, even relatively broad features in the raw data are removed in the first median filtering step. Thus, in the difference data, y-values for the peak and the nearby baseline may be slightly higher, resulting in greater peak area. This is also a function of how close to the peak the start and stop times are chosen, as most of the difference is in the baseline values around the peak.

Choice of the optimum rank value for this method depends in several ways on the particular data being filtered. If there are several peaks of interest, some more broad than others, then the rank value necessary to accurately reproduce the broader peaks should be used. A rank value that is higher than necessary for a sharper peak would result in less error in peak area than a rank value that is too low for a broader peak, if both peaks are of interest.

Another consideration is peak density, the number of peaks within the filter window used. The method works best for well-separated peaks. If the peaks are sharp, such that a lower rank value could be used, but there are enough of them in one window to span more than 50% of the points in that window, they will be filtered incorrectly. Multiple peaks in the raw data will pass through the median filter as one broad peak and will result in low area values and dips below baseline in the difference data. In this case a larger rank value would be needed to give a more accurate treatment of the tight cluster of peaks.

DISCUSSION

Statistically, the median is both robust and nonparametric. No assumptions need be made about the noise distribution in the signal or the population from which the signal data are drawn.[8] The median filter is also resistant to outliers. For a given set of values, a large change in a small number of values would have a large effect on the mean of those values but would have only a small effect on the median. This is in fact the basis of the use of the median filter in this method.

The effects of the moving median filter are quite different from those of other common digital filtering routines. Because it is nonlinear, the moving median filter has no general frequency response function. The response calculated for a particular function will not apply to linear sums of that function or other functions.[1] It is this unique feature which is helpful in our application.

In the first step, we wish to filter out the chromatographic peaks of interest to leave only the baseline drift. The peaks are sharper than the baseline drift and generally contain more high-frequency components, but they also contain some low-frequency components. Thus most linear digital filters which discriminate by frequency are handicapped. High-pass filters lose some of the low-frequency components of a peak as they attempt to block the low-frequency baseline drift. Low-pass filters (used as we use the moving median, in a two-step filter and subtract method) allow low-frequency components of peaks to pass through, but they are then lost in the subtraction step. The moving median has an advantage here because it removes "impulses" relative to a background level, irrespective of frequency. If the filtering window used is of the appropriate size, both high- and low-frequency components of a peak are filtered off together and then restored in the final difference data.

Figure 3 shows the results of some common digital filters applied to the same data seen in Figure 1. These filters are based on the fast Fourier transform (FFT) and as such discriminate on the basis of frequency. The Butterworth filter (Figure 3a) gives a flat response in both the passband and the stopband, and the sharpness of the rolloff (transition between passband and stopband) is determined by the number of filter poles. The minimum number of poles is 2, and the Butterworth and all other filters in this example are two poled. This gives a broader rolloff, but using more than two poles to sharpen the rolloff has the negative effect of increasing ringing in the filtered data.

The Chebyshev filter (Figure 3b) has a flat response in the stopband and gives a sharper rolloff than the Butterworth but allows some ripple in the passband, while the Chebyshev II (or inverse Chebyshev, Figure 3c) allows ripple in the stopband and is flat in the passband.

These filters have a distinct phase response for each frequency present in the input data, which results in a phase shift in the output data. To eliminate this, the filtered data array can be reversed and passed through the filter a second time.[9] All frequencies phase shifted during the first pass will

---

(8) Snedecor, G. W.; Cochran W. G. *Statistical Methods*, 7th ed.; The Iowa State University Press: Ames, Iowa, 1980.

(9) Hamming, R. W. *Digital Filters*, 2nd ed.; Prentice-Hall, Inc.: Englewood Cliffs, NJ, 1983.

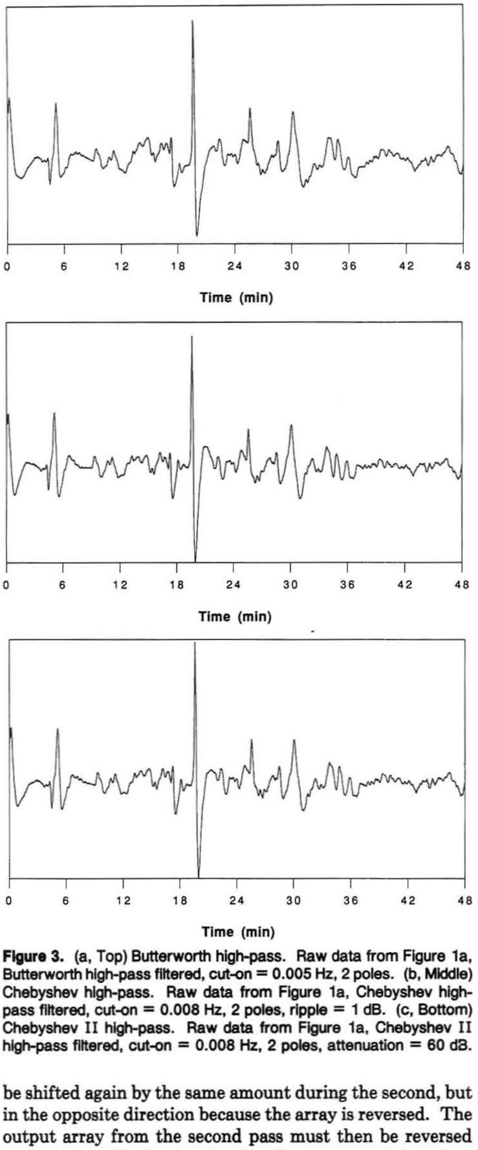

Figure 3. (a, Top) Butterworth high-pass. Raw data from Figure 1a, Butterworth high-pass filtered, cut-on = 0.005 Hz, 2 poles. (b, Middle) Chebyshev high-pass. Raw data from Figure 1a, Chebyshev high-pass filtered, cut-on = 0.008 Hz, 2 poles, ripple = 1 dB. (c, Bottom) Chebyshev II high-pass. Raw data from Figure 1a, Chebyshev II high-pass filtered, cut-on = 0.008 Hz, 2 poles, attenuation = 60 dB.

be shifted again by the same amount during the second, but in the opposite direction because the array is reversed. The output array from the second pass must then be reversed again before display to give the data in its original time sequence.

Results for the Butterworth no-phase filter are shown in Figure 4, both for the high-pass (Figure 4a) and the low-pass-with-subtraction (Figure 4b). These actually give the best results for the linear digital filters tested, but even here the resulting "smoothed" baseline is much worse than that obtained with the moving median.

CONCLUSIONS

The median filtering method described above gives effective removal of baseline drift while maintaining peak heights and areas in the sharper portions of the signal. As with most filtering schemes, it works best when the peaks of interest are on a very different time scale from the undesirable background. In general, sharp peaks on a broad rolling baseline will be handled more easily than broader peaks on the same baseline. Unlike some other filtering methods, it is sensitive to peak density in the input data, and the filtering is more a function of the number of data points across a peak than the particular frequency components of that peak.

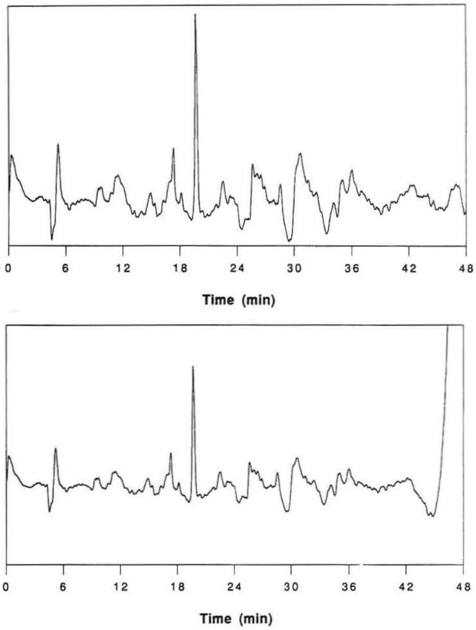

Figure 4. (a, Top) Butterworth no-phase, high-pass. Raw data from Figure 1a, phase-corrected Butterworth high-pass filtered, cut-on = 0.003 Hz, 2 poles. (b, Bottom) Butterworth no-phase, low-pass difference. Raw data from figure 1a, phase-corrected Butterworth low-pass with subtraction of filtered data from raw data. Cut-off = 0.0035 Hz, 2 poles.

The method is easy to program on a personal computer and may find use in a variety of other applications. An appropriate rank value is easily determined using the guidelines above and knowledge of the peaks of interest and, once chosen, generally works on all analyses of that same type. In contrast to the other digital filtering methods we examined, choosing a suitable rank value required much less detailed knowledge of the input data. The other filters tested require in-depth examination of the frequency distribution of the input data or much trial-and-error with the filter coefficients.

ACKNOWLEDGMENT

This research was supported by a grant from the National Institute of Health (GM 39515) and by a gift from Hewlett-Packard. A.W.M. was supported by a fellowship from the Department of Education (Contract No. P200A10047).

RECEIVED for review May 1, 1992. Accepted October 5, 1992.

AUTHOR INDEX

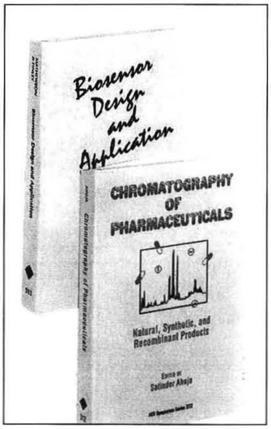

Biosensor Design and Application
CHROMATOGRAPHY OF PHARMACEUTICALS
Natural, Synthetic, and Recombinant Products
Satinder Ahuja

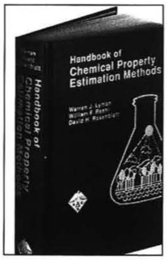

Handbook of Chemical Property Estimation Methods
Warren J. Lyman
William F. Reehl
David H. Rosenblatt

For total performance, nothing compares to our new benchtop GC/MS.

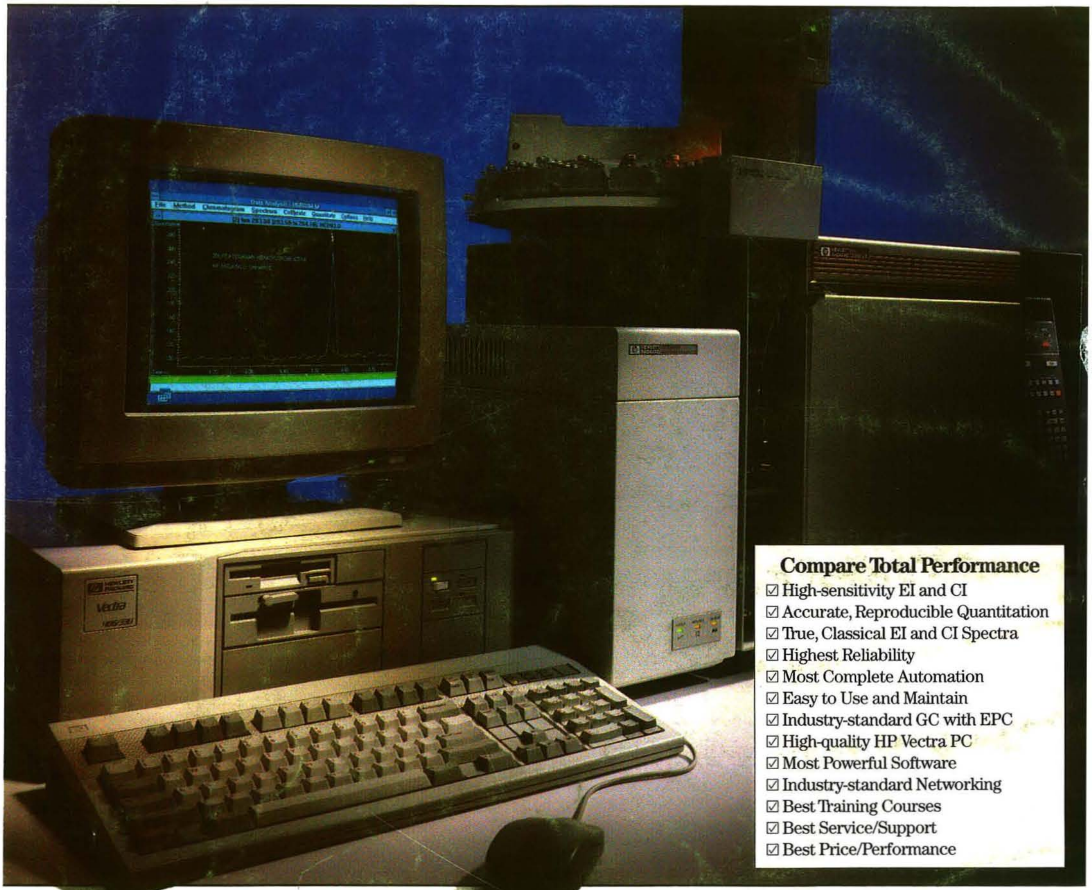

Compare Total Performance

- ☑ High-sensitivity EI and CI
- ☑ Accurate, Reproducible Quantitation
- ☑ True, Classical EI and CI Spectra
- ☑ Highest Reliability
- ☑ Most Complete Automation
- ☑ Easy to Use and Maintain
- ☑ Industry-standard GC with EPC
- ☑ High-quality HP Vectra PC
- ☑ Most Powerful Software
- ☑ Industry-standard Networking
- ☑ Best Training Courses
- ☑ Best Service/Support
- ☑ Best Price/Performance

Compare GC/MS offerings today and you'll find only one stands out on all counts: the new HP 5972A MSD, combined with the latest HP 5890 Series II GC and HP Vectra PC-based ChemStation.

For starters, compare sensitivity. The new HP system provides high-sensitivity classical EI and CI spectra, in both selected ion monitoring (SIM) and scan modes. That means you can perform ultra-trace analyses of complex mixtures at picogram and femtogram levels.

Then compare quantitation. You'll find the new HP 5972A MSD has a large dynamic range, linear over four orders of magnitude. And Electronic Pressure Control on the GC automatically compensates for vacuum at the MSD, assuring constant flow rates. Result: reproducible spectra and accurate quantitation for both trace and high-level components in tough matrices, such as waste water, food and physiological fluids.

The total performance benchtop system also means higher productivity. It lets you completely automate your operation, from injection through printed reports. And its network readiness enhances automation and data sharing throughout your organization. Plus it's backed by HP's top-rated service and support. For details, call **1 800 334-3110**, Ext. 235.

HEWLETT PACKARD

Sales Representative: Circle Reader Service Card No. 45 Literature: Circle Reader Service Card No. 46

© 1992 Hewlett-Packard Company AGO 4120